Computational Investigation of photocatalytic activity of Sn-doped Zinc Oxide nanoparticles

CO Ayo-Olaojo

orcid.org 0000-0003-0677-2290

Dissertation accepted in fulfilment of the requirements for the degree *Master of Science in Chemistry* at the North-West University

Supervisor:	Prof CGCE van Sittert
Co-supervisor:	Mr K Meerholz
Assistant Supervisor:	Prof DC Onwudiwe

Graduation: May 2025

Declaration

I, Caroline Olajumoke Ayo-Olaojo, affirm that the dissertation titled "Computational Investigation of Photocatalytic Activity of Sn-Doped Zinc Oxide Nanoparticles," submitted to fulfil the requirements for the Master of Science degree in Chemistry, is my original and independent work, conducted under the supervision of Prof C.G.C.E. van Sittert, Mr K. Meerholz, and Prof D.C. Onwudiwe. All sources used are acknowledged in the text, and this work has not been submitted in whole or in part to any other tertiary institution.

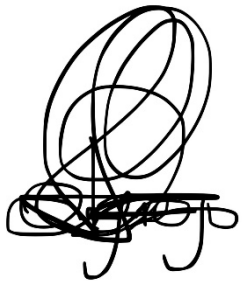

Caroline Olajumoke Ayo-Olaojo

Preface

This dissertation represents an original, independent, and unpublished work by C.O. Ayo-Olaojo, conducted under the supervision of Prof C.G.C.E. van Sittert, Mr K. Meerholz, and Prof D.C. Onwudiwe. The study focuses on a computational investigation within the field of photocatalysis, specifically examining the photocatalytic activity of tin (Sn)-doped zinc oxide (ZnO) nanoparticles. It evaluates how Sn doping reduces ZnO's band gap and work function, improving electron transfer, charge separation, and migration, thereby enhancing its overall photocatalytic activity.

The project primarily investigates the structural and electronic properties of ZnO in three crystal systems using density functional theory (DFT) based calculations. It identifies the most stable crystal system based on surface energies, validates these findings against literature values, and then introduces varying percentages of Sn (6.25%, 12.50%, and 18.75%) into the most stable ZnO crystal system. Using DFT, the study optimises and determines the structural and electronic properties of the resulting Sn-doped ZnO systems. The study then identifies the doping percentage that most effectively reduces the band gap and lowers the work function, recommending it for improved photocatalytic activity.

This dissertation adheres to the formatting guidelines specified in the North-West University's[1] manual for postgraduate studies. It includes a summary, a list of abbreviations, and a table of contents, with the main body comprising five chapters.

Chapter 1 discusses the importance of semiconductor photocatalysts in degrading industrial pollutants and explains the necessity of doping to improve their effectiveness. It outlines the study's specific aims and objectives and provides a broad overview of the methodology used. The problem statement highlights ZnO's limited reactivity to UV light due to its large bandgap, which significantly hampers its use as a photocatalyst. The study proposes doping ZnO with Sn to enhance its photocatalytic activity to overcome this issue.

Chapter 2 presents a comprehensive literature review discussing the fundamentals of photocatalysis, the mechanisms of ZnO, and recent advancements in this material. It also explores the significance of the band gap, the crystal structure and electronic properties of ZnO and its role as a photocatalyst. Additionally, the chapter discusses the computational modelling of ZnO and the effects of doping.

Chapter 3 starts with a comprehensive review of existing research on ZnO bulk and surface studies, exploring how experimental and computational methods have aimed to enhance ZnO's photocatalytic activity. The chapter benchmarks the computational method by comparing it with previous DFT studies on ZnO models in terms of accuracy. Next, the study details the method development phase, which includes generating and optimising ZnO structures in hexagonal wurtzite, cubic rock salt, and cubic zinc-blende (sphalerite) forms. These structures were expanded into 2x2x2 bulk models, and different surfaces were created by cutting along various Miller planes, with separation ensured by a vacuum gap. Finally, the chapter explores the structural and electronic properties of ZnO in three crystal systems, identifying the most stable system based on surface energies. The morphology of the crystal system was determined using the WULFF[2] program to represent the surfaces found on nanoparticles accurately.

Chapter 4 investigates the effects of Sn doping on ZnO. Sn was introduced into the most stable ZnO bulk structure identified in Chapter 3 at concentrations of 6.25%, 12.50%, and 18.75%. The Sn-doped ZnO structures were optimised, and their electronic and structural properties were calculated using DFT to assess the impact of doping. These properties were compared to those of pure ZnO to highlight the changes. The chapter concludes with a comparative analysis of pure ZnO and Sn-doped ZnO, focusing on differences in bandgap and work function, and identifies the doping concentration that results in the most significant bandgap reduction. Additionally, the chapter determines the morphology of the Sn-doped ZnO crystal systems based on surface energies using the WULFF[3] morphology, ensuring an accurate representation of the surfaces found on nanoparticles.

Chapter 5 concludes the study with final remarks and conclusions on the impact of Sn-doping on the photocatalytic activity of ZnO surfaces. This chapter also offers recommendations for future work on calculating the electronic and structural properties of the Sn-doped ZnO nanoparticles.

References

(1) *Manual for Masters and Doctoral Studies, 2016*. North-West University, https://services.nwu.ac.za/sites/services.nwu.ac.za/files/files/research-support/documents/2016-04-06%20ICRI%20Manual%20for%20M%20and%20D%20students.pdf (accessed July 02, 2024).

(2) Rahm, J.; Erhart, P. WulffPack: A Python package for Wulff constructions. *Journal of Open Source Software* **2020**, *5*, 1944. DOI: 10.21105/joss.01944.

(3) Wulff, G. XXV. On the question of the rate of growth and dissolution of the crystal surfaces. *Kristallografiya* **1901**, *34*, 449-530. DOI: 10.1524/ZKRI.1901.34.1.449.

List of Poster Presentations

- Computational Investigation of Zinc Oxide Nanoparticles as Possible Photocatalysts Catalysis South Africa (CATSA). *32nd Annual International CATSA Conference;* Drakensberg, Kwa Zulu Natal South Africa, November 2022.
- Computational Investigation of Zinc Oxide Nanoparticles, South African Chemical Institute (SACI). *44th SACI National Convention,* Stellenbosch Western-Cape South Africa, January 2023.
- A DFT Study of the Properties and Structure of Zinc Oxide, Chem4Energy*,* Potchefstroom North-West South Africa April 2023.

List of Articles

- Ayo-Olaojo, C.O.; Meerholz, K.; Onwudiwe, D.C.; van Sittert, C.G.C.E., Density Functional Theory (DFT) study of the structural and electronic properties of ZnO, to be submitted to the Journal of Molecular Modelling.
- Ayo-Olaojo, C.O.; Meerholz, K.; Onwudiwe, D.C.; van Sittert, C.G.C.E., The investigation of various Sn-doped Zinc Oxide surfaces using Density Functional Theory, to be submitted to the Journal of Molecular Modelling.

Permission to Submit for Degree Purposes

We, the undersigned co-authors of the listed manuscripts, hereby grant permission for its submission as part of Caroline Ayo-Olaojo's Master's degree requirements. We confirm that our contributions to this work are accurate and complete. Additionally, we acknowledge collective responsibility for the results presented in these manuscripts.

- Ayo-Olaojo, C.O.; van Sittert, C.G.C.E.; Meerholz, K.; Onwudiwe, D.C., Density Functional Theory (DFT) study of the structural and electronic properties of ZnO
- Ayo-Olaojo, C.O.; van Sittert, C.G.C.E.; Meerholz, K.; Onwudiwe, D.C., The investigation of various Sn-doped Zinc Oxide surfaces using Density Functional Theory

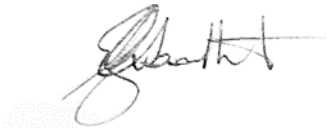

Prof. C.G.C.E. van Sittert

Mr. K. Meerholz

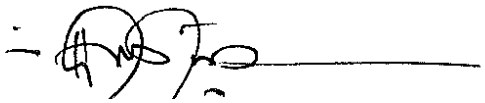

Prof. D.C. Onwudiwe

Acknowledgements

First and foremost, I want to express my gratitude to God for providing me with the strength to navigate through the challenges of my darkest and most uncertain days. Your boundless love has been my guiding force.

I extend my sincere appreciation to the Chemical Resource Beneficiation (CRB) for awarding me a bursary to support my research. Special thanks go to the Laboratory for Applied Molecular Modelling (LAMM), the Centre of High-Performance Computing (CHPC), and the North-West University (NWU) for their provision of equipment and facilities.

I am deeply thankful to my supervisor, Prof Cornie van Sittert, for affording me the opportunity to engage in research under her guidance. Her dedicated efforts have turned a lifelong personal goal into reality. Her words of encouragement, mindfulness, and unwavering support have been invaluable.

To my co-supervisor, Mr Kyle Meerholz, I express my heartfelt gratitude for his involvement in this project. Thank you for your technical, literary, and creative insights, as well as your constructive critiques. Your mentorship has been instrumental in developing my scientific and technological abilities.

To my assistant supervisor, Prof Damian Onwudiwe, I appreciate your role in initiating this project, providing a pathway for me to contribute to the body of knowledge.

A special acknowledgement goes to my mentor and friend, Dr Tsepiso Khutlane. Without your contributions, this project would not have succeeded. Thank you for being a maternal figure in a foreign land, offering support, encouragement, and bright company during my darkest moments.

Dr Jean du Toit, I appreciate your role in organising writing course workshops that significantly aided me in constructing my dissertation. Thank you for consistently inviting me to your courses and for your ever-ready assistance with the language editing of this dissertation.

To my colleagues at the LAMM; Monique, Cherise, Annarie, Theuns, and Cornelius, I am grateful for the various ways in which you contributed to the realisation of this project. Your friendship, above all, is cherished.

To my dearest friends, Opeyemi Johnson Fadeyi, Anouska Nandalall, and Surv. Bolaji Oladotun, your emotional support and encouragement have meant the world to me. I am truly grateful for your kindness and care. I love to you all.

To my loving and ever-supportive Mother, thank you for being my unwavering pillar of support from my elementary days to this very moment. You have been a constant source of light on my educational journey.

Lastly, I dedicate this achievement to my late father in heaven. Daddy, I've made it, and I am confident that you would be proud of me.

Abstract

Photocatalysts, such as zinc oxide (ZnO), are used in various industrial processes, including manufacturing photovoltaic solar cells, optical sensitisers, optoelectronic devices and degradation of organic pollutants. ZnO is particularly effective due to its strong oxidising power, hydrophobicity, notable antimicrobial properties, stability, and non-toxicity. However, its photocatalytic activity is confined mainly to the UV range of the solar spectrum because of its large band gap, resulting in lower efficiency and prompting research for improvement. Additionally, the recombination of photogenerated electron-hole pairs further reduces its photocatalytic efficiency by impeding charge separation.

One of the methods used to enhance the photocatalytic performance of ZnO under visible light, is to reduce its band gap energy of 3.37 eV. Various techniques have been explored to achieve this, including doping with metals and non-metals, quantum dot sensitisation, alloying, surface modification, and nano-structuring. Doping with metals is an efficient approach to band gap reduction, because it creates new electronic states within the band gap, narrowing it and allowing light absorption to extend into the visible light spectrum. This versatile method enables the selection of specific dopants to achieve desired electronic and optical properties. Additionally, doping improves charge separation and reduces recombination rates, enhancing photocatalytic performance.

This study focused on tin (Sn) as the dopant due to its superior performance in previous studies. A computational model was developed to explore the potential of Sn-doped ZnO as photocatalysts. Pure hexagonal wurtzite, the cubic rock salt, and the cubic zinc-blende (sphalerite) crystal structures were sourced from crystal structure databases and expanded to 2x2x2 bulk structures. These bulk structures were optimised, and their electronic properties, such as density of states (DOS), d-band centre, band structure, band gap, and X-ray diffraction, were calculated using Density Functional Theory (DFT) based calculations. The solid-state module Cambridge Serial Total Energy Package (CASTEP) were used to calculate these properties. Validation was achieved by comparing them with literature values.

After optimisation, the hexagonal ZnO bulk structure was cut along several Miller planes: (100), (002), (101), (102), (210), (103), (200), (112), and (201). While the cubic and zinc-blende ZnO bulk structures were cut along planes of (111), (200), (220), (222), (311), and (400). A 15 Å vacuum gap was added between adjacent surfaces to prevent periodic cell interactions. These

surfaces were optimised, and their surface energies and work functions were calculated to evaluate their stability and activity, with further validation against literature values. The predicted morphology was determined using the Wulff construction method with Wulffmaker software. This approach established the equilibrium shape of the ZnO crystal systems, where the size of each surface slab reflects its surface energy and, thus, the crystal's stability.

Following this analysis, the pure hexagonal ZnO crystal structure was doped with Sn using the Supercell program, which systematically created all possible inequivalent site configurations for doping percentages of 6.25%, 12.50%, and 18.75%. This was done by substituting specific Zn atoms with Sn. These configurations were imported into Materials Studio 2020 and optimised. The most stable configurations for each doping percentage were identified based on the lowest final energies. The properties of Sn-doped ZnO bulk structures (DOS, d-band centre, band structure, band gap, X-ray diffraction) were determined. Validation of these structures was done by comparing their properties with available literature data.

The Sn-doped ZnO bulk structures were then cut along the same Miller planes as the pure hexagonal ZnO model, namely (100), (002), (101), (102), (210), (103), (200), (112), and (201). This cut was done to create surface models of the Sn-doped material. Similarly, a 15 Å vacuum gap (to prevent periodic cell interactions) was employed. These doped surfaces were optimised, and their surface energies were calculated and validated against literature values. Again, the morphologies of the doped materials were determined, to determine the equilibrium shape of Sn-doped ZnO crystal systems.

Finally, the properties of pure ZnO and Sn-doped ZnO were compared. The Sn-doped ZnO with the most reduced band gap and lowest work function was identified and recommended for improving the photocatalytic activity of ZnO. However, direct experimental data is needed to support these findings fully. This study concludes that the Sn-doped ZnO model predicts significant improvements to the catalytic potential of Sn-doped ZnO for application as a photocatalyst in the degradation of organic pollutants.

KEYWORDS: ZnO, Sn-doped ZnO, Photocatalyst, DFT, Supercell, CASTEP, Band gap, Surface energies

List of Abbreviations

$2A_{slab}$	Surface area of the slab multiplied by two
2θ	An angle used in X-ray diffraction
ACS	American Chemical Society
AFM	Atomic Force Microscopy
AOP	Advanced Oxidation Processes
BLYP	Becke-Lee-Yang-Parr functional
BZ	Brillouin Zone
CASTEP	Cambridge Serial Total Energy Package
CB	Conduction Band
CBM	Conduction Band Minimum
CHPC	Centre for High-Performance Computing
DDT	Dichlorodiphenyltrichloroethane
DFT	Density Functional Theory
DOS	Density of States
EPA	Environmental Protection Agency
E^{DFT}_{bulk}	DFT energy after optimisation of the bulk structure
$E^{DFT}_{relaxed\ slab}$	DFT energy after optimisation of the slab
E_f	Fermi level
E_g	Band Gap
E_{vac}	Vacuum Level
FCC	Face-Centred Cubic
Fenton's reagent	A mixture of hydrogen peroxide and iron salts, used for oxidation
GGA	General Gradient Approximation
GW	Green's function (G) and the screened Coulomb interaction (W)
HAXPES	Hard X-ray Photoelectron Spectroscopy
HCP	Hexagonal Closed-Packed
HRTEM	High-Resolution Transmission Electron Microscopy
HSE06	Heyd–Scuseria–Ernzerhof hybrid functional
Hubbard U	A correction parameter introduced in DFT calculations to account for on-site electron-electron interactions
ICDD	International Centre for Diffraction Data

k	Wave Vector
LDA	Local Density Approximation
LEDs	Light-Emitting Diodes
MS	Materials Studio
MS 2020	Material Studio 2020
MT	Metal-Terminated
n	Ratio
N-type	Negative-type
NWU	North-West University
OT	Oxygen-Terminated
P-type	Positive-type
PAW	Projector Augmented Wave
PBE	Perdew-Burke-Ernzerhof
PBESol	Perdew-Burke-Ernzerhof for Solids
pDOS	Partial Density of States
pH	Potential of Hydrogen
PW91	Perdew–Wang 91 functional
REACH	Registration, Evaluation, Authorization, and Restriction of Chemicals
ROS	Reactive Oxygen Species
SEM	Scanning Electron Microscopy
STM	Scanning Tunneling Microscopy
TB-mBJ	Tran–Blaha modified Becke–Johnson functional
$U_{d\text{-}Zn}$	Hubbard Correction Parameter for Zinc d-orbitals
$U_{p\text{-}O}$	Hubbard Correction Parameter for Oxygen p-orbitals
USP	Ultrasoft Pseudopotential
UV	Ultraviolet
VB-XPS	Valence Band X-ray Photoelectron Spectroscopy
VB	Valence Band
VBM	Valence Band Maximum
V_o	Oxygen Vacancy
WIEN2K	Vienna University of Technology (TU Wien) year 2000
WULFF	A method used for visualising crystal morphologies named after the Russian crystallographer George Wulff

Wulffmaker	Software for constructing Wulff morphologies
XRD	X-ray Diffraction
Zn_i	Zinc Interstitial

List of Chemical Formula

Ag	Silver
Al	Aluminium
CdO	Cadmium Oxide
CdS	Cadmium Sulphide
CN^-	Cyanide Ion
Co	Cobalt
CO_2	Carbon Dioxide
Cu	Copper
Cu^{2+}	Copper 2+ Ion
Fe	Iron
Fe_2O_3	Iron (III) Oxide or Hematite
Ga	Gallium
GaAs	Gallium Arsenide
Ge	Germanium
H_2O	Water
HNO_3	Nitric acid
HO_2•:	Hydroperoxyl Radical
In	Indium
Li	Lithium
Mg^{2+}	Magnesium 2+ Ion
MgO	Magnesium Oxide
Mn	Manganese
Mn^{2+}	Manganese 2+ Ion
Ni	Nickel
O	Oxygen
OH^-	Hydroxide Ion
O_2•$^-$	Superoxide Anion Radical

PbS	Lead Sulphide
Pt	Platinum
SO_3	Sulphur Trioxide
Si	Silicon
SiO_2	Silicon Dioxide
Sn	Tin
Sn^{2+}	Tin 2+ Ion
Sn^{4+}	Tin 4+ Ion
SnO	Tin(II) Oxide
SnO_2	Tin(IV) Oxide
Ta_2O_5	Tantalum Pentoxide
Ti	Titanium
Ti^{4+}	Titanium 4+ Ion
TiO_2	Titanium Dioxide
WO_3	Tungsten Trioxide
Zn	Zinc
Zn^{2+}	Zinc 2+ Ion
ZnO	Zinc Oxide
ZnS	Zinc Sulphide
Zr	Zirconium
Zr^{2+}	Zirconium 2+ Ion
Zr^{4+}	Zirconium 4+ Ion
ZrO_2	Zirconia

List of Symbols and Units

°C	Degrees Celsius
Γ	Gamma
λ	Wavelength
Φ	Work Function
Å	Angstrom
α	Alpha – angle between the b and c axes
β	Beta – angle between the a and c axes

γ	Gamma – angle between the a and b axes
γ	Surface Energy
γ_r	Surface Energy of optimised structures
Arb. units	Arbitrary Units
e^-	Electron
e^-/h^+	Electron/Hole Pair
eV	Electron Volt
g/cm^3	Grams per Cubic Centimeter
GPa	Gigapascals
h^+	Hole
hv	Photon Energy
J/m^2	Joules per Square Meter
Kα	K-alpha (a type of X-ray emission)
meV	Milli-Electron Volt
min	Minutes
nm	Nanometer
pm	Picometer

Table of Contents

List of Tables

List of Figures

Chapter 1: Introduction

1.1 Background to study

Wastewater from industrial processes contains various pollutants. For example, the wastewater from the textile industry contains harmful organic pollutants, such as 4-nitrophenol.[4] Phenols are toxic to the environment and humans. The presence of substituent groups, such as nitro groups, enhances the persistence of phenols in the environment due to the high stability of this functional group.[5] As the harmful organic pollution increases, the demand for environmental remediation increases.

Semiconductor metal oxides have been reported to possess good photocatalytic properties. Several metal oxides, such as zinc oxide (ZnO),[6] titanium dioxide (TiO_2),[52] cadmium sulphide (CdS)[8] and tungsten trioxide (WO_3),[7] have been reported for environmental remediation.[7, 9-11] The use of semiconductor photocatalysis is a promising approach to degrade organic pollutants due to its ability to utilise light energy (photons of adequate energy in the UV or visible region of the solar spectrum) to degrade the pollutants.[12, 13] Figure 1-1 depicts the photocatalytic mechanism of semiconductors.

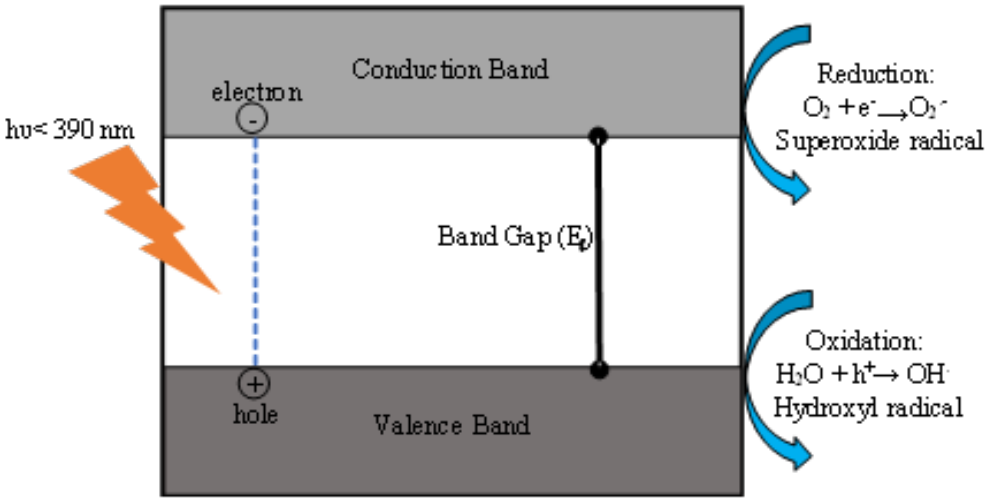

Figure 1-1: ***Semiconductor photocatalytic mechanism for the generation of superoxide and hydroxyl radicals.***

When a semiconductor absorbs photons with energy equal to or exceeding its band gap energy, electrons migrate from the valence band to the conduction band, creating holes in the valence band.[14] The electron-hole pairs facilitate surface-based redox reactions that break down pollutants

into smaller molecules.[15] Specifically, electrons in the conduction band combine with adsorbed oxygen to form superoxide radicals,[17] while holes combine with water molecules or OH^- in the system to form hydroxyl radicals. These reactive species efficiently oxidise pollutants,[16, 53] thus addressing modern environmental challenges through photo-enhanced degradation of pollutants.[18-20]

An example of the mechanism of photocatalytic degradation will be discussed using 4-nitrophenol. The hydroxyl radical attacks the carbon-nitro bond, which leads to the formation of 4-nitrocatechol.[21, 24] (see Figure 1-2).

The 4-nitrocatechol then undergoes denitration (-HNO_3) through a mechanism known as radical addition-elimination to form a phenolic radical. This phenolic radical can either be converted to hydroquinone or catechol. Hydroquinone is then oxidised to p-benzoquinone, and catechol is oxidised to o-benzoquinone. Both p-benzoquinone and o-benzoquinone subsequently undergo ring-opening reactions, with p-benzoquinone forming 2,5-dioxo-3-hexenedioic acid and o-benzoquinone forming maleic acid and muconic acid. These dicarboxylic acids undergo further degradation to form smaller acids such as oxalic acid and acrylic acid, with muconic acid undergoing similar degradation.[4] Ultimately, oxalic acid degrades to formic acid, acrylic acid degrades to malonic acid, and formic acid eventually breaks down into H_2O/CO_2[23] through further oxidation by the strong oxidising radicals.[22] Malonic acid further degrades to produce CO_2, H_2O, and acetic acid (CH_3COOH).

Of the semiconductor photocatalysts listed earlier, ZnO has garnered considerable interest over the past ten years due to its properties, including low cost,[13] non-toxicity,[25] and photochemical and thermal stability,[26] offering environmentally sustainable solutions.[27, 31] ZnO is a II-VI binary compound semiconductor, whose ionicity is on the cusp between covalent and ionic semiconductors due to the electronegativity difference between Zn and O.[28] This partial covalent nature of ZnO is attributed to the arrangement of atoms in the crystal lattice, which enhances the hybrid nature of the bond and boosts its unique combination of ionic and covalent characteristics.[28]

ZnO can crystallise in different forms, each exhibiting distinct structural characteristics. The three common crystal structures of ZnO are hexagonal wurtzite,[29, 30] cubic rock salt,[29] and cubic zinc-blende (sphalerite).[30, 32, 33] For simplicity, we will refer to these structures as hexagonal, cubic, and zinc-blende throughout this work.

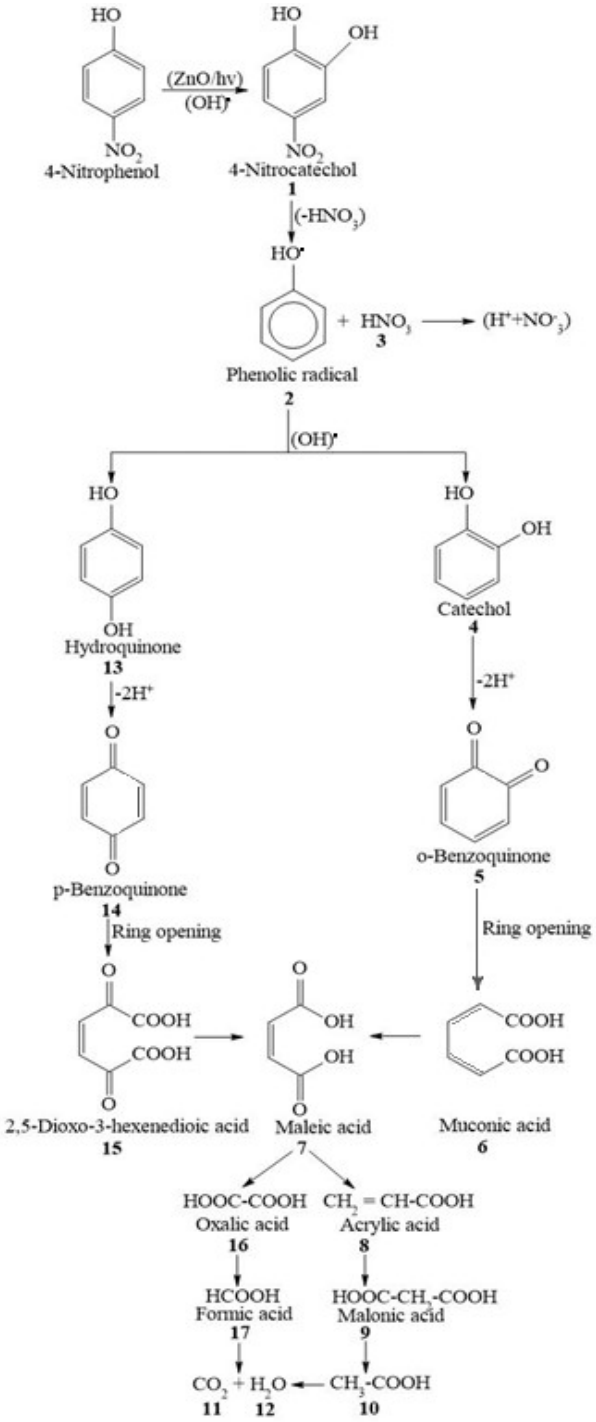

Figure 1-2: Proposed pathway for the degradation of 4-nitrophenol using ZnO.

At standard pressure and temperature, the hexagonal structure is the most prevalent phase of ZnO.[34] The cubic structure appears as a metastable phase under high pressure, around 10 GPa, and cannot be stabilised through epitaxial growth.[35] The zinc-blende structure only becomes stable when grown on cubic substrates.[37]

In the hexagonal ZnO crystal structure, the bonding occurs through the sp^3 hybridisation of electron states, creating four equivalent orbitals.[36] These sp^3 states form the valence band in the resulting ZnO crystal, while the antibonding states constitute the conduction band.[39] This configuration produces a band gap of 3.37 eV[38, 40] situated within the UV spectral range.[43]

The semiconducting properties of ZnO have long been recognised and employed in various applications, including transparent conductive oxides,[41] light-emitting diodes,[44] and UV photodetectors[42] due to its wide band gap and high electron mobility.[45] Recently, ZnO has gained attention as a photocatalyst for environmental remediation, where it degrades pollutants and organic compounds under UV light,[46] leveraging its strong photocatalytic activity[47] and stability.[48] However, despite its promising properties, the photocatalytic performance of ZnO is primarily effective under ultraviolet light (UV) ($\lambda < 390$ nm) and less responsive to visible light due to its wide band gap.[49, 50] This restricts its utilisation of visible light, a significant portion of solar energy, and results in a high recombination rate of electron-hole (e^-/h^+) pairs, reducing its photocatalytic efficiency.

Doping with metals has been shown to reduce the band gap in most semiconductor photocatalysts.[51] Substitution doping, which reduces the band gap in ZnO crystal structure without significantly altering its structural properties, is the primary approach in conventional semiconductor doping.[54]

Doping ZnO with tin (Sn) could be done with either Sn^{2+} or Sn^{4+} ions. Each oxidation state of Sn offers different effects on the properties of the doped ZnO.[55] Sn^{2+} has a different electron configuration and more electrons than Sn^{4+}, leading to distinct electronic interactions within the ZnO lattice.[56] Zn^{2+} and Sn^{2+} have similar electronic configurations with no valence electrons in their outer shells after ionisation, which ensure compatibility in terms of their charge states.[57] Furthermore, doping with Sn^{2+} introduces fewer positive charges compared to doping with Sn^{4+}, resulting in the formation of different types of defects such as oxygen vacancies,[58] interstitial Sn^{2+} ions[59] and substitutional Sn^{2+} ions[60] that leads to the reduction of the band gap.[55] Additionally, previous studies[55] indicate that Sn^{2+} is more effective than Sn^{4+} in reducing the band gap. This effectiveness is because the lower oxidation state of Sn^{2+} also leads to less lattice distortion compared to Sn^{4+}, which helps in maintain better electronic properties and more efficient band gap reduction.

However, the larger ionic radius of Sn^{2+} (1.18 Å) compared to Zn^{2+} (0.74 Å) causes lattice distortions, which alters the electronic band structure of doped ZnO relative to pure ZnO.[61] When Sn^{2+} ions are introduced into the ZnO lattice, they interact with the oxygen atoms, causing changes in bonding and hybridisation.[62] Moreover, the chemical bonding and hybridisation between Sn^{2+} and oxygen atoms in ZnO change the conduction and valence bands.[62] These bands shift in the energy levels.[63] This adjusted band structure effectively reduces the band gap, thereby improving the ability of ZnO to absorb visible light and enhancing its photocatalytic performance.[64]

In addition to changing the band structure, dopants like Sn^{2+} can create trap states or defect sites within the band gap (see Figure 1-3). These trap states arise due to the introduction of defects, as mentioned earlier.[60, 65] Trap states are crucial for preventing recombination and facilitating electron-hole pair separation in the doped materials by capturing electrons or holes, effectively reducing recombination rates and enhancing photocatalytic efficiency.[66]

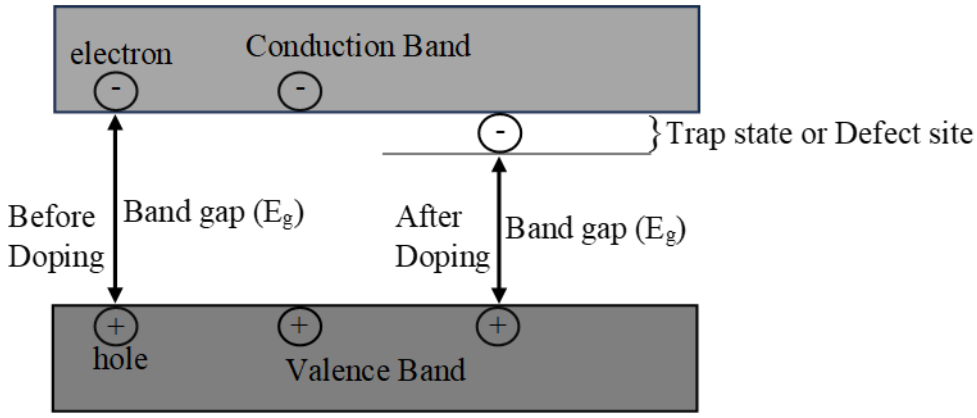

Figure 1-3: ***Introduction of trap states enhancing the separation of electron-hole pairs and reducing the band gap***

However, if the band gap is smaller, the recombination possibility increases because the energy barrier for recombining electron-hole pairs is reduced.[67] To overcome this, the doping concentration must be precisely controlled to create optimal trap states that capture electrons or holes without introducing too many recombination centres.[68]

Several experimental studies on Sn doping of ZnO have been done,[69-74] but only a limited amount on computational studies to explore how Sn doping affects the electronic properties of ZnO to enhance its photocatalytic activity for the degradation of organic pollutants.

1.2 Problem statement and motivation

The widespread use of organic compounds in the industrial sector, particularly in the textile industries, have contributed significantly to the presence of hazardous organic pollutants like 4-nitrophenol in the environment.[75] Semiconductor photocatalysis shows excellent potential for breaking down these pollutants.[76]

ZnO is an appealing photocatalyst,[77,78,79] however, its wide band gap limits its activity mainly to ultraviolet light, reducing its effectiveness under visible light. Furthermore, the high recombination rate of photogenerated electron-hole pairs diminishes its photocatalytic efficiency.

Doping ZnO with other metals to form a hybrid photocatalyst system increases photogenerated electron-hole (e^-/h^+) pair separation[27] by establishing electron traps, which form new energy levels in the band gap and enhance photocatalysis.[31]

In a study done by Onwudiwe *et al.*,[80] Sn was chosen as a dopant to improve the photocatalytic activity of ZnO. The research examined the impact of different Sn concentrations at (5%, 10%, and 20%) on the efficiency of ZnO. The findings revealed that a 10% Sn doping level is ideal, offering the highest efficiency due to an optimal balance between creating trap states that capture electrons or holes while minimising recombination centres.

This study introduces a computational modelling approach to investigate the effects of Sn-doping on the structural and electronic properties of ZnO. This improved understanding of the structural and electronic properties will lead to more efficient photocatalysts, which is beneficial for the degradation of organic pollutants.

1.3 Aim

This study aims to investigate the effects of Sn doping on the structural and electronic properties of ZnO to enhance its photocatalytic activity.

1.4 Objectives

The objectives listed below were addressed to achieve the aim mentioned above:

- Develop and validate a model to optimise and calculate the structural and electronic properties of ZnO.

- Utilise the validated model developed for the ZnO to investigate the effect of Sn-doping on the structural and electronic properties of ZnO.
- Compare the band gap of ZnO with those of the Sn-doped ZnO to assess the improvement in photocatalytic activity.
- Compare the work function of ZnO with Sn-doped ZnO to assess the improvement in charge separation.

1.5 Method of investigation

All the calculations in this study were performed using the Cambridge Serial Total Energy Package (CASTEP) module in Biovia Material Studio (MS2020)[81] software on the Lengau cluster at the Centre for High-Performance Computing (CHPC),[82] South Africa. CASTEP was employed to calculate the electronic and structural properties of the bulk structures to determine the most stable structure. The open-source software, Supercell program,[83] was employed for doping, while the Wulffmaker program[2] was used to ascertain morphologies.

1.6 References

(2) Rahm, J.; Erhart, P. WulffPack: A Python package for Wulff constructions. *Journal of Open Source Software* **2020**, *5*, 1944. DOI: 10.21105/joss.01944.

(4) Rajamanickam, D.; Shanthi, M. Photocatalytic degradation of an organic pollutant by zinc oxide – solar process. *Arabian Journal of Chemistry* **2016**, *9*, S1858-S1868. DOI: 10.1016/j.arabjc.2012.05.006.

(5) Ksibi, M.; Zemzemi, A.; Boukchina, R. Photocatalytic degradability of substituted phenols over UV irradiated TiO_2. *Journal of Photochemistry and Photobiology A: Chemistry* **2003**, *159* (1), 61-70.

(6) Abou Zeid, S.; Perez, A.; Bastide, S.; Le Pivert, M.; Rossano, S.; Remita, H.; Hautière, N.; Leprince-Wang, Y. Antibacterial and photocatalytic properties of ZnO nanostructure decorated coatings. *Coatings* **2023**, *14* (1), 41.

(7) Czech, B.; Zygmunt, P.; Kadirova, Z. C.; Yubuta, K.; Hojamberdiev, M. Effective photocatalytic removal of selected pharmaceuticals and personal care products by elsmoreite/tungsten oxide@ ZnS photocatalyst. *Journal of Environmental Management* **2020**, *270*, 110870.

(8) Villani, M.; Calestani, D.; Lazzarini, L.; Zanotti, L.; Mosca, R.; Zappettini, A. Extended functionality of ZnO nanotetrapods by solution-based coupling with CdS nanoparticles. *Journal of Materials Chemistry* **2012**, *22*, 5694-5699. DOI: 10.1039/c2jm16164h.

(9) Akintelu, S. A.; Folorunso, A. S.; Folorunso, F. A.; Oyebamiji, A. K. Green synthesis of copper oxide nanoparticles for biomedical application and environmental remediation. *Heliyon* **2020**, *6* (7).

(10) Masudy-Panah, S.; Katal, R.; Khiavi, N. D.; Shekarian, E.; Hu, J.; Gong, X. A high-performance cupric oxide photocatalyst with palladium light trapping nanostructures and a hole transporting layer for photoelectrochemical hydrogen evolution. *Journal of Materials Chemistry A* **2019**, *7* (39), 22332-22345.

(11) Sabzehei, K.; Hadavi, S.; Bajestani, M. G.; Sheibani, S. Comparative evaluation of copper oxide nano-photocatalyst characteristics by formation of composite with TiO_2 and ZnO. *Solid State Sciences* **2020**, *107*, 106362.

(12) Mao, T.; Liu, M.; Lin, L.; Cheng, Y.; Fang, C. A study on doping and compound of zinc oxide photocatalysts. *Polymers* **2022**, *14*. DOI: 10.3390/polym14214484.

(13) Mohamad, A. A.; Hassan, M. S.; Yaakob, M. K.; Taib, M. F. M.; Badrudin, F. W.; Hassan, O. H.; Yahya, M. Z. A. First-principles calculation on electronic properties of zinc oxide by zinc–air system. *Journal of King Saud University - Engineering Sciences* **2017**, *29* (3), 278-283. DOI: 10.1016/j.jksues.2015.08.002.

(14) Kumar, S. G.; Rao, K. K. Comparison of modification strategies towards enhanced charge carrier separation and photocatalytic degradation activity of metal oxide semiconductors (TiO_2, WO_3 and ZnO). *Applied Surface Science* **2017**, *391*, 124-148.

(15) Hoffmann, M. R.; Martin, S. T.; Choi, W.; Bahnemann, D. W. Environmental applications of semiconductor photocatalysis. *Chemical Reviews* **1995**, *95* (1), 69-96. DOI: 10.1021/cr00033a004.

(16) Roselin, L. S.; Rajarajeswari, G.; Selvin, R.; Sadasivam, V.; Sivasankar, B.; Rengaraj, K. Sunlight/ZnO-mediated photocatalytic degradation of reactive red 22 using thin film flat bed flow photoreactor. *Solar Energy* **2002**, *73* (4), 281-285.

(17) Pelaez, M.; Nolan, N. T.; Pillai, S. C.; Seery, M. K.; Falaras, P.; Kontos, A. G.; Dunlop, P. S. M.; Hamilton, J. W. J.; Byrne, J. A.; O'Shea, K.; et al. A review on the visible light active titanium dioxide photocatalysts for environmental applications. *Applied Catalysis B: Environmental* **2012**, *125*, 331-349. DOI: 10.1016/j.apcatb.2012.05.036.

(18) Xie, L.; Du, T.; Wang, J.; Ma, Y.; Ni, Y.; Liu, Z.; Zhang, L.; Yang, C.; Wang, J. Recent advances on heterojunction-based photocatalysts for the degradation of persistent organic pollutants. *Chemical Engineering Journal* **2021**, *426*, 130617.

(19) Thompson, T. L.; Yates, J. T. Surface science studies of the photoactivation of TiO_2 new photochemical processes. *Chemical Reviews* **2006**, *106* (10), 4428-4453. DOI: 10.1021/cr050172k.

(20) Linsebigler, A. L.; Lu, G.; Yates, J. T., Jr. Photocatalysis on TiO_2 surfaces: principles, mechanisms, and selected results. *Chemical Reviews* **1995**, *95* (3), 735-758. DOI: 10.1021/cr00035a013.

(21) Goi, A.; Trapido, M.; Tuhkanen, T. A study of toxicity, biodegradability, and some by-products of ozonised nitrophenols. *Advances in Environmental Research* **2004**, *8* (3), 303-311. DOI: 10.1016/S1093-0191(02)00102-8.

(22) Derikvandi, H.; Nezamzadeh-Ejhieh, A. Increased photocatalytic activity of NiO and ZnO in photodegradation of a model drug aqueous solution: Effect of coupling, supporting, particles size and calcination temperature. *Journal of Hazardous Materials* **2017**, *321*, 629-638. DOI: 10.1016/j.jhazmat.2016.09.056.

(23) Nezamzadeh-Ejhieh, A.; Khorsandi, S. Photocatalytic degradation of 4-nitrophenol with ZnO supported nano-clinoptilolite zeolite. *Journal of Industrial and Engineering Chemistry* **2014**, *20* (3), 937-946. DOI: 10.1016/j.jiec.2013.06.026.

(24) Di Paola, A.; Augugliaro, V.; Palmisano, L.; Pantaleo, G.; Savinov, E. Heterogeneous photocatalytic degradation of nitrophenols. *Journal of Photochemistry and Photobiology A: Chemistry* **2003**, *155* (1), 207-214. DOI: 10.1016/S1010-6030(02)00390-8.

(25) Douloumis, A.; Vrithias, N. R. E.; Katsarakis, N.; Remediakis, I. N.; Kopidakis, G. Tuning the workfunction of ZnO through surface doping with Mn from first-principles simulations. *Surface Science* **2022**, *726*. DOI: 10.1016/j.susc.2022.122175.

(26) Ibrahim, A. A.; Kumar, R.; Umar, A.; Kim, S. H.; Bumajdad, A.; Ansari, Z. A.; Baskoutas, S. Cauliflower-shaped ZnO nanomaterials for electrochemical sensing and photocatalytic applications. *Electrochimica Acta* **2016**, *222*, 463-472. DOI: 10.1016/J.ELECTACTA.2016.10.199.

(27) Mohd Adnan, M. A.; Julkapli, N. M.; Abd Hamid, S. B. Review on ZnO hybrid photocatalyst: Impact on photocatalytic activities of water pollutant degradation. *Reviews in Inorganic Chemistry* **2016**, *36*, 77-104. DOI: 10.1515/revic-2015-0015.

(28) Morkoç, H.; Özgür, U. m. Zinc oxide: Fundamentals, materials and device technology. *British Library Cataloguing-in-Publication Data* **2009**, 477.

(29) Farmer, N.; O'Neill, H. S. C. The miscibility gap between the rock salt and wurtzite phases in the MgO–ZnO binary system to 3.5 GPa. *European Journal of Mineralogy* **2023**, *35* (6), 1051-1071.

(30) Shabbir, S.; Shaari, A.; Haq, B. U.; Ahmed, R.; Ahmed, M. Investigations of novel polymorphs of ZnO for optoelectronic applications. *Optik* **2020**, *206*, 164285.

(31) Qi, K.; Xing, X.; Zada, A.; Li, M.; Wang, Q.; Liu, S.-y.; Lin, H.; Wang, G. Transition metal doped ZnO nanoparticles with enhanced photocatalytic and antibacterial performances: Experimental and DFT studies. *Ceramics International* **2020**, *46* (2), 1494-1502. DOI: 10.1016/j.ceramint.2019.09.116.

(32) Dedova, T. *Chemical spray pyrolysis deposition of zinc sulfide thin films and zinc oxide nanostructured layers*; Tallinn University of Technology Tallinn, Estonia, **2007**.

(33) Yates, B.; Cooper, R.; Kreitman, M. Low-temperature thermal expansion of zinc oxide. Vibrations in zinc oxide and sphalerite zinc sulfide. *Physical Review B* **1971**, *4* (4), 1314.

(34) Sahani, R.; Dixit, A. A comprehensive review on zinc oxide bulk and nano-structured materials for ionizing radiation detection and measurement applications. *Materials Science in Semiconductor Processing* **2022**, *151*, 107040.

(35) Coleman, V. A.; Jagadish, C. Basic properties and applications of ZnO. In *Zinc oxide bulk, thin films and nanostructures*, Elsevier, **2006**; pp 1-20.

(36) Klingshirn, C. F.; Meyer, B. K.; Waag, A.; Hoffmann, A.; Geurts, J.; Geurts, J. Crystal structure, chemical binding, and lattice properties. In *In Zinc Oxide: from fundamental properties towards novel applications*, Springer, 2010; pp 7-37.

(37) Fan, Z.; Lu, J. G. Zinc oxide nanostructures: synthesis and properties. *Journal of Nanoscience and Nanotechnology* **2005**, *5* (10), 1561-1573.

(38) Kishwar, S.; Hasan, K.; Tzamalis, G.; Nur, O.; Willander, M.; Kwack, H.; Dang, D. L. S. Electro-optical and cathodoluminescence properties of low temperature grown ZnO nanorods/p-GaN white light emitting diodes. *Physica Status Solidi (a)* **2010**, *207* (1), 67-72.

(39) Ivanov, I.; Pollman, J. First surface electronic structure of a wurtzite-type semiconductor the polar and nonpolar surfaces of ZnO. *Solid State Communications* **1980**, *36* (4), 361-364.

(40) Ul Hasan, K.; Alvi, N.; Lu, J.; Nur, O.; Willander, M. Single nanowire-based UV photodetectors for fast switching. *Nanoscale Research Letters* **2011**, *6*, 1-6.

(41) Özgür, Ü.; Hofstetter, D.; Morkoc, H. ZnO devices and applications: a review of current status and future prospects. *Proceedings of the IEEE* **2010**, *98* (7), 1255-1268.

(42) Liu, K.; Sakurai, M.; Aono, M. ZnO-based ultraviolet photodetectors. *Sensors* **2010**, *10* (9), 8604-8634.

(43) Panda, N.; Sahu, D.; Acharya, B.; Nayak, P. High UV absorption efficiency of nanocrystalline ZnO synthesized by ultrasound assisted wet chemical method. *Current Applied Physics* **2015**, *15* (3), 389-396.

(44) Rahman, F. Zinc oxide light-emitting diodes: a review. *Optical Engineering* **2019**, *58* (1), 010901-010901.

(45) Sharma, D. K.; Shukla, S.; Sharma, K. K.; Kumar, V. A review on ZnO: Fundamental properties and applications. *Materials Today: Proceedings* **2022**, *49*, 3028-3035.

(46) Ahmaruzzaman, M. Metal oxides (ZnO, CuO and NiO)-based nanostructured materials for photocatalytic remediation of organic contaminants. *Nanotechnology for Environmental Engineering* **2023**, *8* (1), 219-235.

(47) Güell, F.; Galdámez-Martínez, A.; Martínez-Alanis, P. R.; Catto, A. C.; da Silva, L. F.; Mastelaro, V. R.; Santana, G.; na Dutt, A. ZnO-based nanomaterials approach for photocatalytic and sensing applications: recent progress and trends. *Materials Advances* **2023**, *4*, 3685-3707.

(48) Ong, C. B.; Ng, L. Y.; Mohammad, A. W. A review of ZnO nanoparticles as solar photocatalysts: Synthesis, mechanisms and applications. *Renewable and Sustainable Energy Reviews* **2018**, *81*, 536-551.

(49) Li, W.; Wang, G.; Feng, Y.; Li, Z. Efficient photocatalytic performance enhancement in Co-doped ZnO nanowires coupled with CuS nanoparticles. *Applied Surface Science* **2018**, *428*, 154-164. DOI: 10.1016/J.APSUSC.2017.09.049.

(50) Xiaohua, Z.; Shuai, S.; Guangli, W.; Caizhu, L.; Zhe, Q.; Xiangdong, L.; Jianguo, Z. Facile synthesis of the flower-like ternary heterostructure of Ag/ZnO encapsulating carbon spheres with enhanced photocatalytic performance. *Applied Surface Science* **2017**, *406*, 1-11.

(51) Khaki, M. R. D.; Shafeeyan, M. S.; Raman, A. A. A.; Daud, W. M. A. W. Application of doped photocatalysts for organic pollutant degradation-A review. *Journal of Environmental Management* **2017**, *198*, 78-94.

(52) Khan, H.; Shah, M. U. H. Modification strategies of TiO_2 based photocatalysts for enhanced visible light activity and energy storage ability: A review. *Journal of Environmental Chemical Engineering* **2023**, 111532.

(53) Height, M. J.; Pratsinis, S. E.; Mekasuwandumrong, O.; Praserthdam, P. Ag-ZnO catalysts for UV-photodegradation of methylene blue. *Applied Catalysis B: Environmental* **2006**, *63* (3-4), 305-312.

(54) Zhou, S. Y.; Gweon, G. H.; Fedorov, A. V.; First, P.; De Heer, W. A.; Lee, D. H.; Guinea, F.; Castro Neto, A. H.; Lanzara, A. Substrate-induced bandgap opening in epitaxial graphene. *Nature Materials* **2007**, *6* (10), 770-775.

(55) Yang, W.; Zhang, B.; Zhang, Q.; Wang, L.; Song, B.; Ding, Y.; Wong, C. Adjusting the band structure and defects of ZnO quantum dots via tin doping. *RSC Advances* **2017**, *7* (19), 11345-11354.

(56) Zhang, S.; Wang, J.; Wang, J.; Wang, K.-Y.; Zhao, M.; Zhang, L.; Wang, C. A gradient Sn^{4+}@ Sn^{2+} core@ shell structure induced by a strong metal oxide–support interaction for enhanced CO_2 electroreduction. *Dalton Transactions* **2022**, *51* (42), 16135-16144.

(57) Zatsepin, D.; Boukhvalov, D.; Kurmaev, E.; Zhidkov, I.; Kim, S.; Cui, L.; Gavrilov, N.; Cholakh, S. XPS and DFT study of Sn incorporation into ZnO and TiO_2 host matrices by pulsed ion implantation. *Physica Status Solidi (b)* **2015**, *252* (8), 1890-1896.

(58) Batzill, M.; Diebold, U. The surface and materials science of tin oxide. *Progress in Surface Science* **2005**, *79* (2-4), 47-154.

(59) Das, A.; Gautam, S. K.; Shukla, D.; Singh, F. Correlations of charge neutrality level with electronic structure and pd hybridization. *Scientific Reports* **2017**, *7* (1), 40843.

(60) Dawson, M. Synthesis and characterization of $CH_3NH_3SnI_3$, Mn doped $CH_3NH_3SnI_3$ and oxygen-deficient TiO_2 as visible-light active semiconductors. Universidade Federal de São Carlos, São Carlos, 2020.

(61) Prakash, T.; Jayaprakash, R.; Espro, C.; Neri, G.; Ranjith Kumar, E. Effect of Sn doping on microstructural and optical properties of ZnO nanoparticles synthesized by microwave irradiation method. *Journal of Materials Science* **2014**, *49*, 1776-1784.

(62) Su, Y.; Zhu, B.; Guan, K.; Gao, S.; Lv, L.; Du, C.; Peng, L.; Hou, L.; Wang, X. Particle size and structural control of $ZnWO_4$ nanocrystals via Sn^{2+} doping for tunable optical and visible photocatalytic properties. *The Journal of Physical Chemistry C* **2012**, *116* (34), 18508-18517.

(63) Bagus, P. S.; Illas, F.; Pacchioni, G.; Parmigiani, F. Mechanisms responsible for chemical shifts of core-level binding energies and their relationship to chemical bonding. *Journal of Electron Spectroscopy and Related Phenomena* **1999**, *100* (1-3), 215-236.

(64) Zhang, Y.; Zhou, J.; Chen, X.; Feng, Q.; Cai, W. MOF-derived C-doped ZnO composites for enhanced photocatalytic performance under visible light. *Journal of Alloys and Compounds* **2019**, *777*, 109-118.

(65) Henrich, V. E.; Cox, P. A. *The surface science of metal oxides*; Cambridge university press, **1994**.

(66) Zhou, W.; Fu, H. Defect-mediated electron–hole separation in semiconductor photocatalysis. *Inorganic Chemistry Frontiers* **2018**, *5* (6), 1240-1254.

(67) Rahman, F. Solid-state lighting with wide band gap semiconductors. *MRS Energy & Sustainability* **2014**, *1*, E6.

(68) Bozyigit, D.; Lin, W. M.; Yazdani, N.; Yarema, O.; Wood, V. A quantitative model for charge carrier transport, trapping and recombination in nanocrystal-based solar cells. *Nature Communications* **2015**, *6* (1), 6180.

(69) Agarwal, M. B.; Sharma, A.; Malaidurai, M.; Thangavel, R. Effect of Sn doping on structural, mechanical, optical and electrical properties of ZnO nanoarrays prepared by sol-gel and hydrothermal process. *Superlattices and Microstructures* **2018**, *117*, 342-350.

(70) Aydin, H.; El-Nasser, H.; Aydin, C.; Al-Ghamdi, A. A.; Yakuphanoglu, F. Synthesis and characterization of nanostructured undoped and Sn-doped ZnO thin films via sol–gel approach. *Applied Surface Science* **2015**, *350*, 109-114.

(71) Beura, R.; Pachaiappan, R.; Thangadurai, P. A detailed study on Sn^{4+} doped ZnO for enhanced photocatalytic degradation. *Applied Surface Science* **2018**, *433*, 887-898. DOI: 10.1016/j.apsusc.2017.10.127.

(72) Beura, R.; Thangadurai, P. Effect of Sn doping in ZnO on the photocatalytic activity of ZnO-Graphene nanocomposite with improved activity. *Journal of Environmental Chemical Engineering* **2018**, *6* (4), 5087-5100.

(73) Caglar, Y.; Aksoy, S.; Ilican, S.; Caglar, M. Crystalline structure and morphological properties of undoped and Sn doped ZnO thin films. *Superlattices and Microstructures* **2009**, *46* (3), 469-475. DOI: 10.1016/j.spmi.2009.05.005.

(74) Dhamodharan, P.; Manoharan, C.; Dhanapandian, S.; Bououdina, M.; Ramalingam, S. Preparation and characterization of spray deposited Sn-doped ZnO thin films onto ITO subtracts as photoanode in dye sensitized solar cell. *Journal of Materials Science: Materials in Electronics* **2015**, *26*, 4830-4839.

(75) Fu, J.; Yu, J.; Jiang, C.; Cheng, B. g-C_3N_4-Based Heterostructured Photocatalysts. *Advanced Energy Materials* **2018**, *8* (3). DOI: 10.1002/aenm.201701503.

(76) Ramalingam, G.; Perumal, N.; Priya, A.; Rajendran, S. A review of graphene-based semiconductors for photocatalytic degradation of pollutants in wastewater. *Chemosphere* **2022**, *300*, 134391.

(77) Weldegebrieal, G. K. Synthesis method, antibacterial and photocatalytic activity of ZnO nanoparticles for azo dyes in wastewater treatment: A review. *Inorganic Chemistry Communications* **2020**, *120*, 108140.

(78) Baibara, O.; Radchenko, M.; Karpyna, V.; Ievtushenko, A. A review of the some aspects for the development of ZnO based photocatalysts for a variety of applications. *Physics and Chemistry of Solid State* **2021**, *22* (3), 585-594.

(79) Verma, R.; Pathak, S.; Srivastava, A. K.; Prawer, S.; Tomljenovic-Hanic, S. ZnO nanomaterials: Green synthesis, toxicity evaluation and new insights in biomedical applications. *Journal of Alloys and Compounds* **2021**, *876*, 160175.

(80) Oyewo, O. A.; Ramaila, S.; Mavuru, L.; Onwudiwe, D. C. Enhanced photocatalytic degradation of methyl orange using Sn-ZnO/GO nanocomposite. *Journal of Photochemistry and Photobiology* **2022**, *11*. DOI: 10.1016/j.jpap.2022.100131.

(81) Dassault; Systemes. *Biovia Material Studio Castep*. **2020**. https://www.3ds.com/fileadmin/PRODUCTS-SERVICES/BIOVIA/PDF/biovia-material-studio-castep.pdf (accessed 2023 April 08, 2023).

(82) *National Intergrated Cyberinfrastructure System (NICIS) - Centre for High Performance Computing (CHPC)*. **2017**. https://www.chpc.ac.za/index.php/resources). (accessed 2023 April 08, 2023).

(83) Okhotnikov, K.; Charpentier, T.; Cadars, S. Supercell program: a combinatorial structure-generation approach for the local-level modeling of atomic substitutions and partial occupancies in crystals. *Journal of Cheminformatics* **2016**, *8*, 1-15.

Chapter 2: Literature Study

2.1 Introduction

Environmental pollution remains a critical challenge for developed and developing nations, significantly impacting ecosystems through various anthropogenic sources. These pollutants include toxic organic compounds, such as chlorinated and non-chlorinated aliphatic and aromatic compounds,[84, 85] dyes,[86, 87] and surfactants,[88, 89] each contributing uniquely to air, water, and soil pollution.[90]

Chlorinated aliphatic compounds like trichloroethylene[91] and perchloroethylene[92] are used in industrial activities such as metal degreasing and dry cleaning.[93, 94] These volatile and persistent substances contaminate air, soil, and groundwater,[95] leading to severe health issues, including liver and kidney damage, and are considered probable human carcinogens.[96] Additionally, they contribute to ozone layer depletion, intensifying climate change and increasing harmful ultraviolet radiation exposure.[97] Non-chlorinated aliphatic compounds, like hexane and butane,[98] though less persistent compared to their chlorinated counterparts, still pose significant health and environmental risks.[99] They contribute to ground-level ozone formation (smog), causing respiratory problems and reduce crop yields.[100] Moreover, they can contaminate soil and water bodies, harming aquatic life and disrupting ecosystems.[101]

Aromatic compounds such as benzene, toluene, and xylene[102, 103] are extensively used to produce plastics,[104] resins,[105] and synthetic fibres.[106] These highly toxic and carcinogenic substances,[107] like benzene, are linked to leukaemia and other blood disorders.[108, 109] They contribute to air pollution and smog,[110] and, pose long-term groundwater contamination risks, affecting drinking water supplies.[111-113] Dyes used in the textile,[114] paper,[115] and leather industries[116] are often toxic,[117] mutagenic,[118] and carcinogenic,[119] persisting in the environment due to their complex chemical structures.[120] Industrial discharge of dyes, such as 4-nitrophenol, into water bodies causes severe water pollution,[121] harming aquatic life by inhibiting photosynthesis,[122] disrupting reproductive systems,[123] and accumulating in the food chain,[124] ultimately impacting human health.[87] Surfactants, key components in household detergents,[125] personal care products,[126] and industrial cleaners,[127] also have harmful environmental effects.[128] Anionic surfactants, such as linear alkylbenzene sulfonates, persist in the environment and are toxic to aquatic organisms,[129]

damaging cell membranes and altering microbial communities in water bodies.[130] They can increase the solubility and mobility of other toxic compounds, exacerbating pollution issues.[131, 132]

As a result, stringent environmental regulations govern the use and disposal of persistent pollutants,[133] driving researchers to explore clean and sustainable methods. For instance, the Stockholm Convention aims to eliminate or restrict Persistent Organic Pollutants[134] like dioxins, polychlorinated biphenyls, and certain pesticides like dichlorodiphenyltrichloroethane (DDT).[135] In the United States, the Resource Conservation and Recovery Act[136] manages hazardous waste, including chlorinated solvents and heavy metals,[137, 138] while the Clean Water Act[139] regulates pollutant discharge to protect water quality.[140] In the European Union, REACH (Registration, Evaluation, Authorisation, and Restriction of Chemicals)[141] mandates chemical risk management,[142] and the Water Framework Directive[143] controls pollution from various sources.[144] The Canadian Environmental Protection Act[145] oversees hazardous chemical management to safeguard human health and the environment.[146] These regulations aim to prevent pollutants from harming human health and the environment.[147]

South Africa has a similar robust framework for chemical management and environmental protection, guided by national legislation such as the National Environmental Management Act[148] and the Hazardous Substances Act.[149] The country also participates in key international agreements, including the Stockholm, Rotterdam, and Basel Conventions, to control hazardous substances and waste.[150] Specific initiatives like the National Environmental Management: Waste Act[151] and the National Water Act[152] address chemical waste and water pollution, respectively. Through these measures and its commitment to international cooperation, South Africa aligns its policies with global standards to safeguard human health and the environment.[153]

In addition to these legislative efforts, various advanced techniques have been developed and are employed to process pollutants and generate clean energy. One such advanced technique is photocatalysis.

Photocatalysis processes pollutants using renewable solar energy to drive oxidation and reduction processes necessary for removing persistent organic compounds and microorganisms from water.[154] It is widely applied in water and air purification,[155] as well as in developing self-cleaning,[156] self-sterilising,[157] antifogging,[158] and anticorrosive surfaces.[159] Additionally, photocatalysis is utilised in lithography,[160] photochromic materials,[161] microchemical systems,[162] and environmentally friendly organic synthesis and hydrogen generation.[163]

The practical application of photocatalysis in environmental cleanup and clean energy generation faces challenges but offers significant potential.

2.2 Photocatalysis

The history of photocatalysis began in 1972 with Fujishima and Honda's[164] discovery that water could be split into oxygen and hydrogen using an illuminated TiO_2 single crystal electrode. This breakthrough attracted exploration into various materials for environmental cleanup, particularly for degrading organic pollutants. In 1977, Frank and Bard[165] demonstrated the photocatalytic oxidation of CN^- and SO_3 using semiconductors like titanium dioxide (TiO_2), zinc oxide (ZnO), cadmium sulphide (CdS), hematite (Fe_2O_3), and tungsten trioxide (WO_3). This breakthrough expanded the application of photocatalysis beyond water splitting to pollution remediation and wastewater treatment.

2.2.1 Mechanism of photocatalysis in the treatment of wastewater

In a typical photocatalytic process, the primary role of a photocatalyst is to convert solar energy into chemical energy, driving oxidation and reduction reactions. When solar energy irradiates the photocatalyst, it excites an electron from the valence band (VB) to the conduction band (CB), resulting in the formation of an electron-hole pair[166]:

$$\text{Catalyst} + h\nu \rightarrow e^-_{CB} + h^+_{VB} \quad \text{.....(2.1)}$$

In an aqueous medium, the generated holes (h^+) interact with water (H_2O) and hydroxide ions (OH^-) to produce highly reactive hydroxyl radicals (•OH), which play a crucial role in the oxidation processes for wastewater treatment[167]:

$$H_2O + h^+_{VB} \rightarrow \bullet OH + H^+ \quad \text{.....(2.2)}$$

$$OH^- + h^+_{VB} \rightarrow \bullet OH \quad \text{.....(2.3)}$$

The electrons (e^-) in the conduction band can reduce dissolved oxygen (O_2) to superoxide anion radicals ($O_2\bullet^-$):

$$O_2 + e^-_{CB} \rightarrow O_2^{\bullet -} \quad \text{.....(2.4)}$$

These superoxide anion radicals can further react with hydrogen ions (H^+) to form hydroperoxyl radicals ($HO_2\bullet$):

$$O_2^- + H^+ \rightarrow HO_2^\bullet \quad (2.5)$$

These radicals and other reactive species contribute to the degradation of pollutants, such as the oxidation of dye wastewater, facilitated by photo-induced positive holes:

$$\text{Dye wastewater} + \bullet OH \rightarrow \text{Oxidation products} \quad (2.6)$$

Moreover, reduction facilitated by photo-induced negative electrons:

$$\text{Dye wastewater} + O_2^{\bullet -} \rightarrow \text{Reduction products} \quad (2.7)$$

$$\text{Dye wastewater} + HO_2^\bullet \rightarrow \text{Reduction products} \quad (2.8)$$

Various semiconductor-based photocatalysts, including TiO_2,[168, 169] ZnO,[170, 171] Fe_2O_3,[172-174] zirconia (ZrO_2),[175, 176] WO_3,[177, 178] and tantalum pentoxide (Ta_2O_5),[179] effectively absorb light to initiate reactions that break down persistent pollutants, making them useful in wastewater treatment applications.[76, 180, 181]

2.2.2 Advancements in photocatalysis

Over the past two decades, significant advancements in photocatalysis include novel material synthesis,[182] nanostructure development,[183, 184] efficient pollutant degradation,[53, 185] antimicrobial function development[6] and energy generation processes.[186] Research has further expanded the understanding of photocatalysis, focusing on electron transfer processes,[164] lattice and electronic structure,[187] generation of reactive radicals,[188] chemisorption,[189] photooxidation,[190] green synthesis,[191] hydrogen generation,[185] surface modification,[49] and surface chemistry.[192]

Surface modification and improved surface chemistry could be accomplished through composite fabrication,[193] nanostructure engineering[194] and doping.[195] Composite fabrication creates heterogeneous surfaces and unique interfacial chemistries, such as combining TiO_2 with graphene to improve electron transfer and reactivity.[196] Nanostructure engineering increases surface area and introduces defects and quantum effects; for instance, creating ZnO nanorods increases surface reactivity and adsorption capabilities.[197] Doping introduces impurities (metals or non-metals) that can change the work function and surface energy of the material, impacting interactions with its environment. For example, doping TiO_2 with nitrogen enhances photocatalytic activity under visible light.[198] Doping with non-metals like sulphur or nitrogen can also enhance chemisorption

and light absorption, further boosting photocatalytic efficiency.[189] Doping with metals enhances photocatalyst efficiency and stability.[199]

Together, these surface modification processes enable the customisation of materials for applications in catalysis,[200] sensing,[201] energy conversion,[202] and environmental remediation.[203]

Additionally, photocatalysis is integrated into advanced oxidation processes (AOPs) that use oxidising agents such as hydrogen peroxide, ozone, and Fenton's reagent for pollutant detoxification.[204-207] These processes often combine UV radiation and photocatalysis to accelerate degradation,[208] with recent advancements using ultrasound, microwave radiation, and electrolysis to further enhance pollutant decomposition.[209]

2.2.3 Importance of band gap

The band gap is the energy difference between the VB and the CB. The size of the band gap is crucial for the activation of a photocatalyst by light, as the energy of incoming photons must meet or exceed this gap to allow electron transitions and the formation of electron-hole pairs essential for photocatalysis.

For instance, TiO_2, with a band gap of approximately 3.2 eV,[52] and ZnO, with a band gap of around 3.37 eV,[210] are effective at absorbing UV light. In contrast, CdS, with a smaller band gap of about 2.4 eV,[8] and WO_3, with a band gap of around 2.8 eV,[14] are capable of utilising visible light for photocatalytic applications. For practical applications, particularly in solar energy conversion, photocatalysts with band gaps that absorb visible light (around 1.8 to 3.0 eV) are preferred, as they can harness most of the solar spectrum efficiently.[211]

Furthermore, the band gap's characteristics influence the separation and stability of the electron-hole pairs generated during photocatalysis.[212] Effective separation of these pairs is vital to avoid their rapid recombination, which can otherwise diminish photocatalytic efficiency.[213] A well-chosen band gap helps to maintain the separation of these charge carriers for longer periods, enhancing the overall performance of the photocatalyst.[214] The stability of the band gap under light exposure is also a key factor. A stable band gap ensures that the photocatalyst does not undergo quick degradation or lose its activity over time when exposed to light.[215] This stability helps maintain the material's effectiveness and longevity, making it a more reliable choice for prolonged photocatalytic applications.[216]

In addition to the band gap's fundamental role in determining the energy requirements for photocatalysis, its alignment with the redox potentials of reactants is crucial for effective photocatalytic reactions.[217] The CB of a photocatalyst must be positioned lower than the reduction potential of the target reactant, and the VB band must be positioned higher than the oxidation potential.[218] This alignment ensures that the electrons excited to the CB can efficiently reduce the reactants while the holes in the VB can oxidise them. This excitation is essential for driving the redox reactions needed for photocatalytic degradation of pollutants.[219]

ZnO stands out among its semiconductor counterparts as a particularly suitable material for photocatalysis due to band gap manipulation potential,[220] room temperature ultraviolet lasing[221], and device applications.[222]

2.3 ZnO as photocatalyst

ZnO offers several advantages over TiO_2, despite the latter being widely studied for its UV light activity.[223] ZnO boasts cost-effectiveness,[224] flexibility,[225] and superior electron mobility,[226] making it a strong contender for photocatalytic applications. Its affordability and availability further enhance suitability for large-scale industrial processes.[227] Additionally, ZnO is known for its resilience to chemical and thermal stress, allowing it to maintain photocatalytic activity in harsh environments over extended periods.[228] Its ability to be synthesised in various nanostructures,[6] such as nanoparticles,[229] nanorods,[230] nanowires,[226] and nanosheets,[170] increases its surface area-to-volume ratio, providing numerous active sites for reactions and enhancing efficiency.[231] ZnO is also biocompatible[78] and environmentally friendly,[232] with lower toxicity than other semiconductor photocatalysts, making it ideal for water purification and air treatment applications.[233] Moreover, the strong electron mobility in ZnO facilitates efficient charge carrier movement,[212] accelerating photocatalytic reactions and improving overall performance.

2.3.1 Crystal structure

ZnO, a group II-VI compound semiconductor, occupies a unique position between covalent and ionic semiconductors due to its intermediate ionicity. It exhibits three distinct crystal systems: hexagonal wurtzite, cubic rock salt, and cubic zinc-blende (also known as sphalerite),[234] [228] referred to here as hexagonal, cubic, and zinc-blende, respectively. These structures are characterised by tetrahedral coordination, where each anion is surrounded by four cations arranged at the corners of a tetrahedron, reflecting sp^3 covalent bonding. However, their ionic nature contributes to a higher bandgap than would be expected from purely covalent materials.

Under standard conditions, hexagonal ZnO is the most thermodynamically stable phase.[235] The zinc-blende structure of ZnO is metastable and can only be stabilised through heteroepitaxial growth on cubic substrates like ZnS,[236] GaAs/ZnS,[237] and Pt/Ti/SiO^2/Si[238]. While the cubic structure forms under high pressures, around 9.5-10 GPa, leading to a volume reduction of approximately 17%. Despite this, the cubic phase may remain metastable at ambient pressures above 100 °C.[239]

The images in Figures 2-1 highlight the distinct morphologies of the hexagonal,[240-242] cubic,[240-242] and zinc-blende[240-242] ZnO crystal systems as observed through scanning electron microscopy (SEM).

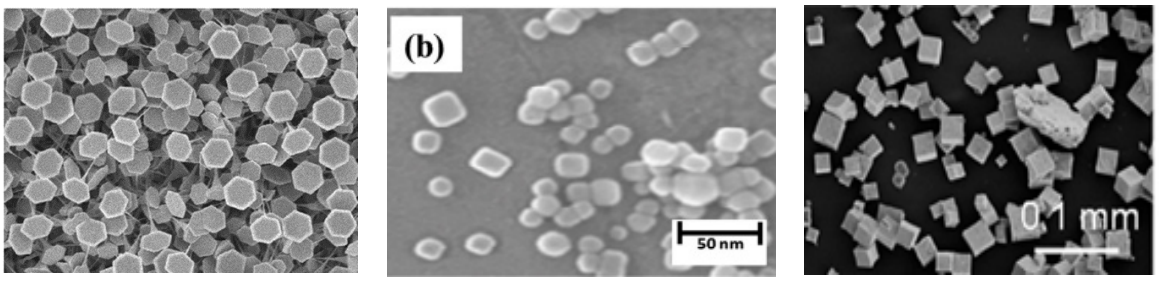

(a) (b) (c)

Figure 2-1: The SEM images of the three crystal systems of ZnO from published literature, namely, (a) hexagonal[240]

(The illustration was provided by American Chemical Society (ACS) Publications: Nano Letters no copyrights required for use DOI: 10.1021/nl025884u.) (b) cubic[241] (The illustration was provided by Elsevier Materials Today: Proceedings no copyrights required for use DOI: 10.1016/j.matpr.2017.11.257.) and (c) zinc-blende[242] (The illustration was provided by American Chemical Society (ACS) Publications: Inorganic Chemistry no copyrights required for use DOI: 10.1021/ic4017849.).https://pubs.acs.org/page/copyright/permissions.html

These variations in morphology play an important role in determining the physical and chemical properties of each system. The hexagonal structure (Figure 2-1 (a)), characterised by anisotropic growth, features well-defined facets and elongated shapes, enhancing its electronic properties and surface reactivity, which are particularly valuable for photocatalysis. The cubic structure (Figure 2-1 (b)), with its symmetrical and dense arrangement, typically displays uniform particle sizes, contributing to improved mechanical strength and thermal stability. Meanwhile, the zinc-blende structure (Figure 2-1 (c)), known for its tetrahedral coordination, exhibits a more isotropic morphology that can affect its electronic band structure and overall conductivity.

2.3.2 Electronic properties

The key to evaluating the electronic properties of ZnO, particularly its band gap, lies in understanding its density of states (DOS) and band structure. These properties are central to the role of ZnO in photocatalysis, optoelectronics, and other applications.

2.3.2.1 Density of States (DOS)

The electronic structure of ZnO is described in detail through its density of states (DOS), which outlines the distribution and availability of electron states within the structure. The VB is primarily shaped by Zn-3d and O-2p states, while the CB features contributions from Zn 4s and 4p states. Notably, the DOS intensity near the valence band maximum (VBM) is generally low due to the high dispersion of the band, indicating a lower density of electronic states available for occupation. In contrast, the conduction band minimum (CBM) exhibits a higher DOS intensity, reflecting more localised states. A detailed analysis using partial DOS (pDOS) further highlights that Zn-3d states are localised, and produce a significant peak around -7 eV, while O-2p states dominate near the VBM. Zn 4s orbital play a key role in forming the CB, influencing charge carrier behaviour.

DOS calculations can simulate experimental techniques like valence band X-ray photoelectron spectroscopy (VB-XPS) [243-248] and hard X-ray photoelectron spectroscopy (HAXPES),[249] considering factors such as atomic orbital photoionisation cross-sections and peak broadening effects analysed by Yeh and Lindau[250] and Scofield.[251] These analyses have been pivotal in studying the influence of oxygen vacancies, structural defects, and doping (e.g., with Sn or Ga) on the electronic structure of ZnO, as well as in understanding surface and interface properties.

2.3.2.2 Band structure

Band structures are graphical representations that show how the energy levels of electrons (called eigenvalues) change with respect to the wave vector, 'k'. Ideally, a band structure would cover all possible 'k' values for a material. However, due to computational limitations, focusing on specific paths that pass through high-symmetry points within the first Brillouin Zone (BZ) is common practise.

A band structure initially provides insights into the fundamental characteristics of the band gap, indicating whether it is indirect or direct, and its magnitude. The occupied states, constituting the VB, have their highest energy point, typically set at zero, termed the VBM. Above this band gap lie the empty states forming the CB, with the lowest point identified as the CBM. Notably, for the

hexagonal structure of ZnO, both the VBM and the CBM occur at the same 'k' values, specifically at k = 0, the Γ point.[252] This direct band gap typically ranges from 3.2eV[253] to 3.37 eV,[178, 254] enabling efficient light absorption and emission, which is valuable for optoelectronic and photocatalysis applications.

Conversely, ZnO in cubic or zinc-blende structures is predicted to exhibit an indirect band gap,[45, 255] where the VBM and CBM are located at different k-points. This indirect gap results in less efficient optical transitions, altering ZnO's optical properties in these forms. These differences in band gap behaviour are strongly influenced by crystal symmetry. The hexagonal wurtzite structure facilitates direct transitions due to its symmetry, whereas the cubic and zinc-blende structures tend to exhibit an indirect band gap. This transition is because their symmetry alters the relative alignment of the conduction band (CB) and valence band (VB), requiring a momentum change for electronic transitions.

However, the key feature of the band structure of ZnO is the magnitude of its band gap. The band gap allows ZnO to absorb UV light, which is essential for initiating photocatalytic reactions. This wide absorption capacity contributes significantly to its efficacy in photocatalysis, particularly when exposed to UV light, where it can create electron-hole pairs that initiate redox reactions, leading to the breakdown of organic pollutants and the oxidation of various substances.[256] However, to extend its photocatalytic activity into the visible light spectrum, efforts are being made to reduce its band gap using doping.

2.3.2.3 Doping

The modification of the electronic properties of semiconductors could be achieved through doping.[257] Doping can be tailored to modify the bandgap,[253] increase carrier concentration, and enhance optical absorption,[71] thereby making ZnO more suitable for specific applications, including transparent conducting oxides[258] and UV/visible light-responsive photocatalysts.[259] During doping, impurities are introduced into the crystal structure of the semiconductor. The nature of the dopant is essential for modifying the semiconductor for different applications. Donor impurities add extra electrons, creating n-type semiconductors (Figure 2-2 (a)) with negative charge carriers. In contrast, acceptor impurities generate holes, resulting in p-type semiconductors (Figure 2-2 (b)) with positive charge carriers.[260]

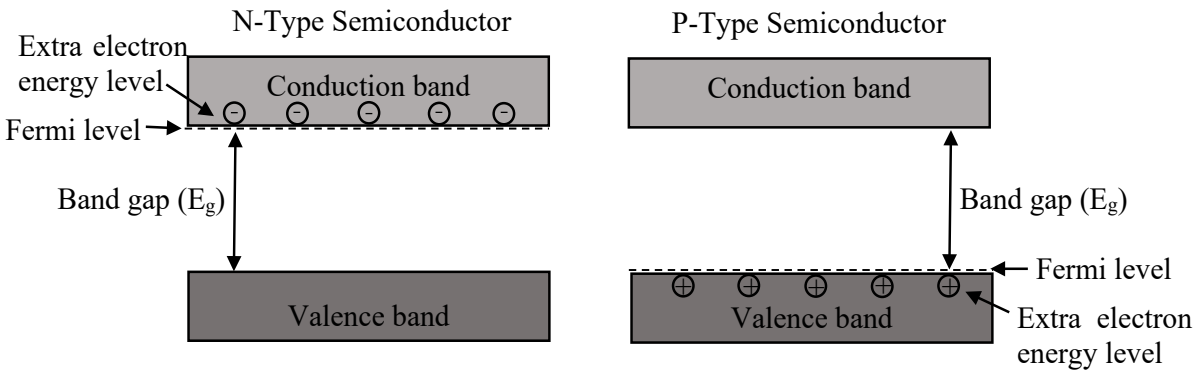

Figure 2-2: Comparison of n-type and p-type semiconductors.

The n-type semiconductors are doped with elements that have more valence electrons than the host material, resulting in excess free electrons (negative charge carriers). In contrast, p-type semiconductors are doped with elements that have fewer valence electrons, creating holes (positive charge carriers) that facilitate electrical conduction. The energy band diagrams in Figure 2-2 highlight the shifts in the Fermi level, which is closer to the CB in n-type semiconductors and closer to the VB in p-type semiconductors. This ability to control charge carriers is crucial for devices such as transistors, diodes, and solar cells.[261]

ZnO is an n-type semiconductor, even in its pure form, due to the presence of intrinsic defects such as oxygen vacancies (V_o) and zinc interstitials (Zn_i), which act as shallow donors, contributing free electrons to the CB.[262] This n-type characteristic is vital for enhancing photocatalytic activity and facilitating the efficient separation of charge carriers when the material is exposed to UV light.

Doping the crystal lattice of ZnO with transition metals stands as a widely recognised method for adjusting ZnO's bandgap, thereby altering the morphology, particle size, and crystallite size of the ZnO host to transform it into a visible-light-responsive photocatalyst. This process impedes the growth of ZnO, leading to the creation of smaller nanostructures possessing larger surface areas. Introducing transition metal cations into the ZnO lattice through substitutions modifies the Zn environment, reshaping its electronic band structure and introducing various crystal defects, notably oxygen vacancies. These vacancies can efficiently trap electrons, enhancing the separation efficiency of photo-generated electrons and holes.

Elements, such as aluminium (Al),[258] gallium (Ga),[263] or indium (In)[264], can further enhance n-type conductivity by donating additional electrons when substituting Zn atoms in the lattice.[265] These dopants, being group III elements, have three valence electrons compared to Zn's two, allowing them to donate additional electrons when they substitute Zn atoms in the lattice. Doping

ZnO[25, 266-268] with transition metals like Mn, Co, and Cu modifies its electronic structure, improving charge separation and enabling absorption of visible light, thus enhancing its performance under different light sources.[269] Similarly, Sn^{2+} can be used to dope ZnO, donating electrons to the CB and thereby enhancing the n-type semiconductor.[270]

The resulting increase in free electrons improves the electrical conductivity of ZnO, making it suitable for applications in transparent conductive oxides,[258] ultraviolet (UV) photodetectors,[42] and gas sensors.[231, 271, 272] Moreover, the optical absorption edge of ZnO extends into the visible light region upon doping with transition metals like Ag, Mn, Cu, Fe, Ni, and Si. However, the primary challenge with n-type ZnO is controlling the concentration and distribution of these dopants, as well as intrinsic defects to achieve consistent and desirable electronic properties.[273, 274] Nevertheless, ongoing investigations into hexagonal wurtzite ZnO as diluted magnetic semiconductors have been active, aiming to achieve effective transition-metal-doped ZnO with Curie temperatures surpassing room temperature. In contrast, certain semiconductors like transition-metal-doped Si, Ge, and Li were less commonly utilised due to their lower Curie temperatures compared to room temperature. These developments demonstrate ZnO's versatility as a promising material for future optoelectronic and magnetic applications.

2.4 Computational modelling of ZnO

The computational modelling of ZnO involves a comprehensive set of theoretical and simulation techniques aimed at understanding and predicting the material's properties, behaviour, and potential applications across various scales. This modelling approach is crucial for enhancing the performance of ZnO in fields like electronics, optoelectronics,[30] and photocatalysis.[78] A central aspect of this modelling is electronic structure calculations, primarily using density functional theory (DFT).[275] DFT is instrumental in determining the band structure, DOS, and the effects of doping, defects, or strain on the electronic properties of ZnO.[276]

However, standard DFT methods, such as the GGA/PBE method,[13, 277-280] tend to significantly underestimate the band gap, with reported values ranging between 0.65 eV[281] and 1.0 eV.[282] These values are significantly lower than the experimental value of around 3.37 eV.[55, 283] This underestimation is due to the limitations of GGA, which poorly estimates the binding energy in d-states, causing over-hybridisation with anion p valence states, resulting in a smaller band gap.[284]

To address these limitations, advanced methods like Tran–Blaha modified Becke–Johnson (TB-mBJ)[258] and hybrid functionals (GGA-PBE-HSE06)[285] have been used, providing improved band gap estimations of 2.70 eV and 2.49 eV, respectively. However, these estimations are still below the experimental 3.37 eV.[55, 283]

Using the GGA + U method, which adds the Hubbard U correction to better account for localised d and p states, has achieved band gaps closer to the experimental value of 3.37 eV.[286] Applying U for both Zn and O states ($U_{d\text{-}Zn}$ between 5-10.5 eV and $U_{p\text{-}O}$ between 7-8 eV) has successfully reproduced the correct band gap.[263, 284, 287-289] Recent calculations incorporating these parameters in various functionals (LDA + U, GGA-PBE + U, GGA-PBESol + U) have shown improved agreement with experimental data.[287, 288, 290]

Beyond band structure calculations, ZnO modelling also explores the influence of point defects, such as vacancies, interstitials, and antisites, on electrical and optical properties of ZnO.[291] These defects can act as charge traps or recombination centres, significantly impacting the material's conductivity, transparency, and photocatalytic efficiency.[292] Simulations also explore the effects of various dopants such as aluminium (Al),[293] gallium (Ga),[187] tin (Sn),[294] and transition metals on the electronic structure of ZnO.[295]

Surface and interface studies in ZnO computational modelling are equally important. These studies involve calculating the surface energies of different ZnO Miller planes, such as (002), (100), and (101), which are essential for predicting the stability and equilibrium shapes of ZnO nanostructures.[296] The Wulff construction[297] is often used to determine the equilibrium morphology of ZnO nanocrystals by minimising the total surface energy.

The impact of doping or surface modifications on ZnO morphology can also be explored through these models, offering insights into how to control the shape and size of nanostructures for enhanced performance in various applications.

2.5 References

(6) Abou Zeid, S.; Perez, A.; Bastide, S.; Le Pivert, M.; Rossano, S.; Remita, H.; Hautière, N.; Leprince-Wang, Y. Antibacterial and photocatalytic properties of ZnO nanostructure decorated coatings. *Coatings* **2023**, *14* (1), 41.

(8) Villani, M.; Calestani, D.; Lazzarini, L.; Zanotti, L.; Mosca, R.; Zappettini, A. Extended functionality of ZnO nanotetrapods by solution-based coupling with CdS nanoparticles. *Journal of Materials Chemistry* **2012**, *22*, 5694-5699. DOI: 10.1039/c2jm16164h.

(13) Mohamad, A. A.; Hassan, M. S.; Yaakob, M. K.; Taib, M. F. M.; Badrudin, F. W.; Hassan, O. H.; Yahya, M. Z. A. First-principles calculation on electronic properties of zinc oxide by zinc–air system. *Journal of King Saud University - Engineering Sciences* **2017**, *29* (3), 278-283. DOI: 10.1016/j.jksues.2015.08.002.

(14) Kumar, S. G.; Rao, K. K. Comparison of modification strategies towards enhanced charge carrier separation and photocatalytic degradation activity of metal oxide semiconductors (TiO_2, WO_3 and ZnO). *Applied Surface Science* **2017**, *391*, 124-148.

(25) Douloumis, A.; Vrithias, N. R. E.; Katsarakis, N.; Remediakis, I. N.; Kopidakis, G. Tuning the workfunction of ZnO through surface doping with Mn from first-principles simulations. *Surface Science* **2022**, *726*. DOI: 10.1016/j.susc.2022.122175.

(30) Shabbir, S.; Shaari, A.; Haq, B. U.; Ahmed, R.; Ahmed, M. Investigations of novel polymorphs of ZnO for optoelectronic applications. *Optik* **2020**, *206*, 164285.

(42) Liu, K.; Sakurai, M.; Aono, M. ZnO-based ultraviolet photodetectors. *Sensors* **2010**, *10* (9), 8604-8634.

(45) Sharma, D. K.; Shukla, S.; Sharma, K. K.; Kumar, V. A review on ZnO: Fundamental properties and applications. *Materials Today: Proceedings* **2022**, *49*, 3028-3035.

(49) Li, W.; Wang, G.; Feng, Y.; Li, Z. Efficient photocatalytic performance enhancement in Co-doped ZnO nanowires coupled with CuS nanoparticles. *Applied Surface Science* **2018**, *428*, 154-164. DOI: 10.1016/J.APSUSC.2017.09.049.

(52) Khan, H.; Shah, M. U. H. Modification strategies of TiO_2 based photocatalysts for enhanced visible light activity and energy storage ability: A review. *Journal of Environmental Chemical Engineering* **2023**, 111532.

(53) Height, M. J.; Pratsinis, S. E.; Mekasuwandumrong, O.; Praserthdam, P. Ag-ZnO catalysts for UV-photodegradation of methylene blue. *Applied Catalysis B: Environmental* **2006**, *63* (3-4), 305-312.

(55) Yang, W.; Zhang, B.; Zhang, Q.; Wang, L.; Song, B.; Ding, Y.; Wong, C. Adjusting the band structure and defects of ZnO quantum dots via tin doping. *RSC Advances* **2017**, *7* (19), 11345-11354.

(71) Beura, R.; Pachaiappan, R.; Thangadurai, P. A detailed study on Sn^{4+} doped ZnO for enhanced photocatalytic degradation. *Applied Surface Science* **2018**, *433*, 887-898. DOI: 10.1016/j.apsusc.2017.10.127.

(76) Ramalingam, G.; Perumal, N.; Priya, A.; Rajendran, S. A review of graphene-based semiconductors for photocatalytic degradation of pollutants in wastewater. *Chemosphere* **2022**, *300*, 134391.

(78) Baibara, O.; Radchenko, M.; Karpyna, V.; Ievtushenko, A. A review of the some aspects for the development of ZnO based photocatalysts for a variety of applications. *Physics and Chemistry of Solid State* **2021**, *22* (3), 585-594.

(84) Huang, B.; Lei, C.; Wei, C.; Zeng, G. Chlorinated volatile organic compounds (Cl-VOCs) in environment—sources, potential human health impacts, and current remediation technologies. *Environment International* **2014**, *71*, 118-138.

(85) Field, J.; Sierra-Alvarez, R. Biodegradability of chlorinated aromatic compounds. *Science dossier. Euro Chlor* **2007**, 15-33.

(86) Hanafi, M. F.; Sapawe, N. A review on the water problem associate with organic pollutants derived from phenol, methyl orange, and remazol brilliant blue dyes. *Materials Today: Proceedings* **2020**, *31*, A141-A150.

(87) Alsukaibi, A. K. Various approaches for the detoxification of toxic dyes in wastewater. *Processes* **2022**, *10* (10), 1968.

(88) Cheng, M.; Zeng, G.; Huang, D.; Yang, C.; Lai, C.; Zhang, C.; Liu, Y. Tween 80 surfactant-enhanced bioremediation: toward a solution to the soil contamination by hydrophobic organic compounds. *Critical Reviews in Biotechnology* **2018**, *38* (1), 17-30.

(89) Jackson, M.; Eadsforth, C.; Schowanek, D.; Delfosse, T.; Riddle, A.; Budgen, N. Comprehensive review of several surfactants in marine environments: fate and ecotoxicity. *Environmental Toxicology and Chemistry* **2016**, *35* (5), 1077-1086.

(90) Cameotra, S. S.; Dhanjal, S. Environmental nanotechnology: nanoparticles for bioremediation of toxic pollutants. In *Bioremediation technology: recent advances*, Springer, **2010**; pp 348-374.

(91) Long, J. L.; Stensel, H. D.; Ferguson, J. F.; Strand, S. E.; Ongerth, J. E. Anaerobic and aerobic treatment of chlorinated aliphatic compounds. *Journal of Environmental Engineering* **1993**, *119* (2), 300-320.

(92) Tibui, A. Biodegradation of aliphatic chlorinated hydrocarbon (PCE, TCE and DCE) in contaminated soil. Universitetsbibliotek: **2006**.

(93) Syal, S. *Reductive dechlorination in a continuous flow electrolysis cell*; Michigan State University, **1992**.

(94) Doherty, R. E. A history of the production and use of carbon tetrachloride, tetrachloroethylene, trichloroethylene and 1, 1, 1-trichloroethane in the United States: part 1—historical background; carbon tetrachloride and tetrachloroethylene. *Environmental Forensics* **2000**, *1* (2), 69-81.

(95) Zachara, J.; Wobber, F. RG Riley. **1992**.

(96) Lash, L. H.; Parker, J. C. Hepatic and renal toxicities associated with perchloroethylene. *Pharmacological Reviews* **2001**, *53* (2), 177-208.

(97) Wuebbles, D.; Patten, K.; Wang, D.; Youn, D.; Martínez-Avilés, M.; Francisco, J. Three-dimensional model evaluation of the Ozone Depletion Potentials for n-propyl bromide, trichloroethylene and perchloroethylene. *Atmospheric Chemistry & Physics Discussions* **2010**, *10* (7).

(98) Liu, Z. *Reductive dehalogenation of chlorinated aliphatic compounds in electrolytic systems*; The University of Arizona, **1999**.

(99) Rouf, Z.; Dar, I. Y.; Javaid, M.; Dar, M. Y.; Jehangir, A. Volatile organic compounds emission from building sector and its adverse effects on human health. *Ecological and Health Effects of Building Materials* **2022**, 67-86.

(100) Alimba, C. G. Dna and systemic damage induced by landfill leachates, and health impacts of human exposure to landfills in Lagos and Ibadan, Nigeria. University of Ibadan, **2013**.

(101) Chaturvedi, S.; Khurana, S. P. Importance of actinobacteria for bioremediation. In *In Plant biotechnology: progress in genomic era*, Springer, 2019; pp 277-307.

(102) Mukherjee, A. K.; Bordoloi, N. K. Biodegradation of benzene, toluene, and xylene (BTX) in liquid culture and in soil by Bacillus subtilis and Pseudomonas aeruginosa strains and a formulated bacterial consortium. *Environmental Science and Pollution Research* **2012**, *19*, 3380-3388.

(103) Cagliari, J.; Fedrizzi, F.; Rodrigues Finotti, A.; Echevenguá Teixeira, C.; do Nascimento Filho, I. Volatilization of monoaromatic compounds (benzene, toluene, and xylenes; BTX) from gasoline: Effect of the ethanol. *Environmental Toxicology and Chemistry: An International Journal* **2010**, *29* (4), 808-812.

(104) Liu, K.; Ramirez, A.; Zhang, X.; Çağlayan, M.; Gong, X.; Gascon, J.; Chowdhury, A. D. Interplay between particle size and hierarchy of zeolite ZSM-5 during the CO_2-to-aromatics process. *ChemSusChem* **2023**, *16* (19), e202300608.

(105) Bellussi, G. Zeolite catalysts for the production of chemical commodities: BTX derivatives. In *Studies in Surface Science and Catalysis*, Vol. 154; Elsevier, **2004**; pp 53-65.

(106) Ramirez Brenes, R. G.; Alhadeff, E. M.; Bojorge, N.; Trales, L. E.; Pazos, G. A. BTX production by breaking down lignin: Current status and future prospects. *Biofuels, Bioproducts and Biorefining* **2023**, *17* (3), 664-681.

(107) Morakinyo, O. M.; Mokgobu, M. I.; Mukhola, M. S.; Engelbrecht, J. C. Health risk assessment of exposure to ambient concentrations of benzene, toluene and xylene in Pretoria West, South Africa. *African Journal of Science, Technology, Innovation and Development* **2017**, *9* (4), 489-496.

(108) McHale, C. M.; Zhang, L.; Smith, M. T. Current understanding of the mechanism of benzene-induced leukemia in humans: implications for risk assessment. *Carcinogenesis* **2012**, *33* (2), 240-252.

(109) Snyder, R. Leukemia and benzene. *International Journal of Environmental Research and Public Health* **2012**, *9* (8), 2875-2893.

(110) Lu, X.; Qin, M.; Xie, P.; Shen, L.; Duan, J.; Liang, S.; Fang, W.; Liu, J.; Liu, W. Ambient BTX observation nearby main roads in Hefei during summer time. *Aerosol and Air Quality Research* **2017**, *17* (4), 933-943.

(111) Vaezihir, A.; Zare, M.; Raeisi, E.; Molson, J.; Barker, J. Field-scale modeling of benzene, toluene, ethylbenzene, and xylenes (BTEX) released from multiple source zones. *Bioremediation Journal* **2012**, *16* (3), 156-176.

(112) Yu, B.; Yuan, Z.; Yu, Z.; Xue-song, F. BTEX in the environment: An update on sources, fate, distribution, pretreatment, analysis, and removal techniques. *Chemical Engineering Journal* **2022**, *435*, 134825.

(113) Ma, L.; Hurtado, A.; Eguilior, S.; Borrajo, J. F. L. Acute and chronic risk assessment of BTEX in the return water of hydraulic fracturing operations in Marcellus Shale. *Science of The Total Environment* **2024**, *906*, 167638.

(114) Affat, S. S. Classifications, advantages, disadvantages, toxicity effects of natural and synthetic dyes: a review. *University of Thi-Qar Journal of Science* **2021**, *8* (1), 130-135.

(115) Hunger, K. *Industrial dyes: chemistry, properties, applications*; John Wiley & Sons, **2007**.

(116) Slama, H. B.; Chenari Bouket, A.; Pourhassan, Z.; Alenezi, F. N.; Silini, A.; Cherif-Silini, H.; Oszako, T.; Luptakova, L.; Golińska, P.; Belbahri, L. Diversity of synthetic dyes from textile industries, discharge impacts and treatment methods. *Applied Sciences* **2021**, *11* (14), 6255.

(117) Ismail, M.; Akhtar, K.; Khan, M.; Kamal, T.; Khan, M. A.; M Asiri, A.; Seo, J.; Khan, S. B. Pollution, toxicity and carcinogenicity of organic dyes and their catalytic bio-remediation. *Current Pharmaceutical Design* **2019**, *25* (34), 3645-3663.

(118) Chung, K.-T. The significance of azo-reduction in the mutagenesis and carcinogenesis of azo dyes. *Mutation Research/Reviews in Genetic Toxicology* **1983**, *114* (3), 269-281.

(119) Mathur, N.; Bhatnagar, P.; Sharma, P. Review of the mutagenicity of textile dye products. *Universal Journal of Environmental Research & Technology* **2012**, *2* (2).

(120) Ali, H. Biodegradation of synthetic dyes—a review. *Water, Air, & Soil Pollution* **2010**, *213*, 251-273.

(121) Maheshwari, K.; Agrawal, M.; Gupta, A. Dye pollution in water and wastewater. In *In Novel materials for dye-containing wastewater treatment*, Springer, 2021; pp 1-25.

(122) Sharma, J.; Sharma, S.; Soni, V. Classification and impact of synthetic textile dyes on Aquatic Flora: A review. *Regional Studies in Marine Science* **2021**, *45*, 101802.

(123) Dutta, S.; Adhikary, S.; Bhattacharya, S.; Roy, D.; Chatterjee, S.; Chakraborty, A.; Banerjee, D.; Ganguly, A.; Nanda, S.; Rajak, P. Contamination of textile dyes in aquatic environment: Adverse impacts on aquatic ecosystem and human health, and its

management using bioremediation. *Journal of Environmental Management* **2024**, *353*, 120103.

(124) Tkaczyk, A.; Mitrowska, K.; Posyniak, A. Synthetic organic dyes as contaminants of the aquatic environment and their implications for ecosystems: A review. *Science of The Total Environment* **2020**, *717*, 137222.

(125) Yangxin, Y.; Jin, Z.; Bayly, A. E. Development of surfactants and builders in detergent formulations. *Chinese Journal of Chemical Engineering* **2008**, *16* (4), 517-527.

(126) Knepper, T. P.; Berna, J. L. Surfactants: properties, production, and environmental aspects. *Comprehensive Analytical Chemistry* **2003**, *40*, 1-49.

(127) Karsa, D. R.; Houston, J. What are surfactants. In *In Chemistry and technology of surfactants*, Vol. 1; Wiley, 2006.

(128) Johnson, P.; Trybala, A.; Starov, V.; Pinfield, V. J. Effect of synthetic surfactants on the environment and the potential for substitution by biosurfactants. *Advances in Colloid and Interface Science* **2021**, *288*, 102340.

(129) Jardak, K.; Drogui, P.; Daghrir, R. Surfactants in aquatic and terrestrial environment: occurrence, behavior, and treatment processes. *Environmental Science and Pollution Research* **2016**, *23*, 3195-3216.

(130) Rebello, S.; Asok, A. K.; Mundayoor, S.; Jisha, M. Surfactants: chemistry, toxicity and remediation. *Pollutant Diseases, Remediation and Recycling* **2013**, 277-320.

(131) Rasheed, T.; Shafi, S.; Bilal, M.; Hussain, T.; Sher, F.; Rizwan, K. Surfactants-based remediation as an effective approach for removal of environmental pollutants—A review. *Journal of Molecular Liquids* **2020**, *318*, 113960.

(132) Badmus, S. O.; Amusa, H. K.; Oyehan, T. A.; Saleh, T. A. Environmental risks and toxicity of surfactants: overview of analysis, assessment, and remediation techniques. *Environmental Science and Pollution Research* **2021**, 1-20.

(133) Wong, M. H.; Wu, S. C.; Deng, W. J.; Yu, X.; Luo, Q.; Leung, A.; Wong, C.; Luksemburg, W.; Wong, A. Export of toxic chemicals–a review of the case of uncontrolled electronic-waste recycling. *Environmental Pollution* **2007**, *149* (2), 131-140.

(134) Vanden Bilcke, C. The Stockholm convention on persistent organic pollutants. *Rev. Eur. Comp. & Int'l Envtl. L.* **2002**, *11*, 328.

(135) Rummel-Bulska, I. United Nations Environment Programme. *Pol. Q. Int'l Aff.* **1995**, *4*, 129.

(136) Allegri Sr, T. H. The Resource Conservation and Recovery Act (RCRA). In *Handling and Management of Hazardous Materials and Waste*, Springer, **1986**; pp 361-382.

(137) Wagner, T. P. *The complete guide to the hazardous waste regulations: RCRA, TSCA, HMTA, OSHA, and Superfund*; John Wiley & Sons, **1999**.

(138) Marnell, M. F. EPA's Resonsibilities under RCRA: Administrative Law Issues. *Ecology LQ* **1980**, *9*, 555.

(139) Cooter, W. S. Clean Water Act assessment processes in relation to changing US Environmental Protection Agency management strategies. *Environmental Science & Technology* **2004**, *38* (20), 5265-5273.

(140) Rules, P. Clean Water Act methods update rule for the analysis of effluent. *Federal Register* **2015**, *80* (33).

(141) Williams, E. S.; Panko, J.; Paustenbach, D. J. The European Union's REACH regulation: a review of its history and requirements. *Critical Reviews in Toxicology* **2009**, *39* (7), 553-575.

(142) Talampas, S. I. Study on the different strategies and approaches followed by companies in Portugal and Spain to comply with Reach regulations. Universidade do Algarve (Portugal), **2017**.

(143) Voulvoulis, N.; Arpon, K. D.; Giakoumis, T. The EU Water Framework Directive: From great expectations to problems with implementation. *Science of The Total Environment* **2017**, *575*, 358-366.

(144) Brack, W.; Dulio, V.; Ågerstrand, M.; Allan, I.; Altenburger, R.; Brinkmann, M.; Bunke, D.; Burgess, R. M.; Cousins, I.; Escher, B. I. Towards the review of the European Union Water Framework Directive: recommendations for more efficient assessment and management of chemical contamination in European surface water resources. *Science of The Total Environment* **2017**, *576*, 720-737.

(145) Davies, J. CEPA—The Canadian. Environmental Protection Act. *JAPCA* **1988**, *38* (9), 1111-1113.

(146) Havas, M. Re: Canadian Environmental Protection Act (CEPA) Review. **2016**.

(147) Udom, G. J.; Frazzoli, C.; Ekhator, O. C.; Onyena, A. P.; Bocca, B.; Orisakwe, O. E. Pervasiveness, bioaccumulation and subduing environmental health challenges posed by polycyclic aromatic hydrocarbons (PAHs): A systematic review to settle a one health strategy in Niger Delta, Nigeria. *Environmental Research* **2023**, 115620.

(148) Van der Linde, M. *National Environmental Management Act 107 of 1998 (NEMA)*; Juta Law, **2009**.

(149) Terblanche, F. J. A legal framework for the transboundary movement of hazardous waste in South Africa and Lesotho. North-West University, **2007**.

(150) Behrens, A. A legal analysis of multilateral environmental agreements dealing with hazardous products and hazardous waste. University of Capetown, 2003.

(151) Nhamo, G. Environmental Law and policy reform surrounding packaging waste management in South Africa. *South African Journal of Environmental Law and Policy* **2007**, *14* (2), 136-157.

(152) Nkosi, B. R.; Odeku, K. O. Analysis of water pollution control laws in South Africa. *Mediterranean Journal of Social Sciences* **2014**, *5*, 2572-2582.

(153) Pegram, G.; Mazibuko, G.; Hollingworth, B.; Anderson, E. Strategic review of current and emerging governance systems related to water in the environment in South Africa. *Gezina, WRC Report* **2006**, (1514/1), 06.

(154) Fouad, K.; Bassyouni, M.; Alalm, M. G.; Saleh, M. Y. Recent developments in recalcitrant organic pollutants degradation using immobilized photocatalysts. *Applied Physics A* **2021**, *127* (8), 612.

(155) Hay, S. O.; Obee, T.; Luo, Z.; Jiang, T.; Meng, Y.; He, J.; Murphy, S. C.; Suib, S. The viability of photocatalysis for air purification. *Molecules* **2015**, *20* (1), 1319-1356.

(156) Li, F.; Liu, G.; Liu, F.; Yang, S. A review of self-cleaning photocatalytic surface: Effect of surface characteristics on photocatalytic activity for NO. *Environmental Pollution* **2023**, 121580.

(157) Lin, C.-P.; Chen, H.; Nakaruk, A.; Koshy, P.; Sorrell, C. Effect of annealing temperature on the photocatalytic activity of TiO_2 thin films. *Energy Procedia* **2013**, *34*, 627-636.

(158) Talinungsang; Upadhaya, D.; Kumar, P.; Purkayastha, D. D. Superhydrophilicity of photocatalytic ZnO/SnO_2 heterostructure for self-cleaning applications. *Journal of Sol-gel Science and Technology* **2019**, *92*, 575-584.

(159) Ma, Y.; Wang, H.; Sun, L.; Liu, E.; Fei, G.; Fan, J.; Kang, Y.-M. Unidirectional electron transport from graphitic-C_3N_4 for novel remote and long-term photocatalytic anti-corrosion on Q235 carbon steel. *Chemical Engineering Journal* **2022**, *429*, 132520.

(160) Panzarasa, G.; Soliveri, G. Photocatalytic lithography. *Applied Sciences* **2019**, *9* (7), 1266.

(161) Kayani, A. B. A.; Kuriakose, S.; Monshipouri, M.; Khalid, F. A.; Walia, S.; Sriram, S.; Bhaskaran, M. UV photochromism in transition metal oxides and hybrid materials. *Small* **2021**, *17* (32), 2100621.

(162) Rashmi Pradhan, S.; Colmenares-Quintero, R. F.; Colmenares Quintero, J. C. Designing microflowreactors for photocatalysis using sonochemistry: A systematic review article. *Molecules* **2019**, *24* (18), 3315.

(163) Qi, M.-Y.; Conte, M.; Anpo, M.; Tang, Z.-R.; Xu, Y.-J. Cooperative coupling of oxidative organic synthesis and hydrogen production over semiconductor-based photocatalysts. *Chemical Reviews* **2021**, *121* (21), 13051-13085.

(164) Fujishima, A.; Honda, K. Electrochemical photolysis of water at a semiconductor electrode. *Nature* **1972**, *238* (5358), 37-38.

(165) Frank, S. N.; Bard, A. J. Heterogeneous photocatalytic oxidation of cyanide and sulfite in aqueous solutions at semiconductor powders. *The Journal of Physical Chemistry* **1977**, *81* (15), 1484-1488.

(166) Konstantinou, I. K.; Albanis, T. A. TiO_2-assisted photocatalytic degradation of azo dyes in aqueous solution: kinetic and mechanistic investigations: A review. *Applied Catalysis B: Environmental* **2004**, *49* (1), 1-14. DOI: 10.1016/j.apcatb.2003.11.010.

(167) Das, A.; Adak, M. K.; Mahata, N.; Biswas, B. Wastewater treatment with the advent of TiO_2 endowed photocatalysts and their reaction kinetics with scavenger effect. *Journal of Molecular Liquids* **2021**, *338*, 116479.

(168) Chen, N.; Li, Y.; Deng, D.; Liu, X.; Xing, X.; Xiao, X.; Wang, Y. Acetone sensing performances based on nanoporous TiO_2 synthesized by a facile hydrothermal method. *Sensors and Actuators B: Chemical* **2017**, *238*, 491-500. DOI: 10.1016/j.snb.2016.07.094.

(169) Yu, Z.; Qu, X.; Yang, W.; Peng, J.; Xu, Z. A facile hydrothermal synthesis and memristive switching performance of rutile TiO_2 nanowire arrays. *Journal of Alloys and Compounds* **2016**, *688*, 37-43. DOI: 10.1016/j.jallcom.2016.07.167.

(170) Duo, S.; Li, Y.; Liu, Z.; Zhong, R.; Liu, T.; Xu, H. Preparation of ZnO from 2 D nanosheets to diverse 1 D nanorods and their structure, surface area, photocurrent, optical and photocatalytic properties by simple hydrothermal synthesis. *Journal of Alloys and Compounds* **2017**, *695*, 2563-2579. DOI: 10.1016/j.jallcom.2016.11.162.

(171) Zhou, Y.; Xu, L.; Wu, Z.; Li, P.; He, J. Optical and photocatalytic properties of nanocrystalline ZnO powders synthesized by a low-temperature hydrothermal method. *Optik* **2017**, *130*, 673-680. DOI: 10.1016/j.ijleo.2016.10.119.

(172) Jin, W. X.; Ma, S. Y.; Tie, Z. Z.; Jiang, X. H.; Li, W. Q.; Luo, J.; Xu, X. L.; Wang, T. T. Hydrothermal synthesis of monodisperse porous cube, cake and spheroid-like α-Fe_2O_3 particles and their high gas-sensing properties. *Sensors and Actuators B: Chemical* **2015**, *220*, 243-254. DOI: 10.1016/j.snb.2015.05.098.

(173) Li, Z.; Lin, Z.; Wang, N.; Huang, Y.; Wang, J.; Liu, W.; Fu, Y.; Wang, Z. Facile synthesis of α-Fe_2O_3 micro-ellipsoids by surfactant-free hydrothermal method for sub-ppm level H_2S detection. *Materials & Design* **2016**, *110*, 532-539. DOI: 10.1016/j.matdes.2016.08.035.

(174) Fang, J.; Xu, J.; Chen, J.; Huang, X.; Wang, X. Enhanced photocatalytic activity of molecular imprinted nano α-Fe_2O_3 by hydrothermal synthesis using methylene blue as structure-directing agent. *Colloids and Surfaces A: Physicochemical and Engineering Aspects* **2016**, *508*, 124-134. DOI: 10.1016/j.colsurfa.2016.08.048.

(175) Areeb, A.; Yousaf, T.; Murtaza, M.; Zahra, M.; Zafar, M. I.; Waseem, A. Green photocatalyst Cu/NiO doped zirconia for the removal of environmental pollutants. *Materials Today Communications* **2021**, *28*, 102678.

(176) Sayama, K.; Arakawa, H. Photocatalytic decomposition of water and photocatalytic reduction of carbon dioxide over zirconia catalyst. *The Journal of Physical Chemistry* **1993**, *97* (3), 531-533.

(177) Wei, S.; Han, L.; Wang, M.; Zhang, H.; Du, W.; Zhou, M. Hollow cauliflower-like WO_3 nanostructures: Hydrothermal synthesis and their CO sensing properties. *Materials Letters* **2017**, *186*, 259-262. DOI: 10.1016/j.matlet.2016.10.016.

(178) Yu, Y.; Zeng, W.; Yu, L.; Wu, S. A novel $WO_3 \cdot H_2O$ nanostructure assembled with nanorods: Hydrothermal synthesis, growth and their gas sensing properties. *Materials Letters* **2016**, *180*, 51-54. DOI: 10.1016/j.matlet.2016.05.113.

(179) Li, J.; Dai, W.; Wu, G.; Guan, N.; Li, L. Fabrication of Ta_2O_5 films on tantalum substrate for efficient photocatalysis. *Catalysis Communications* **2015**, *65*, 24-29. DOI: 10.1016/j.catcom.2015.02.006.

(180) Kusmierek, E. Semiconductor electrode materials applied in photoelectrocatalytic wastewater treatment—an overview. *Catalysts* **2020**, *10* (4), 439.

(181) Opoku, F.; Govender, K. K.; van Sittert, C. G. C. E.; Govender, P. P. Recent progress in the development of semiconductor-based photocatalyst materials for applications in photocatalytic water splitting and degradation of pollutants. *Advanced Sustainable Systems* **2017**, *1* (7), 1700006.

(182) Corrigan, N.; Shanmugam, S.; Xu, J.; Boyer, C. Photocatalysis in organic and polymer synthesis. *Chemical Society Reviews* **2016**, *45* (22), 6165-6212.

(183) Fresno, F.; Portela, R.; Suárez, S.; Coronado, J. M. Photocatalytic materials: recent achievements and near future trends. *Journal of Materials Chemistry A* **2014**, *2* (9), 2863-2884.

(184) Xu, C.; Anusuyadevi, P. R.; Aymonier, C.; Luque, R.; Marre, S. Nanostructured materials for photocatalysis. *Chemical Society Reviews* **2019**, *48* (14), 3868-3902.

(185) Mancuso, A.; Iervolino, G. Synthesis and application of innovative and environmentally friendly photocatalysts: a review. *Catalysts* **2022**, *12* (10), 1074.

(186) Kumar, S.; Kumar, A.; Kumar, A.; Krishnan, V. Nanoscale zinc oxide based heterojunctions as visible light active photocatalysts for hydrogen energy and environmental remediation. *Catalysis Reviews* **2020**, *62* (3), 346-405. DOI: 10.1080/01614940.2019.1684649.

(187) Lee, M.-H.; Peng, Y.-C.; Wu, H.-C. Effects of intrinsic defects on electronic structure and optical properties of Ga-doped ZnO. *Journal of Alloys and Compounds* **2014**, *616*, 122-127.

(188) Benzaouak, A.; Ellouzi, I.; Ouanji, F.; Touach, N.; Kacimi, M.; Ziyad, M.; El Mahi, M.; Lotfi, E. M. Photocatalytic degradation of Methylene Blue (MB) dye in aqueous solution by ferroelectric $Li_{1-x}Ta_{1-x}W_xO_3$ materials. *Colloids and Surfaces A: Physicochemical and Engineering Aspects* **2018**, *553*, 586-592.

(189) Cao, S.; Fan, B.; Feng, Y.; Chen, H.; Jiang, F.; Wang, X. Sulfur-doped g-C_3N_4 nanosheets with carbon vacancies: General synthesis and improved activity for simulated solar-light photocatalytic nitrogen fixation. *Chemical Engineering Journal* **2018**, *353*, 147-156.

(190) Wang, S.; Wang, Y.; Li, L.; Li, L.; Fu, G.; Shi, R.; Zou, X.; Zhang, Z.; Luo, F. Green synthesis of Ag/TiO_2 composite coated porous vanadophosphates with enhanced visible-light photo-degradation and catalytic reduction performance for removing organic dyes. *Dalton Transactions* **2020**, *49* (23), 7920-7931.

(191) Mohapatra, T.; Manekar, S.; Kumar Sahu, V.; Soni, A. K.; Banerjee, S.; Ghosh, P. Green synthesized Ag-TiO_2 for degradation of organic dye through visible light driven photo-reactor and its kinetics. *International Journal of Chemical Reactor Engineering* **2021**, *19* (9), 893-900.

(192) Kamat, P. V. Photochemistry on nonreactive and reactive (semiconductor) surfaces. *Chemical Reviews* **1993**, *93* (1), 267-300.

(193) John, M. J.; Anandjiwala, R. D. Recent developments in chemical modification and characterization of natural fiber-reinforced composites. *Polymer Composites* **2008**, *29* (2), 187-207.

(194) Wu, G.; Li, P.; Feng, H.; Zhang, X.; Chu, P. K. Engineering and functionalization of biomaterials via surface modification. *Journal of Materials Chemistry B* **2015**, *3* (10), 2024-2042.

(195) Qiu, P.; Zhou, N.; Chen, H.; Zhang, C.; Gao, G.; Cui, D. Recent advances in lanthanide-doped upconversion nanomaterials: synthesis, nanostructures and surface modification. *Nanoscale* **2013**, *5* (23), 11512-11525.

(196) Kusiak-Nejman, E.; Morawski, A. W. TiO2/graphene-based nanocomposites for water treatment: A brief overview of charge carrier transfer, antimicrobial and photocatalytic performance. *Applied Catalysis B: Environmental* **2019**, *253*, 179-186.

(197) Fang, J.; Fan, H.; Ma, Y.; Wang, Z.; Chang, Q. Surface defects control for ZnO nanorods synthesized by quenching and their anti-recombination in photocatalysis. *Applied Surface Science* **2015**, *332*, 47-54.

(198) Chen, D.; Jiang, Z.; Geng, J.; Wang, Q.; Yang, D. Carbon and nitrogen co-doped TiO_2 with enhanced visible-light photocatalytic activity. *Industrial & Engineering Chemistry Research* **2007**, *46* (9), 2741-2746.

(199) Basavarajappa, P. S.; Patil, S. B.; Ganganagappa, N.; Reddy, K. R.; Raghu, A. V.; Reddy, C. V. Recent progress in metal-doped TiO_2, non-metal doped/codoped TiO_2 and TiO_2 nanostructured hybrids for enhanced photocatalysis. *International Journal of Hydrogen Energy* **2020**, *45* (13), 7764-7778.

(200) Zhu, W.; Chen, Z.; Pan, Y.; Dai, R.; Wu, Y.; Zhuang, Z.; Wang, D.; Peng, Q.; Chen, C.; Li, Y. Functionalization of hollow nanomaterials for catalytic applications: nanoreactor construction. *Advanced Materials* **2019**, *31* (38), 1800426.

(201) Amani, H.; Arzaghi, H.; Bayandori, M.; Dezfuli, A. S.; Pazoki-Toroudi, H.; Shafiee, A.; Moradi, L. Controlling cell behavior through the design of biomaterial surfaces: a focus on surface modification techniques. *Advanced Materials Interfaces* **2019**, *6* (13), 1900572.

(202) Dou, S.; Tao, L.; Wang, R.; El Hankari, S.; Chen, R.; Wang, S. Plasma-assisted synthesis and surface modification of electrode materials for renewable energy. *Advanced Materials* **2018**, *30* (21), 1705850.

(203) Dutt, M. A.; Hanif, M. A.; Nadeem, F.; Bhatti, H. N. A review of advances in engineered composite materials popular for wastewater treatment. *Journal of Environmental Chemical Engineering* **2020**, *8* (5), 104073.

(204) Kurian, M. Advanced oxidation processes and nanomaterials-a review. *Cleaner Engineering and Technology* **2021**, *2*, 100090.

(205) Pandis, P. K.; Kalogirou, C.; Kanellou, E.; Vaitsis, C.; Savvidou, M. G.; Sourkouni, G.; Zorpas, A. A.; Argirusis, C. Key points of advanced oxidation processes (AOPs) for wastewater, organic pollutants and pharmaceutical waste treatment: A mini review. *ChemEngineering* **2022**, *6* (1), 8.

(206) Papić, S.; Koprivanac, N.; Božić, A. L.; Vujević, D.; Dragičević, S. K.; Kušić, H.; Peternel, I. Advanced oxidation processes in azo dye wastewater treatment. *Water Environment Research* **2006**, *78* (6), 572-579.

(207) Rekhate, C. V.; Srivastava, J. Recent advances in ozone-based advanced oxidation processes for treatment of wastewater-A review. *Chemical Engineering Journal Advances* **2020**, *3*, 100031.

(208) Titchou, F. E.; Zazou, H.; Afanga, H.; El Gaayda, J.; Akbour, R. A.; Nidheesh, P. V.; Hamdani, M. Removal of organic pollutants from wastewater by advanced oxidation processes and its combination with membrane processes. *Chemical Engineering and Processing-Process Intensification* **2021**, *169*, 108631.

(209) Dhamorikar, R. S.; Lade, V. G.; Kewalramani, P. V.; Bindwal, A. B. Review on integrated advanced oxidation processes for water and wastewater treatment. *Journal of Industrial and Engineering Chemistry* **2024**.

(210) Arif, A.; Belahssen, O.; Gareh, S.; Benramache, S. The calculation of band gap energy in zinc oxide films. *Journal of Semiconductors* **2015**, *36* (1), 013001.

(211) Acar, C.; Dincer, I. *2.17 Photoactive Materials*; Elsevier, 2018.

(212) Li, H.; Zhou, Y.; Tu, W.; Ye, J.; Zou, Z. State-of-the-art progress in diverse heterostructured photocatalysts toward promoting photocatalytic performance. *Advanced Functional Materials* **2015**, *25* (7), 998-1013.

(213) Yanagi, R.; Zhao, T.; Solanki, D.; Pan, Z.; Hu, S. Charge separation in photocatalysts: mechanisms, physical parameters, and design principles. *ACS Energy Letters* **2021**, *7* (1), 432-452.

(214) Koe, W. S.; Lee, J. W.; Chong, W. C.; Pang, Y. L.; Sim, L. C. An overview of photocatalytic degradation: photocatalysts, mechanisms, and development of photocatalytic membrane. *Environmental Science and Pollution Research* **2020**, *27* (3), 2522-2565.

(215) Li, T.; Zhao, L.; He, Y.; Cai, J.; Luo, M.; Lin, J. Synthesis of g-C_3N_4/$SmVO_4$ composite photocatalyst with improved visible light photocatalytic activities in RhB degradation. *Applied Catalysis B: Environmental* **2013**, *129*, 255-263.

(216) Sun, M.-H.; Huang, S.-Z.; Chen, L.-H.; Li, Y.; Yang, X.-Y.; Yuan, Z.-Y.; Su, B.-L. Applications of hierarchically structured porous materials from energy storage and conversion, catalysis, photocatalysis, adsorption, separation, and sensing to biomedicine. *Chemical Society Reviews* **2016**, *45* (12), 3479-3563.

(217) Zhang, P.; Wang, T.; Gong, J. Current mechanistic understanding of surface reactions over water-splitting photocatalysts. *Chem* **2018**, *4* (2), 223-245.

(218) Corma, A.; Garcia, H. Photocatalytic reduction of CO_2 for fuel production: Possibilities and challenges. *Journal of Catalysis* **2013**, *308*, 168-175.

(219) Ling, G. Z. S.; Ng, S. F.; Ong, W. J. Tailor-engineered 2D cocatalysts: harnessing electron–hole redox center of 2D g-C_3N_4 photocatalysts toward solar-to-chemical conversion and environmental purification. *Advanced Functional Materials* **2022**, *32* (29), 2111875.

(220) Borysiewicz, M. A. ZnO as a functional material, a review. *Crystals* **2019**, *9* (10), 505.

(221) Bharti, D. B.; Bharati; V, A. Synthesis of ZnO nanoparticles using a hydrothermal method and a study its optical activity. *Luminescence* **2017**, *32* (3), 317-320. DOI: 10.1002/bio.3180.

(222) Rong, P.; Ren, S.; Yu, Q. Fabrications and applications of ZnO nanomaterials in flexible functional devices-a review. *Critical Reviews in Analytical Chemistry* **2019**, *49* (4), 336-349.

(223) Lian, P.; Qin, A.; Liao, L.; Zhang, K. Progress on the nanoscale spherical TiO2 photocatalysts: Mechanisms, synthesis and degradation applications. *Nano Select* **2021**, *2* (3), 447-467.

(224) Theerthagiri, J.; Salla, S.; Senthil, R.; Nithyadharseni, P.; Madankumar, A.; Arunachalam, P.; Maiyalagan, T.; Kim, H.-S. A review on ZnO nanostructured materials: energy, environmental and biological applications. *Nanotechnology* **2019**, *30* (39), 392001.

(225) Maiti, S.; Pal, S.; Chattopadhyay, K. K. Recent advances in low temperature, solution processed morphology tailored ZnO nanoarchitectures for electron emission and photocatalysis applications. *CrystEngComm* **2015**, *17* (48), 9264-9295.

(226) Consonni, V.; Briscoe, J.; Kärber, E.; Li, X.; Cossuet, T. ZnO nanowires for solar cells: A comprehensive review. *Nanotechnology* **2019**, *30* (36), 362001.

(227) Abou Zeid, S.; Leprince-Wang, Y. Advancements in ZnO-based photocatalysts for water treatment: A comprehensive review. *Crystals* **2024**, *14* (7), 611.

(228) Raha, S.; Ahmaruzzaman, M. ZnO nanostructured materials and their potential applications: progress, challenges and perspectives. *Nanoscale Advances* **2022**, *4* (8), 1868-1925.

(229) Gnaneswari, M. D.; Marimuthu, K.; Chandrasekar, B.; Leonora, J. M. Chemically prepared P-Type Sn doped ZnO nanoparticles: Synthesis, characterization and its antibacterial properties. *Journal of Crystal Growth* **2024**, *627*, 127548.

(230) Illy, B. N.; Ingham, B.; Toney, M. F.; Nandhakumar, I.; Ryan, M. P. Understanding the selective etching of electrodeposited ZnO nanorods. *Langmuir* **2014**, *30* (46), 14079-14085. DOI: 10.1021/la503765a.

(231) Ahmad, R.; Majhi, S. M.; Zhang, X.; Swager, T. M.; Salama, K. N. Recent progress and perspectives of gas sensors based on vertically oriented ZnO nanomaterials. *Advances in Colloid and Interface Science* **2019**, *270*, 1-27.

(232) Raizada, P.; Sudhaik, A.; Singh, P. Photocatalytic water decontamination using graphene and ZnO coupled photocatalysts: A review. *Materials Science for Energy Technologies* **2019**, *2* (3), 509-525.

(233) Maynez-Navarro, O.; Sánchez-Salas, J. Focus on zinc oxide as a photocatalytic material for water treatment. *International Journal of Bioremediation & Biodegradation* **2018**, *106*. DOI: 10.29011/IJBB-106/100006.

(234) Charifi, Z.; Baaziz, H.; Hussain Reshak, A. Ab-initio investigation of structural, electronic and optical properties for three phases of ZnO compound. *physica status solidi (b)* **2007**, *244* (9), 3154-3167. DOI: 10.1002/pssb.200642471.

(235) Leitner, J.; Bartůněk, V.; Sedmidubský, D.; Jankovský, O. Thermodynamic properties of nanostructured ZnO. *Applied Materials Today* **2018**, *10*, 1-11.

(236) Kogure, T.; Bando, Y. Formation of ZnO nanocrystals in the cubic phase was reported by electron-beam induced oxidation of ZnS surfaces during TEM observations. *Journal of Electron Microscopy* **1993**, *47*, 7903-7909.

(237) Ashrafi, A. A.; Ueta, A.; Avramescu, A.; Kumano, H.; Suemune, I.; Ok, Y.-W.; Seong, T.-Y. Growth and characterization of hypothetical zinc-blende ZnO films on GaAs (001) substrates with ZnS buffer layers. *Applied Physics Letters* **2000**, *76* (5), 550-552.

(238) Kim, S.-K.; Jeong, S.-Y.; Cho, C.-R. Structural reconstruction of hexagonal to cubic ZnO films on Pt/Ti/SiO_2/Si substrate by annealing. *Applied Physics Letters* **2003**, *82* (4), 562-564.

(239) Bates, C. H.; White, W. B. New high-pressure polymorph of zinc oxide. *Science* **1962**, *137* (3534), 993.

(240) Lao, J. Y.; Huang, J. Y.; Wang, D. Z.; Ren, Z. F. ZnO nanobridges and nanonails. *Nano Letters* **2003**, *3* (2), 235-238. DOI: 10.1021/nl025884u.

(241) Maheshwary, P. B.; Handa, C. C.; Nemade, K. R. Effect of shape on thermophysical and heat transfer properties of ZnO/R-134a manorefrigerant. *Materials Today: Proceedings* **2018**, *5* (1, Part 1), 1635-1639. DOI: 10.1016/j.matpr.2017.11.257.

(242) Kimitsuka, Y.; Hosono, E.; Ueno, S.; Zhou, H.; Fujihara, S. Fabrication of porous cubic architecture of ZnO using Zn-terephthalate MOFs with characteristic microstructures. *Inorganic Chemistry* **2013**, *52* (24), 14028-14033.

(243) Savory, C. N.; Ganose, A. M.; Travis, W.; Atri, R. S.; Palgrave, R. G.; Scanlon, D. O. An assessment of silver copper sulfides for photovoltaic applications: theoretical and experimental insights. *Journal of Materials Chemistry A* **2016**, *4* (32), 12648-12657.

(244) Sathasivam, S.; Arnepalli, R. R.; Bhachu, D. S.; Lu, Y.; Buckeridge, J.; Scanlon, D. O.; Kumar, B.; Singh, K. K.; Visser, R. J.; Blackman, C. S. Single step solution processed GaAs thin films from $GaMe_3$ and T $BuAsH_2$ under ambient pressure. *The Journal of Physical Chemistry C* **2016**, *120* (13), 7013-7019.

(245) Bhachu, D. S.; Moniz, S. J.; Sathasivam, S.; Scanlon, D. O.; Walsh, A.; Bawaked, S. M.; Mokhtar, M.; Obaid, A. Y.; Parkin, I. P.; Tang, J. Bismuth oxyhalides: synthesis, structure and photoelectrochemical activity. *Chemical Science* **2016**, *7* (8), 4832-4841.

(246) Sathasivam, S.; Williamson, B. A.; Kafizas, A.; Althabaiti, S. A.; Obaid, A. Y.; Basahel, S. N.; Scanlon, D. O.; Carmalt, C. J.; Parkin, I. P. Computational and experimental study of Ta_2O_5 thin films. *The Journal of Physical Chemistry C* **2017**, *121* (1), 202-210.

(247) Körber, C.; Krishnakumar, V.; Klein, A.; Panaccione, G.; Torelli, P.; Walsh, A.; Da Silva, J.; Wei, S.-H.; Egdell, R.; Payne, D. Electronic structure of In_2O_3 and Sn-doped In_2O_3 by hard x-ray photoemission spectroscopy. *Physical Review B* **2010**, *81* (16), 165207.

(248) Williamson, B. A.; Buckeridge, J.; Brown, J.; Ansbro, S.; Palgrave, R. G.; Scanlon, D. O. Engineering valence band dispersion for high mobility p-type semiconductors. *Chemistry of Materials* **2017**, *29* (6), 2402-2413.

(249) Walsh, L. Applications of hard X-ray photoelectron spectroscopy in semiconductor materials characterisation. Dublin City University, 2014.

(250) Yeh, J.; Lindau, I. Atomic subshell photoionization cross sections and asymmetry parameters: $1 \leqslant Z \leqslant 103$. *Atomic Data and Nuclear Data Tables* **1985**, *32* (1), 1-155.

(251) Scofield, J. Lawrence Livermore Laboratory Report No. *UCRL-51326* **1973**.

(252) Li, H.; Schirra, L. K.; Shim, J.; Cheun, H.; Kippelen, B.; Monti, O. L.; Bredas, J.-L. Zinc oxide as a model transparent conducting oxide: a theoretical and experimental study of the impact of hydroxylation, vacancies, interstitials, and extrinsic doping on the electronic properties of the polar ZnO (0002) surface. *Chemistry of Materials* **2012**, *24* (15), 3044-3055.

(253) Krithiga, R.; Sankar, S.; Subhashree, G. Na to tailor the band gap and morphology of ZnO nanograins. *Journal of Materials Science: Materials in Electronics* **2014**, *25*, 103-110.

(254) Yang, C.; Li, X.; Gu, Y.; Yu, W.; Gao, X.; Zhang, Y. ZnO based oxide system with continuous bandgap modulation from 3.7 to 4.9 eV. *Applied Physics Letters* **2008**, *93* (11).

(255) Zagorac, D.; Schön, J.; Zagorac, J.; Jansen, M. Prediction of structure candidates for zinc oxide as a function of pressure and investigation of their electronic properties. *Physical Review B* **2014**, *89* (7), 075201.

(256) Abdul Hamid, S. B.; Teh, S. J.; Lai, C. W. Photocatalytic water oxidation on ZnO: a review. *Catalysts* **2017**, *7* (3), 93.

(257) Zhao, W.; Ding, J.; Zou, Y.; Di, C.-a.; Zhu, D. Chemical doping of organic semiconductors for thermoelectric applications. *Chemical Society Reviews* **2020**, *49* (20), 7210-7228.

(258) Slassi, A.; Naji, S.; Benyoussef, A.; Hamedoun, M.; El Kenz, A. On the transparent conducting oxide Al doped ZnO: First Principles and Boltzmann equations study. *Journal of Alloys and Compounds* **2014**, *605*, 118-123. DOI: 10.1016/j.jallcom.2014.03.177.

(259) Kaneva, N. V.; Dimitrov, D. T.; Dushkin, C. D. Effect of nickel doping on the photocatalytic activity of ZnO thin films under UV and visible light. *Applied Surface Science* **2011**, *257* (18), 8113-8120. DOI: 10.1016/j.apsusc.2011.04.119.

(260) Jain, V. K. Semiconductors. In *Solid State Physics*, Springer, 2022; pp 295-330.

(261) Ouyang, W.; Teng, F.; He, J. H.; Fang, X. Enhancing the photoelectric performance of photodetectors based on metal oxide semiconductors by charge-carrier engineering. *Advanced Functional Materials* **2019**, *29* (9), 1807672.

(262) Morasae, S. M., Zirak; Amene, N.; Elham, K.; Alireza, Z. M. Recent progress on doped ZnO nanostructures for visible-light photocatalysis. *Thin Solid Films* **2016**, *605*.

(263) Lee, Y.-S.; Peng, Y.-C.; Lu, J.-H.; Zhu, Y.-R.; Wu, H.-C. Electronic and optical properties of Ga-doped ZnO. *Thin Solid Films* **2014**, *570*, 464-470. DOI: 10.1016/j.tsf.2014.04.037.

(264) Huang, C.; Wang, M.; Deng, Z.; Cao, Y.; Liu, Q.; Huang, Z.; Liu, Y.; Guo, W.; Huang, Q. Effects of hydrogen annealing on the structural, optical and electrical properties of indium-doped zinc oxide films. *Journal of Materials Science: Materials in Electronics* **2010**, *21*, 1221-1227.

(265) Papadimitriou, D. N. Engineering of optical and electrical properties of electrodeposited highly doped Al: ZnO and In: ZnO for cost-effective photovoltaic device technology. *Micromachines* **2022**, *13* (11), 1966.

(266) Rezkallah, T.; Djabri, I.; Koç, M. M.; Erkovan, M.; Chumakov, Y.; Chemam, F. Investigation of the electronic and magnetic properties of Mn doped ZnO using the FP-LAPW method. *Chinese Journal of Physics* **2017**, *55* (4), 1432-1440. DOI: 10.1016/j.cjph.2017.02.021.

(267) Akcan, D.; Ozharar, S.; Ozugurlu, E.; Arda, L. The effects of Co/Cu Co-doped ZnO thin films: An optical study. *Journal of Alloys and Compounds* **2019**, *797*, 253-261. DOI: 10.1016/j.jallcom.2019.05.126.

(268) Ma, Z.; Ren, F.; Ming, X.; Long, Y.; Volinsky, A. A. Cu-doped ZnO electronic structure and optical properties studied by first-principles calculations and experiments. *Materials (Basel)* **2019**, *12* (1). DOI: 10.3390/ma12010196 From NLM PubMed-not-MEDLINE.

(269) Opoku, F.; Govender, K. K.; van Sittert, C. G. C. E.; Govender, P. P. Understanding the mechanism of enhanced charge separation and visible light photocatalytic activity of

modified wurtzite ZnO with nanoclusters of ZnS and graphene oxide: from a hybrid density functional study. *New Journal of Chemistry* **2017**, *41* (16), 8140-8155.

(270) Ganesh, V.; Yahia, I.; AlFaify, S.; Shkir, M. Sn-doped ZnO nanocrystalline thin films with enhanced linear and nonlinear optical properties for optoelectronic applications. *Journal Of Physics And Chemistry Of Solids* **2017**, *100*, 115-125.

(271) Kang, Y.; Yu, F.; Zhang, L.; Wang, W.; Chen, L.; Li, Y. Review of ZnO-based nanomaterials in gas sensors. *Solid State Ionics* **2021**, *360*, 115544. DOI: 10.1016/j.ssi.2020.115544.

(272) Spencer, M. J. S. Gas sensing applications of 1D-nanostructured zinc oxide: Insights from density functional theory calculations. *Progress in Materials Science* **2012**, *57* (3), 437-486. DOI: 10.1016/j.pmatsci.2011.06.001.

(273) Ellmer, K.; Bikowski, A. Intrinsic and extrinsic doping of ZnO and ZnO alloys. *Journal of Physics D: Applied Physics* **2016**, *49* (41), 413002.

(274) Xiu, F.; Xu, J.; Joshi, P. C.; Bridges, C. A.; Parans Paranthaman, M. ZnO doping and defect engineering—A review. *Semiconductor materials for solar photovoltaic cells* **2016**, 105-140.

(275) Cheng, X.; Li, F.; Zhao, Y. A DFT investigation on ZnO clusters and nanostructures. *Journal of Molecular Structure: THEOCHEM* **2009**, *894* (1-3), 121-127. DOI: 10.1016/j.theochem.2008.10.023.

(276) Haffad, S.; Cicero, G.; Samah, M. Structural and electronic properties of ZnO nanowires: a theoretical study. *Energy Procedia* **2011**, *10*, 128-137.

(277) Yaakob, M.; Hussin, N.; Taib, M.; Kudin, T.; Hassan, O.; Ali, A.; Yahya, M. First principles LDA+ U calculations for ZnO materials. *Integrated Ferroelectrics* **2014**, *155* (1), 15-22.

(278) Wu, J.; Hu, J.; Shao, L.; Xu, J.; Song, K.; Zheng, P. First-principle investigation of K–N dual-acceptor codoping for p-ZnO. *Materials Science in Semiconductor Processing* **2015**, *29*, 245-249.

(279) Xia, C.; Wang, F.; Hu, C. Theoretical and experimental studies on electronic structure and optical properties of Cu-doped ZnO. *Journal of Alloys and Compounds* **2014**, *589*, 604-608. DOI: 10.1016/j.jallcom.2013.11.066.

(280) Cao, H.; Lu, P.; Cai, N.; Zhang, X.; Yu, Z.; Gao, T.; Wang, S. First-principles study on electronic and magnetic properties of (Mn, Fe)-codoped ZnO. *Journal of Magnetism and Magnetic Materials* **2014**, *352*, 66-71.

(281) Hamzah, N.; Samat, M.; Johari, N.; Faizal, A.; Hassan, O.; Ali, A.; Zakaria, R.; Hussin, N.; Yahya, M.; Taib, M. First-principle LDA+ U and GGA+ U calculations on structural and electronic properties of wurtzite ZnO. *Solid State Science and Technology 30* (1), 20-36.

(282) Harun, K.; Salleh, N. A.; Deghfel, B.; Yaakob, M. K.; Mohamad, A. A. DFT+ U calculations for electronic, structural, and optical properties of ZnO wurtzite structure: A review. *Results in Physics* **2020**, *16*, 102829.

(283) Liu, Y.; Xu, H.; Liu, C.; Liu, W. Recent progress in ZnO-based heterojunction ultraviolet light-emitting devices. *Chinese Science Bulletin* **2014**, *59* (12), 1219-1227. DOI: 10.1007/s11434-014-0206-9.

(284) Ma, X.; Wu, Y.; Lv, Y.; Zhu, Y. Correlation effects on lattice relaxation and electronic structure of ZnO within the GGA+ U formalism. *The Journal of Physical Chemistry C* **2013**, *117* (49), 26029-26039.

(285) Luo, J.-H.; Liu, Q.; Yang, L.-N.; Sun, Z.-Z.; Li, Z.-S. First-principles study of electronic structure and optical properties of (Zr–Al)-codoped ZnO. *Computational Materials Science* **2014**, *82*, 70-75.

(286) Benrezgua, E.; Zoukel, A.; Deghfel, B.; Boukhari, A.; Amari, R.; Kheawhom, S.; Mohamad, A. A. A review on DFT+ U scheme for structural, electronic, optical and magnetic properties of copper doped ZnO wurtzite structure. *Materials Today Communications* **2022**, *31*, 103306.

(287) Harun, K.; Yaakob, M. K.; Taib, M. F. M.; Sahraoui, B.; Ahmad, Z. A.; Mohamad, A. A. Efficient diagnostics of the electronic and optical properties of defective ZnO nanoparticles synthesized using the sol–gel method: experimental and theoretical studies. *Materials Research Express* **2017**, *4* (8), 085908.

(288) Harun, K.; Mansor, N.; Yaakob, M. K.; Taib, M. F. M.; Ahmad, Z. A.; Mohamad, A. A. On the verification of sol–gel-derived ZnO nanoparticle properties using first-principles calculation. *Journal of Sol-gel Science and Technology* **2016**, *80*, 56-67.

(289) Honglin, L.; Yingbo, L.; Jinzhu, L.; Ke, Y. Experimental and first-principles studies of structural and optical properties of rare earth (RE= La, Er, Nd) doped ZnO. *Journal of Alloys and Compounds* **2014**, *617*, 102-107.

(290) Harun, K.; Mansor, N.; Ahmad, Z. A.; Mohamad, A. A. Electronic properties of ZnO nanoparticles synthesized by Sol-gel method: a LDA+ U calculation and experimental study. *Procedia Chemistry* **2016**, *19*, 125-132.

(291) Tang, C.; Spencer, M. J. S.; Barnard, A. S. Activity of ZnO polar surfaces: an insight from surface energies. *Physical Chemistry Chemical Physics* **2014**, *16*, 22139-22144. DOI: 10.1039/C4CP03221G.

(292) Pauporté, T.; Magne, C. Impedance spectroscopy study of N719-sensitized ZnO-based solar cells. *Thin Solid Films* **2014**, *560*, 20-26. DOI: 10.1016/j.tsf.2013.11.121.

(293) Narjis, A.; El Aakib, H.; Boukendil, M.; El Hasnaoui, M.; Nkhaili, L.; Aberkouks, A.; Outzourhit, A. Controlling the structural properties of pure and aluminum doped zinc oxide nanoparticles by annealing. *Journal of King Saud University - Science* **2020**, *32* (1), 1074-1080. DOI: 10.1016/j.jksus.2019.10.004.

(294) Bougrine, A.; El Hichou, A.; Addou, M.; Ebothé, J.; Kachouane, A.; Troyon, M. Structural, optical and cathodoluminescence characteristics of undoped and tin-doped ZnO thin films prepared by spray pyrolysis. *Materials Chemistry and Physics* **2003**, *80* (2), 438-445, Article. DOI: 10.1016/S0254-0584(02)00505-9 Scopus.

(295) Liu, J.; Fan, X. F.; Sun, C. Q.; Zhu, W. Transparent conductivity modulation of ZnO by group-IVA doping. *Chemical Physics Letters* **2016**, *649*, 78-83. DOI: 10.1016/j.cplett.2016.02.033.

(296) Marana, N.; Longo, V.; Longo, E.; Martins, J.; Sambrano, J. Electronic and structural properties of the (1010) and (1120) ZnO surfaces. *The Journal of Physical Chemistry A* **2008**, *112* (38), 8958-8963.

(297) Catto, A. C.; Ferrer, M. M.; Lopes, O. F.; Mastelaro, V. R.; Andrés, J.; da Silva, L. F.; Longo, E.; Avansi, W. The role of counter-ions in crystal morphology, surface structure and photocatalytic activity of ZnO crystals grown onto a substrate. *Applied Surface Science* **2020**, *529*, 147057. DOI: 10.1016/j.apsusc.2020.147057.

Chapter 3: Density Functional Theory study of the structural and electronic properties of ZnO

3.1 Abstract

The investigation of the stability of zinc oxide (ZnO) previously focused on the structural and electronic properties of ZnO, such as density of states (DOS), band structure, d-band centre, X-ray diffraction (XRD), and surface energy. Of these properties, surface energy was shown to be the best property to assess the stability of metal oxide systems. However, studies that used Density Functional Theory (DFT) for evaluating representative surfaces and their associated surface energies are limited to the three most prevalent crystal systems of ZnO namely: hexagonal, cubic, and zinc-blende. This study explored the structural and electronic characteristics of ZnO in the three crystal systems using DFT and aimed to identify the crystal system with the highest stability based on surface energies. Additionally, the study leveraged the surface energies to construct ZnO nanoparticles and visualise their morphologies. The research involved optimising ZnO bulk structures, cleaving surfaces from them, calculating surface energies, and comparing band gaps and work functions across the three crystal systems. The results demonstrated that the hexagonal crystal system of ZnO exhibited the highest stability, considering surface energies. The work function exhibited notable variations across the different crystal systems, with the hexagonal crystal system showing the most favourable work function values. This conclusion is supported by other factors such as DOS, band structure, d-band centre, and XRD. This finding agrees with the experimental reports that established the hexagonal wurtzite structure of ZnO as the most thermodynamically stable and, hence, the most common among the three structures. It also suggests that further investigation into the hexagonal crystal system could enhance our understanding of the characteristics of ZnO and provide valuable insights for potential applications. Further exploration of the hexagonal crystal system is recommended.

3.2 Introduction

Zinc oxide (ZnO), a well-established and versatile II-VI group semiconductor compound,[298] has gained significant attention for its interesting properties and potential applications in multiple fields, such as photocatalysis,[299] optoelectronics,[267, 300, 301] and sensors.[301] Its ability to facilitate photocatalytic reactions in environmental remediation,[186] water splitting, and solar energy conversion is attributed to its wide band gap and high electron mobility.[302] Its wide band gap

energy of 3.37 eV and its high exciton binding energy of 60 meV also make it suitable for efficient optoelectronic devices like light-emitting diodes (LEDs), ultraviolet (UV) detectors, and transparent conducting electrodes.[283] Furthermore, ZnO-based sensors are highly regarded for their exceptional sensitivity, selectivity, and rapid response times, making them applicable in gas, bio-sensing, and chemical sensing applications.[271]

However, because ZnO could exist in various crystal systems, the specific crystal system for a specific application is unknown. The three most prevalent crystals are the hexagonal wurtzite, the cubic rock salt, and the cubic zinc-blende, also known as sphalerite.[234] For clarity and simplicity in this chapter, we will refer to these crystal systems as hexagonal, cubic, and zinc-blende, respectively. The ground state of ZnO has a hexagonal crystal system. However, ZnO can undergo a phase transformation from the hexagonal crystal system to the cubic crystal system at a pressure of 9.5 GPa.[303] Furthermore, the zinc-blende crystal system can be achieved through experimental growth techniques, such as molecular beam epitaxy,[304] on a substrate with a cubic crystal system.[298]

A considerable amount of research,[276, 305-309] encompassing both experimental and computational approaches, has been conducted to depict the structural and electronic properties of ZnO accurately. However, from an experimental viewpoint, the accurate representation of the structural and electronic properties of the three crystal systems remains a subject of ongoing discussion due to the challenges encountered in predicting precise values for the electronic band gap energy,[310] associated electronic properties[284] and stability of the three crystal systems.[311] A fundamental understanding of ZnO crystal systems' structural stability, surface energies, and characteristics is crucial for assessing their relevance for future applications. It will also enable researchers to optimise them for future applications.

Numerous computational methodologies within the framework of Density Functional Theory (DFT) have been employed to investigate the fundamental characteristics of ZnO,[303] which include the variations in energy,[312] lattice parameters,[272] band structure, density of states (DOS),[313] and surface energies[314] for each specific crystal system, thus contributing to a deeper understanding of ZnO. For example, Baktiar *et al.*[303] extensively studied the structural properties of the three crystal systems of ZnO. Both the local density approximation (LDA) and the generalised gradient approximation (GGA) were employed for this purpose, and the electronic properties were investigated by utilising the Tran–Blaha modified Becke–Johnson (mBJ) potential within the WIEN2K code.[315] Similarly, Hua-Gen Yu[316] presented an optimised methodology to investigate

ZnO systems, wherein the exchange functional within the hybrid BLYP functional was adjusted to overcome the limitations of the DFT method, namely the underestimation of the band gap.

The aim of this study is to develop a theoretical framework based on DFT calculations to investigate the structural and electronic properties of ZnO. Considering previous studies,[13, 31, 268, 309, 317-325] this investigation begun by undertaking a comprehensive benchmark analysis of previous studies on different ZnO bulk and surface studies to identify the most suitable approach for this research. Table 3-1 presents a summary of the parameters derived from the bulk structure and surface studies in the literature.

The pseudopotentials and functionals utilised in this study were determined upon completing the benchmark analysis. Subsequently, further benchmarking studies were conducted to determine the optimal k-point grid and cut-off value for the three most prevalent crystal systems of ZnO. The new framework developed in this study will enable the understanding of the crystal system and electronic properties, as well as the surface characteristics and associated surface energies across all three crystal systems of ZnO.

Table 3-1: ***A summary of the cut-off energies, k-points, pseudopotentials and functionals used in various ZnO bulk structure and surface studies.***

	Functional	Cut-off energy (eV)	k-points	Pseudopotentials	References
Bulk structure	GGA/ PBE	500	7×7×7	-	[31]
	LDA/GGA/PW91	500	4×4×4	PAW	[317]
	GGA/PBE	400	4×4×4	USP	[318]
	GGA/ PBE	300	-	PAW	[319]
	GGA/PBE	450	-	USP	[320]
Surface					
	GGA/LDA	612	4×4×1	-	[321]
	GGA/PW91	400	7×7×1	USP	[322]
	GGA/PBE	380	3×3×2	USP	[323]
	GGA/PBE	400	15×15×9	-	[324]
	GGA/PBE	380	6×6×2	-	[325]
	GGA/PBE	400	5×5×1	PAW	[309]
	GGA/PBE	340	5×5×4	USP	[13]
	GGA/PBE	-	9×9×6	USP	[268]

Note: GGA: Generalised gradient approximation,[326] PBE: Perdew–Burke–Ernzerhof scheme,[327] LDA: Local Density Approximation,[328] PW91: Perdew–Wang 91 scheme,[329] PAW: Projector Augmented Wave,[330] and USP: Ultrasoft pseudopotential.[331]

3.3 Computational method

3.3.1 Cluster and Software

Theoretical calculations were performed within the DFT framework utilising the Cambridge Serial Total Energy Package (CASTEP) module[332] of the Biovia Materials Studios (MS 2020) software package[81] to determine the structural and electronic properties of ZnO. All the calculations were run on the Lengau cluster at the Centre of High-Performance Computing (CHPC) in South Africa.[82]

3.3.2 Unit Cells

Unit cells of the three crystal systems of pure ZnO (Figure 3-1), namely hexagonal, cubic, and zinc-blende, were imported from the Materials Project database[333] into the Biovia MS 2020 software package[81] visualiser. The hexagonal crystal system consists of two interpenetrating hexagonal closed-packed (hcp) cells with a $P6_3mc$ space group. The cubic and zinc-blende crystal systems are both face-centred cubic (fcc). The cubic structure has an $Fm\bar{3}m$ space group, and the zinc-blende crystal system has an $\bar{F}43m$ space group.

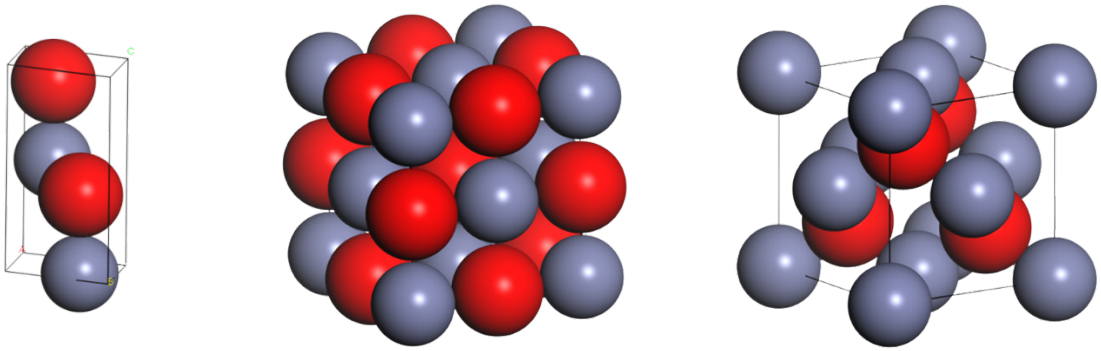

(a) (b) (c)

Figure 3-1: The unit cell structures of the three crystal systems of ZnO, namely, (a) hexagonal, (b) cubic, and (c) zinc-blende (grey and red represent Zn and O atoms, respectively).

The structures of these imported unit cells were compared with existing literature values to ensure accuracy.

3.3.3 Bulk structure construction and optimisation

3.3.3.1 Construction

The 2×2×2 bulk structures were constructed by duplicating the imported unit cells in all three directions of the Cartesian coordinates using the visualiser of the Biovia MS 2020 software package.[81]

3.3.3.2 Optimisation

All the bulk structures were relaxed to obtain the most stable geometry.

3.3.3.2.1 Computational details

The relaxation was done by using the CASTEP module within the Biovia MS 2020 software package.[81] The electron-ion interactions within the system were effectively modelled using the ultrasoft pseudopotentials (USP) method.[44] To address the exchange and correlation effects within the electronic structure, the Perdew-Burke-Ernzerhof (PBE)[45] exchange-correlation functional was chosen, known for its reliability in describing a wide range of materials. This functional was implemented using the general gradient approximation (GGA).

In terms of energy convergence, maximum force, maximum stress, and maximum displacement, the tolerance values were set at 1.0 x 10^{-5} eV/atom, 0.03 eV/Å, 0.05 GPa, and 1.0 x 10^{-3} Å, respectively. The calculations did not consider the spin polarisation because there is no magnetic

moment in a ZnO system. However, the k-point grid and cut-off energy were benchmarked to ensure computational accuracy, using the Monkhorst-Pack grid to accurately sample the Brillouin Zone (BZ) in reciprocal space.[46]

3.3.3.2.2 k-Point grid benchmarking

The k-point grid benchmarking was conducted using a variety of k-point grids, ranging from 3×3×3 to 15×15×15. Based on a thorough literature review,[31, 317-320] a 400 eV cut-off energy was chosen for k-point optimisation to determine the appropriate k-point grid.

The 3×3×3 k-point grid, though relatively small, struck a good balance between accuracy and computational efficiency. It was chosen as the minimum grid size because it produced a converged result, unlike the 1×1×1 grid, which is commonly used as an initial choice but proved inadequate for this system. In contrast, the maximum grid selected was 15×15×15 because it is dense enough to appropriately characterise the electronic properties without exponentially increasing the processing time.

In this optimisation process, the accuracy of different k-point grids was assessed by plotting the energy per atom versus the number of k-points per grid. These findings aimed to establish the minimum number of k-points necessary to achieve convergence. This benchmarking process is important because using a lower number of k-points per grid may lead to inaccurate results, while using a higher number generally enhances calculation accuracy but at the expense of increased computational time.

3.3.3.2.3 Cut-off energy benchmarking

After the k-point benchmarking process, several cut-off energy values ranging from 250 eV to 600 eV with a 50-eV interval difference were tested for the k-point grid. These findings aimed to determine an optimal energy cut-off suitable for achieving convergence in the optimisation of ZnO bulk structures. A higher energy cut-off value will produce a more accurate result at the expense of increased computational time. The expected outcome was identifying the lowest cut-off energy within a tolerance of 1.0×10^{-5} eV/atom tolerance, at which convergence was achieved.

3.3.4 Bulk properties

The CASTEP module within the Biovia MS 2020 software package[81] was utilised to calculate the structural and electronic properties of the different crystal systems of ZnO.

3.3.4.1 Structural properties

The computational settings specified in section 3.3.3.2.1 with optimum k-point grid and cut-off value were applied to achieve the most stable geometry during the optimisation. Following geometry optimisation, the lattice parameters, cell angles, volume, density, total atoms, and final energy derived for the bulk structures of ZnO were compared for validation purposes with existing literature.

For further validation, the XRD patterns of all the ZnO bulks were generated in the Reflex tools of the Biovia MS 2020 software package.[81] The DFT framework was used, with a copper source, Cu Kα (λ=1.541 Å), as the incident radiation. The minimum and maximum 2-Theta limits were set to 5° and 90°, respectively. The patterns were calculated by determining the positions and intensities of the diffraction peaks based on the atom positions in the bulk structure, the X-ray wavelength, and the diffraction geometry. The calculated XRD patterns were compared with the experimental XRD patterns[80].

3.3.4.2 Electronic properties

The electronic properties, namely, DOS, d-band centre and band gap, were determined after a single-point energy calculation using the same settings as for the geometry optimisation.

3.3.4.2.1 Density of states (DOS)

The occupation probabilities of electronic states at each energy level were combined to determine the total density of states (DOS) by summing all k-points and energy levels, showcasing contributions from all angular momentum projections (s, p, d, f) on all atoms in the ZnO bulk structures. Additionally, the partial density of states (pDOS) was derived by aggregating the occupation probabilities for specific energy levels across all k-points, illustrating the contributions from each atomic orbital. This arrangement of energy levels in the valence band (VB) and conduction band (CB) ensures that the Fermi level is at zero energy.

The d-band of ZnO in each bulk structure was characterised by analysing the pDOS, which isolates the contribution of the d-orbitals.

3.3.4.2.2 d-band centre

The d-band centre is closely related to the catalytic activity of a material. A d-band centre closer to the Fermi level (higher d-band centre) indicates that d-electrons are less tightly bound, which

can affect the material's interaction with adsorbates and its overall electronic behaviour. The enhanced interactions with adsorbates generally suggest higher reactivity.

Integrations over the energy spectrum of the d-band within the pDOS were performed to determine the position of the d-band centre for the ZnO bulk structures. The d-band is centred relative to either the valence band maximum (VBM) or the Fermi level. Further details on this calculation process are presented in Appendix A3, Table A3-1.

3.3.4.2.3 Band gap

The band structures for each system of the ZnO bulk structures were calculated, and the energy values were determined at each k-point within the BZ. Subsequently, these energy values were plotted against the corresponding k-vectors to generate the band structure, from which the band gap was determined. The band gap refers to the energy interval in which there are no overlaps between energy bands. The band gap is particularly relevant for insulators and semiconductors, signifying the energy span between the highest occupied energy level (VB) and the lowest unoccupied energy level (CB). The disparity in energy levels between the upper limit of the VB and the lower limit of the CB defines the magnitude of the band gap. A comparison between the calculated band gap values for the crystal systems being investigated and literature values was conducted.

However, DFT/GGA methods are recognised for underestimating band gap values in transition metal oxides such as ZnO.[334] To overcome this limitation, various techniques are employed to enhance the electronic energy gaps.[335] Among these, a widely utilised and computationally efficient method is adding the Hubbard correction (U) as in (LDA)+U, also known as (GGA)+U.[336] The U introduces empirical on-site Coulomb energy to specific orbitals. This modification addresses the self-interaction error frequently observed in DFT calculations using GGA functionals.[337] The (DFT)+U approach significantly enhances the accuracy of electronic structure calculations for transition metal oxides by more effectively accounting for electron-electron interactions in localised d and p orbitals.[338] This approach leads to predictions that more closely match reliable experimental values for band gaps and electronic properties compared to GGA.[326, 339] Therefore, the (GGA)+U method is effectively addressing the band gap underestimation problem.

Previous research[284, 287, 340-343] has proposed a wide range of U values for Zn 3d orbitals (7 to 15 eV) and O 2p orbitals (6 to 9 eV), based on experimental data regarding the electronic states of

ZnO's hexagonal crystal system. There is no standardised method for determining the optimal U values. In this study, the band gap was further analysed using U values of $U_{d\text{-}Zn}$ = 10 eV and $U_{p\text{-}O}$ = 7 eV, as suggested by Lee[263] for the hexagonal crystal system.

3.3.5 Surface model construction and optimisation

3.3.5.1 Construction

The three optimised ZnO bulk structures were cleaved along several Miller index planes to produce different surfaces using the visualiser in the Biovia MS 2020 software package.[81] These surfaces, identified through experimental XRD, included the (111), (200), (220), (311), (222), and (400) surfaces of both the cubic and zinc-blende crystal systems, as well as the (100), (002), (101), (102), (210), (103), (200), (112), and (201) surfaces of the hexagonal crystal system.

The surface models consisted of a material slab with periodic boundary conditions and a vacuum slab in the orthogonal direction. The dimensions of the surfaces, /a/ x /b/, ranged from 6.5780 Å to 15.5714 Å. The slab systems had a fractional thickness ranging from 1 Å to 2 Å. Depending on the surface, the material slab comprised two to eight layers, totalling 32 to 128 atoms per slab. Some slabs were metal terminated (MT), while others were oxygen terminated (OT). A vacuum gap of 15 Å was added for all surface models, as it was found to be sufficient to prevent interaction between the repeating material slabs.

3.3.5.2 Optimisation

All surface models (slab systems) were relaxed to identify the most stable geometry (structural properties) and to investigate the influence of different surface terminations on the surface properties of various ZnO crystal systems. However, preserving the surface structure is crucial when investigating surface properties. Throughout the optimisation process, the dimensions and shape of all the surface models were kept fixed, and the atoms were allowed to move. This approach focused solely on how the atoms' positions changed within the surface models without altering the overall dimensions of the material slabs to ensure that the modelled surface accurately represents the physical and chemical properties of the ZnO surface. Temperature variations were not considered, because the surface energy is not affected by changes in temperature due to the dissimilar vibrations of the slab and bulk structure.[344]

3.3.5.2.1 Computational details

The computational settings used for the bulk structures in section 3.3.3.2.1 and the cut-off energy (400 eV) were applied, as determined for the bulk structures in section 3.3.3.2.3. However, the k-point grid was benchmarked for the (101) hexagonal surface using the Monkhorst-Pack grid to accurately sample the BZ in reciprocal space to ensure the computational accuracy of the slab systems.[46] The selection of the (101) hexagonal surface was based on the surface's prominence in existing literature.[345, 346]

3.3.5.2.2 k-point grid benchmarking for (101) hexagonal surface

The k-point benchmarking for the (101) surface varied k-point grids ranging from 1×1×1 to 11×11×1. In contrast to the benchmarking of k-points for the bulk structures, the minimum k-point chosen for the surface was 1×1×1. The reason for this choice was that the electronic structure of the surface effectively becomes a two-dimensional system. Since most electronic activity happens right at the surface, the need for many k-points in the c-direction is reduced.

3.3.5.3 Surface properties

Following the optimisation, the surface energies (γ), work function and morphology of the crystal system were determined.

3.3.5.3.1 Surface energies

The stability of surfaces can be characterised by calculating their surface energies (γ), which are considered a measure of thermodynamic stability.[347] This can be achieved by applying the following equation to estimate the surface energies:

$$\gamma_r = \frac{E^{DFT}{}_{relaxed\ slab} - n \times E^{DFT}{}_{bulk}}{2A_{slab}} \quad (3.1)$$

Where γ_r represents the surface energy and $E^{DFT}{}_{relaxed\ slab}$ and $E^{DFT}{}_{bulk}$ represent the DFT energies after optimisation of the slab and bulk structure, respectively. $2A_{slab}$ represents the surface area multiplied by two which accounts for both upper and lower surfaces of the bulk and n represents the ratio of the number of Zn and O atoms in the material slab to the number in the bulk structure.

3.3.5.3.2 Work function

Work function is an additional property used to analyse the stability of the surface. It represents the minimum energy required to remove an electron from the surface into the vacuum. The work function (Φ) was calculated as the difference between the vacuum level (E_{vac}) and the Fermi level

(E_f) of the system ($\Phi = E_{vac} - E_f$). This calculated work function is essential for understanding and predicting the electronic behaviour of ZnO in photocatalysis and surface reactions, as it influences electron emission and surface charge distribution.

3.3.5.3.3 Morphology

The Wulff construction method[3] was employed to predict the equilibrium shape of the crystal surfaces. This method involved the identification of the lattice, point group, and the number of facet families, otherwise known as the Miller planes, associated with the desired shape. Furthermore, the distinct ZnO system Miller planes and their respective derived surface energies were entered into the Wulff construction program.[2] Subsequently, the program generated the predicted morphology of the crystal systems. This morphology represents the crystal surface's stability, wherein the size of each surface is directly proportional to its respective surface energy. The purpose of conducting this construction was to explain the prevalence of certain surfaces over others in the various systems of ZnO while also examining the influence of surface energies on the overall crystal shape and morphology.

3.4 Results and discussion

3.4.1 Unit Cells

The lattice parameters of the imported ZnO unit cells of the crystal systems were compared to existing literature values, as shown in Table 3-2.

Table 3-2: ***Comparison of the lattice parameters of the imported ZnO unit cell for the various crystal systems with literature.***

ZnO crystal system	Lattice parameters (Å)					
	a = b			c		
	Imported unit cell[333]	Literature values	Deviation (%)	Imported unit cell[333]	Literature values	Deviation (%)
Hexagonal	3.289	3.289[25, 348, 349]	0.000	5.307	5.308[25, 348, 349]	0.019
			1.216		5.206[318]	1.903
		3.249[318]	0.273		5.330[350]	0.433
		3.280[350]				
Cubic	4.339	4.334[351]	0.115	4.339	4.334[351]	0.115
Zinc-blende	4.630	4.632[352]	0.043	4.630	4.632[352]	0.043

This comparison of lattice parameters (Table 3-2) indicates a close match between the lattice parameters of the imported unit cells and the reported literature values. The highest percentage

deviation in the compared lattice parameters was only 1.903%. This minimal percentage deviation confirmed that the imported unit cells could be used further in this study.

3.4.2 Bulk structure construction and optimisation

3.4.2.1 Construction

In Figure 3-2, the structures of the expanded ZnO bulk structures are depicted, providing a comprehensive view of the atomic arrangement and the overall crystalline framework.

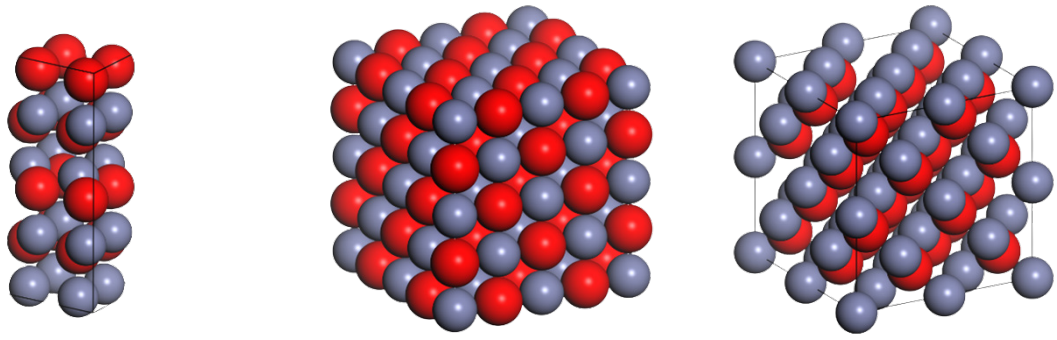

(a) (b) (c)

*Figure 3-2: **The expanded bulk structures of the three systems of ZnO, namely, (a) hexagonal, (b) cubic, and (c) zinc-blende (grey and red represent Zn and O atoms, respectively).***

3.4.2.2 Optimisation

3.4.2.2.1 k-point grid benchmarking

The k-point benchmarking aimed to find the minimum number of k-points needed for accurate results. Using too few k-points can lead to inaccuracies, while using more improves accuracy but takes longer to compute.

In Figure 3-3, the optimisation energy per atom for the different ZnO bulk structures (hexagonal, cubic and zinc-blende) are plotted against the number of k-points for various k-point grids ranging from 3×3×3 to 15×15×15.

The 3×3×3 k-point grid exhibited a high optimised energy because it samples the BZ less finely. The k-point grid may not effectively capture subtle electronic interactions and structural details. The energy significantly decreased when moving from the 3×3×3 grid to the 5×5×5 grid. However, when transitioning from the 5×5×5 grid to the 11×11×11 grid, the bulk structure converged. Specifically, in both hexagonal and cubic crystal systems, the energy decreased from 5×5×5 to 7×7×7, then increased from 7×7×7 to 9×9×9, followed by a decrease in the hexagonal system but

an increase in the cubic system from 9×9×9 to 11×11×11. In the zinc-blende crystal system, the energy increased from 5×5×5 to 7×7×7, then decreased from 7×7×7 to 9×9×9, and further to 11×11×11. In other words, the energy difference between consecutive k-point grids, which might have been observed or was significant between the 3×3×3 grid and the 5×5×5 grid, was no longer evident when transitioning from the 5×5×5 grid to the 9×9×9 grid. The energy did not vary considerably from the 11×11×11 k-point grid to the 15×15×15 k-point grid, indicating that the structure converged.

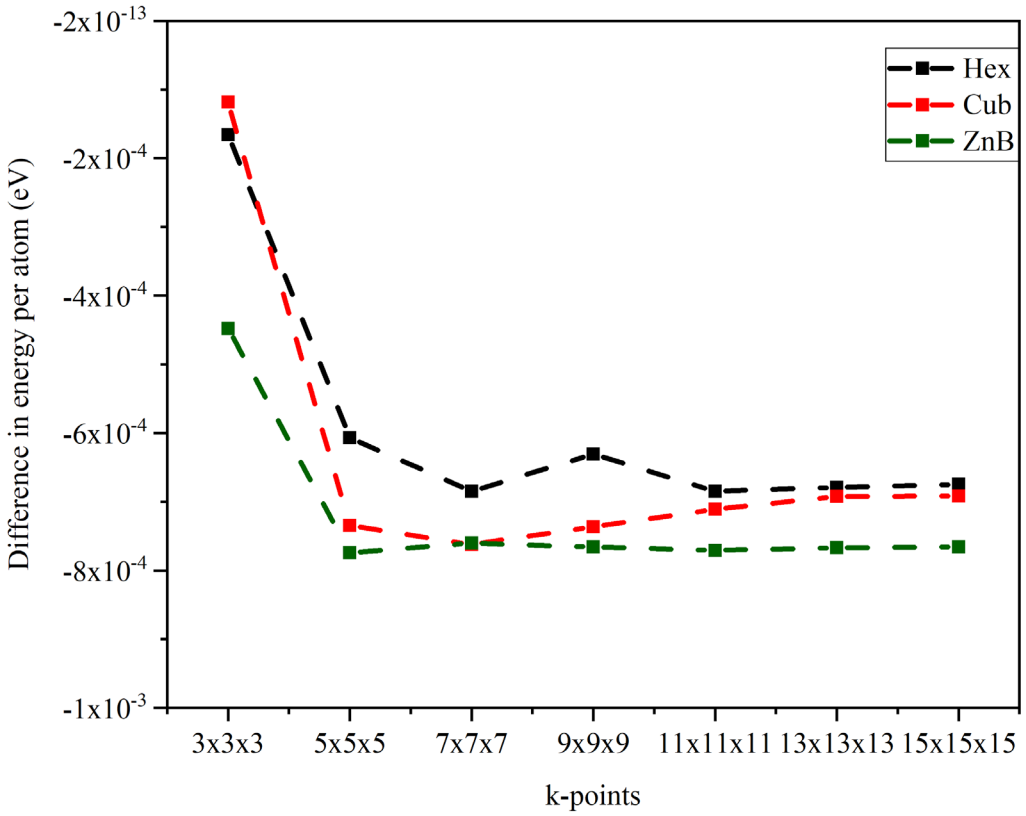

Figure 3-3: ***The difference in optimised energy per atom for the different crystal systems of the ZnO bulk structures with various k-point grids and 400 eV cut-off energy.***

Table 3-3 illustrates a consistent trend across all crystal systems (hexagonal, cubic, and zinc-blende): an increase in the size of the k-point grid, from 3×3×3 to 11×11×11, led to longer computational times and thus higher computational costs. This trend indicates the relationship between grid size and computational time, but it varied across different crystal systems. Essentially, the table shows how both the size of the k-point grid and the crystal system affected computational time.

Table 3-3: The time taken for k-point optimisation for the different crystal systems of ZnO at an energy cut-off of 400 eV.

	Computational time (mins)		
k-point grid	Hexagonal	Cubic	Zinc-blende
3×3×3	4.78	8.58	12.56
5×5×5	19.51	34.57	39.23
7×7×7	37.02	89.02	97.39
9×9×9	83.33	161.56	181.70
11×11×11	154.12	281.04	470.80
13×13×13	192.41	252.69	275.81
15×15×15	177.77	368.46	369.90

In the hexagonal system, computational time decreased from 13×13×13 to 15×15×15, contrary to the typical trend of increasing time from 3×3×3 to 13×13×13. Meanwhile, in the cubic and zinc-blende systems, there was a decrease in computational time from 11×11×11 to 13×13×13, followed by an increase from 13×13×13 to 15×15×15. This decrease differs from the usual trend of increasing time from 3×3×3 to 11×11×11. Time increased until 11×11×11, then it fluctuated, indicating the point where convergence occurred. As the energy levelled out, the computational time also levelled out, explaining the fluctuations observed beyond the 11×11×11 grid size. Increasing the k-point grid size further did not significantly improve accuracy, yet computational time remained reasonable. The intersection of energy and time signifies a balance between accuracy and computational cost.

Consequently, to achieve a balance between computational costs and accuracy across the different crystal systems of the ZnO bulk structures, the Monkhorst-Pack[353] 11×11×11 k-point grid was identified as optimal for investigating the bulk properties. This k-point grid agreed with the results of previous study[354] that investigated the bulk properties.

3.4.2.2.2 Cut-off energy benchmarking

The cut-off energy benchmarking was performed using the 11×11×11 k-point grid, identified after the k-point benchmarking process. The comparison of the optimised energy per atom for the various ZnO bulk structures (hexagonal, cubic, and zinc-blende) against the various energy cut-off values ranging from 250 eV to 600 eV is shown in Figure 3-4.

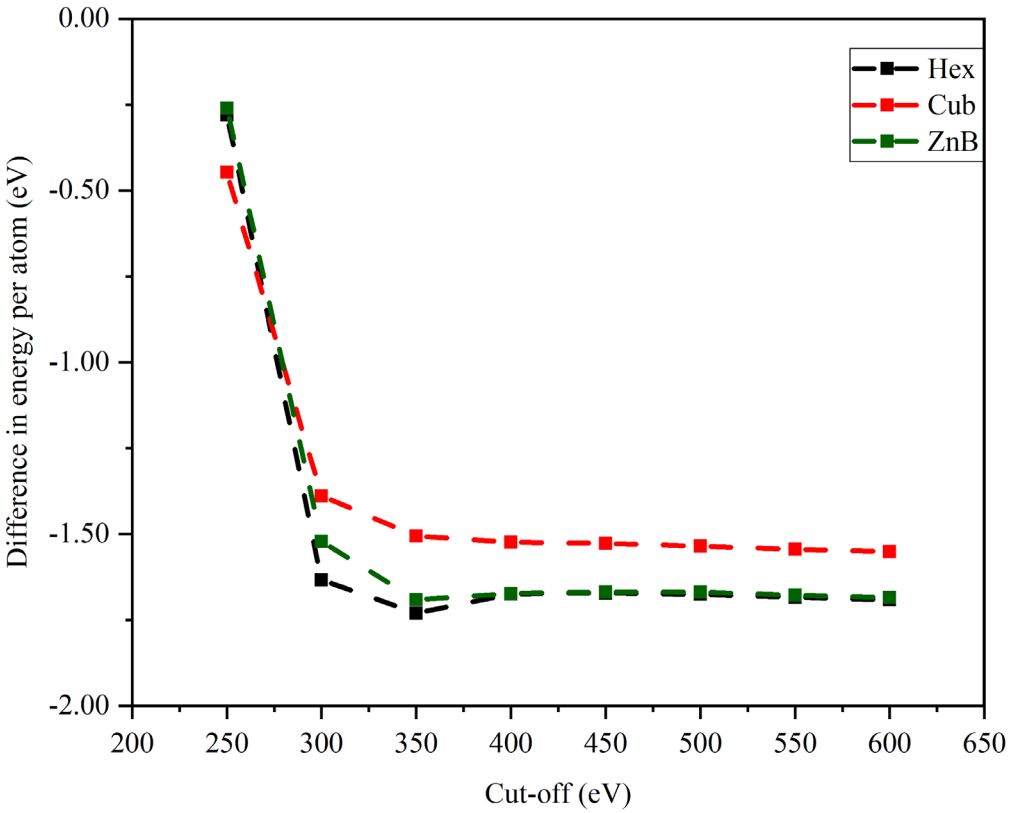

Figure 3-4: ***The difference in optimised energy per atom for the different crystal systems of ZnO bulk structures with various cut-off energies using an 11x11x11 k-point grid.***

Using an energy cut-off of 250 eV was not ideal for this study because the plane-wave basis set is not large enough to accurately represent the system's wave functions and electronic states. Consequently, it may not capture the details of the system accurately enough, leading to less meaningful results. Notably, the energy decreased significantly from the 300 eV cut-off to the 350 eV cut-off. The energy was found to be specifically unstable in the hexagonal crystal system. The instability at 350 eV in the hexagonal crystal system was caused by the limited detail in representing the electronic structure. The hexagonal crystal system of ZnO consists of an elongated tetrahedron and a distinctive arrangement of atoms, leading to variations in bond lengths and angles. These variations significantly impacted the ability of the calculation to achieve energy convergence at lower cut-off values. The energy cut-off did not vary considerably from 400 eV to 600 eV.

Table 3-4 outlines the computational time needed to optimise cut-off energies for various ZnO crystal systems.

Table 3-4: The computational time for cut-off energy optimisation for the different crystal systems of ZnO using an 11x11x11 k-point grid.

	Computational time (mins)		
Cut-off energy (eV)	Hexagonal	Cubic	Zinc-blende
250	-	-	1829.74
300	-	399.94	1087.29
350	272.73	-	341.70
400	115.84	155.29	309.83
450	86.68	196.69	236.97
500	-	238.05	241.61
550	87.47	352.09	471.68
600	91.32	494.54	326.72

Across all the systems, lower cut-off energy values generally resulted in higher computational time, which decreased from 250 eV to 450 eV, indicating faster optimisation. After which, an increase in computational time was observed with increasing cut-off energy from 500 eV to 600 eV. The cut-off energy of 400 eV to expand the wave functions of the valence electrons was identified as striking a balance between computational efficiency and accuracy. This choice is supported by previous studies that used energy cut-off values within the range of 400 eV,[318, 354] 450 eV,[320] and 500 eV[31 317] to optimise their bulk properties.

3.4.3 Bulk properties

3.4.3.1 Structural properties

The lattice parameters, cell angles, volume, density, total atoms, and final energy derived for the bulk structures of ZnO are listed in Table 3-5.

As a result of the expansion of the unit cells into 2×2×2 bulks, it was necessary to divide the ZnO bulk lattice parameters in Table 3-5 by two. This division allows for the derivation of relatable data to the optimised ZnO crystal system documented in the literature. The values in Table 3-5 indicate a close agreement between the lattice parameters, cell angles, cell volumes, densities, total cell atoms, and final energies obtained in the present work and those in the literature.

Table 3-5: ***The lattice parameters, cell angles, cell volumes, densities, total cell atoms, and final energies obtained from various systems of the optimised bulk structures.***

ZnO crystal system	Hexagonal			Cubic			Zinc-blende		
Lattice parameters (Å)	a	b	c	a	B	c	a	b	c
This work	6.597	6.597	10.612	8.662	8.662	8.662	9.286	9.286	9.286
This work /2	3.299	3.299	5.306	4.331	4.331	4.331	4.643	4.643	4.643
Literature values	3.298[3]	3.298[6]	5.306[7]	4.331[11]	4.331[13]	4.331[15]	4.620[18]	4.620[21]	4.620[23]
Deviation (%)	0.030	0.030	0.030	0	0	0	0.495	0.495	0.495
Cell angles (°)	α	β	γ	α	B	γ	α	β	γ
This work	90	90	120	90	90	90	90	90	90
Literature values	90[26]	90[28]	120[30]	90[30]	90[34]	90[36]	90[38]	90[41]	90[42]
Volume (Å^3)									
Bulk volume this work	398.892			649.965			800.809		
Unit cell volume this work	49.862			81.246			100.101		
Unit cell volume literature values	47.590[45]			81.680[46]			94.730[47]		
Density (g/cm^3)									
This work	5.420			6.653			5.400		
Literature values	5.420,[48] 5.700[49]			6.620[50]			5.710[51]		
Total cell atoms	32			64			64		
Final energy (eV)	-34357.558			-68705.476			-68715.056		
Final energy/atoms (eV/atom)	-1073.674			-1073.523			-1073.673		

The maximum percentage deviations observed were as follows: 0.495% for lattice parameters, 0% for cell angles, 5.68% for cell volumes, and 5.42% for densities, all confirming the validity of the ZnO model developed in this study.

Figure 3-5 depicts the calculated powder XRD pattern of the hexagonal, cubic and zinc-blende ZnO crystal systems.

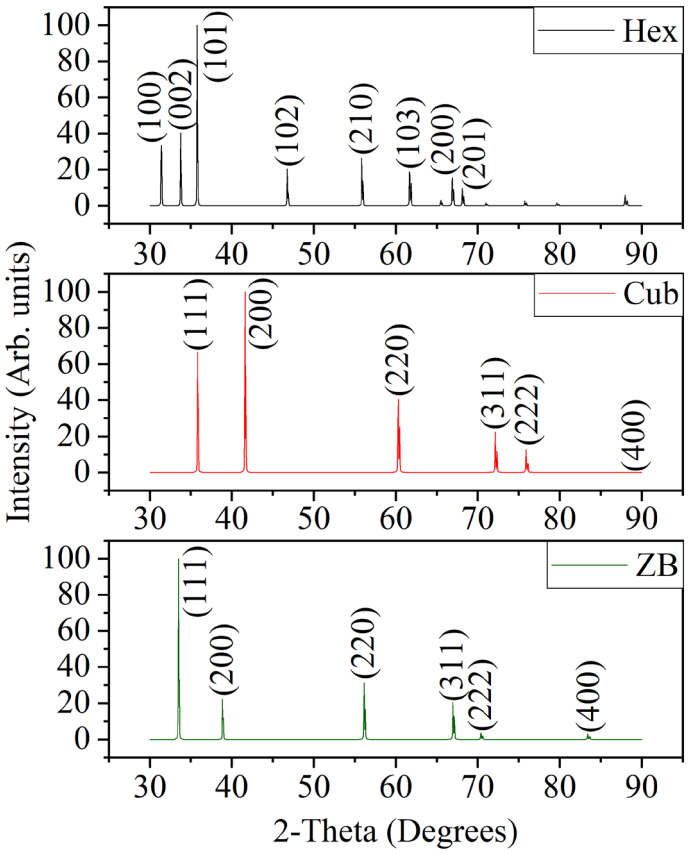

Figure 3-5: ***The computed XRD pattern of ZnO bulk structures (a) hexagonal, (b) cubic and (c) zinc-blende.***

The observed peaks in Figure 3-5(a) corresponded to the (100), (002), (101), (102), (210), (103), (200), (112), and (201) planes of ZnO. Additionally, the cubic and zinc-blende crystal systems both indicated diffraction peaks for the (111), (200), (220), (311), (222), and (400) planes, as shown in Figure 3-5(b) and (c), respectively. The computed XRD patterns were compared to XRD patterns found in the literature[80, 333] to validate the DFT calculations (see Table 3-6). The values demonstrate a significant correspondence between the 2θ values obtained in this study and those reported in the existing literature.[80, 333]

Table 3-6: Comparison of XRD patterns for crystal systems of ZnO bulk structures between calculations from this work and experimental studies [80, 333]

ZnO crystal system	hkl	2θ (°)		Intensity	
		This work	Literature values[80, 333]	This work	Literature values[80, 333]
Hexagonal	(100)	31.4	31.4	35.4	50.8
	(002)	33.8	34.3	55.4	39.1
	(101)	35.8	36.8	100.0	100.0
	(102)	46.8	47.6	22.06	22.5
	(210)	55.7	56.9	24.7	34.3
	(103)	61.7	62.8	19.9	33.4
	(200)	66.8	66.7	15.1	5.0
	(112)	68.1	68.2	9.6	28.2
	(201)	71.0	69.4	2.3	14.7
Cubic	(111)	35.7	35.9	43.9	80.9
	(200)	46.8	41.6	18.7	100.0
	(220)	61.7	60.3	19.1	59.8
	(311)	71.0	72.2	1.7	32.3
	(222)	75.8	75.9	2.9	18.7
	(400)	88.0	90.6	4.8	8.5
Zinc-blende	(111)	33.4	34.1	100	100
	(200)	38.8	39.5	26.0	28.2
	(220)	56.0	57.2	27.3	43.2
	(311)	66.8	68.2	22.0	35.3
	(222)	70.2	71.7	4.27	6.6
	(400)	83.2	85.1	3.29	6.1

The maximum variation observed among the 2θ values was only 3%, which is a reasonable variation and substantiates the credibility of the ZnO model. The calculated XRD patterns exhibited broad peak positions, indicating good agreement with the standard International Centre for Diffraction Data (ICDD) files.[355]

The decrease in the calculated peak intensities, as presented in Table 3-6, can be ascribed to the limitations of DFT approximations. Specifically, the exchange-correlation functionals may not fully capture the complexity of the system and the boundary conditions of the periodic systems. These DFT approximations can result in discrepancies between the calculated and experimental XRD intensities. Additionally, experimental XRD patterns can be affected by inherent uncertainties and limitations, such as instrumental broadening, sample preparation issues, or impurities. These factors can contribute to differences between the computed and experimental XRD intensities.

3.4.3.2 Electronic properties

3.4.3.2.1 Density of states (DOS)

As shown in Figure 3-6, the DOS of ZnO indicated that the oxygen 2s levels contributed to the lowest bands around −18.0 eV.

The VB was associated with the zinc 3d orbitals and the oxygen 2p orbitals, covering the energy range from −6.0 eV to −0.2 eV. The lower part of the CB was primarily comprised of zinc 4s.

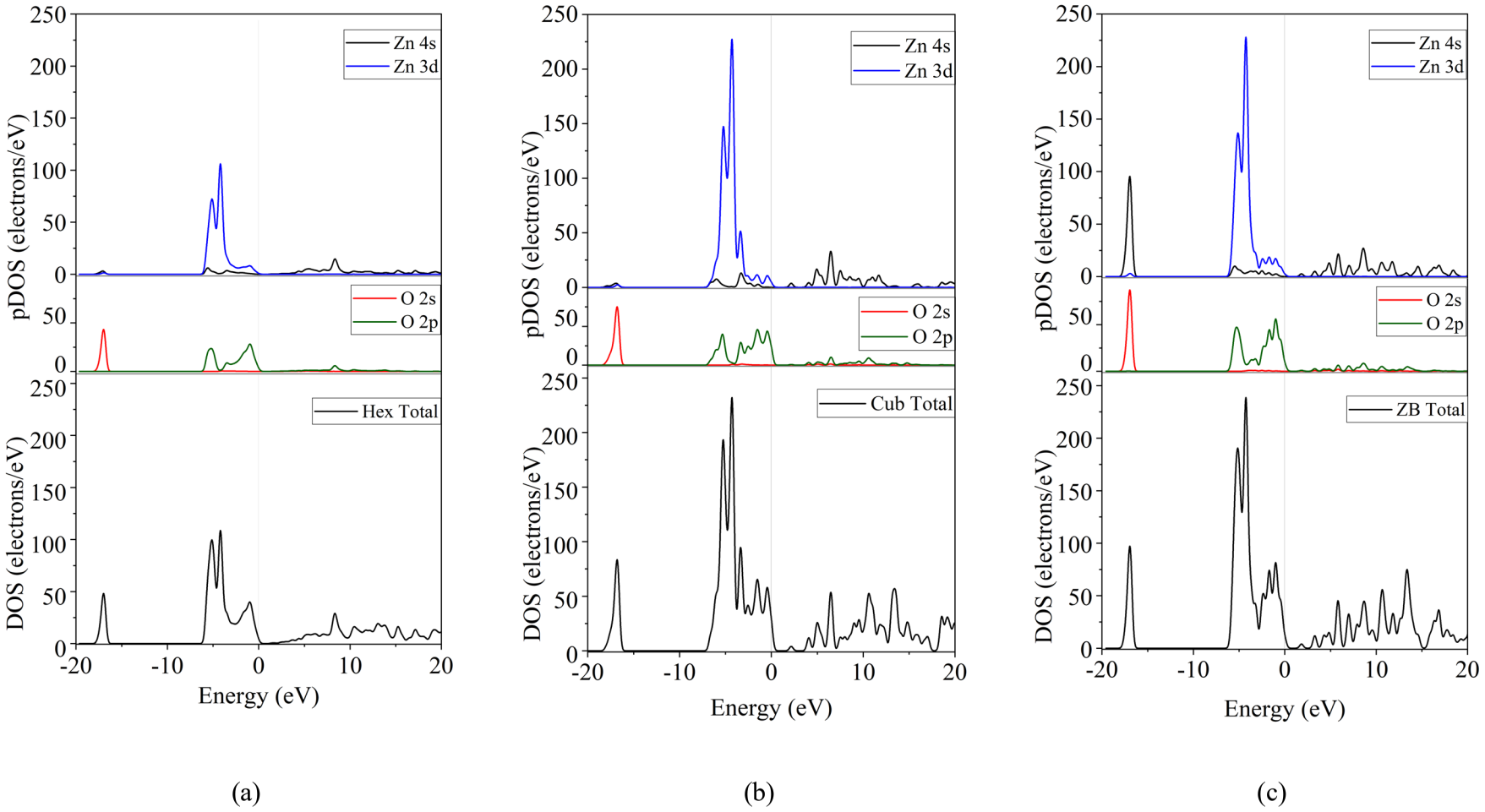

Figure 3-6: pDOS and DOS for the different crystal systems of ZnO bulk structures, namely, (a) hexagonal, (b) cubic, and (c) zinc-blende.

In Figure 3-7, the pDOS for Zn-d orbitals of the hexagonal, cubic, and zinc-blende crystal systems of ZnO are compared. This comparison facilitated an in-depth understanding of the electron distribution and behaviour within the Zn-d orbitals across these three crystal systems. The analysis showed the variations in the d-bands among these crystal systems.

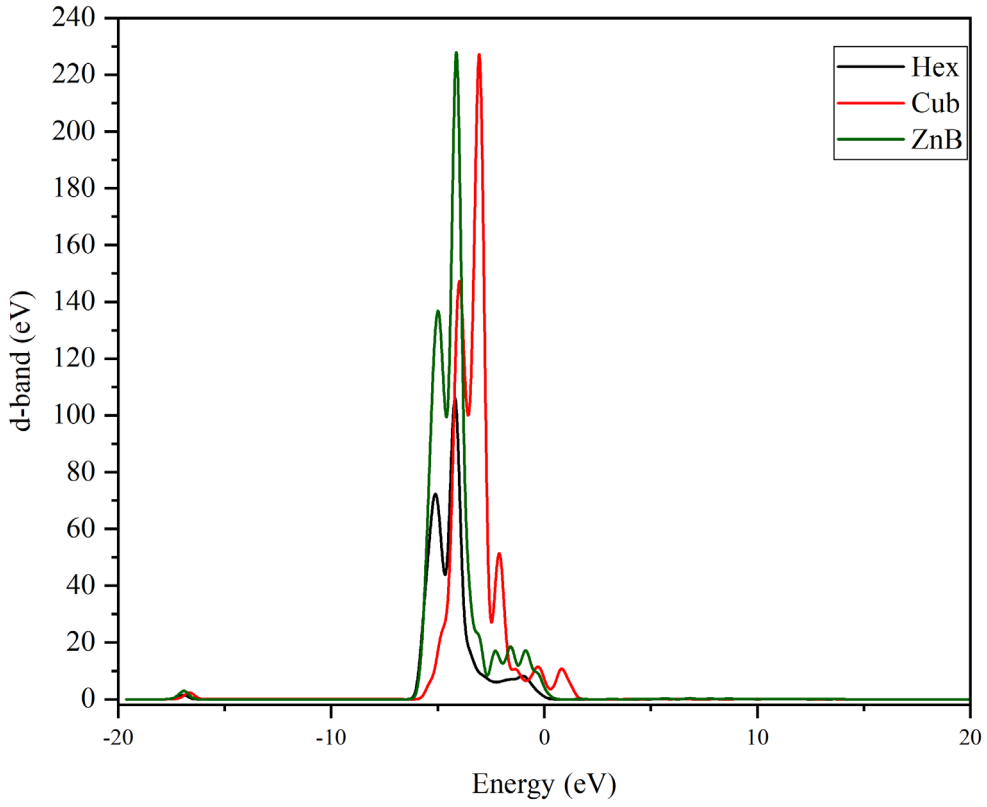

Figure 3-7: ***Comparison of the pDOS (d-band) for the hexagonal, cubic and zinc-blende crystal systems of ZnO bulk structures with their corresponding energies.***

The analysis of the pDOS for the d-band in various ZnO crystal systems showed that the band initially spreads out widely and then splits into two separate bands. These bands had a total width of about 2.5 eV, as shown in Figure 3-7. This widening of the d bands happens because of a strong interaction between the p and d bands. The way atoms are packed in the hexagonal crystal system and the bond angles and lengths allow the O 2p and Zn 4s orbitals to align more closely than in the cubic and zinc-blende crystal system. This close alignment leads to a greater overlap of these orbitals, enhancing the interactions between the p and d bands. As a result, the interaction between these bands becomes increasingly significant, transitioning from the cubic crystal system, through the zinc-blende, to the complex hexagonal crystal system. This progression not only affects the

interactions but also leads to an increased width in the proximity of the O 2p and Zn 4s bands, as illustrated in Figure 3-6.

3.4.3.2.2 d-band centre

The calculated d-band centre values for the ZnO crystal systems relative to the VBM were as follows: hexagonal = 7.204 eV, cubic = 6.287 eV, and zinc-blende = 6.464 eV. These values showed a slight variation among the different ZnO crystal systems, with the hexagonal system having the highest d-band centre and the cubic system the lowest. The position of the d-band centre relative to the VBM can significantly influence the electronic properties of ZnO.

This variation suggests differences in the binding strength and electronic environment of the d-electrons in each structure. The proximity of the d-band centre to the VBM in the hexagonal crystal system implies stronger interactions with adsorbates, potentially enhancing catalytic applications compared to the cubic and zinc-blende crystal systems. These results provide a basis for predicting the catalytic behaviour of the ZnO crystal systems.

3.4.3.2.3 Band gap

The band structures of the optimised ZnO bulk structures are illustrated in Figure 3-8. In the hexagonal crystal system, the band gap was 0.727 eV. Both the valence band maximum (VBM) and conduction band minimum (CBM) were located at the Q point along the G-G path within the BZ. This arrangement results in a "direct" band gap, allowing electrons to transition directly from the VB to the CB with minimal momentum changes. Such systems typically exhibit superior electronic properties.[356]

Conversely, a band gap of 0.730 eV was observed in the cubic crystal system. Here, the CBM was positioned at the Q point, while the VBM was slightly beyond the Q point toward the Z point. This results in an "indirect" band gap, where the VBM and CBM do not coincide in momentum space. Consequently, electrons undergoing transitions between these bands must significantly alter their momentum, leading to lower transition probabilities and less efficient electronic properties.[357]

In the zinc-blende crystal system, a band gap of 0.630 eV was observed. Like the cubic system, the VBM and CBM were situated slightly beyond the Q point toward the Z point, resulting in an "indirect" band gap configuration. This behaviour is intrinsically linked to the crystal structure and the specific electronic properties resulting from the atomic arrangement and bonding characteristics of the zinc-blende phase.

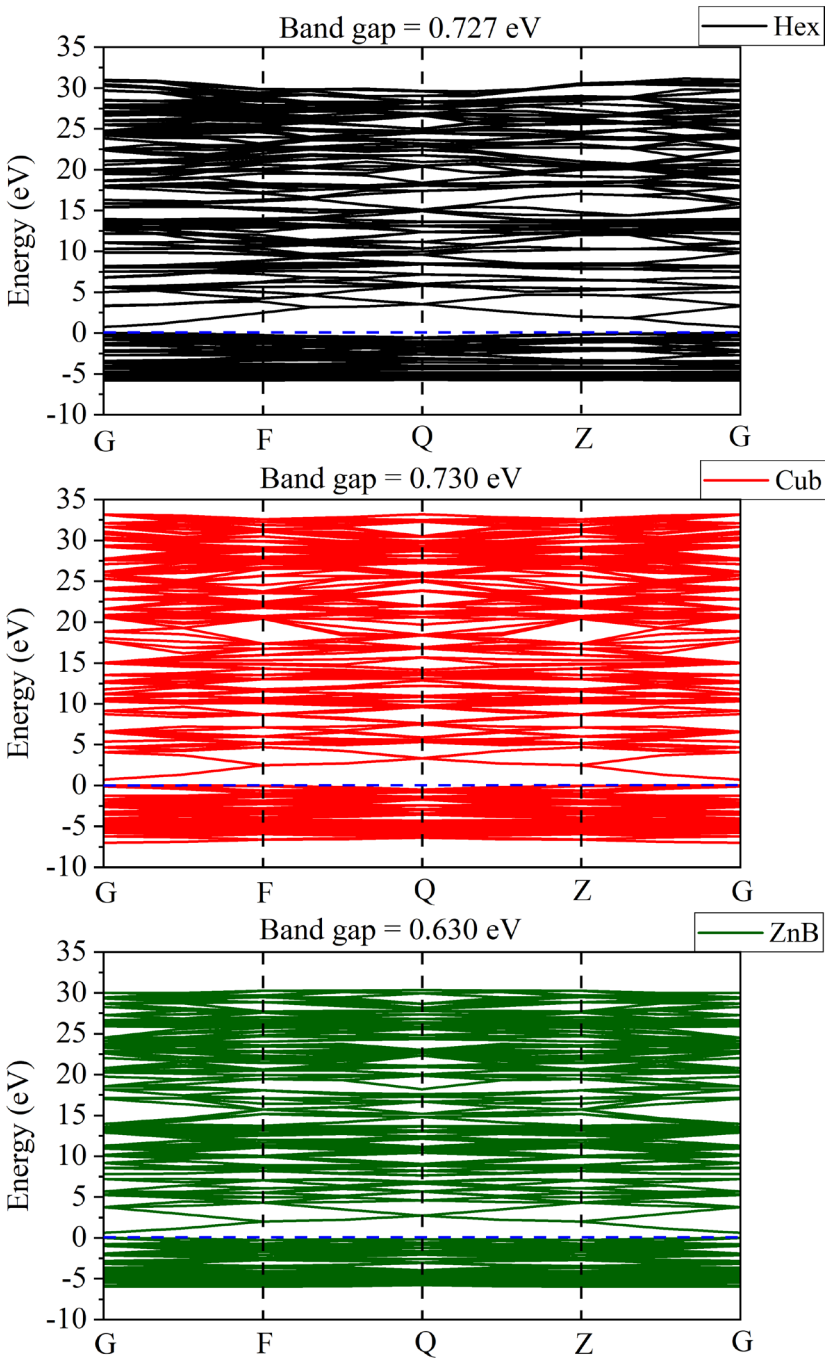

Figure 3-8: ***The computed band structure for the hexagonal, cubic and zinc-blende crystal systems of ZnO bulk structures using GGA/PBE.***

Additionally, the hexagonal crystal system's band structure was significantly more complex than the cubic and zinc-blende crystal systems. This complexity is primarily attributed to the doubled number of atoms within the unit cell. The presence of more atoms per unit cell in the hexagonal crystal system introduced additional atomic orbitals into the electronic structure. Consequently, this led to a greater number of bands within the electronic band structure of the crystal system.

More bands result in more complex interactions between electrons, which can affect the band gaps and the electronic properties of the system. The calculated band gap values in comparison with published literature values, are listed in Table 3-7.

Table 3-7: ***The band gap values for the different crystal systems of ZnO bulk structures.***

ZnO crystal system	Band gap (eV)				
	This work		Literature values		
	GGA/PBE	(GGA)+U $U_{d\text{-}Zn}$ = 10 eV, $U_{p\text{-}O}$ = 7 eV	GGA/PBE or GGA/PW91	(GGA)+U $U_{d\text{-}Zn}$ = 10 eV, $U_{p\text{-}O}$ = 7 eV	Experimental work
Hexagonal	0.727 eV	3.265 eV	0.730 eV[351] 0.760 eV[234]	3.370 eV[321, 263]	3.370 eV[238]
Cubic	0.730 eV	3.288 eV	0.750 eV[234, 351]	4.050 eV[358]	2.450 eV[359]
Zinc-blende	0.630 eV	-	0.640 eV[351] 0.650 eV[234]	3.250 eV[358]	3.180 eV[360]

The experimental literature reports band gap values of 3.370 eV[238] for the ZnO hexagonal crystal system, 2.450 eV[359] for the cubic crystal system, and 3.180 eV[360] for the zinc-blende crystal system. Computationally calculated literature values using the GGA/PBE functional yield band gaps of 0.730 eV.[351] 0.750 eV,[234, 351] and 0.640 eV[351] for the hexagonal, cubic, and zinc-blende crystal systems, respectively. After adding a U value of $U_{d\text{-}Zn}$ = 10 eV and $U_{p\text{-}O}$ = 7 eV,[284, 321] the computational band gaps increase to 3.370 eV,[321] 4.050 eV,[358] and 3.250 eV,[358] for the ZnO hexagonal, cubic, and zinc-blende crystal systems, respectively. The hexagonal and the zinc-blende crystal system values agree with experimental values.[238, 359, 360]

This research obtained band gap values of 0.727 eV, 0.730 eV, and 0.630 eV for the hexagonal, cubic, and zinc-blende crystal structures, respectively, using the GGA/PBE functional. These values closely align with those computed using the GGA/PBE or GGA/PW91 functional found in existing literature.[234, 351] After implementing $U_{d\text{-}Zn}$ = 10 eV and $U_{p\text{-}O}$ = 7 eV as proposed by Lee,[263] band gap values of 3.265 eV and 3.288 eV for the hexagonal and cubic crystal systems, respectively, were obtained.

Comparing the band gap values reported in Lee's study[263] with the band gap value for the hexagonal crystal system obtained in this study, a 3% deviation is observed. This decrease in the band gap can be attributed to the limitations of the PBE/GGA method, specifically the issue of self-interaction correction with the standard exchange-correlation functional.[361] However, the band gap value obtained for the cubic crystal system was significantly lower than the computed literature value listed in Table 3-7. A 23% reduction in the band gap energy of the cubic crystal

system was observed compared to Dixit's study.[358] However, the band gap value obtained in this study is closer to the experimental value listed in Table 3-7.

3.4.4 Surface model construction and optimisation

3.4.4.1 Construction

A top view of the different surfaces can be found in Appendix A3, Table A3-2.

3.4.4.2 Optimisation

3.4.4.2.1 k-point grid benchmarking for (101) hexagonal surface

Figure 3-9(a) shows the optimised energy per atom obtained from the MT (101) hexagonal surface, whilst Figure 3-9(b) shows the optimised energy per atom obtained from the OT (101) hexagonal surface plotted against the number of k-points for a widespread of k-point grids from 1×1×1 to 11×11×1.

During the k-point benchmarking, the 1×1×1 k-point exhibited a high optimised energy because it samples the BZ less finely, potentially missing subtle electronic interactions and structural details. A similar outcome was observed with the 3×3×1 k-point grid, which had a low k-point density and would have resulted in less accurate calculations. The optimised energy for the 5×5×1 k-point grid was suitable for the cubic and zinc-blende crystal systems but was unstable for the hexagonal crystal system in both the MT and OT surfaces. However, when transitioning from the 5×5×1 grid to the 11×11×1 grid, the bulk structure converged. Specifically, in the hexagonal crystal systems, the energy decreased from 3×3×1 to 5×5×1, then increased from 5×5×1 to 7×7×1. The energy remained consistent from the 7×7×1 k-point grid to the 11×11×1 k-point grid, indicating convergence of the structure.

(a)

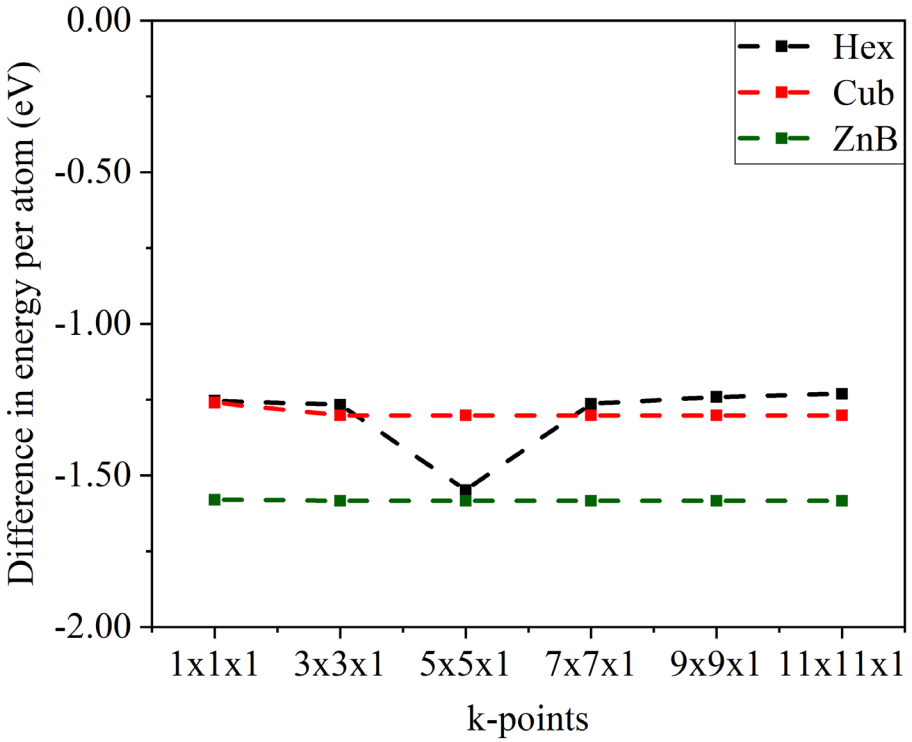

(b)

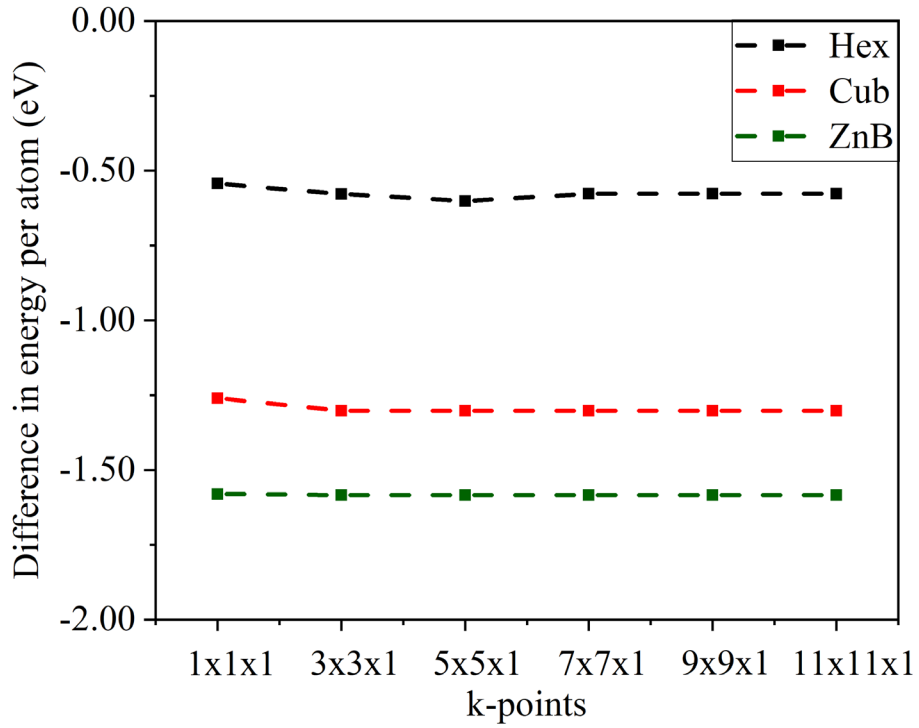

Figure 3-9: ***The difference in optimised energy per atom for the different crystal systems of ZnO (101) (a) MT and (b) OT surfaces with various k-point grids.***

Table 3-8 shows that as the k-point grid size increased from 1×1×1 to 11×11×1 at a 400 eV energy cut-off, computational times and costs rose across all crystal systems (hexagonal, cubic, and

zinc-blende). This trend highlights how grid size and crystal system impact computational efficiency.

Table 3-8: ***The time taken for k-point optimisation for the different crystal systems of ZnO at an energy cut-off of 400 eV.***

	Computational time (mins)			
k-point grid	Hexagonal		Cubic	Zinc-blende
	MT	OT		
1×1×1	24.06	90.24	23.92	13.09
3×3×1	279.82	489.28	46.46	97.81
5×5×1	1439.59	2295.24	293.00	292.25
7×7×1	712.47	1926.95	247.91	509.63
9×9×1	1621.39	2538.29	418.30	502.84
11×11×1	3619.74	4714.90	658.44	705.69

In the hexagonal (MT and OT) and cubic systems, computational time decreased from the 5×5×1 to the 7×7×1 grid, then increased from 7×7×1 to 11×11×1, deviating from the typical trend of increased time from 1×1×1 to 5×5×1. In the zinc-blende system, computational time decreased from 7×7×1 to 9×9×1, followed by an increase from 9×9×1 to 11×11×1, differing from the usual trend of increasing time from 1×1×1 to 7×7×1. Time increased until 5×5×1, then fluctuated, indicating the point of convergence. As energy stabilised, so did computational time, explaining the fluctuations beyond the 7×7×1 grid. Increasing the grid size further did not significantly enhance accuracy, and computational time remained manageable. The intersection of energy stability and computational time marks a balance between accuracy and cost. Thus, the Monkhorst-Pack[353] 7×7×1 k-point grid was determined to be optimal for balancing computational cost and accuracy across different ZnO bulk crystal systems. This grid was also ideal for investigating the surface properties of Sn-doped ZnO structures, particularly given the added complexity of oxygen-terminated (OT) surfaces, which require more computational time than metal-terminated (MT) surfaces. The choice of a 7×7×1 k-point grid aligns with findings from an earlier study.[322]

3.4.4.3 Surface properties

Table 3-9 displays the total energy per atom values for each surface. In the hexagonal crystal system, the total energy per atom values across various surfaces showed a consistent range, approximately -1073.54 to -1072.94 eV/atom, indicating stability within this crystal system. Similarly, the cubic crystal system exhibited a relatively consistent total energy per atom range, ranging from about -1073.36 to -1073.15 eV/atom. On the other hand, the zinc-blende crystal system displayed a broader range of total energy per atom values, spanning from approximately

-1073.53 to -1072.26 eV/atom, suggesting a greater variation among different surfaces within this crystal system compared to the hexagonal and cubic systems.

Table 3-9: ***The total energies, number of atoms in a cell and total energies/atoms obtained for the optimisation of different surface terminations of the three crystal systems.***

ZnO Crystal system	Surface	Total energy (eV)	Total no. of atoms in cell	Total energy/atoms (eV/atom)
Hexagonal	(100)	-68705.26	64	-1073.52
	$(002)_{MT}$	-34353.20	32	-1073.54
	$(002)_{OT}$	-34334.17	32	-1072.94
	$(101)_{MT}$	-68703.69	64	-1073.50
	$(101)_{OT}$	-68695.24	64	-1073.36
	$(102)_{MT}$	-68698.01	64	-1073.41
	$(102)_{OT}$	-68699.72	64	-1073.43
	$(103)_{MT}$	-68703.65	64	-1073.49
	$(103)_{OT}$	-68696.56	64	-1073.38
	$(112)_{MT}$	-68688.78	64	-1073.26
	$(112)_{OT}$	-68697.61	64	-1073.40
	(200)	-34339.24	32	-1073.10
	$(201)_{MT}$	-68685.74	64	-1073.21
	$(201)_{OT}$	-68700.14	64	-1073.44
	(210)	-68696.78	64	-1073.39
Cubic	$(111)_{MT}$	-68688.46	64	-1073.26
	$(111)_{OT}$	-68687.32	64	-1073.24
	(200)	-34347.59	32	-1073.36
	(220)	-34340.77	32	-1073.15
	$(222)_{MT}$	-68688.46	64	-1073.26
	$(222)_{OT}$	-68687.32	64	-1073.24
	$(311)_{MT}$	-68685.62	64	-1073.21
	$(311)_{OT}$	-68687.86	64	-1073.25
	(400)	-34347.59	32	-1073.36
Zinc-blende	$(111)_{MT}$	-137407.39	128	-1073.50
	$(111)_{OT}$	-137337.96	128	-1072.95
	$(200)_{MT}$	-68685.54	64	-1073.21
	$(200)_{OT}$	-68685.44	64	-1073.21
	(220)	-68703.74	64	-1073.50
	$(222)_{MT}$	-68706.16	64	-1073.53
	$(222)_{OT}$	-68624.58	64	-1072.26
	$(311)_{MT}$	-137377.44	128	-1073.26
	$(311)_{OT}$	-137372.69	128	-1073.22
	$(400)_{MT}$	-34333.94	32	-1072.94

3.4.4.3.1 Surface energies

Surface energy is influenced by various factors, including the bonding, surface structure and atomic arrangement.[28] Generally, the crystal system exhibiting the lowest surface energy is more stable.

In the hexagonal system of ZnO, every zinc (Zn) atom is surrounded by four oxygen (O) atoms in a tetrahedral coordination. Similarly, each oxygen atom is surrounded by four zinc atoms in the same manner. The tetrahedra in this crystal system are elongated and exhibit hexagonal symmetry, contributing to a densely packed and compact structure. Although this arrangement can reduce surface energy for specific orientations in the hexagonal crystal system of ZnO, based on the data presented in Table 3-10, it does not uniformly result in lower surface energy across all surfaces compared to the cubic and zinc-blende crystal systems. However, overall, some cubic surfaces, such as the (200) and (311) orientations, exhibited lower surface energies than many of the hexagonal and zinc-blende surfaces. Specifically, the cubic (200) surface had one of the lowest surface energies at 0.549 J/m^2, which was lower than several surfaces in both the hexagonal and zinc-blende crystal systems. This variation in surface energy across different crystal systems arises from differences in atomic packing and coordination.

In the hexagonal crystal system, the $(002)_{OT}$ surface termination showed a calculated surface energy that is 19.80% lower than the literature value. In contrast, the $(101)_{OT}$ and $(102)_{OT}$ terminations had calculated energies 3.05% lower and 15.77% higher, respectively, than some literature values. Similarly, in the cubic crystal system, the $(111)_{OT}$ surface termination exhibited a calculated energy 36.86% lower than the literature value.[362]

These differences between the calculated and literature surface energies can be attributed to several factors. Firstly, variations in computational methods and parameters used in the calculations may lead to discrepancies in results. The surface energies obtained through experimentation are subject to uncertainties, including potential contamination by surface-active elements like oxygen, which can lower surface tension measurements.[363] Meanwhile, in the zinc-blende crystal system, the $(111)_{MT}$ termination had a calculated surface energy that is 4.02% lower than the values reported in the literature.[291] Measurements that account for these factors are often considered more reliable, as they may better represent the true surface tension.

Table 3-10: ***Calculated surface energies and work function for the hexagonal, cubic and zinc-blende crystal systems and corresponding values from the literature.***

ZnO crystal system	Surface[a]	Calculated surface energies[b] (J/m^2)	Literature values (J/m^2)		Work function[c] (eV)	Literature values (eV)	
			Comp.	Exp.		Comp.	Exp.
Hexagonal	(100)	**0.596**	0.68 [364]	-	4.961	4.900[365]	4.500[366]
	$(002)_{MT}$	0.807	-	-	4.124	5.076[367]	4.080[368],4.710[367]
	$(002)_{OT}$	4.331	-	5.40 [230]	7.235	6.900[369], 7.700[25]	-
	$(101)_{MT}$	1.113	1.12 [370]	-	**3.728**	-	-
	$(101)_{OT}$	1.939	2.00 [371], 1.85 [372]	-	4.011	-	-
	$(102)_{MT}$	1.338	-	-	4.413	-	-
	$(102)_{OT}$	1.204	1.04 [322]	-	5.688	-	-
	(210)	0.795	0.85 [314]	-	5.253	5.200[365]	-
	$(103)_{MT}$	**0.685**	-	-	5.333	-	-
	$(103)_{OT}$	1.109	-	-	4.241	-	-
	(200)	2.101	-	-	5.420	-	-
	$(112)_{MT}$	1.483	1.40[296]	-	4.433	-	-
	$(112)_{OT}$	0.986	-	-	4.784	-	-
	$(201)_{MT}$	1.610	-	-	4.944	-	-
	$(201)_{OT}$	0.821	-	-	3.904	-	-
Cubic	$(111)_{MT}$	0.905	-	-	3.777	-	-
	$(111)_{OT}$	0.966	1.53 [362]	-	3.602	-	-
	(200)	0.549	-	-	4.790	-	-
	(220)	0.900		-	4.469	-	-
	$(311)_{MT}$	0.610		-	3.784	-	-
	$(311)_{OT}$	**0.541**		-	**3.590**	-	-
	$(222)_{MT}$	0.905		-	4.822	-	-
	$(222)_{OT}$	0.966		-	5.311	-	-
	(400)	**0.548**		-	4.792	-	-
Zinc-blende	$(111)_{MT}$	1.061		1.02 [291]	4.176	-	-
	$(111)_{OT}$	4.304		-	6.823	-	-
	$(200)_{MT}$	2.757		-	5.435	-	-
	$(200)_{OT}$	2.766		-	5.714	-	-
	(220)	**0.747**		-	5.227	-	-
	$(311)_{MT}$	1.420		-	4.315	-	-
	$(311)_{OT}$	1.548		-	7.182	-	-
	$(222)_{MT}$	**0.416**		-		-	-
	$(222)_{OT}$	4.225		-	4.501	-	-
	$(400)_{MT}$	2.203		-	4.258	-	-
	$(400)_{OT}$	2.203		-	**4.068**	-	-

Note: [a]Various surface subscripts indicate different terminations either Metal-Terminated (MT) or Oxygen-Terminated (OT). [b]Each crystal system's lowest surface energies shown in the morphology are indicated in bold. [c]Each crystal system's lowest work functions shown in the morphology are indicated in bold

Additionally, surface reconstructions and limitations of the exchange-correlation functional employed in calculations may account for discrepancies between the calculated and experimental surface energies.[363]

In summary, it is important to acknowledge that stability is not solely determined by surface energy. Other factors, such as bulk energies, lattice matching with substrates, and growth conditions, also play significant roles.[220] Therefore, simply comparing the surface energy of the three ZnO crystal systems was insufficient to determine the most stable crystal system, as each crystal system exhibited distinct surface properties that were not directly comparable based on our calculations. A more comprehensive analysis incorporating a broader range of considerations is required to accurately ascertain the relative stability of the different ZnO crystal systems.

One such consideration is the work function, which is a key property reflecting the surface's electronic structure.

3.4.4.3.2 Work function

The work function is predominantly influenced by the surface's electronic structure, focusing on electronic stability and behaviour rather than structural stability. In Table 3-10 shows the work functions for various terminations of the most extensively studied ZnO surfaces in the hexagonal, cubic, and zinc-blende crystal systems, along with a limited number of corresponding literature values.

The calculated work functions for surfaces in the hexagonal crystal system in this study showed varying degrees of agreement with both computational and experimental values reported in the literature. For example, the work function for the (100) surface in the hexagonal crystal system was calculated at 4.961 eV, closely matching the computational value of 4.900 eV[365] with a 1.24% deviation but showing a larger deviation of 10.24% from the experimental value of 4.500 eV.[373] The larger deviation from the experimental value is likely due to the influence of surface conditions during work function measurements, such as adsorbed contaminants, surface roughness, or surface reconstructions under which the experimental data were obtained. Additionally, differences in computational methods, such as the choice of exchange-correlation functional may also contribute to this deviation.

Similarly, the $(002)_{MT}$ surface had a calculated work function of 4.124 eV, which deviates by 1.08% from the experimental literature value of 4.080 eV[368] but differs significantly from the reported computational value of 5.076 eV,[367] indicating potential discrepancies in computational methods. For the $(002)_{OT}$ surface, the calculated work function of 7.235 eV deviated by 4.86% from the computational value of 6.900 eV.[369] The 4.86% deviation likely arises from differences

in the computational methods, such as the choice of exchange-correlation functional, treatment of surface states, or the precision in modelling surface termination and reconstruction.

The (210) surface where the work function of 5.253 eV, calculated using DFT calculations within VASP with GGA-PBE functionals and cleaved surfaces derived from fully relaxed supercells, closely matches the computational value of 5.200 eV[365] (1.02% deviation) is a stronger validation of the computational approach. However, for many other surfaces, limited experimental data makes it challenging to fully validate the calculated work functions, highlighting the need for more comprehensive experimental studies across different ZnO crystal systems.

The cubic ZnO system showed that the calculated work functions ranged from 3.590 eV to 5.311 eV across various surfaces. However, the absence of comparative data can be attributed to limited research focus on the cubic ZnO system, which is less commonly studied than the hexagonal system due to the latter's prevalence in natural forms of ZnO. Similarly, the zinc-blende crystal system exhibited calculated work functions ranging from 4.068 eV to 7.182 eV, but a notable lack of literature values for comparison is evident due to its metastable nature under ambient conditions, which explains the scarcity of experimental data. In contrast, the $(002)_{OT}$ surface in the hexagonal system exhibited the highest work function at 7.235 eV, suggesting that it is less likely to undergo surface reactions. This property may be advantageous for applications that require stable electronic properties, such as in certain electronic devices.

Surfaces with lower work functions are not always the most structurally stable; their reduced energy barrier for electron emission is due to their electronic properties rather than their structural stability. However, in photocatalysis, these surfaces might be more effective because the lower work function facilitates electron emission and enhances catalytic activity.

Among the various surfaces studied, the lowest work functions were observed for the $(101)_{MT}$ surface in the hexagonal crystal system, the $(311)_{OT}$ surface in the cubic crystal system, and the $(400)_{OT}$ surface in the zinc-blende crystal system, as shown in Table 3-10. For the $(101)_{MT}$ surface in the hexagonal system, the low work function is due to the unique arrangement of surface atoms that creates a favourable electronic environment for electron emission. In the cubic crystal system, the $(311)_{OT}$ surface exhibited a low work function because of its surface electronic structure, which allows for easier electron release. Similarly, the $(400)_{OT}$ surface in the zinc-blende crystal system had a reduced work function attributed to its specific surface dipole moments and electronic state alignments. These lower work functions across these surfaces result from their distinct electronic

configurations, including factors such as surface dipole moments, electron density, and the alignment of electronic states, all of which facilitate electron emission and contribute to their lower work function values.

3.4.4.3.3 Morphology

The ideal morphology of the ZnO was described by employing Wulff construction[3] based on the calculated surface energies in Table 3-10. As illustrated in Figure 3-10, only two of the eight calculated surfaces were visible in the hexagonal crystal system. These surfaces can be seen on the hexagonal morphology of ZnO under ideal vacuum conditions.[374] The (100) surface contributes to the sides of the hexagonal shape, while the (103) surface makes up the top and bottom surface.

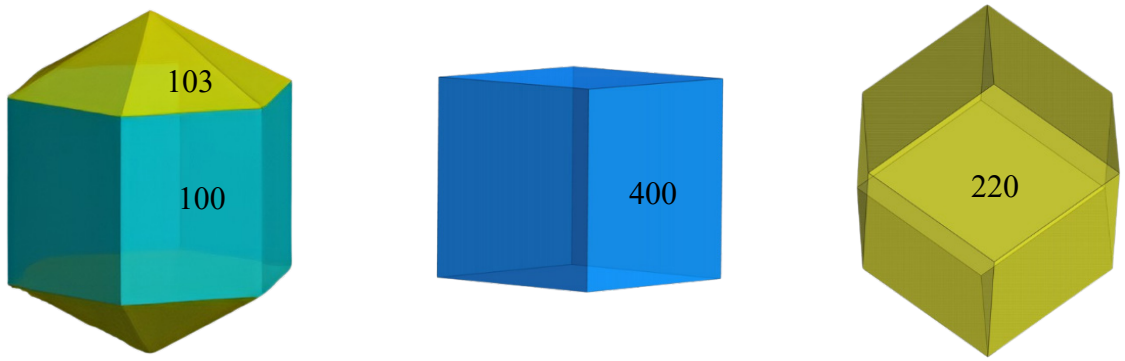

Figure 3-10: ***The Wulff construction's predictions for the pure ZnO structure (a) hexagonal, (b) cubic, and (c) zinc-blende.***

In contrast, both the cubic and zinc-blende crystal systems of zinc oxide (ZnO) exhibited only one of the six calculated surfaces. Specifically, for the cubic crystal system, the (400) surface is the one that is visible under ideal vacuum conditions.[362] Conversely, for the zinc-blende crystal system, the (220) surface is the one that is visible under ideal vacuum conditions.[298] The projected Wulff shapes of ZnO were compared with the previously reported values in the literature.[297, 362] The hexagonal shape closely aligned with the findings of Catto,[297] whose work focused on the crystal morphology and surface structure of ZnO crystals, indicating a reliable and consistent representation. Additionally, the cubic and zinc-blende shapes were found to be consistent with the research study conducted by Koster.[362] A comparative analysis of the projected Wulff shapes with the work of Catto[297] and Koster,[362] validated the accuracy and reliability of the developed model.

3.5 Conclusion

The aim of this chapter was to develop a theoretical framework based on DFT calculations to investigate the structural and electronic properties of ZnO. This aim was successfully achieved by thoroughly evaluating and optimising the three most prevalent ZnO crystal systems, determining the optimal k-point grid and energy cut-off, analysing structural and electronic properties as well as surface properties, and validating the model against established literature values.

The k-point benchmarking for ZnO bulk structures across hexagonal, cubic, and zinc-blende crystal systems demonstrated that a finer k-point grid improves accuracy. However, grids beyond 11×11×11 do not significantly affect the results. Therefore, the 11×11×11 k-point grid was identified as providing an optimal balance between accuracy and computational cost, consistent with a previous study.[354] For cut-off energy benchmarking using this grid, a 400 eV cut-off effectively balanced computational efficiency and accuracy. Lower cut-off energies, such as 250 eV, failed to provide accurate results due to inadequate wave function representation, while higher cut-offs showed minimal energy variations but increased computational time. Thus, a 400 eV cut-off was deemed reliable for balancing accuracy and efficiency.

The bulk structure optimisation of ZnO confirmed that the lattice parameters, cell angles, volume, density, total atoms, and final energy closely match literature values,[55, 266, 333, 375-377] with deviations up to 0.495% for lattice parameters and 5.68% for cell volumes. This bulk structure was further validated by computed powder X-ray diffraction (XRD) patterns, which showed a maximum variation of only 3% in 2θ values compared to experimental data.[80, 333] Although slight discrepancies in peak intensities were observed due to DFT approximations and experimental uncertainties, the overall results affirmed the reliability of the computational approach.

The density of states (DOS) and partial density of states (pDOS) analyses provided insights into the electronic structure. The DOS revealed that oxygen 2s levels contributed to the lowest energy bands around −18.0 eV, with the valence band (VB) spanning from −6.0 eV to −0.2 eV, primarily formed by zinc 3d and oxygen 2p orbitals, while the conduction band (CB) was dominated by zinc 4s orbitals. The pDOS for Zn-d orbitals, illustrated in Figure 3-7, indicated broadening and splitting into two bands with a width of about 2.5 eV due to strong p-d interactions. In the hexagonal system, closer alignment of O 2p and Zn 4s orbitals enhanced these interactions compared to the cubic and zinc-blende systems, resulting in a wider band near these orbitals. The d-band centre values for ZnO crystal systems were: hexagonal = 7.204 eV, cubic = 6.287 eV, and

zinc-blende = 6.464 eV. The hexagonal system, with the highest d-band centre, indicates stronger d-electron interactions and potentially superior catalytic performance. The band structures revealed that the hexagonal system had a direct band gap of 0.727 eV, while the cubic and zinc-blende systems exhibited indirect band gaps of 0.730 eV and 0.630 eV, respectively. The more complex band structure of the hexagonal system, attributed to its doubled unit cell, resulted in a greater number of bands and intricate interactions. Band gap values were in close agreement with literature,[187, 234, 238, 321, 351, 358-360] validating the computational method.

Applying Hubbard U corrections resulted in band gap energies of 3.265 eV for the hexagonal system and 3.288 eV for the cubic system. These values align reasonably well with experimental data. For the hexagonal system, the calculated value of 3.265 eV had a 3.12% deviation from the experimental value of 3.370 eV.[238] In contrast, the cubic system's calculated band gap of 3.288 eV showed a 34.20% deviation from the experimental value of 2.450 eV.[359] These results suggest that the Hubbard U correction effectively captures the electronic properties of these ZnO crystal systems.

The k-point benchmarking for ZnO surface slabs revealed that while increasing the k-point grid size generally improves accuracy, the benefits diminish significantly beyond the 7×7×1 grid, with a corresponding increase in computational time. Therefore, the 7×7×1 grid was identified as optimal for ensuring both computational efficiency and result reliability.

Surface property analysis demonstrated stable total energy per atom values for the hexagonal and cubic crystal systems, confirming their reliability. In contrast, the zinc-blende system exhibited a broader range of total energy values, indicating greater surface variability. This variation underscores the importance of considering surface stability when analysing different crystal systems. The study also evaluated surface terminations by analysing surface energies.

In the hexagonal crystal system, the surface energy difference between metal-terminated (MT) and oxygen-terminated (OT) surfaces ranged from 0.4 J/m^2 to 3.7 J/m^2. For the cubic crystal system, this difference varied from 0.02 J/m^2 to 0.6 J/m^2. In the zinc-blende system, the range was from 0.001 J/m^2 to 4.0 J/m^2.

For the surface energies, the (100), metal-terminated (002), and (103) surfaces emerged as the most stable for the hexagonal system, the (400) surface for the cubic system, and the (220) surface for the zinc-blende system. These surfaces were used to construct Wulff shapes of the ZnO crystal systems, which agrees with the morphology in the literature.[297, 362]

Although surface energy is a significant factor in determining stability, it is important to note that the ZnO crystal systems are inherently incomparable due to their distinct structures and the variation in surfaces studied. Therefore, relying solely on surface energies may not provide a complete assessment of the stability of the three crystal systems of ZnO models. The stability of a crystal system is influenced by multiple factors, encompassing the overall energy of the crystal structure, atomic arrangement and bonding, and the presence of defects or impurities. These factors can profoundly impact the relative stability of different crystal systems, even if their surface energies exhibit disparities.

However, these results provide valuable insights and help refine computational strategies for ZnO surface slabs. Previous research[378] has established that the hexagonal crystal system of ZnO exhibits the highest stability among the different crystal systems. This stability arises from its unique crystal structure, low surface energy values, and inherent thermodynamic stability. In contrast, although the cubic crystal system also exhibits relatively low surface energy values and a propensity for stability, experimental evidence[379] shows that it can only maintain stability when subjected to high temperature and pressure, unlike the hexagonal crystal system, which remained stable under normal conditions. Conversely, the zinc-blende crystal system exhibited significantly higher surface energy values, indicating a pronounced extent of instability.

Essential insights into the electronic properties of these materials were gained by the calculated work functions for various terminations of ZnO surfaces in hexagonal, cubic, and zinc-blende crystal systems, as shown in Table 3-10. For instance, the (100) surface of the hexagonal ZnO crystal system showed a calculated work function of 4.961 eV, aligning well with literature values.[365, 373] Similarly, the $(002)_{MT}$ and (210) surfaces exhibited work functions closely matching reported values,[365, 367, 368] further validating the hexagonal model with a maximum deviation of only 4.8%.

The range of work functions for hexagonal ZnO spanned from 3.728 eV to 7.235 eV, with oxygen-terminated surfaces generally having slightly higher work functions than metal-terminated surfaces, barring a few exceptions. The cubic ZnO system showed work functions ranging from 3.590 eV to 5.311 eV, with the $(311)_{OT}$ surface deviating from the general trend by having a higher work function than its metal-terminated counterpart. The zinc-blende system presented work functions between 4.068 eV and 7.182 eV, with similar trends influenced by surface dipole moments and atomic arrangements.

The highest work function values were observed for surfaces like hexagonal $(002)_{OT}$, cubic $(222)_{OT}$, and zinc-blende $(311)_{OT}$, suggesting a lower likelihood of surface reactions. High work functions are associated with surfaces that are less likely to emit electrons easily, which can contribute to stable electronic properties. This stability is advantageous for applications that require consistent electronic performance, such as in certain electronic devices.

The surfaces with the lowest work functions, specifically the $(101)_{MT}$ surface in the hexagonal system, the $(311)_{OT}$ surface in the cubic system, and the $(400)_{OT}$ surface in the zinc-blende system, have electronic configurations that make it easier for electrons to be emitted. This easy election emission implies that these surfaces are more prone to releasing electrons due to their electronic properties, such as surface dipole moments and electronic state alignments. However, this ease of electron emission does not necessarily correlate with structural stability, meaning that while these surfaces are good at emitting electrons, they may not be the most stable in terms of their physical structure. However, in photocatalysis, these surfaces might be more effective and enhance catalytic activity.

3.6 References

(2) Rahm, J.; Erhart, P. WulffPack: A Python package for Wulff constructions. *Journal of Open Source Software* **2020**, *5*, 1944. DOI: 10.21105/joss.01944.

(3) Wulff, G. XXV. On the question of the rate of growth and dissolution of the crystal surfaces. *Kristallografiya* **1901**, *34*, 449-530. DOI: 10.1524/ZKRI.1901.34.1.449.

(6) Abou Zeid, S.; Perez, A.; Bastide, S.; Le Pivert, M.; Rossano, S.; Remita, H.; Hautière, N.; Leprince-Wang, Y. Antibacterial and photocatalytic properties of ZnO nanostructure decorated coatings. *Coatings* **2023**, *14* (1), 41.

(7) Czech, B.; Zygmunt, P.; Kadirova, Z. C.; Yubuta, K.; Hojamberdiev, M. Effective photocatalytic removal of selected pharmaceuticals and personal care products by elsmoreite/tungsten oxide@ ZnS photocatalyst. *Journal of Environmental Management* **2020**, *270*, 110870.

(11) Sabzehei, K.; Hadavi, S.; Bajestani, M. G.; Sheibani, S. Comparative evaluation of copper oxide nano-photocatalyst characteristics by formation of composite with TiO_2 and ZnO. *Solid State Sciences* **2020**, *107*, 106362.

(13) Mohamad, A. A.; Hassan, M. S.; Yaakob, M. K.; Taib, M. F. M.; Badrudin, F. W.; Hassan, O. H.; Yahya, M. Z. A. First-principles calculation on electronic properties of zinc oxide by zinc–air system. *Journal of King Saud University - Engineering Sciences* **2017**, *29* (3), 278-283. DOI: 10.1016/j.jksues.2015.08.002.

(15) Hoffmann, M. R.; Martin, S. T.; Choi, W.; Bahnemann, D. W. Environmental applications of semiconductor photocatalysis. *Chemical Reviews* **1995**, *95* (1), 69-96. DOI: 10.1021/cr00033a004.

(18) Xie, L.; Du, T.; Wang, J.; Ma, Y.; Ni, Y.; Liu, Z.; Zhang, L.; Yang, C.; Wang, J. Recent advances on heterojunction-based photocatalysts for the degradation of persistent organic pollutants. *Chemical Engineering Journal* **2021**, *426*, 130617.

(21) Goi, A.; Trapido, M.; Tuhkanen, T. A study of toxicity, biodegradability, and some by-products of ozonised nitrophenols. *Advances in Environmental Research* **2004**, *8* (3), 303-311. DOI: 10.1016/S1093-0191(02)00102-8.

(23) Nezamzadeh-Ejhieh, A.; Khorsandi, S. Photocatalytic degradation of 4-nitrophenol with ZnO supported nano-clinoptilolite zeolite. *Journal of Industrial and Engineering Chemistry* **2014**, *20* (3), 937-946. DOI: 10.1016/j.jiec.2013.06.026.

(25) Douloumis, A.; Vrithias, N. R. E.; Katsarakis, N.; Remediakis, I. N.; Kopidakis, G. Tuning the workfunction of ZnO through surface doping with Mn from first-principles simulations. *Surface Science* **2022**, *726*. DOI: 10.1016/j.susc.2022.122175.

(26) Ibrahim, A. A.; Kumar, R.; Umar, A.; Kim, S. H.; Bumajdad, A.; Ansari, Z. A.; Baskoutas, S. Cauliflower-shaped ZnO nanomaterials for electrochemical sensing and photocatalytic applications. *Electrochimica Acta* **2016**, *222*, 463-472. DOI: 10.1016/J.ELECTACTA.2016.10.199.

(28) Morkoç, H.; Özgür, U. m. Zinc oxide: Fundamentals, materials and device technology. *British Library Cataloguing-in-Publication Data* **2009**, 477.

(30) Shabbir, S.; Shaari, A.; Haq, B. U.; Ahmed, R.; Ahmed, M. Investigations of novel polymorphs of ZnO for optoelectronic applications. *Optik* **2020**, *206*, 164285.

(31) Qi, K.; Xing, X.; Zada, A.; Li, M.; Wang, Q.; Liu, S.-y.; Lin, H.; Wang, G. Transition metal doped ZnO nanoparticles with enhanced photocatalytic and antibacterial performances: Experimental and DFT studies. *Ceramics International* **2020**, *46* (2), 1494-1502. DOI: 10.1016/j.ceramint.2019.09.116.

(34) Sahani, R.; Dixit, A. A comprehensive review on zinc oxide bulk and nano-structured materials for ionizing radiation detection and measurement applications. *Materials Science in Semiconductor Processing* **2022**, *151*, 107040.

(36) Klingshirn, C. F.; Meyer, B. K.; Waag, A.; Hoffmann, A.; Geurts, J.; Geurts, J. Crystal structure, chemical binding, and lattice properties. In *In Zinc Oxide: from fundamental properties towards novel applications*, Springer, 2010; pp 7-37.

(38) Kishwar, S.; Hasan, K.; Tzamalis, G.; Nur, O.; Willander, M.; Kwack, H.; Dang, D. L. S. Electro-optical and cathodoluminescence properties of low temperature grown ZnO nanorods/p-GaN white light emitting diodes. *Physica Status Solidi (a)* **2010**, *207* (1), 67-72.

(41) Özgür, Ü.; Hofstetter, D.; Morkoc, H. ZnO devices and applications: a review of current status and future prospects. *Proceedings of the IEEE* **2010**, *98* (7), 1255-1268.

(42) Liu, K.; Sakurai, M.; Aono, M. ZnO-based ultraviolet photodetectors. *Sensors* **2010**, *10* (9), 8604-8634.

(45) Sharma, D. K.; Shukla, S.; Sharma, K. K.; Kumar, V. A review on ZnO: Fundamental properties and applications. *Materials Today: Proceedings* **2022**, *49*, 3028-3035.

(46) Ahmaruzzaman, M. Metal oxides (ZnO, CuO and NiO)-based nanostructured materials for photocatalytic remediation of organic contaminants. *Nanotechnology for Environmental Engineering* **2023**, *8* (1), 219-235.

(47) Güell, F.; Galdámez-Martínez, A.; Martínez-Alanis, P. R.; Catto, A. C.; da Silva, L. F.; Mastelaro, V. R.; Santana, G.; na Dutt, A. ZnO-based nanomaterials approach for photocatalytic and sensing applications: recent progress and trends. *Materials Advances* **2023**, *4*, 3685-3707.

(48) Ong, C. B.; Ng, L. Y.; Mohammad, A. W. A review of ZnO nanoparticles as solar photocatalysts: Synthesis, mechanisms and applications. *Renewable and Sustainable Energy Reviews* **2018**, *81*, 536-551.

(49) Li, W.; Wang, G.; Feng, Y.; Li, Z. Efficient photocatalytic performance enhancement in Co-doped ZnO nanowires coupled with CuS nanoparticles. *Applied Surface Science* **2018**, *428*, 154-164. DOI: 10.1016/J.APSUSC.2017.09.049.

(50) Xiaohua, Z.; Shuai, S.; Guangli, W.; Caizhu, L.; Zhe, Q.; Xiangdong, L.; Jianguo, Z. Facile synthesis of the flower-like ternary heterostructure of Ag/ZnO encapsulating

carbon spheres with enhanced photocatalytic performance. *Applied Surface Science* **2017**, *406*, 1-11.

(51) Khaki, M. R. D.; Shafeeyan, M. S.; Raman, A. A. A.; Daud, W. M. A. W. Application of doped photocatalysts for organic pollutant degradation-A review. *Journal of Environmental Management* **2017**, *198*, 78-94.

(55) Yang, W.; Zhang, B.; Zhang, Q.; Wang, L.; Song, B.; Ding, Y.; Wong, C. Adjusting the band structure and defects of ZnO quantum dots via tin doping. *RSC Advances* **2017**, *7* (19), 11345-11354.

(80) Oyewo, O. A.; Ramaila, S.; Mavuru, L.; Onwudiwe, D. C. Enhanced photocatalytic degradation of methyl orange using Sn-ZnO/GO nanocomposite. *Journal of Photochemistry and Photobiology* **2022**, *11*. DOI: 10.1016/j.jpap.2022.100131.

(81) Dassault; Systemes. *Biovia Material Studio Castep*. **2020**. https://www.3ds.com/fileadmin/PRODUCTS-SERVICES/BIOVIA/PDF/biovia-material-studio-castep.pdf (accessed 2023 April 08, 2023).

(82) *National Intergrated Cyberinfrastructure System (NICIS) - Centre for High Performance Computing (CHPC)*. **2017**. https://www.chpc.ac.za/index.php/resources). (accessed 2023 April 08, 2023).

(186) Kumar, S.; Kumar, A.; Kumar, A.; Krishnan, V. Nanoscale zinc oxide based heterojunctions as visible light active photocatalysts for hydrogen energy and environmental remediation. *Catalysis Reviews* **2020**, *62* (3), 346-405. DOI: 10.1080/01614940.2019.1684649.

(187) Lee, M.-H.; Peng, Y.-C.; Wu, H.-C. Effects of intrinsic defects on electronic structure and optical properties of Ga-doped ZnO. *Journal of Alloys and Compounds* **2014**, *616*, 122-127.

(220) Borysiewicz, M. A. ZnO as a functional material, a review. *Crystals* **2019**, *9* (10), 505.

(230) Illy, B. N.; Ingham, B.; Toney, M. F.; Nandhakumar, I.; Ryan, M. P. Understanding the selective etching of electrodeposited ZnO nanorods. *Langmuir* **2014**, *30* (46), 14079-14085. DOI: 10.1021/la503765a.

(234) Charifi, Z.; Baaziz, H.; Hussain Reshak, A. Ab-initio investigation of structural, electronic and optical properties for three phases of ZnO compound. *Physica Status Solidi (b)* **2007**, *244* (9), 3154-3167. DOI: 10.1002/pssb.200642471.

(238) Kim, S.-K.; Jeong, S.-Y.; Cho, C.-R. Structural reconstruction of hexagonal to cubic ZnO films on Pt/Ti/SiO_2/Si substrate by annealing. *Applied Physics Letters* **2003**, *82* (4), 562-564.

(263) Lee, Y.-S.; Peng, Y.-C.; Lu, J.-H.; Zhu, Y.-R.; Wu, H.-C. Electronic and optical properties of Ga-doped ZnO. *Thin Solid Films* **2014**, *570*, 464-470. DOI: 10.1016/j.tsf.2014.04.037.

(266) Rezkallah, T.; Djabri, I.; Koç, M. M.; Erkovan, M.; Chumakov, Y.; Chemam, F. Investigation of the electronic and magnetic properties of Mn doped ZnO using the FP-

LAPW method. *Chinese Journal of Physics* **2017**, *55* (4), 1432-1440. DOI: 10.1016/j.cjph.2017.02.021.

(267) Akcan, D.; Ozharar, S.; Ozugurlu, E.; Arda, L. The effects of Co/Cu Co-doped ZnO thin films: An optical study. *Journal of Alloys and Compounds* **2019**, *797*, 253-261. DOI: 10.1016/j.jallcom.2019.05.126.

(268) Ma, Z.; Ren, F.; Ming, X.; Long, Y.; Volinsky, A. A. Cu-doped ZnO electronic structure and optical properties studied by first-principles calculations and experiments. *Materials (Basel)* **2019**, *12* (1). DOI: 10.3390/ma12010196 From NLM PubMed-not-MEDLINE.

(271) Kang, Y.; Yu, F.; Zhang, L.; Wang, W.; Chen, L.; Li, Y. Review of ZnO-based nanomaterials in gas sensors. *Solid State Ionics* **2021**, *360*, 115544. DOI: 10.1016/j.ssi.2020.115544.

(272) Spencer, M. J. S. Gas sensing applications of 1D-nanostructured zinc oxide: Insights from density functional theory calculations. *Progress in Materials Science* **2012**, *57* (3), 437-486. DOI: 10.1016/j.pmatsci.2011.06.001.

(276) Haffad, S.; Cicero, G.; Samah, M. Structural and electronic properties of ZnO nanowires: a theoretical study. *Energy Procedia* **2011**, *10*, 128-137.

(283) Liu, Y.; Xu, H.; Liu, C.; Liu, W. Recent progress in ZnO-based heterojunction ultraviolet light-emitting devices. *Chinese Science Bulletin* **2014**, *59* (12), 1219-1227. DOI: 10.1007/s11434-014-0206-9.

(284) Ma, X.; Wu, Y.; Lv, Y.; Zhu, Y. Correlation effects on lattice relaxation and electronic structure of ZnO within the GGA+ U formalism. *The Journal of Physical Chemistry C* **2013**, *117* (49), 26029-26039.

(287) Harun, K.; Yaakob, M. K.; Taib, M. F. M.; Sahraoui, B.; Ahmad, Z. A.; Mohamad, A. A. Efficient diagnostics of the electronic and optical properties of defective ZnO nanoparticles synthesized using the sol–gel method: experimental and theoretical studies. *Materials Research Express* **2017**, *4* (8), 085908.

(291) Tang, C.; Spencer, M. J. S.; Barnard, A. S. Activity of ZnO polar surfaces: an insight from surface energies. *Physical Chemistry Chemical Physics* **2014**, *16*, 22139-22144. DOI: 10.1039/C4CP03221G.

(296) Marana, N.; Longo, V.; Longo, E.; Martins, J.; Sambrano, J. Electronic and structural properties of the (1010) and (1120) ZnO surfaces. *The Journal of Physical Chemistry A* **2008**, *112* (38), 8958-8963.

(297) Catto, A. C.; Ferrer, M. M.; Lopes, O. F.; Mastelaro, V. R.; Andrés, J.; da Silva, L. F.; Longo, E.; Avansi, W. The role of counter-ions in crystal morphology, surface structure and photocatalytic activity of ZnO crystals grown onto a substrate. *Applied Surface Science* **2020**, *529*, 147057. DOI: 10.1016/j.apsusc.2020.147057.

(298) Ashrafi, A. B. M. A.; Jagadish, C. Review of zincblende ZnO: Stability of metastable ZnO phases. *Journal of Applied Physics* **2007**, *102*, 071101.

(299) Sun, Y.; Chen, L.; Bao, Y.; Zhang, Y.; Wang, J.; Fu, M.; Wu, J.; Ye, D. The applications of morphology controlled ZnO in catalysis. *Catalysts* **2016**, *6* (12), 188. DOI: 10.3390/catal6120188.

(300) Katea, S. N.; Broqvist, P.; Kullgren, J.; Hemmer, E.; Westin, G. Fast, low-cost synthesis of ZnO:Eu nanosponges and the nature of Ln doping in ZnO. *Inorganic Chemistry* **2020**, *59* (11), 7584-7602. DOI: 10.1021/acs.inorgchem.0c00472.

(301) Kamarulzaman, N.; Kasim, M. F.; Rusdi, R. Band gap narrowing and widening of ZnO nanostructures and doped materials. *Nanoscale Research Letters* **2015**, *10*. DOI: 10.1186/s11671-015-1034-9.

(302) Liccardo, L.; Lushaj, E.; Dal Compare, L.; Moretti, E.; Vomiero, A. Nanoscale ZnO/α-Fe_2O_3 heterostructures: Toward efficient and low-cost photoanodes for water splitting. *Small Science* **2022**, *2* (3), 2100104. DOI: 10.1002/smsc.202100104.

(303) Ul Haq, B.; Ahmed, R.; Goumri-Said, S.; Shaari, A.; Afaq, A. Electronic structure engineering of ZnO with the modified Becke–Johnson exchange versus the classical correlation potential approaches. *Phase Transitions* **2013**, *86* (12), 1167-1177. DOI: 10.1080/01411594.2012.755183.

(304) Novikov, S. V.; Kent, A.; Foxon, C. Molecular beam epitaxy as a growth technique for achieving free-standing zinc-blende GaN and wurtzite AlxGa1-xN. *Progress in Crystal Growth and Characterization of Materials* **2017**, *63* (2), 25-39.

(305) Xin, C. S.; Wenxia, F.; Quan, H. H.; Zhenbao, F.; Xu, W. Y. Structural and electronic properties of ZnO under high pressure. *Journal of Alloys and Compounds* **2009**, *476* (1-2), 306-310.

(306) Xu, H.; Zhang, R.; Zhang, X.; Rosa, A.; Frauenheim, T. Structural and electronic properties of ZnO nanotubes from density functional calculations. *Nanotechnology* **2007**, *18* (48), 485713.

(307) Amrani, B.; Chiboub, I.; Hiadsi, S.; Benmessabih, T.; Hamdadou, N. Structural and electronic properties of ZnO under high pressures. *Solid State Communications* **2006**, *137* (7), 395-399.

(308) Zhang, Y.; Fang, D.-Q.; Zhang, S.-L.; Huang, R.; Wen, Y.-H. Structural and electronic properties of ZnO/GaN heterostructured nanowires from first-principles study. *Physical Chemistry Chemical Physics* **2016**, *18* (4), 3097-3102.

(309) Wakhare, S. Y.; Deshpande, M. D. Structural, electronic and optical properties of metalloid element (B, Si, Ge, As, Sb, and Te) doped g-ZnO monolayer: A DFT study. *Journal of Molecular Graphics and Modelling* **2020**, *101*, 107753. DOI: 10.1016/j.jmgm.2020.107753 From NLM Medline.

(310) Gerosa, M.; Bottani, C. E.; Di Valentin, C.; Onida, G.; Pacchioni, G. Accuracy of dielectric-dependent hybrid functionals in the prediction of optoelectronic properties of metal oxide semiconductors: a comprehensive comparison with many-body GW and experiments. *Journal of Physics: Condensed Matter* **2018**, *30* (4), 044003. DOI: 10.1088/1361-648X/aa9725.

(311) Wöll, C. The chemistry and physics of zinc oxide surfaces. *Progress in Surface Science* **2007**, *82* (2), 55-120. DOI: 10.1016/j.progsurf.2006.12.002.

(312) Rohrer, J.; Albe, K. Thermodynamic stability and electronic structure of pristine wurtzite ZnO 0001 inversion domain boundaries. *Physical Review Materials* **2021**, *5* (2), 023601.

(313) Raymand, D.; Jacobsson, T. J.; Hermansson, K.; Edvinsson, T. Investigation of vibrational modes and phonon density of states in ZnO quantum dots. *The Journal of Physical Chemistry C* **2012**, *116* (12), 6893-6901.

(314) Meyer, B.; Marx, D. Density-functional study of the structure and stability of ZnO surfaces. *Physical Review B* **2003**, *67* (3). DOI: 10.1103/physrevb.67.035403.

(315) Blaha, P.; Schwarz, K.; Madsen, G. K.; Kvasnicka, D.; Luitz, J. wien2k. *An augmented plane wave plus local orbitals program for calculating crystal properties* **2001**, *60* (1).

(316) Yu, H.-G. An optimal density functional theory method for GaN and ZnO. *Chemical Physics Letters* **2011**, *512* (4-6), 231-236.

(317) Erhart, P.; Albe, K.; Klein, A. First-principles study of intrinsic point defects in ZnO: Role of band structure, volume relaxation, and finite-size effects. *Physical Review B* **2006**, *73* (20). DOI: 10.1103/PhysRevB.73.205203.

(318) Sowjanya, M.; Shariq, M.; Alajlani, Y.; Pamu, D.; Chowdhury, R.; Jayaganthan, R.; Taqiullah, S. M. Structural and optical properties of pure wurtzite ZnO under uniaxial strain based on first-principles study. *Acta Physica Polonica A* **2020**, *137* (3), 361-367. DOI: 10.12693/APhysPolA.137.361.

(319) Pandey, A.; Scherich, H.; Drabold, D. A. Density functional theory model of amorphous zinc oxide (a-ZnO) and a-X0.375Z0.625O (X= Al, Ga and In). *Journal of Non-Crystalline Solids* **2017**, *455*, 98-101. DOI: 10.1016/j.jnoncrysol.2016.10.035.

(320) Ozugurlu, E. Cd-doped ZnO nanoparticles: An experimental and first-principles DFT studies. *Journal of Alloys and Compounds* **2021**, *861*. DOI: 10.1016/j.jallcom.2021.158620.

(321) Supatutkul, C.; Pramchu, S.; Jaroenjittichai, A. P.; Laosiritaworn, Y. Density functional theory investigation of surface defects in Sn-doped ZnO. *Surface and Coatings Technology* **2016**, *298*, 53-57. DOI: 10.1016/j.surfcoat.2016.04.013.

(322) Spencer, M. J. S.; Wong, K. W. J.; Yarovsky, I. Density functional theory modelling of and surfaces: Structure, properties and adsorption of N_2O. *Materials Chemistry and Physics* **2010**, *119* (3), 505-514. DOI: 10.1016/j.matchemphys.2009.10.005.

(323) Qi, M.; Hou, Q.; Li, Y.; Gu, Y.; Yang, A. Effects and mechanism of (Be/Mg/Ca) doping and point defects (VZn, Hi) on the p-type conductivity of ZnO: A first-principles study. *Solid State Communications* **2022**, *343*. DOI: 10.1016/j.ssc.2022.114653.

(324) Sriram, S.; Lalithambika, K. C.; Thayumanavan, A. Experimental and theoretical investigations of photocatalytic activity of Cu doped ZnO nanoparticles. *Optik* **2017**, *139*, 299-308. DOI: 10.1016/j.ijleo.2017.04.013.

(325) Wen, J.-Q.; Zhang, J.-M.; Chen, G.-X.; Wu, H.; Yang, X. The structural, electronic and optical properties of Nd doped ZnO using first-principles calculations. *Physica E: Low-dimensional Systems and Nanostructures* **2018**, *98*, 168-173. DOI: 10.1016/j.physe.2018.01.002.

(326) Perdew, J. P.; Burke, K.; Ernzerhof, M. Generalized gradient approximation made simple. *Physical Review Letters* **1996**, *77* (18), 3865.

(327) Perdew, J. P.; Burke, K.; Ernzerhof, M. Generalized Gradient Approximation Made Simple. *Physical Review Letters* **1997**, *77* (18), 3865-3868. DOI: 10.1103/PhysRevLett.77.3865.

(328) Perdew, J. P. Unified theory of exchange and correlation beyond the local density approximation. *Electronic Structure of Solids' 91* **1991**, *11*.

(329) Perdew, J. P.; Wang, Y. Accurate and simple analytic representation of the electron-gas correlation energy. *Physical Review B* **1992**, *45* (23), 13244.

(330) Blöchl, P. E. Projector augmented-wave method. *Physical Review B* **1994**, *50* (24), 17953.

(331) Vanderbilt, D. Soft self-consistent pseudopotentials in a generalized eigenvalue formalism. *Physical Review B* **1990**, *41* (11), 7892-7895. DOI: 10.1103/physrevb.41.7892 From NLM PubMed-not-MEDLINE.

(332) Clark, S. J.; Segall, M. D.; Pickard, C. J.; Hasnip, P. J.; Probert, M. I. J.; Refson, K.; Payne, M. C. First principles methods using CASTEP. *Zeitschrift für Kristallographie - Crystalline Materials* **2005**, *220* (5-6), 567-570. DOI: 10.1524/zkri.220.5.567.65075.

(333) Jain, A.; Ong, S. P.; Hautier, G.; Chen, W.; Richards, W. D.; Dacek, S.; Cholia, S.; Gunter, D.; Skinner, D.; Ceder, G.; et al. The materials project: A materials genome approach to accelerating materials innovation. *APL Materials* **2013**, *1* (1), 011002. DOI: 10.1063/1.4812323.

(334) McLeod, J.; Wilks, R.; Skorikov, N.; Finkelstein, L.; Abu-Samak, M.; Kurmaev, E.; Moewes, A. Band gaps and electronic structure of alkaline-earth and post-transition-metal oxides. *Physical Review B* **2010**, *81* (24), 245123.

(335) Ferreira, L. G.; Marques, M.; Teles, L. K. Approximation to density functional theory for the calculation of band gaps of semiconductors. *Physical Review B* **2008**, *78* (12), 125116.

(336) Cococcioni, M.; De Gironcoli, S. Linear response approach to the calculation of the effective interaction parameters in the LDA+ U method. *Physical Review B* **2005**, *71* (3), 035105.

(337) Tsuneda, T.; Hirao, K. Self-interaction corrections in density functional theory. *The Journal of Chemical Physics* **2014**, *140* (18).

(338) Capdevila-Cortada, M.; Łodziana, Z.; López, N. Performance of DFT+ U approaches in the study of catalytic materials. *ACS Catalysis* **2016**, *6* (12), 8370-8379.

(339) Kohn, W.; Sham, L. J. Self-consistent equations including exchange and correlation effects. *Physical Review* **1965**, *140* (4A), A1133.

(340) Deng, X. Y.; Liu, G. H.; Jing, X. P.; Tian, G. S. On-site correlation of p-electron in d10 semiconductor zinc oxide. *International Journal of Quantum Chemistry* **2014**, *114* (7), 468-472.

(341) Farooq, R.; Mahmood, T.; Anwar, A. W.; Abbasi, G. N. First-principles calculation of electronic and optical properties of graphene like ZnO (G-ZnO). *Superlattices and Microstructures* **2016**, *90*, 165-169.

(342) Wen, J.-Q.; Han, Y.-S.; Yang, X.; Zhang, J.-M. Computational research of electronic, optical and magnetic properties of Ce and Nd co-doped ZnO. *Journal Of Physics And Chemistry Of Solids* **2019**, *125*, 90-95.

(343) Zhang, H.; Lu, S.; Xu, W.; Yuan, F. First-principles study of Si atoms adsorbed on ZnO (0001) surface and the effect on electronic and optical properties. *Surface Science* **2014**, *625*, 30-36.

(344) Getman, R. B.; Xu, Y.; Schneider, W. F. Thermodynamics of environment-dependent oxygen chemisorption on Pt(111). *The Journal of Physical Chemistry C* **2008**, *112* (26), 9559-9572. DOI: 10.1021/JP800905A.

(345) Saha, S.; Pal, S.; Sarkar, P.; Rosa, A.; Frauenheim, T. A complete set of self-consistent charge density-functional tight-binding parametrization of zinc chalcogenides (ZnX; X= O, S, Se, and Te). *Journal of Computational Chemistry* **2012**, *33* (12), 1165-1178.

(346) Paleico, M. L.; Behler, J. Global optimization of copper clusters at the ZnO ($10\bar{1}0$) surface using a DFT-based neural network potential and genetic algorithms. *The Journal of Chemical Physics* **2020**, *153* (5).

(347) Kresse, G.; Dulub, O.; Diebold, U. Competing stabilization mechanism for the polar ZnO (0001)-Zn surface. *Physical Review B* **2003**, *68* (24), 245409.

(348) Yao, G. Y.; Fan, G. H.; Zhao, F.; Ma, J. H.; Chen, J.; Zheng, S. W.; Zeng, S. M.; He, L. F.; Zhang, T. In assisted realization of p-type C-doped ZnO: A first-principles study. *Physica B: Condensed Matter* **2012**, *407* (17), 3539-3542. DOI: 10.1016/j.physb.2012.05.019.

(349) Harun, K.; Salleh, N. A.; Deghfel, B.; Yaakob, M. K.; Mohamad, A. A. DFT + U calculations for electronic, structural, and optical properties of ZnO wurtzite structure: A review. *Results in Physics* **2020**, *16*. DOI: 10.1016/j.rinp.2019.102829.

(350) Slassi, A.; Lakouari, N.; Ziat, Y.; Zarhri, Z.; Fakhim Lamrani, A.; Hlil, E. K.; Benyoussef, A. Ab initio study on the electronic, optical and electrical properties of Ti-, Sn- and Zr-doped ZnO. *Solid State Communications* **2015**, *218*, 45-48. DOI: 10.1016/j.ssc.2015.06.010.

(351) Schleife, A.; Fuchs, F.; Furthmüller, J.; Bechstedt, F. First-principles study of ground- and excited-state properties of MgO, ZnO, and CdO polymorphs. *Physical Review B* **2006**, *73*, 245212. DOI: 10.1103/PHYSREVB.73.245212/FIGURES/9/MEDIUM.

(352) Wang, Z.; Wang, F.; Wang, L.; Jia, Y.; Sun, Q. First-principles study of negative thermal expansion in zinc oxide. *Journal of Applied Physics* **2013**, *114* (6), 063508. DOI: 10.1063/1.4817902.

(353) Monkhorst, H. J.; Pack, J. D. Special points for Brillouin-zone integrations. *Physical Review B* **1976**, *13* (12), 5188-5192. DOI: 10.1103/PhysRevB.13.5188.

(354) Sikam, P.; Moontragoon, P.; Jumpatam, J.; Pinitsoontorn, S.; Thongbai, P.; Kamwanna, T. Structural, optical, electronic and magnetic properties of Fe-doped ZnO nanoparticles synthesized by combustion method and first-principle calculation. *Journal of Superconductivity and Novel Magnetism* **2016**, *29* (12), 3155-3166. DOI: 10.1007/s10948-016-3690-0.

(355) Hubbard, C.; O'Connor, B. International centre for diffraction data (ICDD). **2002**.

(356) Morkoc, b. H.; Strite, S.; Gao, G.; Lin, M.; Sverdlov, B.; Burns, M. Large-band-gap SiC, III-V nitride, and II-VI ZnSe-based semiconductor device technologies. *Journal of Applied Physics* **1994**, *76* (3), 1363-1398.

(357) Deinert, J.-C. Zinc oxide surfaces and interfaces: Electronic structure and dynamics of excited states. Technische Universität Berlin, 2016.

(358) Dixit, H.; Saniz, R.; Lamoen, D.; Partoens, B. The quasiparticle band structure of zincblende and rocksalt ZnO. *Journal of Physics: Condensed Matter* **2010**, *22* (12), 125505. DOI: 10.1088/0953-8984/22/12/125505.

(359) Segura, A.; Sans, J.; Manjón, F.; Munoz, A.; Herrera-Cabrera, M. Optical properties and electronic structure of rock-salt ZnO under pressure. *Applied Physics Letters* **2003**, *83* (2), 278-280.

(360) Martínez-Pérez, L.; Muñoz-Aguirre, N.; Muñoz-Aguirre, S.; Zelaya-Angel, O. Nanometric structures of highly oriented zinc blende ZnO thin films. *Materials Letters* **2015**, *139*, 63-65. DOI: 10.1016/j.matlet.2014.10.054.

(361) Polo, V.; Kraka, E.; Cremer, D. Electron correlation and the self-interaction error of density functional theory. *Molecular Physics* **2002**, *100* (11), 1771-1790.

(362) Koster, R. S.; Fang, C. M.; Dijkstra, M.; Van Blaaderen, A.; Van Huis, M. A. Stabilization of rock salt ZnO nanocrystals by low-energy surfaces and Mg additions: A first-principles study. *The Journal of Physical Chemistry C* **2015**, *119* (10), 5648-5656. DOI: 10.1021/jp511503b.

(363) Tran, R.; Xu, Z.; Radhakrishnan, B.; Winston, D.; Sun, W.; Persson, K. A.; Ong, S. P. Surface energies of elemental crystals. *Scientific Data* **2016**, *3* (1), 1-13.

(364) Sun, B.; Yang, X.; Zhao, D.; Zhang, L. First-principles study of adsorption mechanism of NH_3 on different ZnO surfaces on organics photocatalytic degradation purpose. *Computational Materials Science* **2018**, *141*, 133-140. DOI: 10.1016/J.COMMATSCI.2017.09.013.

(365) Kuo, F.-L.; Li, Y.; Solomon, M.; Du, J.; Shepherd, N. D. Workfunction tuning of zinc oxide films by argon sputtering and oxygen plasma: an experimental and computational study. *Journal of Physics D: Applied Physics* **2012**, *45* (6), 065301.

(366) Hofmann, O. T.; Deinert, J.-C.; Xu, Y.; Rinke, P.; Stähler, J.; Wolf, M.; Scheffler, M. Large work function reduction by adsorption of a molecule with a negative electron affinity: Pyridine on ZnO (1010) (101). *The Journal of Chemical Physics* **2013**, *139* (17).

(367) Wei, M.; Li, C.-F.; Deng, X.-R.; Deng, H. Surface work function of transparent conductive ZnO films. *Energy Procedia* **2012**, *16*, 76-80.

(368) Kim, T.; Yoshitake, M.; Yagyu, S.; Nemsak, S.; Nagata, T.; Chikyow, T. XPS study on band alignment at Pt-O-terminated ZnO interface. *Surface and Interface Analysis* **2010**, *42* (10-11), 1528-1531.

(369) Sun, W.; Jha, J. K.; Shepherd, N. D.; Du, J. Interface structures of ZnO/MoO_3 and their effect on workfunction of ZnO surfaces from first principles calculations. *Computational Materials Science* **2018**, *141*, 162-169.

(370) Na, S.-H.; Park, C.-H. First-principles study of the surface of wurtzite ZnO and ZnS - implications for nanostructure formation. *Journal of the Korean Physical Society* **2009**, *54* (9(2)), 867-872. DOI: 10.3938/jkps.54.867.

(371) Jiang, W.; Xia, Y.; Pan, A.; Luo, Y.; Su, Y.; Zhao, S.; Wang, T.; Zhao, L. Facet-dependent gas adsorption selectivity on ZnO: A DFT study. *Chemosensors* **2022**, *10* (10), 436. DOI: 10.3390/chemosensors10100436.

(372) Beltrán, A.; Andrés, J.; Calatayud, M.; Martins, J. B. L. Theoretical study of ZnO (1010) and Cu/ZnO (1010) surfaces. *Chemical Physics Letters* **2001**, *338* (4), 224-230. DOI: 10.1016/S0009-2614(01)00238-X.

(373) Hofmann, O. T.; Deinert, J.-C.; Xu, Y.; Rinke, P.; Stähler, J.; Wolf, M.; Scheffler, M. Large work function reduction by adsorption of a molecule with a negative electron affinity: Pyridine on ZnO. *The Journal of Chemical Physics* **2013**, *139* (17).

(374) Venkatesh, P. S.; Jeganathan, K. Investigations on the morphological evolution of zinc oxide nanostructures and their optical properties. *CrystEngComm* **2014**, *16* (32), 7426-7433.

(375) Muiva, C.; Sathiaraj, S. T.; Maabong, K. Chemical spray pyrolysis path to synthesis of ZnO microsausages from aggregation of elongated double tipped nanoparticles. *Materials Science Forum* **2012**, *706-709*, 2577-2582. DOI: 10.4028/MSF.706-709.2577.

(376) Wróbel, J.; Kurzydłowski, K. J.; Hummer, K.; Kresse, G.; Piechota, J. Calculations of ZnO properties using the Heyd-Scuseria-Ernzerhof screened hybrid density functional. *Physical Review B* **2009**, *80* (15). DOI: 10.1103/PhysRevB.80.155124.

(377) Oshikiri, M.; Aryasetiawan, F. Band gaps and quasiparticle energy calculations on ZnO, ZnS, and ZnSe in the zinc-blende structure by the GW approximation. *Physical Review B* **1999**, *60* (15), 10754-10757. DOI: 10.1103/PhysRevB.60.10754.

(378) Bejar, L.; Medina, A.; Vargas, R.; Herrera, G.; Alfonso, I. Microanalysis of the elemental distribution in particles of $Zn(OH)_2$ obtained by chemical precipitation. *Microscopy and Microanalysis* **2012**, *18* (S2), 1044-1045. DOI: 10.1017/s1431927612007076.

(379) Sokolov, P. S.; Baranov, A. N.; Dobrokhotov, Z. V.; Solozhenko, V. L. Synthesis and thermal stability of cubic ZnO in the salt nanocomposites. *Russian Chemical Bulletin* **2010**, *59* (2), 325-328. DOI: 10.1007/s11172-010-0082-7.

Chapter 4: The investigation of various Sn-doped Zinc Oxide surfaces using Density Functional Theory

4.1 Abstract

Zinc oxide (ZnO) has been widely used as a semiconductor photocatalyst. However, the wide band gap of ZnO impedes its efficiency in visible light in creating electron-hole pairs. Experimental studies have shown that the width of the band gap can be reduced by doping the hexagonal (wurtzite) crystal system of ZnO with tin (Sn). These experimental studies tested the influence of various concentrations of Sn-doping on the reduction of the bandgap of ZnO. However, the band gap reduction and electronic properties at different concentrations of Sn-doping still need further exploration. In this investigation, a Supercell framework was employed to introduce varying percentages (6.25%, 12.50% and 18.75%) of Sn into the hexagonal crystal system of ZnO. The resulting Sn-doped ZnO was optimised, and various electronic properties, including the band gap, were calculated using density functional theory (DFT) based calculations. Additionally, different surfaces were cut from the optimised Sn-doped ZnO crystal systems, and their calculated surface energies were employed to visualise their crystal morphologies using the WULFF program. This investigation presents an innovative method to investigate the influence of Sn-doping on the electronic properties and morphology of Sn-doped ZnO, which could lead to improved photocatalytic performance of ZnO.

4.2 Introduction

Over the past decade, zinc oxide (ZnO) as a semiconductor photocatalyst has garnered considerable interest[27] due to its low cost,[13] non-toxicity,[25] and photochemical and thermal stability.[26] These properties make it an appealing solution for environmental sustainability.[31] However, the photocatalytic performance of ZnO is limited because it primarily responds to ultraviolet (UV) light ($\lambda < 390$ nm) and is less effective with visible light, which constitutes a large portion of the solar spectrum.[49, 50] This limitation is due to the wide band gap of ZnO, which restricts its absorption to UV light, and the high recombination rates of electron-hole (e^-/h^+) pairs, reducing its efficiency.

Reducing the band gap[262] (3.37eV)[321] of ZnO is a key strategy for improving its visible light photocatalytic performance.[325] A prominent method for improving photocatalytic performance in visible light is doping.

Doping is effective for band gap engineering as it introduces trap states (localised energy levels), narrowing the band gap and extending light absorption into the visible spectrum[380]. These trap states can capture and hold charge carriers (electrons or holes). Thus, modifying the band structure, reducing recombination, and promoting charge carrier migration enhance efficiency.[66, 381] However, excessive doping can hinder efficiency by introducing recombination centres.[382]

While doping is highly effective and widely researched, the best approach depends on the specific application and desired properties of the doped ZnO material, as it allows for choosing different dopants to achieve specific electronic and optical properties, making it versatile.[383]

Doping could be done via quantum dot sensitisation,[384] alloying,[385] surface modification,[386] nanostructuring,[387] with transition metals,[31] non-metals,[388] and codoping.[389, 390] Doping with quantum dot sensitisation involves using quantum dots like cadmium sulphide (CdS) and lead sulphide (PbS) to extend the absorption spectrum of ZnO into the visible range.[384] Alloying ZnO with other semiconductors, such as magnesium oxide (MgO) or cadmium oxide (CdO), can adjust the band gap by combining different electronic properties. Surface modification with organic molecules, polymers, or nanomaterials can change surface states and the electronic structure, enhancing photocatalytic activity.[386, 391] Nanostructuring ZnO into nanorods, nanowires, and nanoparticles introduces quantum confinement effects that alter the band gap and improve light absorption and charge carrier dynamics.[229, 230, 392]

Doping with transition metals (such as copper (Cu), iron (Fe), manganese (Mn), cobalt (Co), or nickel (Ni)) or non-metals (such as nitrogen, carbon, sulphur, phosphorus)[189, 388] introduces trap states within the band gap,[31] narrowing it and enhancing photocatalytic activity by improving electron-hole separation and promoting charge carrier migration. Codoping with metals and non-metals can more effectively modify the electronic structure, resulting in better band gap narrowing and enhanced properties.[390]

However, in this study the focus will be on transition metal doping. The introduction of transition metal dopants with distinct oxidation states into the ZnO lattice alters the electronic structure of ZnO, influencing the band structure, charge mobility, and surface reactivity.[350] This modification

can broaden the absorption range of light, improving light utilisation efficiency in photocatalysis. Table 4-1 highlights how various transition metal dopants affect the band gap of ZnO.

Table 4-1: ***Summary of transition metal dopants, doping percentage, temperature of doping, initial (before doping) and final (after doping) band gaps, and band gap differences.***

Dopant	Doping (%)	Temp. (°C)	Method	Initial band gap (eV)	Final band gap (eV)	Band gap diff. (eV)	Ref.
Mg	7.00	600.00	Experimental	3.34	3.21	0.13	[393]
Ti	5.40	300.00	Experimental	3.30	3.14	0.16	[394]
Mn	1.00	300.00	Experimental	3.33	3.32	0.01	[301]
Cu	1.00	300.00	Experimental	3.33	3.29	0.04	[301]
Cu	2.15	600.00	Experimental	3.34	3.15	0.19	[393]
Zr	2.00	400.00	Experimental	3.29	3.27	0.02	[395]
Sn	3.00	25.00	Experimental	3.18	2.45	0.63	[396]
Sn	5.00	300.00	Experimental	3.34	3.05	0.29	[393]

Note: Temp. refers to the temperature at which the doping process was carried out, Initial band gap refers to the band gap energy of ZnO before doping; Final band gap indicates the band gap energy of ZnO after doping; and the Band gap diff. refers to the energy difference between the Initial band gap and the Final band gap.

Dopants with a similar oxidation state to Zn^{2+} can substitute Zn without causing charge imbalances, while those with different oxidation states introduce compensating defects like oxygen vacancies, affecting the band gap. For example, Cu^{2+} reduces the band gap by creating acceptor states, with a greater reduction at higher doping levels (e.g., 0.04 eV for 1% Cu versus 0.19 eV for 2.15% Cu). In contrast, Sn^{4+} significantly lowers the band gap, especially at higher concentrations, likely due to deep-level states acting as electron traps.

The dopant's ionic radius compared to Zn^{2+} (0.74 Å) also influences lattice distortion and band gap alteration. Larger or smaller radii can cause lattice strain, impacting the band structure. For instance, Mg^{2+} (0.72 Å) causes minimal lattice distortion and a slight band gap reduction (0.13 eV), while Zr^{2+} (0.86 Å) results in a minor change (0.02 eV), suggesting the lattice accommodates this mismatch. Sn^{4+} (0.83 Å) causes significant band gap reduction, particularly at low temperatures, indicating substantial lattice strain.

Doping temperature and methods further affect dopant incorporation and defect formation. Higher temperatures typically enhance solubility but may lead to secondary phases. For example, Cu

doping at 600°C shows a more significant band gap reduction (0.19 eV) than at 300°C (0.04 eV), indicating higher temperatures promote greater incorporation or different defect states. Sn doping at 25°C results in a drastic band gap reduction compared to 300°C, suggesting low-temperature doping introduces mid-gap states that lower the band gap.

The electronic configuration of dopants is also critical. Transition metals with partially filled d-orbitals can introduce localised states within the band gap, affecting optical and electronic properties. For instance, Mn^{2+}, with a d^5 configuration, minimally affects the band gap (0.01 eV) due to limited interaction with the conduction band. Ti^{4+}, with a d^0 configuration, reduces the band gap by 0.16 eV, likely due to empty d-states below the conduction band.

Dopants such as Ti,[394, 397] Zr[390, 395] and Sn[55, 396] have demonstrated intriguing optoelectronic features, such as enhanced light absorption,[398] improved charge carrier mobility,[399] increased conductivity[350] and modified band gap energies[400] due to the distinctive oxidation numbers of Ti^{4+}, Zr^{4+}, Sn^{4+} and Sn^{2+} ions in contrast to the native Zn^{2+} ions.

Of all the transition metals listed in Table 4-1, Sn^{2+} has attracted the most interest due to its significant influence on semiconductor properties, which shows that Sn^{2+} achieves the most substantial reduction of the band gap. Specifically, Sn at 3% and 25°C lowers the band gap by 0.63 eV, while 5% Sn at 300°C reduces it by 0.29 eV. When Sn^{2+} replaces Zn^{2+} in the ZnO crystal lattice, even though both ions are divalent and do not introduce additional electrons directly, the presence of Sn^{2+} can still impact the material's electronic properties. Sn^{2+} doping can alter the defect chemistry of the ZnO lattice, potentially leading to the formation of oxygen vacancies or other defect sites. These defects can act as trap states or donor levels within the band gap. The creation of such states can affect carrier concentration and mobility. In this case, Sn^{2+} doping might indirectly increase the number of free electrons by creating additional oxygen vacancies, which serve as donors that contribute extra electrons to the conduction band. These free electrons enhance the n-type semiconductor[401] behaviour of Sn-doped ZnO, where electrons are the majority charge carriers. This property is crucial in applications such as electronics, optoelectronics, and semiconductor device fabrication, where controlling carrier type and concentration is vital for performance.[70, 73, 74] Additionally, n-type semiconductor behaviour is crucial for ZnO's application in photocatalysis because it allows for efficient charge separation and transport, enhancing the material's photocatalytic activity.[71] Therefore, understanding Sn doping in ZnO enables

researchers to customise the material's properties for specific applications requiring n-type conductivity.

Although substantial theoretical research has explored the structural, optical, and electronic properties of Sn-doped ZnO,[70, 73, 74] limited research has been done explicitly using DFT methods to study the photocatalytic properties of Sn-doped ZnO.

4.3 Computational method

4.3.1 Supercell

The Supercell program developed by Okhotnikov *et al.*[83] was utilised to obtain unique bulk structures of ZnO with various percentages (6.25%, 12.50% and 18.75%) of Sn doping. This process was accomplished by importing the hexagonal unit cell of undoped ZnO, comprising two O atoms and two Zn atoms, into the Supercell program. The dimensions of the imported unit cell were doubled in all three Cartesian coordinate directions, resulting in a 2×2×2 ZnO bulk structure (simulation cell) comprising of 32 atoms. Although a larger simulation cell size, such as 3×3×3, would have provided doping percentages closer to the intended values,[402] it would have been computationally expensive. Therefore, a 2×2×2 simulation cell size was employed to enhance data accuracy while still managing the computational cost.

Subsequently, the Supercell program generated various Sn-doped ZnO configurations (bulk structures, $Zn_{x-y}Sn_yO_x$) for the various percentages of Sn. These configurations were achieved by substituting a certain number of Zn atoms in the bulk structures with Sn atoms to attain the desired doping percentage. For example, the 6.25% Sn-doped ZnO had a composition of $Zn_{15}SnO_{16}$, the 12.50% Sn-doped ZnO had a composition of $Zn_{14}Sn_2O_{16}$, and the 18.75% Sn-doped ZnO had a composition of $Zn_{13}Sn_3O_{16}$.

Structurally equivalent configurations were eliminated by the Supercell program, leaving unique configurations. Further information about the simulation process can be found in Appendix A4 Table (A4-1) - (A4-3).

4.3.2 Computational details

The DFT-based calculations were conducted using the Cambridge Serial Total Energy Package (CASTEP) module[332] of the Biovia Materials Studios package (MS 2020).[81] All the calculations were conducted on the Lengau cluster of the Centre of High-Performance Computing (CHPC) in

South Africa.[82] The exchange-correlation functional defined by the general gradient approximation (GGA)[326] developed by Perdew-Burke-Ernzerhof (PBE)[326, 327] was used. The Brillouin-Zone (BZ) integration was performed in the reciprocal space using a Monkhorst-Pack k-point grid[353] of 11×11×11. The electron-ion interactions were characterised using the ultrasoft pseudopotentials (USP) method. The wave functions of the valence electrons were expanded using a plane-wave basis set with an energy cut-off of 400 eV, which ensured that Pulay stress was avoided. Due to the absence of a magnetic moment in the Sn-doped ZnO system, the calculations did not account for spin polarisation effects. To ensure accurate results, convergence tolerances for energy, force, stress, and displacement were set at 1.0 x 10^{-5} eV/atom, 0.03 eV/Å, 0.05 GPa, and 1.0 x 10^{-3} Å, respectively.

4.3.3 Bulk structure optimisation

The unique configurations for $Zn_{15}SnO_{16}$, $Zn_{14}Sn_2O_{16}$ and $Zn_{13}Sn_3O_{16}$ bulk structures were exported from the Supercell program into CASTEP and relaxed to obtain the most stable geometry. The lattice parameters, cell angles, volume and density of the $Zn_{15}SnO_{16}$ and $Zn_{14}Sn_2O_{16}$ bulk structures were compared to literature values. This comparison was done to validate the Sn-doped ZnO model. The model was then applied to the $Zn_{13}Sn_3O_{16}$ bulk structures. The influence of percentage doping on volume and density was investigated.

Following the geometry optimisation, the bulk structures that exhibited the highest stability among the various doping percentages were selected to determine the bulk structure properties.

4.3.4 Bulk structure properties

4.3.4.1 X-ray diffraction (XRD)

Following geometry optimisation, the XRD patterns of the Sn-doped ZnO bulk structures were calculated using the Reflex tools within the Biovia MS 2020 software package.[81] The XRD patterns were calculated by applying a copper source Cu Kα (λ = 1.541 Å) for the incident radiation and setting 2-Theta limits between 5° and 90°. The XRD patterns were determined by calculating the positions and intensities of the diffraction peaks based on factors such as atom placements within the bulk structure, the X-ray wavelength used, and the geometry of the diffraction process. To confirm the accuracy of the DFT calculations, the computed XRD pattern was compared to an experimental XRD pattern.[80] Additionally, the XRD patterns of the Sn-doped ZnO bulk structures

were compared to the XRD pattern of the ZnO bulk structure to determine if Sn-doping influenced the XRD pattern.

4.3.4.2 Electronic properties

The optimised bulk structures were subject to a single-point energy calculation at the same settings given in section 4.3.2 to calculate electronic properties, such as density of states (DOS), d-band centre, and the band structure. These electronic properties were compared to those of the undoped ZnO bulk structure to assess the disparities or similarities in the electronic characteristics between the systems.

4.3.4.2.1 Density of states (DOS)

The total density of states (DOS) in the Sn-doped ZnO bulk structures was calculated by summing the occupation probabilities of electronic states across all k-points and energy levels, reflecting contributions from all angular momentum projections (s, p, d, f) on all atoms. The partial density of states (pDOS) was obtained by summing occupation probabilities for specific energy levels across all k-points, highlighting the contributions from individual atomic orbitals. The arrangement of energy levels in the valence band (VB) and conduction band (CB) positions the Fermi level at zero energy. The pDOS was further used to analyse the d-band of Sn-doped ZnO bulk structures, focusing on the d-orbitals' contributions.

4.3.4.2.2 d-band centre

The d-band centre is critical in determining a material's catalytic activity. A d-band centre closer to the Fermi level (i.e., higher) implies that the d-electrons are less tightly bound, influencing the material's interaction with adsorbates and its overall electronic properties. Generally, stronger interactions with adsorbates indicate higher reactivity. To determine the position of the d-band centre in the Sn-doped ZnO bulk structures, integrations over the energy spectrum of the d-band within the pDOS were conducted. The d-band centre is positioned relative to either the valence band maximum (VBM) or the Fermi level.

4.3.4.2.3 Band gap

This study focused on understanding how the band structure of Sn-doped ZnO bulk structures changes with varying Sn content. Energy levels, representing potential states for electrons, were calculated by solving the Kohn-Sham equations, resulting in energy eigenvalues for various points

in the BZ. The BZ contains unique k-points (wave vectors) describing the crystal's periodic structure. Energy bands that visually represent the band structure and demonstrate how electron energy varies with momentum were generated by plotting energy eigenvalues against k-points. The band structure diagram highlights the valence band (highest energy levels occupied by electrons) and the conduction band (unoccupied energy levels where electrons can move freely). The band gap is a fundamental property of semiconductors that represents the energy difference between the valence and conduction band.[403] Electrons must acquire this amount of energy to transition from the valence band to the conduction band.

The calculated band gap values were compared to literature values. However, it is known that the DFT/GGA method tends to underestimate band gap values[319, 351] in transition metal oxides. The DFT/GGA underestimation stems from the deficiencies to account for on-site electron-electron interaction, particularly in strongly correlated systems such as ZnO.[404]

The limitation of the DFT/GGA method was addressed by adding Hubbard corrections (U_d and U_p) to the calculation method.[335, 405, 404] Selecting the right U_d value is critical for accurately predicting electronic properties like band gaps. Additionally, an over-hybridisation with the anion p valence states occurs, resulting in a smaller band gap due to a strong p-d coupling, leading to the addition of the U_p value.[284] While this method doesn't eliminate the underestimation issue, it does enhance the accuracy of band gap predictions.

For Sn-doped ZnO bulk structures, there is no universal upper limit for the U values. Lee[263] achieved a band gap value of 3.37 eV, which is in good agreement with the experimental band gap of undoped ZnO,[210, 290] by employing U values of $U_{d\text{-}Zn}$ = 10 eV and $U_{p\text{-}O}$ = 7 eV.

The Sn-doped ZnO bulk structures were optimised by incorporating these U values into the DFT/GGA calculation. The U correct band gap values were compared to literature values.

4.3.5 Surface model construction and optimisation

4.3.5.1 Construction

To create various surfaces for analysis, the optimised Sn-doped ZnO bulk structures for each percentage doping were cut along the (100), (002), (101), (102), (210), (103), (112), (200), and (201) Miller planes, identified from experimental X-ray diffraction peaks,[406] using the Visualiser tool in the Biovia MS2020 package.[81] Some of these slabs were metal-terminated (MT), while

others were oxygen-terminated (OT). The selection of these cuts ensured consistency and comparability with the undoped ZnO structure. Depending on the specific cut made, the slab models were composed of two to eight layers in thickness, resulting in a total of 16 to 128 atoms per slab. The surfaces consisted of a material slab with periodic boundary conditions and a vacuum slab in the orthogonal direction.

The \a\ x \b\ dimensions ranging from 1 Å to 2 Å lie within the plane of the surface, where periodic boundary conditions create an infinite surface by seamlessly connecting the slab's edges to its periodic images. This infinite surface minimises edge effects and ensures continuous interactions, which are essential for accurately modelling properties like electronic structure, surface energy, and catalytic activity. To ensure the accuracy of the results and prevent undesired interactions between the repeating layers in the orthogonal \c\ direction, a vacuum slab of 15 Å was found to be appropriate.[321]

4.3.5.2 Optimisation

Geometry optimisation calculations were performed on surface slabs derived from Sn-doped ZnO bulk structures at various doping percentages to investigate the influence of Sn doping on ZnO surfaces. The computational settings, including a 7×7×1 k-point grid based on the Monkhorst-Pack grid[46] and a cut-off energy of 400 eV, were consistent with those used for bulk structure optimisation, as outlined in Section 4.3.2. These settings ensured accurate BZ sampling and reliable convergence.

During optimisation, the lower layers of the surface slabs were fixed to preserve the intended shape and dimensions, ensuring that the Sn-doped ZnO surfaces accurately represented their physical and chemical properties. This static preservation is essential, as surface slabs represent exposed fixed Miller planes, and maintaining their structure is crucial for studying surface properties and reactions. The calculations provided the total energy and the number of ions in the cell for each surface slab, maintaining consistency with the methodology applied to the bulk structures.

4.3.5.3 Surface properties

After optimisation, surface properties were calculated, namely, surface energies (γ), crystal morphology and work function (Φ) for the Sn-doped ZnO surface slabs. Surface energies are vital for understanding the stability, reactivity and morphology of these surfaces. At the same time, the work function is key to understanding electron emission and the overall electronic behaviour of

the material. These properties were evaluated to investigate the influence of Sn-doping percentage, Miller planes, and surface terminations on the stability, reactivity and morphology of the crystal systems.

4.3.5.3.1 Surface energies

Surface energy (γ) is an important parameter for characterising the thermodynamic stability of crystal surfaces. A calculation method involving the final energies of the optimised slabs and bulk structure was employed to determine the surface energies of the surfaces. The equation used to estimate the surface energies is as follows:

$$\gamma_r = \frac{E^{DFT}{}_{relaxed\ slab} - n \times E^{DFT}{}_{bulk}}{2A_{slab}} \quad \text{.....(4.1)}$$

Here, γ_r represents the surface energies calculated after relaxation, with $E^{DFT}{}_{relaxed\ slab}$ and $E^{DFT}{}_{bulk}$, denoting the DFT energies of the relaxed slab and bulk, respectively. $2A_{slab}$ represents the surface area multiplied by two, accounting for both upper and lower surfaces of the bulk. The ratio of the number of Sn-doped ZnO atoms in the slab to the number in the bulk is represented by n.

Surface energy measures the excess energy at a material's surface compared to its bulk. The calculated surface energy values were compared to those of undoped ZnO surfaces to assess the influence of Sn doping. Understanding the surface energy is essential for assessing how Sn doping influences the overall crystal morphology.

4.3.5.3.2 Crystal morphology

The Wulff construction[3] method was employed, using the calculated surface energies of surfaces with different Miller planes and different termination, to determine the equilibrium crystal morphology of Sn-doped ZnO systems. This approach involved using the Wulffmaker software[2] to generate the Wulff morphology[3].

The process included the following steps: identifying the lattice shape, lattice parameters, and point group of the Sn-doped ZnO crystal; determining the number of Miller plane families associated with the desired shape; computing or obtaining the surface energies for the distinct Miller planes of Sn-doped ZnO; inputting the surface energies and crystallographic information into the Wulffmaker software;[2] and constructing the Wulff morphology.

The Wulff morphology graphically represents the stability of a crystal system by showing each surface slab's size in direct proportion to its surface energy. In a Wulff morphology, Miller planes with lower surface energies appear larger in size, indicating greater stability. In comparison, those with higher surface energies are smaller in size or may disappear, reflecting lesser stability. Surface energy affects how different Miller planes grow or shrink over time. This proportional relationship minimises the crystal's total surface energy, leading to a stable configuration. This approach ensures that the resulting equilibrium morphology accurately reflects the relative stabilities of different Miller planes, which is crucial for applications requiring precise control of crystal morphology.

4.3.5.3.3 Work function

The work function measures the minimum energy required to remove an electron from the surface of Sn-doped ZnO into the vacuum. The work function (Φ) is computed as the difference between the vacuum level (E_{vac}) and the Fermi level (E_f), expressed as $\Phi = E_{vac} - E_f$.

For Sn-doped ZnO, a lower work function can enhance electron emission, which is beneficial for photocatalysis as it aids in generating reactive species and improves charge separation, which is essential for effective catalysis. Additionally, the work function influences the interaction of ZnO with adsorbed molecules, impacting surface reactivity and charge distribution, which is significant for sensors and catalysis applications.

4.4 Results and discussion

4.4.1 Supercell

A variety of unique configurations at different doping percentages for Sn-doped ZnO bulk structures (see Appendix A4, Table A4-1 to A4-3) were generated using the Supercell program[83].

4.4.2 Bulk structure optimisation

Table 4-2 presents the results of the bulk structure optimisation, such as lattice parameters, cell angles, volume, density, and final energies.

Due to the expansion of the unit cells into 2×2×2 bulk structures, it was necessary to divide the ZnO bulk lattice parameters in Table 4-2 by two. This division allows for comparison with the optimised Sn-doped ZnO bulk structures documented in the literature. The values in Table 4-2

show a close agreement between the lattice parameters and cell angles obtained in this study and those reported in the literature. The maximum percentage deviations observed at 6.25% and 12.50% doping percentages were only 3.65% and 1.57%, respectively, supporting the validity of the Sn-doped ZnO models. It is also observed that as the Sn^{2+} doping percentage increased, the volume, density, and final energy of the system increased. (see Table 4-2).

Introducing Sn^{2+}, with its larger atomic radius of 1.187 Å compared to 0.654 Å for Zn^{2+}, into the ZnO lattice led to volume expansion with percentage increases of 3.40% at 6.25% doping, 6.60% at 12.50%, and 9.80% at 18.75% doping percentages. The larger Sn^{2+} ions induced lattice strain and distortion, requiring the lattice to adjust to maintain stability, resulting in a greater volume increase with increased doping. The density of the material increased as Sn added mass, with percentage increases of 0.60% at 6.25% doping, 1.50% at 12.50%, and 2.30% at 18.75% doping percentages.

Table 4-2: The cell parameters obtained from various doping percentages of the optimised Sn-doped ZnO bulk structures.

Doping (%)	Description	Sn-doped ZnO bulks	Lattice parameters (Å)			Cell angles (°)			Cell volume (Å^3)	Density (g/cm^3)	Final energy (eV)
			a	b	c	α	β	γ			
0	**This work**	$Zn_{16}O_{16}$	6.597	6.597	10.612	89.999	90.000	120.259	398.892	5.420	**-34357.558**
	This work/2		3.299	3.299	5.306	-	-	-			
	Lit. values		3.298[2]	3.298[5]	5.205[8]	90.000[10]	90.000[13]	120.000[17]			
	Deviation (%)		0.030	0.030	1.940	0.001	0	0.216			
6.25	**This work**	$Zn_{15}SnO_{16}$	6.623	6.623	10.900	90.051	89.949	120.341	412.621	5.454	**-32741.736**
	This work/2		3.312	3.312	5.450	-	-	-			
	Lit. valucs[20]		3.348	3.348	5.380	90.100	89.900	121.000			
	Deviation (%)		1.075	1.075	1.301	0.054	0.055	0.545			
12.50	**This work**	$Zn_{14}Sn_2O_{16}$ configuration 1	6.623	6.695	11.041	90.118	89.336	120.692	420.937	5.557	-31125.809
	This work/2		3.312	3.348	5.521	-	-	-			
	Lit. values[24]		3.371	3.371	5.346	90.200	89.900	121.300			
	Deviation (%)		1.750	0.682	3.273	0.091	0.627	0.501			
	This work	$Zn_{14}Sn_2O_{16}$ configuration 2	6.709	6.706	10.946	90.035	89.926	120.360	425.020	5.504	**-31126.402**
	This work/2		3.355	3.353	5.473	-	-	-			
	Lit. values[13]		3.371	3.371	5.346	90.200	89.900	121.300			
	Deviation (%)		0.475	0.534	2.376	0.183	0.029	0.775			
	This work	$Zn_{14}Sn_2O_{16}$ configuration 3	6.672	6.659	11.081	90.582	89.860	120.614	423.652	5.521	-31125.494
	This work/2		3.336	3.330	5.541	-	-	-			
	Lit. values[31]		3.371	3.371	5.346	90.200	89.900	121.300			
	Deviation (%)		1.038	1.216	3.648	0.424	0.045	0.566			
	This work	$Zn_{14}Sn_2O_{16}$ configuration 4	6.664	6.664	11.032	90.045	89.955	120.388	422.621	5.535	-31126.054
	This work/2		3.332	3.332	5.516	-	-	-			
	Lit. values[28]		3.371	3.371	5.346	90.200	89.900	121.300			
	Deviation (%)		1.157	1.157	3.180	0.172	0.061	0.752			
	This work	$Zn_{14}Sn_2O_{16}$ configuration 5	6.711	6.592	11.032	90.407	91.312	120.157	421.756	5.546	-31125.655
	This work/2		3.356	3.296	5.516	-	-	-			
	Lit. values[29]		3.371	3.371	5.346	90.200	89.900	121.300			
	Deviation (%)		0.445	2.225	3.180	0.230	1.571	0.942			

Table 4-2 (continue): The cell parameters obtained from various doping percentages of the optimised Sn-doped ZnO bulk structures.

Doping (%)	Description	Sn-doped ZnO bulks	Lattice parameters (Å)			Cell angles (°)			Cell volume (Å^3)	Density (g/cm^3)	Final energy (eV)
			a	b	c	α	β	ɣ			
		$Zn_{13}Sn_3O_{16}$									
	This work	configuration 1	6.706	6.838	11.102	89.991	89.971	121.124	435.730	5.572	-29510.500
	This work	configuration 2	6.645	6.706	11.348	90.530	88.655	120.737	434.494	5.587	-29510.176
	This work	configuration 3	6.785	6.658	11.190	90.935	91.337	120.514	435.150	5.579	-29509.962
	This work	configuration 4	6.698	6.652	11.270	89.925	92.180	120.207	433.576	5.599	-29510.075
	This work	configuration 5	6.633	6.741	11.345	90.024	90.761	120.854	435.460	5.575	-29510.192
18.75	**This work**	configuration 6	6.735	6.735	11.196	90.015	89.985	120.412	437.960	5.543	**-29510.725**
	This work	configuration 7	6.671	6.718	11.292	90.058	89.390	120.599	435.592	5.573	-29509.947
	This work	configuration 8	6.678	6.719	11.249	88.393	89.905	120.261	435.709	5.572	-29509.983
	This work	configuration 9	6.598	6.703	11.279	88.592	91.005	119.973	432.006	5.620	-29510.081
	This work	configuration 10	6.645	6.669	11.339	91.207	89.749	120.256	433.934	5.595	-29510.276
	This work	configuration 11	6.680	6.680	11.335	90.426	89.574	120.453	435.954	5.569	-29509.922
	This work	configuration 12	6.688	6.688	11.308	89.786	90.214	119.979	438.083	5.542	-29509.606

Note: The lowest final energies for each percentage are indicated in bold.

The increase in mass generally outweighs the volume expansion, contributing to a higher overall density. Moreover, the presence of Sn^{2+} ions induced lattice strain due to the mismatch in ionic radii between Sn^{2+} and Zn^{2+}, leading to potential defect formation, such as vacancies and interstitials. These defects, and the altered electronic structure contribute to the system's instability, highlighting the complexity of these effects in semiconductors.

For the case of 6.25% Sn-doping, a single unique configuration was identified and deemed suitable for further analysis. The analysis of 12.50% Sn-doped ZnO bulk structures, as shown in Table 4-2, unequivocally indicates that configuration 2 displayed the lowest final energy among the five bulk structures examined. This observation strongly implied that configuration 2 possessed the highest level of stability compared to the other configurations investigated for 12.50% Sn-doped ZnO bulk structures. Similarly, during the examination of the 18.75% Sn-doped ZnO bulk structures listed in Table 4-2, it was noted that configuration 6 exhibited the lowest final energy among the twelve bulk structures analysed. As a result, configuration 6 was identified as the most stable bulk structure among the configurations investigated. Overall, these findings strongly indicate that unique configurations characterised by the lowest final energies correspond to structures with higher stability.

Figure 4-1 illustrates the configurations of undoped ZnO and the most stable Sn-doped ZnO bulk structures identified for the different percentage doping after optimisation.

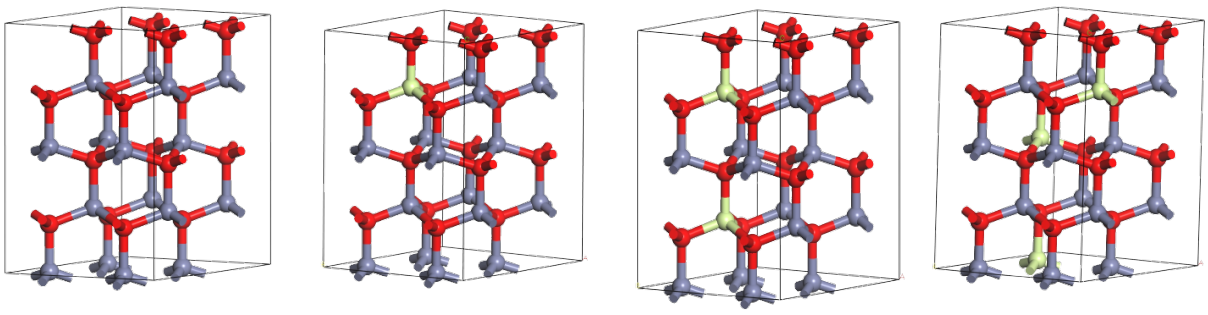

(a) (b) (c) (d)

Figure 4-1: ***The optimised bulk structures of (a) undoped ZnO (0% doping) and the three most stable configurations of Sn-doped ZnO, namely, (b) 6.25%, (c) 12.50% and (d) 18.75%. (Grey, red, and yellow represent Zn, O and Sn atoms, respectively).***

4.4.3 Bulk structure properties

4.4.3.1 X-ray diffraction (XRD)

Figure 4-2 presents calculated XRD patterns of both the ZnO and Sn-doped ZnO bulk structures.

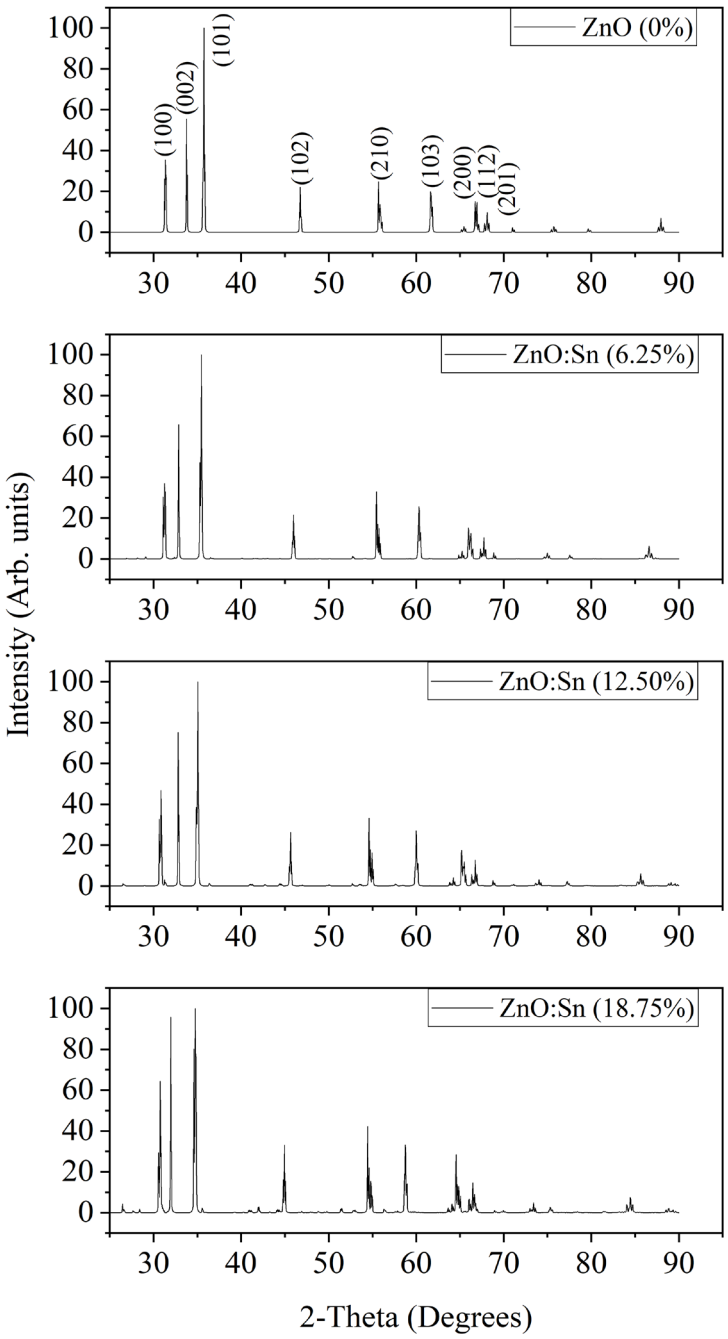

Figure 4-2: ***The comparison of intensity versus 2-Theta in XRD for optimised Sn-doped ZnO bulk structures at various doping percentages: (a) 0%, (b) 6.25%, (c) 12.50%, (d) 18.75%.***

The peaks identified in all the XRD patterns in Figure 4-2, along with the corresponding Miller planes, confirmed the presence of ZnO in the all bulk structures.[406] The structures showcased a polycrystalline nature, indicated by distinct and well-defined diffraction peaks in their XRD patterns, denoting a robust crystalline hexagonal wurtzite structure. This analysis confirmed the successful incorporation of Sn into the ZnO lattice, evidenced by shifts in peak intensities. The increased intensity of the (002) peak with higher Sn doping levels indicated that Sn atoms were

substituting Zn within the lattice rather than forming separate SnO or SnO_2 phases. This enhancement in the (002) peak also reflected improved crystallinity along this plane, likely due to Sn atoms favouring specific substitution sites in the ZnO lattice. By replacing Zn atoms at these preferred positions, Sn promoted a more ordered and stable structure along the (002) plane, reducing defects and structural irregularities in this direction. This improved atomic arrangement enhanced Sn-doped ZnO's electronic properties, as the alignment of atoms facilitated better electron mobility within the lattice, making Sn-doped ZnO particularly suitable for applications such as photocatalysis.

The data presented in Table 4-3, which includes the diffraction angle (2θ), corresponding intensity, and identification of (hkl) planes, reveals significant trends in ZnO and Sn-doped ZnO bulk structures. In the undoped ZnO (0%), the (101) peak was predominant, as demonstrated by a notably strong peak that persists even as the doping level increases.

Table 4-3: ***Calculated X-ray diffraction values obtained from various doping percentages of the optimised Sn-doped ZnO bulk structures.***

	0%		**6.25%**		**12.50%**		**18.75%**	
hkl	**2θ(°)**	**Intensity**	**2θ(°)**	**Intensity**	**2θ(°)**	**Intensity**	**2θ(°)**	**Intensity**
(100)	31.4	35.4	31.3	37.0	30.9	46.8	30.8	64.4
(002)	33.8	55.4	32.9	65.7	32.8	75.2	32.0	95.7
(101)	35.8	100.0	35.5	100.0	35.1	100.0	34.8	100.0
(102)	46.8	22.1	46.0	21.7	45.7	26.3	45.0	33.1
(210)	55.7	24.7	55.5	33.0	54.6	33.2	54.5	42.3
(103)	61.7	19.9	60.3	25.6	60.0	27.0	58.8	33.1
(200)	66.8	15.1	66.0	15.3	65.2	17.5	64.6	28.3
(112)	67.0	14.6	67.8	10.5	66.8	12.6	66.5	14.6
(201)	68.1	9.6	68.9	3.2	68.8	2.6	70.0	1.0

However, with the introduction of Sn doping, the preferred peak shifted to the (002) Miller plane, observed through increased intensities at diffraction angles of 32.9°, 32.8°, and 32.0°. Additionally, other peaks such as (100), (102), (210), and (103) became more prominent with increasing percentage Sn. These observations are consistent with similar findings reported in existing literature,[294, 407] as detailed in Appendix A4 Figure A4-1.

Based on the data provided in Table 4-3 and referencing Figure 4-2, a minor shift towards the left in the 2θ value was detected in the Sn-doped ZnO bulk structures compared to the undoped ZnO structure. This change in the peak position was attributed to the increase in lattice parameters, resulting from the larger radius of Sn^{2+} ions (1.187 Å) in contrast to Zn^{2+} ions (0.654 Å), leading to a modification in the cell size of the hexagonal structure.

4.4.3.2 Electronic properties

4.4.3.2.1 Density of states (DOS)

As illustrated in Figure 4-3, the DOS indicates that the lowest bands, approximately around -18.0 eV was dominated by oxygen 2s levels for undoped ZnO. The valence band extended from around -6.0 eV to 0.2 eV, primarily arising from Zn-3d and O-2p states, while the lower part of the conduction band mainly consisted of Zn-4s.

In Figures 4-3(b), 4-3(c), and 4-3(d), the DOS showed a notable shift of all peaks to lower energies when Sn replaced Zn atoms in ZnO. The incorporation of Sn significantly altered the electronic structure and band characteristics of ZnO. Specifically, Sn-doping introduced contributions from Sn 4d and Sn 5s states, which exhibited a moderate increase in intensity in deeper energy regions (around -24 eV to -19 eV) corresponding to core-like states. There was also a noticeable increase in intensity in the range of -11 eV to -8 eV, below the typical valence band region. The actual valence band, consisting of Zn 3d and O 2p states, was shifted closer to the Fermi level and showed changes in intensity. As the Sn doping percentage increased, the Zn 3d states in the valence band initially rose slightly from 6.25% to 12.50% but decreased significantly at 18.75%.

In Sn-doped ZnO bulk structures, the Sn 4d and 5s states predominantly contributed to the conduction band, with energies ranging from 0.1 eV to 28 eV and their intensity increased moderately with higher doping levels. Doping with Sn replaced Zn atoms, adding extra electrons that created a shallow donor level and expanded the energy levels, forming impurity-induced bands. This expansion, resulting from the interaction of Sn s and d orbitals with the conduction band minimum (CBM), caused the CBM to shift below the Fermi level leading to band degeneracy.

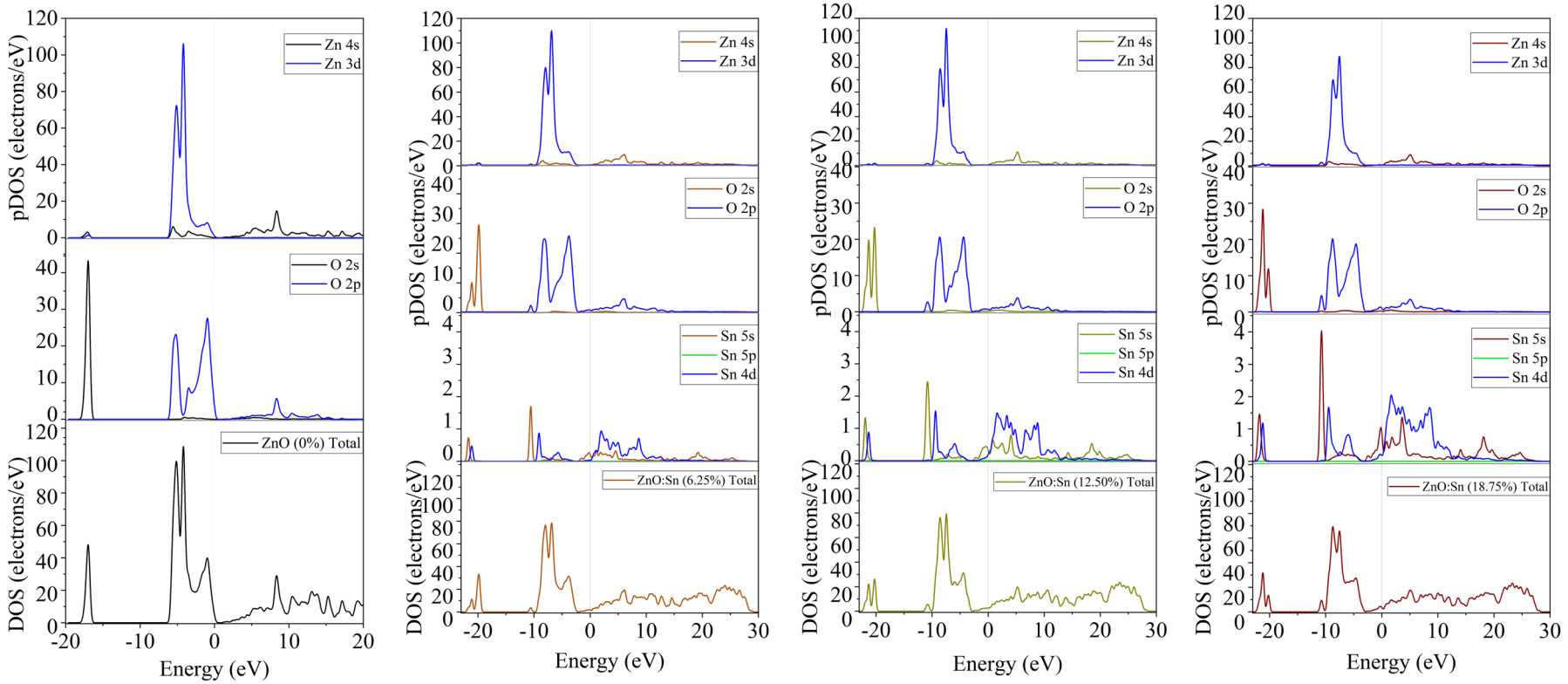

Figure 4-3: ***The comparison of energies versus DOS and pDOS for optimised Sn-doped ZnO bulk structures at various doping percentages: (a) 0%, (b) 6.25%, (c) 12.50%, (d) 18.75%.***

These changes improved the electronic structure of the photocatalyst by increasing the number of charge carriers and enhancing electron mobility and reactivity, indicating that Sn doping was beneficial. However, too much Sn doping may excessively broaden energy levels and increase recombination rates, potentially diminishing the photocatalyst's effectiveness. Thus, precise control of doping levels is essential to optimise performance without causing negative effects.

Figure 4-4 displays the pDOS concerning Zn-d orbitals found in the undoped ZnO and Sn-doped ZnO bulk structures. This comparison aided in gaining a comprehensive insight into how electrons were distributed and how they behaved within the Zn-d orbitals.

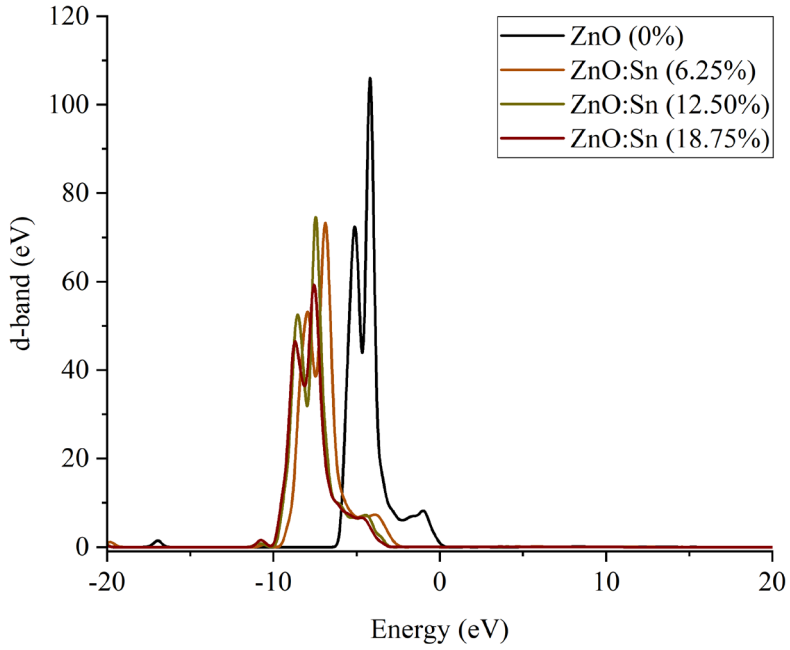

Figure 4-4: ***The pDOS (d-band) for undoped and Sn-doped ZnO bulk structures.***

The graph shows a noticeable shift of the d-band in Sn-doped ZnO bulk structures to lower energies on the left side compared to the undoped ZnO bulk structures. The shift in the d-band varied with the doping percentage, with 18.75% doping showing the most significant shift, followed by 12.50% and 6.25% exhibiting the smallest shift; this variation indicated the influence of Sn concentration on the peak's displacement. Sn doping in ZnO affected the electronic structure by altering the valence and conduction bands. Specifically, it influenced the strengths and positions of various electronic states, including the 3d, 4d, and 5s orbitals. With their extra electrons, Sn atoms interact with these orbitals, causing shifts in their energy levels. This interaction modified the overall electronic density and created new states within the band gap or impacted existing

states in the conduction band. Consequently, doping alters the material's electronic properties, such as its conductivity and band gap, by affecting how these specific electronic states contribute to the material's electronic behaviour.

4.4.3.2.2 d-band centre

The introduction of Sn into the ZnO bulk structure resulted in significant shifts in the d-band, as shown in Figure 4-4, which are crucial for reducing the band gap and enhancing photocatalysis. The calculated d-band centre values relative to the VBM for the ZnO crystal system was 7.204 eV, while the calculated d-band centre values relative to the VBM for the Sn-doped ZnO crystal systems were 6.25% = -1.854 eV, 12.50% = -7.118 eV, and 18.75% = -4.606 eV. As Sn doping increased from 0% to 12.50%, the d-band centre values decreased, indicating shifts in the electronic structure. This lowering of the d-band centre relative to the VBM, with increased Sn content, indicated improved catalytic activity, as it may facilitate better interaction with adsorbates. The additional electrons introduced by Sn doping altered the electronic environment, potentially leading to a reduced band gap. In photocatalysis, this enhances charge carrier dynamics by reducing the recombination rates of photo-generated electron-hole pairs, which are critical for photocatalytic efficiency.

However, at 18.75% doping, the slight upward shift in the d-band centre suggested that the doping effects may be reaching saturation or that structural changes within the ZnO lattice were beginning to offset the electronic advantages imparted by the dopant. This shift implied that while Sn doping initially reduced the band gap and potentially enhanced photocatalytic activity, there was a limit to the benefits of further doping. Beyond a certain level, additional doping may provide minimal enhancements or even negatively impact the material’s photocatalytic performance due to changes in its electronic structure.

4.4.3.2.3 Band gap

Figure 4-5(a) - (d) exhibits the band structures of undoped and Sn-doped ZnO. For undoped ZnO, the calculations performed without the inclusion of U values closely aligned with the existing literature values.[351]

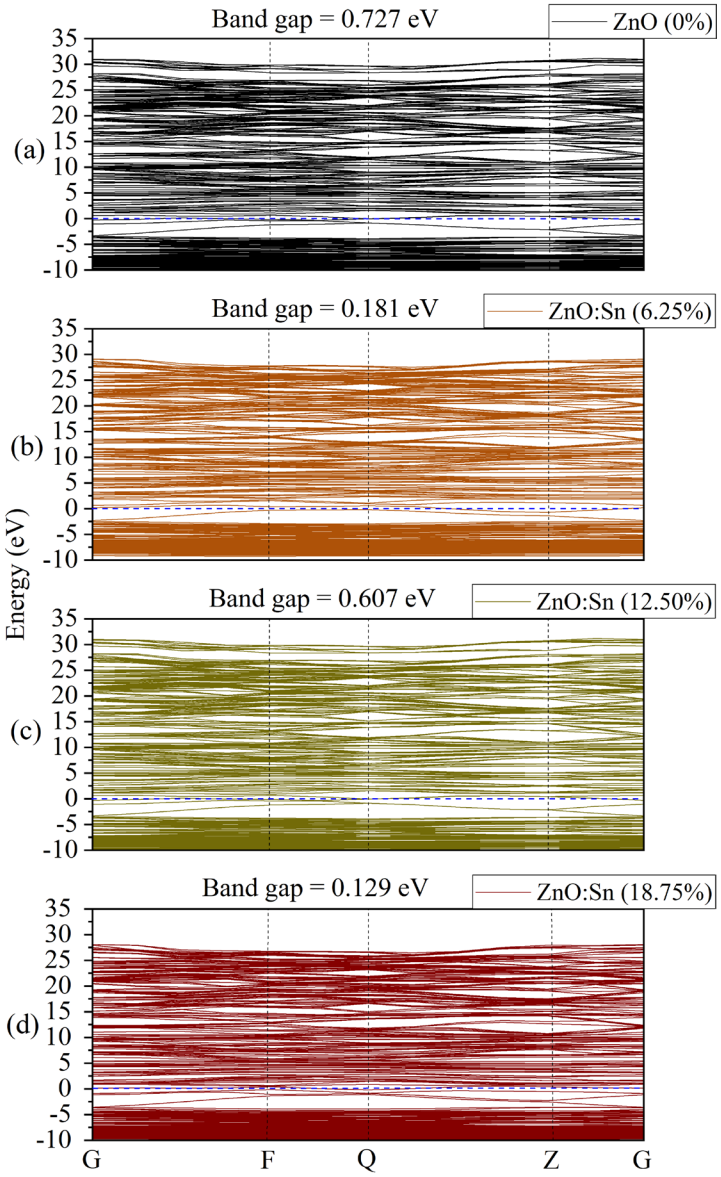

Figure 4-5: ***The comparison of energies versus computed band structure for optimised Sn-doped ZnO bulk structures at various doping levels (a) 0%, (b) 6.25%, (c) 12.50%, (d) 18.75% without the inclusion of the U value.***

At the time this study was conducted, only the band gap results for undoped ZnO using GGA+U could be validated, as there was no existing literature that had applied the U correction to Sn-doped ZnO at doping levels of 6.25%, 12.50%, and 18.75%.

Figure 4-5(a) - (d) demonstrates the significant impact of increasing Sn content in ZnO on its electronic properties, particularly highlighting the shift from a direct to an indirect band gap. In undoped ZnO, the band structure typically exhibited a direct band gap, where the valence band maximum (VBM) and conduction band minimum (CBM) were aligned in momentum space,

enabling efficient electron transitions with minimal momentum change. This direct band gap is desirable in photocatalytic applications because it facilitates more efficient light absorption and the direct excitation of electrons from the valence band to the conduction band. However, with increasing Sn content, ZnO transitions into an indirect band gap semiconductor, where the VBM and CBM were no longer aligned in momentum space. This misalignment requires more complex electron transitions, reducing transition probabilities and photon absorption efficiency and potentially compromising the overall effectiveness of photocatalytic reactions.

The shift from a direct to an indirect band gap became more pronounced with higher Sn concentrations. For example, in a 6.25% Sn-doped ZnO structure, the VBM and CBM remained relatively close, allowing some retention of direct band gap characteristics. However, as Sn concentration increased, the CBM shifts further away from the VBM in the BZ, resulting in a more pronounced indirect band gap. This evolution of the band gap was accompanied by notable changes in its magnitude.

Table 4-4 compares (validation) the magnitude of calculated band gap values with calculated values reported in literature by Yang.[55] Initially, the band gap decreased as Sn content increased from 0% to 6.25%, then rose at 12.50% before decreasing again at 18.75%. Although the trend of calculated band gap values in this study agrees with previously calculated band gap values in the literature, the band gap values were consistently lower than the DFT values found in the literature. The deviation from previously calculated values ranged from 0.41% to 18.73%, depending on the Sn doping content. Various factors have an impact on the electronic structure and, thus, the band gap in Sn-doped ZnO including the choice of exchange-correlation functional, pseudopotentials or the specific approach used to simulate Sn doping in ZnO.

Table 4-4: The band gap values for the different percentages of Sn-doped ZnO bulk structures.

Sn-doped ZnO bulk	This study		Theoretical Lit. values (DFT)				Experimental Lit. values
			Sn^{2+}	Sn^{4+}			
	(GGA-PBE)	(GGA)+U U_{d-Zn} = 10 eV, U_{p-O} = 7 eV	(GGA-PBE)	(GGA-PBE)	(GGA-PW91)	(GGA-PAW)	
0%	0.727 eV (Sn^{4+}: 0.41%) (Exp: 78.43%)	3.265 eV (Exp: 3.12%)	0.806 eV[1]	**0.730 eV[4]** 0.806 eV[7, 9]	0.755 eV[12]	0.760 eV[14]	**3.370 eV**[16] 3.240 eV[19] 3.400 eV[4] 3.610 eV[22]
5.00%	-	-	-	-	-	-	3.240 eV[25]
6.25%	0.181 eV (Sn^{2+}: 8.84%) (Sn^{4+}:20.67%) (Exp: 94.36%)	0.439 eV (Exp:86.32%)	**0.197 eV[27]**	0.485 eV[29]	0.321 eV[32]	**0.150 eV[33]**	**3.210 eV[35]**
10.00%	-	-	-	-	-	-	3.110 eV[37]
12.50%	0.607 eV (Sn^{2+}: 15.93%) (Sn^{4+}: 13.41%)	0.157 eV	0.722 eV[39]	**0.701 eV[40]**	-	-	-
15.00%	-	-	-	-	-	-	3.530 eV[43]
18.75%	0.129 eV	-	-	-	-	-	-
20.00%	-	-	-	-	-	-	3.080 eV[44]

*Note: The values obtained in this study and the literature values indicated in **bold** were used to calculate the percentage deviation. The percentage deviation is given in brackets below the values calculated in this study.*

The reported experimental band gap of undoped ZnO was 3.370 eV.[321, 408-410] In contrast, our initial DFT/GGA calculations produced a much lower band gap of 0.727 eV for undoped ZnO (namely, 78.43% lower), with even smaller values for Sn-doped ZnO: 0.181 eV for 6.25% Sn-doping (namely, 94.36% lower), 0.607 eV for 12.50% Sn-doping, and 0.129 eV for 18.75% Sn-doping.

The underestimation of band gap values as observed in Table 4-4 is a common issue with the DFT/GGA method, which often struggles to accurately represent the electronic properties of transition metal oxides like ZnO. This underestimation is largely due to DFT/GGA method's inability to account for strong electron correlation effects in these structures fully.[269, 411] To improve the accuracy, Hubbard U corrections (with $U_{d\text{-}Zn}$ = 10 eV and $U_{p\text{-}O}$ = 7 eV) were added to better capture the localised nature of Zn 3d and O 2p electrons. This adjustment significantly improved the band gap calculations, yielding a corrected band gap of 3.265 eV for undoped ZnO, with a 3.12% deviation from the experimental value of 3.370 eV, demonstrating close agreement with the experimental data.

For Sn-doped ZnO, experimental band gap values decreased with increasing Sn content up to 10%, with reported values of 3.240 eV[45] (5.00% Sn), 3.210 eV[75] (6.25% Sn), and 3.110 eV[45] (10.00% Sn). Notably, at 15.00% Sn doping, the band gap increased to 3.530 eV[45] exceeding the experimental band gap of undoped ZnO (3.370 eV).[9]

In this study, (GGA)+U calculations, though producing underestimated values, revealed a similar decreasing trend in band gap values from 6.25% to 12.50% Sn doping, suggesting that Sn introduced states within the band gap that acted as shallow donor levels. These states narrowed the band gap and contributed to the n-type behaviour of Sn-doped ZnO. Specifically, Sn^{4+} doping narrowed the gap by introducing extra electrons into the conduction band (CB), while Sn^{2+} doping created oxygen vacancies, increasing free electron concentration.

Reduced band gaps enhance visible-light absorption, making Sn-doped ZnO favourable for applications like photocatalysis. However, for Sn-doped systems in this study, the corrected band gaps were significantly lower than experimental values, with 0.439 eV for 6.25% Sn-doped ZnO (an 86.32% deviation from the experimental 3.210 eV) and 0.157 eV for 12.50% Sn-doped ZnO. Attempts to calculate band gaps for 18.75% Sn doping were unsuccessful, likely due to computational complexity and convergence challenges at higher doping levels. Despite applying Hubbard U corrections, the band gaps remained below expectations, highlighting the limitations of the computational approach in fully capturing the experimental trends.

Fine-tuning the Hubbard U corrections for Sn 4d states may improve accuracy while including spin-orbit coupling can capture effects related to Sn's heavier atomic nature, potentially aligning calculated values more closely with experimental data.

However, to improve accuracy, more advanced techniques like hybrid functionals such as HSE06[376] could be employed, which combine exact exchange from Hartree-Fock with density functional theory to better account for electronic correlations from Sn doping. Additionally, the GW approximation[377] can enhance the description of electron interactions, refining band gap calculations.

4.4.4 Surface model construction and optimisation

4.4.4.1 Construction

Nine surfaces for each percentage doping were obtained by cutting the Sn-doped ZnO bulk structures along the Miller planes identified from experimental X-ray diffraction (listed in section 4.3.5.1), with some MT and others OT terminated. Further information about the surfaces can be found in Appendix A4 (Table A4-4 to A4-54).

4.4.4.2 Optimisation

Table 4-5 shows the total energy and the number of ions in the cell for various Miller planes at different Sn-doping percentages in ZnO. The total energy values and total energy per ion were calculated for Sn-doped ZnO surfaces across various doping percentages. However, comparisons of the energies were only meaningful within the same doping percentage, as the electron count in the system varies with changes in Sn content. The total energy per ion was utilised to identify trends across different Miller planes for each doping percentage to ensure consistency.

The stability of MT and OT surfaces was influenced by the specific Miller plane and Sn doping percentage. Within each doping percentage, the total energy per ion showed a consistent pattern across the Miller planes, highlighting the influence of surface terminations on the material's stability.

Table 4-5: The total energies and number of ions in a cell obtained from the Sn-doped ZnO surface approximations.

Miller planes	No of ions	0%		6.25%		12.50%		18.75%	
		Total energy (eV)	Total energy/ions (eV/atom)	Total energy (eV)	Total energy/ions (eV/atom)	Total energy (eV)	Total energy/ions (eV/atom)	Total energy (eV)	Total energy/ions (eV/atom)
(100)	64	-68705.26	-1073.52	-65479.90	-1023.12	-62247.57	-972.62	-59020.58	-922.20
$(002)_{MT}$	32	-34353.20	-1073.54	-32737.12	-1023.04	-31123.05	-972.60	-29507.38	-922.11
$(002)_{OT}$	32	-34334.17	-1072.94	-32728.29	-1022.76	-31114.64	-972.33	-29502.39	-921.95
$(101)_{MT}$	64	-68703.69	-1073.50	-65462.34	-1022.85	-62244.67	-972.57	-59009.75	-922.03
$(101)_{OT}$	64	-68695.24	-1073.36	-65470.27	-1022.97	-62245.52	-972.59	-59010.12	-922.03
$(102)_{MT}$	64	-68698.01	-1073.41	-65459.82	-1022.81	-62241.71	-972.53	-59000.04	-921.88
$(102)_{OT}$	64	-68699.72	-1073.43	-65466.85	-1022.92	-62239.63	-972.49	-59008.71	-922.01
$(103)_{MT}$	64	-68703.65	-1073.49	-65473.03	-1023.02	-62240.68	-972.51	-59013.06	-922.08
$(103)_{OT}$	64	-68696.56	-1073.38	-65466.53	-1022.91	-62237.47	-972.46	-59005.14	-921.96
$(112)_{MT}$	64	-68688.78	-1073.26	-65461.88	-1022.84	-62236.57	-972.45	-59006.11	-921.97
$(112)_{OT}$	64	-68697.61	-1073.40	-65467.46	-1022.93	-62236.71	-972.45	-59007.41	-921.99
(200)	32	-34339.24	-1073.10	-32726.03	-1022.69	-31112.30	-972.26	-29503.87	-922.00
$(201)_{MT}$	64	-68685.74	-1073.21	-65460.55	-1022.82	-62236.54	-972.45	-59003.74	-921.93
$(201)_{OT}$	64	-68700.14	-1073.44	-65464.04	-1022.88	-62232.92	-972.39	-59007.56	-921.99
(210)	64	-68696.78	-1073.39	-65479.90	-1023.12	-62236.48	-972.45	-59011.32	-922.05

For 0% doping, MT surfaces for the (002), (101), and (103) Miller planes exhibited lower energy values compared to OT surfaces, while for the other planes, OT resulted in lower energy values. At 6.25% doping, the trend remained similar for the (002) and (103) Miller planes, where MT surfaces yielded lower energy values, but OT surfaces dominated in the rest. At 12.50% doping, MT surface resulted in lower energy for the (002), (102), (103), and (201) Miller planes, whereas OT was higher in energy for the remaining Miller planes. Finally, at 18.75% doping, MT surfaces were lower in energy for the (002) and (103) Miller planes, with OT surfaces being more favourable for the others. Although OT surfaces often displayed greater overall stability across a range of Miller planes and doping percentages, MT surfaces were highly competitive, with their stability strongly influenced by both doping percentage and Miller planes. These results suggested that MT surfaces were energetically favourable and significantly contributed to the surface stability of Sn-doped ZnO.

4.4.4.3 Surface properties

4.4.4.3.1 Surface energies

Table 4-6 lists the surface energies across the different Sn-doped ZnO surfaces and doping levels, with fluctuations tied to surface type, presence of doping, and doping percentage. The impact of doping was evident; some surfaces showed decreasing energies with increased doping, while others exhibited an initial decrease followed by an increase at higher doping levels. This complex relationship between doping and surface energy varied among surfaces. These observed variations prompted further exploration using the Wulff construction program[2] to determine crystal morphology.

4.4.4.3.2 Crystal morphology

The morphology of Sn-doped ZnO systems, based on the surface energies of different doping percentages (Table 4-6), was investigated using the Wulff construction method.[3] This method facilitated an examination of the structural evolution as ZnO underwent doping alterations with varying percentages of Sn. The derived morphologies are shown in Figure 4-6.

Table 4-6: Calculated surface energies obtained from various doping percentages of the Sn-doped ZnO surfaces

Surface[a]	Undoped ZnO	Work function (eV)	6.25%	Work function (eV)	12.50%	Work function (eV)	18.75%	Work function (eV)
(100)	**0.596**	4.961	**0.423**	3.872	**0.619**	3.550	**0.103**	3.918
$(002)_{MT}$	**0.807**	4.124	**0.883**	3.904	**0.641**	3.502	**0.638**	4.446
$(002)_{OT}$	4.331	7.235	2.569	4.796	2.247	4.592	1.594	4.911
$(101)_{MT}$	1.113	3.728	2.128	4.765	0.819	3.150	1.179	4.241
$(101)_{OT}$	1.939	4.011	1.329	4.508	0.733	3.940	1.141	4.207
$(102)_{MT}$	1.338	4.413	1.910	4.707	0.896	4.304	1.728	4.694
$(102)_{OT}$	1.204	5.688	1.342	4.860	1.063	4.767	1.029	4.352
(210)	0.795	3.872	0.772	3.872	0.731	3.865	0.454	5.058
$(103)_{MT}$	**0.685**	5.333	**0.644**	4.464	**0.748**	4.369	**0.518**	3.501
$(103)_{OT}$	1.109	4.241	1.045	4.337	0.946	4.282	1.006	4.188
(200)	2.101	5.420	1.861	4.755	1.671	4.673	0.812	4.779
$(112)_{MT}$	1.483	4.433	1.255	4.381	0.944	4.177	0.892	4.659
$(112)_{OT}$	0.986	4.784	0.931	4.367	0.935	4.731	0.816	4.053
$(201)_{MT}$	1.610	4.944	1.297	5.102	0.920	3.943	1.002	4.384
$(201)_{OT}$	0.821	3.904	1.099	4.361	1.125	4.916	0.786	4.074

Note: Each doping percentage's lowest surface energies displayed in the morphology are indicated in bold.

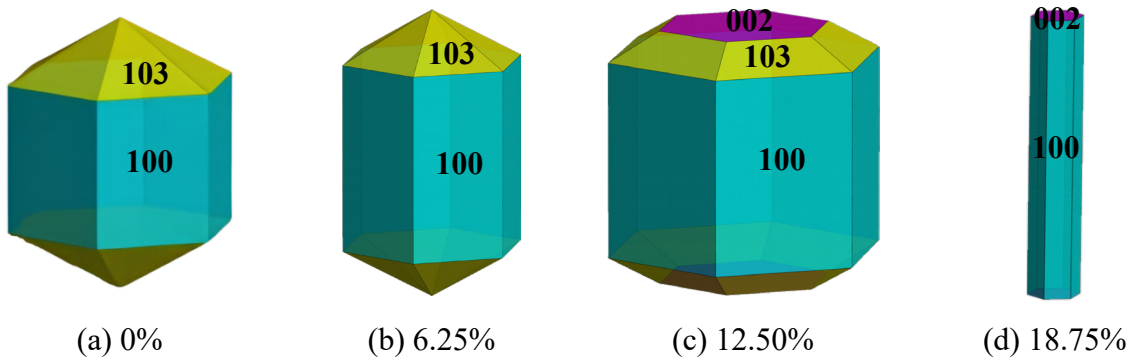

(a) 0% (b) 6.25% (c) 12.50% (d) 18.75%

Figure 4-6: The Wulff construction's predictions for the Sn-doped ZnO structures.

For the undoped (0%) ZnO structure, only two out of the eight calculated surfaces were observable. The (100) surface constituted the sides, while the (103) surface shaped the top and bottom, resulting in a hexagonal bipyramidal structure. Upon introducing 6.25% Sn doping to the ZnO bulk, the crystal structure was predicted to be more elongated than the 0%. This transformation was evident in the reduction of growth in the (100) surface, affecting the sides of the crystal. Similarly, the growth of the (103) surface, forming the top and bottom, decreased, giving the structure an elongated hexagonal bipyramidal shape. Thus, the introduction of 6.25% Sn caused the structure to become slimmer compared to the wider 0% Sn-doped ZnO. Subsequently, with a 12.50% Sn-doped ZnO, there was a significant transformation compared to the undoped and 6.25%

doped structures. The (103) surface, previously shaping the top and bottom of the structure, made room for the (002) surface to emerge in these positions. Consequently, the structure gained a larger size, transforming into a truncated hexagonal prism due to the substantial growth of the (002) surface. As the Sn doping percentage increased to 18.75% in ZnO, the prominence of the (100) and (002) surfaces considerably declined. Moreover, the (103) surface vanished, creating to a slimmer structure resembling an elongated hexagonal prism. The absence of the (103) surface, alongside the reduced growth of the (100) and (002) surfaces, resulted in this modified structure.

Thus, the surface energy analysis across various Miller planes revealed that Sn doping substantially impacted the stability and morphology of ZnO crystals. In particular, doping can lower the surface energy of specific planes, such as the polar (002) plane, enhancing their stability and shaping the overall crystal structure. This targeted stabilisation supported the preferential growth of certain crystal faces, which may increase active sites or modify the surface band structure, ultimately boosting the photocatalytic performance of ZnO. These results highlight the importance of Sn doping in modifying the surface properties, with significantly impacting the ZnO's stability.

To substantiate the observed morphological changes derived from this study's computational work, attempts were made to find corresponding experimental scanning electron microscopy (SEM) images aligning with the various percentages of Sn-doped ZnO. However, only an SEM image for undoped ZnO was found,[412] while the others did not match the exact doping percentages examined in this study. Consequently, SEM images with doping percentages closely aligned with those in this study (as shown in Table 4-7) were utilised.

Table 4-7: SEM images closely matching WULFF shapes and their respective doping percentages.

This work's Wulff shapes	Literature SEM images	
0%	0%[412]	
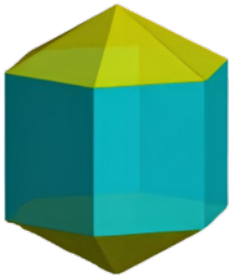	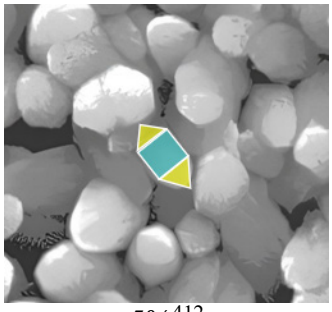	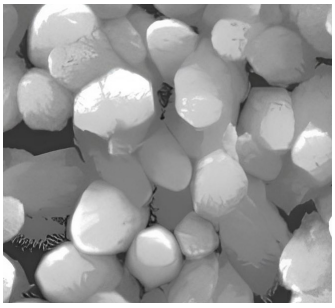
6.25%	5%[412]	
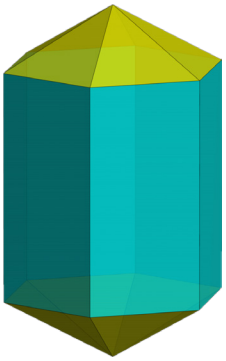	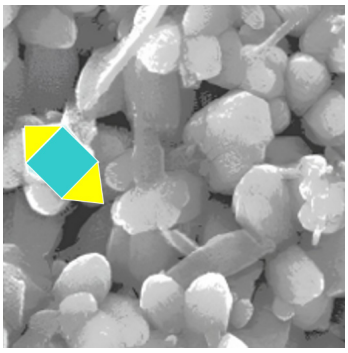	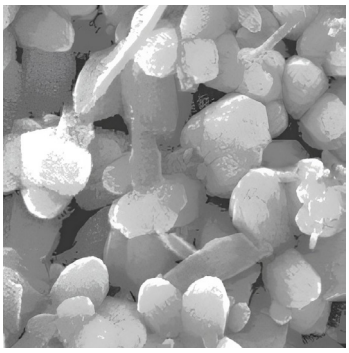
12.50%	10%[69]	
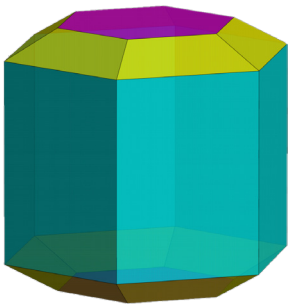	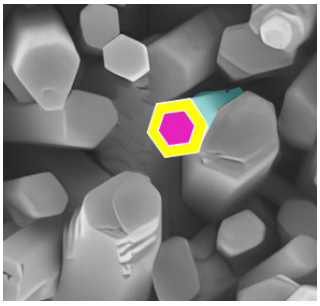	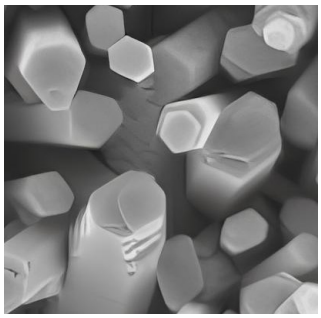
18.75%	15%[413]	
	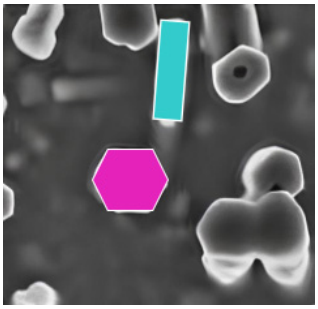	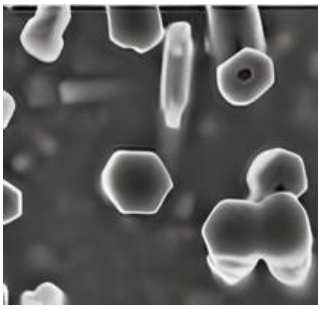

All SEM images from external sources were properly credited, and permissions were obtained in line with copyright guidelines.

To validate the Wulff morphology derived for the 6.25% Sn-doped ZnO, an SEM image representing 5% Sn-doped ZnO[412] was employed. Likewise, the 12.50% morphology was substantiated using an SEM image for 10% Sn-doped ZnO,[69] and the 18.75% morphology was validated with a 15% Sn-doped SEM image.[413]

Upon examining these SEM images, attempts were made to trace the Wulff morphology within them (see Table 4-7). This analysis was undertaken to demonstrate a correlation between the findings of the present computational research and experimental work,[402] indicating that the introduction of Sn to ZnO indeed altered its morphology. Despite the initial limitation in finding directly correlating SEM images, this method provided a comparative basis for the observed morphological changes between the doped and undoped ZnO structures.

4.4.4.3.3 Work function

The work function (Φ) values of Sn-doped ZnO surfaces across various doping percentages are summarised in Table 4-6. This analysis revealed notable variations in work function depending on the Miller plane and doping concentration. For undoped ZnO, the work function values varied significantly across different Miller planes. The $(002)_{OT}$ surface had the highest work function at 7.235 eV, while the $(101)_{MT}$ surface had the lowest at 3.728 eV. At a doping concentration of 6.25%, the general trend was a decrease in work function compared to undoped ZnO. For instance, the work function of the (100) surface decreased from 4.961 eV to 3.872 eV. This trend continued with further doping, as the work function decreased to 3.550 eV at 12.50% doping, but then increased to 3.918 eV at 18.75% doping.

Interestingly, some surfaces, such as $(101)_{MT}$, $(101)_{OT}$, $(102)_{MT}$, $(103)_{OT}$, $(201)_{MT}$, and $(201)_{OT}$, showed an increase in work function at 6.25% doping, contrary to the general trend. Overall, increased Sn doping generally led to a decrease in work function, with the most pronounced reductions observed in the $(101)_{MT}$ and $(002)_{MT}$ planes. This variability suggests that the effect of doping on work function was highly dependent on the specific Miller plane and the doping level. Some surfaces exhibited clear trends of decreasing or increasing work function with higher doping, while others displayed irregular fluctuations, indicating complex interactions and dependencies.

4.5 Conclusion

In this investigation, research aimed to explore the structural and electronic properties of various Sn-doped ZnO surfaces to enhance ZnO's photocatalytic performance. Several key findings emerged from this investigation.

It was observed that as the doping percentages increased, the lattice parameters of the ZnO bulks also increased. This increase occurred because the atomic radius of Sn is larger than that of Zn, leading to an expansion of the crystal lattice when Sn atoms replaced Zn atoms.

Secondly, a significant change was noticed in the DOS when Sn was introduced into the ZnO structure. This change caused a shift in the energy peaks within the DOS, reducing the band gaps of the ZnO structures. The shift in DOS indicated alterations in the electronic structure of the bulk because of Sn doping.

To confirm the presence of Sn in the ZnO bulk structure, an XRD analysis was conducted. This analysis revealed an increase in the intensity of the (002) peak as the doping level increased, along with a subtle increase in other XRD peaks. The enhanced intensity of the (002) peak indicated the successful incorporation of Sn into the ZnO lattice.

When comparing the band gap values of the Sn-doped ZnO bulk structures with undoped ZnO, it was evident that the band gaps were significantly reduced by Sn doping. The undoped ZnO exhibited a band gap value of 0.727 eV, while the 6.25% Sn-doped ZnO had a much lower band gap of 0.181 eV, and the 12.50% showed a higher band gap of 0.607 eV. The 18.75% doping level yielded the lowest band gap value, measuring 0.129 eV. However, the Hubbard U value was introduced to ensure consistency with experimental values, which adjusted the undoped ZnO band gap to 3.265 eV, a closer match to the experimental value of 3.37 eV.[321] Interestingly, introducing Sn into the ZnO bulk resulted in a notable reduction in band gap, suggesting improved photocatalytic activity in visible light. This reduction continued as doping levels increased, but there was a percentage of Sn doping beyond which the effectiveness dropped. This finding highlights the need for further exploration and investigation of lower Sn doping percentages within the range of 1 to 12% to precisely identify the point at which band gap reduction levels off. Achieving this involves working with larger bulk structures or surface slabs, which will impose greater computational demands. Additionally, adding Hubbard values for Sn could improve the band gap values of Sn doped ZnO.

Furthermore, the study examined the band structures and demonstrated that Sn-doped ZnO changed the undoped ZnO structure from a direct band gap to an indirect band gap upon doping. This change in band structure may contribute to the improved visible light photocatalytic properties of Sn-doped ZnO, by potentially enhancing charge carrier separation.

Additionally, the morphology and electronic properties of Sn-doped ZnO were examined and compared with experimental literature. The Wulff construction method demonstrated that increasing Sn doping altered the crystal morphology from hexagonal bipyramids to elongated and truncated prisms. These changes were caused by stabilising specific crystal surfaces (Miller

planes), showing how Sn doping can modify the structure and surface properties of ZnO to potentially enhance its photocatalytic performance.

The analysis of work function revealed that Sn doping influences the work function based on the Miller plane and doping level. Overall, most surfaces showed a decrease in work function at moderate doping levels. These findings highlight the potential of Sn doping to optimise the stability, morphology, and electronic properties of ZnO, improving its photocatalytic activity.

In conclusion, the research confirmed that Sn doping effectively reduced the band gap of ZnO, enhancing its performance in visible light. The study identified the most stable surface configurations, presented the morphologies, and provided valuable insights into the impact of Sn doping on ZnO's structural and electronic properties. This work contributes to developing more efficient photocatalytic materials with potential environmental benefits.

4.6 References

(1) *Manual for Masters and Doctoral Studies, 2016*. North-West University, https://services.nwu.ac.za/sites/services.nwu.ac.za/files/files/research-support/documents/2016-04-06%20ICRI%20Manual%20for%20M%20and%20D%20students.pdf (accessed July 02, 2024).

(2) Rahm, J.; Erhart, P. WulffPack: A Python package for Wulff constructions. *Journal of Open Source Software* **2020**, *5*, 1944. DOI: 10.21105/joss.01944.

(3) Wulff, G. XXV. On the question of the rate of growth and dissolution of the crystal surfaces. *Kristallografiya* **1901**, *34*, 449-530. DOI: 10.1524/ZKRI.1901.34.1.449.

(4) Rajamanickam, D.; Shanthi, M. Photocatalytic degradation of an organic pollutant by zinc oxide – solar process. *Arabian Journal of Chemistry* **2016**, *9*, S1858-S1868. DOI: 10.1016/j.arabjc.2012.05.006.

(5) Ksibi, M.; Zemzemi, A.; Boukchina, R. Photocatalytic degradability of substituted phenols over UV irradiated TiO_2. *Journal of Photochemistry and Photobiology A: Chemistry* **2003**, *159* (1), 61-70.

(7) Czech, B.; Zygmunt, P.; Kadirova, Z. C.; Yubuta, K.; Hojamberdiev, M. Effective photocatalytic removal of selected pharmaceuticals and personal care products by elsmoreite/tungsten oxide@ ZnS photocatalyst. *Journal of Environmental Management* **2020**, *270*, 110870.

(8) Villani, M.; Calestani, D.; Lazzarini, L.; Zanotti, L.; Mosca, R.; Zappettini, A. Extended functionality of ZnO nanotetrapods by solution-based coupling with CdS nanoparticles. *Journal of Materials Chemistry* **2012**, *22*, 5694-5699. DOI: 10.1039/c2jm16164h.

(9) Akintelu, S. A.; Folorunso, A. S.; Folorunso, F. A.; Oyebamiji, A. K. Green synthesis of copper oxide nanoparticles for biomedical application and environmental remediation. *Heliyon* **2020**, *6* (7).

(10) Masudy-Panah, S.; Katal, R.; Khiavi, N. D.; Shekarian, E.; Hu, J.; Gong, X. A high-performance cupric oxide photocatalyst with palladium light trapping nanostructures and a hole transporting layer for photoelectrochemical hydrogen evolution. *Journal of Materials Chemistry A* **2019**, *7* (39), 22332-22345.

(12) Mao, T.; Liu, M.; Lin, L.; Cheng, Y.; Fang, C. A study on doping and compound of zinc oxide photocatalysts. *Polymers* **2022**, *14*. DOI: 10.3390/polym14214484.

(13) Mohamad, A. A.; Hassan, M. S.; Yaakob, M. K.; Taib, M. F. M.; Badrudin, F. W.; Hassan, O. H.; Yahya, M. Z. A. First-principles calculation on electronic properties of zinc oxide by zinc–air system. *Journal of King Saud University - Engineering Sciences* **2017**, *29* (3), 278-283. DOI: 10.1016/j.jksues.2015.08.002.

(14) Kumar, S. G.; Rao, K. K. Comparison of modification strategies towards enhanced charge carrier separation and photocatalytic degradation activity of metal oxide semiconductors (TiO_2, WO_3 and ZnO). *Applied Surface Science* **2017**, *391*, 124-148.

(16) Roselin, L. S.; Rajarajeswari, G.; Selvin, R.; Sadasivam, V.; Sivasankar, B.; Rengaraj, K. Sunlight/ZnO-mediated photocatalytic degradation of reactive red 22 using thin film flat bed flow photoreactor. *Solar Energy* **2002**, *73* (4), 281-285.

(17) Pelaez, M.; Nolan, N. T.; Pillai, S. C.; Seery, M. K.; Falaras, P.; Kontos, A. G.; Dunlop, P. S. M.; Hamilton, J. W. J.; Byrne, J. A.; O'Shea, K.; et al. A review on the visible light active titanium dioxide photocatalysts for environmental applications. *Applied Catalysis B: Environmental* **2012**, *125*, 331-349. DOI: 10.1016/j.apcatb.2012.05.036.

(19) Thompson, T. L.; Yates, J. T. Surface science studies of the photoactivation of TiO_2 new photochemical processes. *Chemical Reviews* **2006**, *106* (10), 4428-4453. DOI: 10.1021/cr050172k.

(20) Linsebigler, A. L.; Lu, G.; Yates, J. T., Jr. Photocatalysis on TiO_2 surfaces: principles, mechanisms, and selected results. *Chemical Reviews* **1995**, *95* (3), 735-758. DOI: 10.1021/cr00035a013.

(22) Derikvandi, H.; Nezamzadeh-Ejhieh, A. Increased photocatalytic activity of NiO and ZnO in photodegradation of a model drug aqueous solution: Effect of coupling, supporting, particles size and calcination temperature. *Journal of Hazardous Materials* **2017**, *321*, 629-638. DOI: 10.1016/j.jhazmat.2016.09.056.

(24) Di Paola, A.; Augugliaro, V.; Palmisano, L.; Pantaleo, G.; Savinov, E. Heterogeneous photocatalytic degradation of nitrophenols. *Journal of Photochemistry and Photobiology A: Chemistry* **2003**, *155* (1), 207-214. DOI: 10.1016/S1010-6030(02)00390-8.

(25) Douloumis, A.; Vrithias, N. R. E.; Katsarakis, N.; Remediakis, I. N.; Kopidakis, G. Tuning the workfunction of ZnO through surface doping with Mn from first-principles simulations. *Surface Science* **2022**, *726*. DOI: 10.1016/j.susc.2022.122175.

(26) Ibrahim, A. A.; Kumar, R.; Umar, A.; Kim, S. H.; Bumajdad, A.; Ansari, Z. A.; Baskoutas, S. Cauliflower-shaped ZnO nanomaterials for electrochemical sensing and photocatalytic applications. *Electrochimica Acta* **2016**, *222*, 463-472. DOI: 10.1016/J.ELECTACTA.2016.10.199.

(27) Mohd Adnan, M. A.; Julkapli, N. M.; Abd Hamid, S. B. Review on ZnO hybrid photocatalyst: Impact on photocatalytic activities of water pollutant degradation. *Reviews in Inorganic Chemistry* **2016**, *36*, 77-104. DOI: 10.1515/revic-2015-0015.

(28) Morkoç, H.; Özgür, U. m. Zinc oxide: Fundamentals, materials and device technology. *British Library Cataloguing-in-Publication Data* **2009**, 477.

(29) Farmer, N.; O'Neill, H. S. C. The miscibility gap between the rock salt and wurtzite phases in the MgO–ZnO binary system to 3.5 GPa. *European Journal of Mineralogy* **2023**, *35* (6), 1051-1071.

(31) Qi, K.; Xing, X.; Zada, A.; Li, M.; Wang, Q.; Liu, S.-y.; Lin, H.; Wang, G. Transition metal doped ZnO nanoparticles with enhanced photocatalytic and antibacterial performances: Experimental and DFT studies. *Ceramics International* **2020**, *46* (2), 1494-1502. DOI: 10.1016/j.ceramint.2019.09.116.

(32) Dedova, T. *Chemical spray pyrolysis deposition of zinc sulfide thin films and zinc oxide nanostructured layers*; Tallinn University of Technology Tallinn, Estonia, **2007**.

(33) Yates, B.; Cooper, R.; Kreitman, M. Low-temperature thermal expansion of zinc oxide. Vibrations in zinc oxide and sphalerite zinc sulfide. *Physical Review B* **1971**, *4* (4), 1314.

(35) Coleman, V. A.; Jagadish, C. Basic properties and applications of ZnO. In *Zinc oxide bulk, thin films and nanostructures*, Elsevier, **2006**; pp 1-20.

(37) Fan, Z.; Lu, J. G. Zinc oxide nanostructures: synthesis and properties. *Journal of Nanoscience and Nanotechnology* **2005**, *5* (10), 1561-1573.

(39) Ivanov, I.; Pollman, J. First surface electronic structure of a wurtzite-type semiconductor the polar and nonpolar surfaces of ZnO. *Solid State Communications* **1980**, *36* (4), 361-364.

(40) Ul Hasan, K.; Alvi, N.; Lu, J.; Nur, O.; Willander, M. Single nanowire-based UV photodetectors for fast switching. *Nanoscale Research Letters* **2011**, *6*, 1-6.

(43) Panda, N.; Sahu, D.; Acharya, B.; Nayak, P. High UV absorption efficiency of nanocrystalline ZnO synthesized by ultrasound assisted wet chemical method. *Current Applied Physics* **2015**, *15* (3), 389-396.

(44) Rahman, F. Zinc oxide light-emitting diodes: a review. *Optical Engineering* **2019**, *58* (1), 010901-010901.

(49) Li, W.; Wang, G.; Feng, Y.; Li, Z. Efficient photocatalytic performance enhancement in Co-doped ZnO nanowires coupled with CuS nanoparticles. *Applied Surface Science* **2018**, *428*, 154-164. DOI: 10.1016/J.APSUSC.2017.09.049.

(50) Xiaohua, Z.; Shuai, S.; Guangli, W.; Caizhu, L.; Zhe, Q.; Xiangdong, L.; Jianguo, Z. Facile synthesis of the flower-like ternary heterostructure of Ag/ZnO encapsulating carbon spheres with enhanced photocatalytic performance. *Applied Surface Science* **2017**, *406*, 1-11.

(55) Yang, W.; Zhang, B.; Zhang, Q.; Wang, L.; Song, B.; Ding, Y.; Wong, C. Adjusting the band structure and defects of ZnO quantum dots via tin doping. *RSC Advances* **2017**, *7* (19), 11345-11354.

(66) Zhou, W.; Fu, H. Defect-mediated electron–hole separation in semiconductor photocatalysis. *Inorganic Chemistry Frontiers* **2018**, *5* (6), 1240-1254.

(69) Agarwal, M. B.; Sharma, A.; Malaidurai, M.; Thangavel, R. Effect of Sn doping on structural, mechanical, optical and electrical properties of ZnO nanoarrays prepared by sol-gel and hydrothermal process. *Superlattices and Microstructures* **2018**, *117*, 342-350.

(70) Aydin, H.; El-Nasser, H.; Aydin, C.; Al-Ghamdi, A. A.; Yakuphanoglu, F. Synthesis and characterization of nanostructured undoped and Sn-doped ZnO thin films via sol–gel approach. *Applied Surface Science* **2015**, *350*, 109-114.

(71) Beura, R.; Pachaiappan, R.; Thangadurai, P. A detailed study on Sn^{4+} doped ZnO for enhanced photocatalytic degradation. *Applied Surface Science* **2018**, *433*, 887-898. DOI: 10.1016/j.apsusc.2017.10.127.

(73) Caglar, Y.; Aksoy, S.; Ilican, S.; Caglar, M. Crystalline structure and morphological properties of undoped and Sn doped ZnO thin films. *Superlattices and Microstructures* **2009**, *46* (3), 469-475. DOI: 10.1016/j.spmi.2009.05.005.

(74) Dhamodharan, P.; Manoharan, C.; Dhanapandian, S.; Bououdina, M.; Ramalingam, S. Preparation and characterization of spray deposited Sn-doped ZnO thin films onto ITO subtracts as photoanode in dye sensitized solar cell. *Journal of Materials Science: Materials in Electronics* **2015**, *26*, 4830-4839.

(80) Oyewo, O. A.; Ramaila, S.; Mavuru, L.; Onwudiwe, D. C. Enhanced photocatalytic degradation of methyl orange using Sn-ZnO/GO nanocomposite. *Journal of Photochemistry and Photobiology* **2022**, *11*. DOI: 10.1016/j.jpap.2022.100131.

(81) Dassault; Systemes. *Biovia Material Studio Castep*. **2020**. https://www.3ds.com/fileadmin/PRODUCTS-SERVICES/BIOVIA/PDF/biovia-material-studio-castep.pdf (accessed 2023 April 08, 2023).

(82) *National Intergrated Cyberinfrastructure System (NICIS) - Centre for High Performance Computing (CHPC)*. **2017**. https://www.chpc.ac.za/index.php/resources). (accessed 2023 April 08, 2023).

(83) Okhotnikov, K.; Charpentier, T.; Cadars, S. Supercell program: a combinatorial structure-generation approach for the local-level modeling of atomic substitutions and partial occupancies in crystals. *Journal of Cheminformatics* **2016**, *8*, 1-15.

(189) Cao, S.; Fan, B.; Feng, Y.; Chen, H.; Jiang, F.; Wang, X. Sulfur-doped g-C_3N_4 nanosheets with carbon vacancies: General synthesis and improved activity for simulated solar-light photocatalytic nitrogen fixation. *Chemical Engineering Journal* **2018**, *353*, 147-156.

(210) Arif, A.; Belahssen, O.; Gareh, S.; Benramache, S. The calculation of band gap energy in zinc oxide films. *Journal of Semiconductors* **2015**, *36* (1), 013001.

(229) Gnaneswari, M. D.; Marimuthu, K.; Chandrasekar, B.; Leonora, J. M. Chemically prepared P-Type Sn doped ZnO nanoparticles: Synthesis, characterization and its antibacterial properties. *Journal of Crystal Growth* **2024**, *627*, 127548.

(230) Illy, B. N.; Ingham, B.; Toney, M. F.; Nandhakumar, I.; Ryan, M. P. Understanding the selective etching of electrodeposited ZnO nanorods. *Langmuir* **2014**, *30* (46), 14079-14085. DOI: 10.1021/la503765a.

(262) Morasae, S. M., Zirak; Amene, N.; Elham, K.; Alireza, Z. M. Recent progress on doped ZnO nanostructures for visible-light photocatalysis. *Thin Solid Films* **2016**, *605*.

(263) Lee, Y.-S.; Peng, Y.-C.; Lu, J.-H.; Zhu, Y.-R.; Wu, H.-C. Electronic and optical properties of Ga-doped ZnO. *Thin Solid Films* **2014**, *570*, 464-470. DOI: 10.1016/j.tsf.2014.04.037.

(269) Opoku, F.; Govender, K. K.; van Sittert, C. G. C. E.; Govender, P. P. Understanding the mechanism of enhanced charge separation and visible light photocatalytic activity of modified wurtzite ZnO with nanoclusters of ZnS and graphene oxide: from a hybrid density functional study. *New Journal of Chemistry* **2017**, *41* (16), 8140-8155.

(284) Ma, X.; Wu, Y.; Lv, Y.; Zhu, Y. Correlation effects on lattice relaxation and electronic structure of ZnO within the GGA+ U formalism. *The Journal of Physical Chemistry C* **2013**, *117* (49), 26029-26039.

(290) Harun, K.; Mansor, N.; Ahmad, Z. A.; Mohamad, A. A. Electronic properties of ZnO nanoparticles synthesized by Sol-gel method: a LDA+ U calculation and experimental study. *Procedia Chemistry* **2016**, *19*, 125-132.

(294) Bougrine, A.; El Hichou, A.; Addou, M.; Ebothé, J.; Kachouane, A.; Troyon, M. Structural, optical and cathodoluminescence characteristics of undoped and tin-doped ZnO thin films prepared by spray pyrolysis. *Materials Chemistry and Physics* **2003**, *80* (2), 438-445, Article. DOI: 10.1016/S0254-0584(02)00505-9 Scopus.

(301) Kamarulzaman, N.; Kasim, M. F.; Rusdi, R. Band gap narrowing and widening of ZnO nanostructures and doped materials. *Nanoscale Research Letters* **2015**, *10*. DOI: 10.1186/s11671-015-1034-9.

(319) Pandey, A.; Scherich, H.; Drabold, D. A. Density functional theory model of amorphous zinc oxide (a-ZnO) and a-X0.375Z0.625O (X= Al, Ga and In). *Journal of Non-Crystalline Solids* **2017**, *455*, 98-101. DOI: 10.1016/j.jnoncrysol.2016.10.035.

(321) Supatutkul, C.; Pramchu, S.; Jaroenjittichai, A. P.; Laosiritaworn, Y. Density functional theory investigation of surface defects in Sn-doped ZnO. *Surface and Coatings Technology* **2016**, *298*, 53-57. DOI: 10.1016/j.surfcoat.2016.04.013.

(325) Wen, J.-Q.; Zhang, J.-M.; Chen, G.-X.; Wu, H.; Yang, X. The structural, electronic and optical properties of Nd doped ZnO using first-principles calculations. *Physica E: Low-dimensional Systems and Nanostructures* **2018**, *98*, 168-173. DOI: 10.1016/j.physe.2018.01.002.

(326) Perdew, J. P.; Burke, K.; Ernzerhof, M. Generalized gradient approximation made simple. *Physical Review Letters* **1996**, *77* (18), 3865.

(327) Perdew, J. P.; Burke, K.; Ernzerhof, M. Generalized Gradient Approximation Made Simple. *Physical Review Letters* **1997**, *77* (18), 3865-3868. DOI: 10.1103/PhysRevLett.77.3865.

(332) Clark, S. J.; Segall, M. D.; Pickard, C. J.; Hasnip, P. J.; Probert, M. I. J.; Refson, K.; Payne, M. C. First principles methods using CASTEP. *Zeitschrift für Kristallographie - Crystalline Materials* **2005**, *220* (5-6), 567-570. DOI: 10.1524/zkri.220.5.567.65075.

(335) Ferreira, L. G.; Marques, M.; Teles, L. K. Approximation to density functional theory for the calculation of band gaps of semiconductors. *Physical Review B* **2008**, *78* (12), 125116.

(350) Slassi, A.; Lakouari, N.; Ziat, Y.; Zarhri, Z.; Fakhim Lamrani, A.; Hlil, E. K.; Benyoussef, A. Ab initio study on the electronic, optical and electrical properties of Ti-, Sn- and Zr-

doped ZnO. *Solid State Communications* **2015**, *218*, 45-48. DOI: 10.1016/j.ssc.2015.06.010.

(351) Schleife, A.; Fuchs, F.; Furthmüller, J.; Bechstedt, F. First-principles study of ground- and excited-state properties of MgO, ZnO, and CdO polymorphs. *Physical Review B* **2006**, *73*, 245212. DOI: 10.1103/PHYSREVB.73.245212/FIGURES/9/MEDIUM.

(353) Monkhorst, H. J.; Pack, J. D. Special points for Brillouin-zone integrations. *Physical Review B* **1976**, *13* (12), 5188-5192. DOI: 10.1103/PhysRevB.13.5188.

(376) Wróbel, J.; Kurzydłowski, K. J.; Hummer, K.; Kresse, G.; Piechota, J. Calculations of ZnO properties using the Heyd-Scuseria-Ernzerhof screened hybrid density functional. *Physical Review B* **2009**, *80* (15). DOI: 10.1103/PhysRevB.80.155124.

(377) Oshikiri, M.; Aryasetiawan, F. Band gaps and quasiparticle energy calculations on ZnO, ZnS, and ZnSe in the zinc-blende structure by the GW approximation. *Physical Review B* **1999**, *60* (15), 10754-10757. DOI: 10.1103/PhysRevB.60.10754.

(380) Marcelino, R. B.; Amorim, C. C. Towards visible-light photocatalysis for environmental applications: band-gap engineering versus photons absorption—a review. *Environmental Science and Pollution Research* **2019**, *26*, 4155-4170.

(381) Carr, J. A.; Chaudhary, S. The identification, characterization and mitigation of defect states in organic photovoltaic devices: a review and outlook. *Energy & Environmental Science* **2013**, *6* (12), 3414-3438.

(382) Du, C.; Yan, B.; Lin, Z.; Yang, G. Enhanced carrier separation and increased electron density in 2D heavily N-doped $ZnIn_2S_4$ for photocatalytic hydrogen production. *Journal of Materials Chemistry A* **2020**, *8* (1), 207-217.

(383) Pradhan, N.; Sarma, D. Advances in light-emitting doped semiconductor nanocrystals. *The Journal of Physical Chemistry Letters* **2011**, *2* (21), 2818-2826.

(384) Leschkies, K. S.; Divakar, R.; Basu, J.; Enache-Pommer, E.; Boercker, J. E.; Carter, C. B.; Kortshagen, U. R.; Norris, D. J.; Aydil, E. S. Photosensitization of ZnO nanowires with CdSe quantum dots for photovoltaic devices. *Nano Letters* **2007**, *7* (6), 1793-1798.

(385) Cao, L.; Jiang, J.; Zhu, L. Realization of band-gap engineering of ZnO thin films via Ca alloying. *Materials Letters* **2013**, *100*, 201-203.

(386) Liqiang, J.; Baiqi, W.; Baifu, X.; Shudan, L.; Keying, S.; Weimin, C.; Honggang, F. Investigations on the surface modification of ZnO nanoparticle photocatalyst by depositing Pd. *Journal of Solid State Chemistry* **2004**, *177* (11), 4221-4227.

(387) Patil, S. S.; Mali, M. G.; Tamboli, M. S.; Patil, D. R.; Kulkarni, M. V.; Yoon, H.; Kim, H.; Al-Deyab, S. S.; Yoon, S. S.; Kolekar, S. S. Green approach for hierarchical nanostructured Ag-ZnO and their photocatalytic performance under sunlight. *Catalysis Today* **2016**, *260*, 126-134.

(388) Sharma, V.; Prasad, M.; Jadkar, S.; Pal, S. Influence of carbon and phosphorus doping on electronic properties of ZnO. *Journal of Materials Science: Materials in Electronics* **2016**, *27*, 12318-12322.

(389) He, H.; Zhuge, F.; Ye, Z.; Zhu, L.; Wang, F.; Zhao, B.; Huang, J. Strain and its effect on optical properties of Al-N codoped ZnO films. *Journal of Applied Physics* **2006**, *99* (2).

(390) Duan, X.-Y.; Zhao, Y.-J.; Yao, R.-H. Pushing p-type conductivity in ZnO by (Zr, N) codoping: A first-principles study. *Solid State Communications* **2008**, *147* (5), 194-197. DOI: 10.1016/j.ssc.2008.05.027.

(391) Gowrishankar, S.; Balakrishnan, L.; Gopalakrishnan, N. Band gap engineering in Zn (1− x) CdxO and Zn (1− x) MgxO thin films by RF sputtering. *Ceramics International* **2014**, *40* (1), 2135-2142.

(392) Sekar, A.; Kim, S.; Umar, A.; Hahn, Y. Catalyst-free synthesis of ZnO nanowires on Si by oxidation of Zn powders. *Journal of Crystal Growth* **2005**, *277* (1-4), 471-478.

(393) Nazim, V. S.; El-Sayed, G. M.; Amer, S. M.; Nadim, A. H. Optimization of metal dopant effect on ZnO nanoparticles for enhanced visible LED photocatalytic degradation of citalopram: comparative study and application to pharmaceutical cleaning validation. *Sustainable Environment Research* **2023**, *33* (1), 39.

(394) Park, Y. R.; Kim, K. J. Optical and electrical properties of Ti-doped ZnO films: observation of semiconductor–metal transition. *Solid State Communications* **2002**, *123* (3), 147-150. DOI: 10.1016/S0038-1098(02)00217-X.

(395) Paul, G. K.; Bandyopadhyay, S.; Sen, S. K.; Sen, S. Structural, optical and electrical studies on sol–gel deposited Zr doped ZnO films. *Materials Chemistry and Physics* **2003**, *79* (1), 71-75. DOI: 10.1016/S0254-0584(02)00454-6.

(396) Qu, X.; Bai, L.; Meng, Q.; Jia, D. Electronic structure and optical properties of Sn-doped ZnO. *Physica B: Condensed Matter* **2012**, *407* (2), 268-270.

(397) Bergum, K.; Hansen, P.-A.; Fjellvåg, H.; Nilsen, O. Structural, electrical and optical characterization of Ti-doped ZnO films grown by atomic layer deposition. *Journal of Alloys and Compounds* **2014**, *616*, 618-624.

(398) Noh, Y. W.; Lee, J. H.; Jin, I. S.; Park, S. H.; Jung, J. W. Tailored electronic properties of Zr-doped SnO2 nanoparticles for efficient planar perovskite solar cells with marginal hysteresis. *Nano Energy* **2019**, *65*, 104014.

(399) Dalapati, G. K.; Sharma, H.; Guchhait, A.; Chakrabarty, N.; Bamola, P.; Liu, Q.; Saianand, G.; Krishna, A. M. S.; Mukhopadhyay, S.; Dey, A. Tin oxide for optoelectronic, photovoltaic and energy storage devices: a review. *Journal of Materials Chemistry A* **2021**, *9* (31), 16621-16684.

(400) Kondrotas, R.; Pakštas, V.; Franckevičius, M.; Suchodolskis, A.; Tumėnas, S.; Jašinskas, V.; Juškėnas, R.; Krotkus, A.; Muska, K.; Kauk-Kuusik, M. Band gap engineering by cationic substitution in $Sn(Zr_{1-x}Ti_x)Se_3$ alloy for bottom sub-cell application in solar cells. *Journal of Materials Chemistry A* **2023**, *11* (48), 26488-26498.

(401) Adelowo, E.; Fasasi, A.; Adeoye, M.; Alayande, S. Structural and optical properties of tin doped zinc oxide fibres prepared by electrospinning technique. *Chemistry and Materials Research* **2013**, *3* (13), 96-106.

(402) Onwudiwe, D. C. Photocatalytic reduction of hexavalent chromium using Zn_2SnO_4–ZnO modified g-C_3N_4 composite. North-West University: 2023.

(403) Singh, M.; Goyal, M.; Devlal, K. Size and shape effects on the band gap of semiconductor compound nanomaterials. *Journal of Taibah University for Science* **2018**, *12* (4), 470-475.

(404) Anisimov, V. I.; Zaanen, J.; Andersen, O. K. Band theory and Mott insulators: Hubbard U instead of Stoner I. *Physical Review B* **1991**, *44* (3), 943.

(405) Jiang, H.; Gomez-Abal, R. I.; Rinke, P.; Scheffler, M. First-principles modeling of localized d states with the GW LDA+ U approach. *Physical Review B* **2010**, *82* (4), 045108.

(406) File, P. D. Joint Committee on Powder Diffraction Standards (JCPDS). *ASTM, Philadelphia, PA* **1997**.

(407) Paraguay D, F.; Morales, J.; Estrada L, W.; Andrade, E.; Miki-Yoshida, M. Influence of Al, In, Cu, Fe and Sn dopants in the microstructure of zinc oxide thin films obtained by spray pyrolysis. *Thin Solid Films* **2000**, *366* (1-2), 16-27, Article. DOI: 10.1016/S0040-6090(00)00752-5 Scopus.

(408) Shanshool, H. M.; Yahaya, M.; Yunus, W. M. M.; Abdullah, I. Y. Investigation of energy band gap in polymer/ZnO nanocomposites. *Journal of Materials Science: Materials in Electronics* **2016**, *27*, 9804-9811.

(409) Yung, K. C.; Liem, H.; Choy, H. Enhanced redshift of the optical band gap in Sn-doped ZnO free standing films using the sol–gel method. *Journal of Physics D: Applied Physics* **2009**, *42* (18), 185002.

(410) Cheng, J.; Zhang, Y.; Guo, R. ZnO microtube ultraviolet detectors. *Journal of Crystal Growth* **2008**, *310* (1), 57-61.

(411) Hautier, G.; Miglio, A.; Waroquiers, D.; Rignanese, G.-M.; Gonze, X. How does chemistry influence electron effective mass in oxides? A high-throughput computational analysis. *Chemistry of Materials* **2014**, *26* (19), 5447-5458.

(412) Thomas, D.; Vattappalam, S. C.; Mathew, S.; Augustine, S. Appraisal on textured grain growth and photoconductivity of ZnO thin film SILAR. *Advances in Chemistry* **2014**, *549019*.

(413) Shi, X.; Zhao, X.; Duan, L.; Sun, H.; Liu, J.; Bai, X.; Guan, M.; Cao, M.; Liu, J. Notable shift of ultraviolet intensity on Sn-doped ZnO nanostructure fabricated by sol–gel method. *Journal of Sol-gel Science and Technology* **2013**, *66*, 301-305.

Chapter 5: Conclusions and Recommendations for Future work

As stated in Chapter 1 of this study, organic pollutants from textile industries in wastewater are harmful to both the environment and human health. A promising solution to degrade these pollutants is semiconductor photocatalysis,[12, 13] with ZnO being a key material due to its low cost,[13] non-toxicity,[25] and stability.[26] However, ZnO's wide band gap restricts its photocatalytic activity primarily to ultraviolet (UV) light, which represents only about 5% of the solar spectrum, thus significantly reducing its efficiency under visible light that accounts for approximately 45% of solar energy.[49, 50]

To improve the photocatalytic efficiency of ZnO, doping with Sn is proposed. Sn doping can reduce the band gap and create trap states that prevent electron-hole recombination, thus enhancing photocatalytic activity.[60, 65] So, the aim of this study was the development and evaluation of a density functional theory (DFT) model to investigate the effects of Sn doping on the structural and electronic properties of ZnO to enhance its photocatalytic activity.

However, to achieve this aim, it was essential to establish a comprehensive understanding of the field of photocatalysis and identify relevant computational models. This foundational knowledge was acquired through a review of the literature presented in Chapter 2.

5.1 Conclusions and Recommendations

Building on the knowledge from the literature review, three computational models for hexagonal wurtzite, cubic rock salt, and zinc-blende ZnO[234] were developed in Chapter 3, using the Cambridge Serial Total Energy Package (CASTEP)[332] module within the Biovia Materials Studio package (MS 2020).[81] These models were validated against the literature.

The chapter began with a k-point grid and cut-off energy benchmarking to optimise computational parameters for accurately exploring ZnO crystal structure bulk properties. Compared to the other k-point grids and cut-off energies, an 11×11×11 k-point grid and 400 eV cut-off energy were found to be optimal for all bulk structures, balancing energy convergence and computational efficiency.

The study highlighted the distinct electronic properties, such as density of state (DOS), band structure, d-band centre, and structural properties, such as X-ray diffraction (XRD) patterns and surface energies, of each crystal system, focusing on their implications for potential applications in photocatalysis.

The DOS analysis revealed that zinc 3d and oxygen 2p orbitals dominated the valence band (VB), while zinc 4s orbitals were prevalent in the conduction band (CB). The calculated d-band centre values relative to the valence band maximum (VBM) for ZnO crystal systems showed slight variations, with hexagonal ZnO having the highest value at 7.204 eV, followed by zinc-blende at 6.464 eV, and cubic at 6.287 eV. These differences reflect variations in the binding strength and electronic environment of the d-electrons across the structures. The closer d-band centre to the VBM in the hexagonal system suggests stronger interactions with adsorbates, potentially improving its catalytic performance compared to the cubic and zinc-blende forms. The d-band centre analysis also showed significant interactions between p and d orbitals, particularly in the hexagonal system, affecting band gap narrowing. The computed band gaps of 0.727 eV for hexagonal, 0.730 eV for cubic, and 0.630 eV for zinc-blende aligned well with existing computational literature,[234, 351] though they underestimated the band gap in comparison with experimental values (3.370 eV for hexagonal, 2.450 eV for cubic, and 3.180 eV for zinc-blende).[238, 359, 360] Hubbard corrections with U_d-Zn and U_p-O parameters[284, 321] provided closer approximations (3.370 eV for hexagonal,[321] 4.050 eV for cubic,[284] and 3.250 eV for zinc-blende[284]) to experimental outcomes, highlighting the challenges of DFT/GGA methods in accurately predicting band gaps for complex oxides like ZnO.

The X-ray diffraction (XRD) patterns for hexagonal, cubic, and zinc-blende ZnO were calculated and compared with the literature,[80] showing close agreement with experimental data[355] despite some variations in peak intensities and slight differences in peak positions. For example, in the hexagonal crystal system, slight differences in the 2θ values were observed for peaks (100), (002), and (101), with computed values of 31.4°, 33.8°, and 35.8°, compared to experimental values of 31.4°, 34.3°, and 36.8°. These discrepancies were also seen in the corresponding peak intensities, where computed values were 35.4, 55.4, and 100.0, compared to experimental values of 50.8, 39.1, and 100.0. In the cubic crystal system, the (111) peak had a computed 2θ value of 35.7° versus an experimental value of 35.9°, with intensity values of 43.9 (computed) compared to 80.9 (experimental). For the zinc-blende system, the (111) peak showed a computed 2θ of 33.4° against an experimental value of 34.1°, with matching intensity values of 100.0. These variations and slight differences are common in computational studies and can result from sample preparation, instrument limitations, and the inherent complexity of crystal structures. The close correspondence between calculated and experimental data confirms the reliability of the computational methods employed in this study, laying the groundwork for further investigation into the electronic and structural properties of ZnO across various applications.

Additionally, surface model optimisations clarified the electronic and structural properties of various surface terminations, such as metal-terminated (MT) and oxygen-terminated (OT), across the crystal systems.

The work function analysis of the various ZnO surfaces across hexagonal, cubic, and zinc-blende crystal systems highlighted significant variations in their electronic properties, influenced by Miller planes such as (002), (101), or (100) and either MT or OT surface terminations. Among undoped ZnO, the hexagonal $(002)_{OT}$ surface exhibited the highest work function at 7.235 eV, indicating less favourable conditions for surface reactions. In contrast, the hexagonal $(101)_{MT}$ surface had the lowest work function at 3.728 eV, suggesting easier electron emission. This analysis explores how variations in work function across different Miller planes and terminations influence the catalytic activity and electron emission efficiency of ZnO, as higher work functions reduce surface reactivity while lower work functions promote electron transfer, enhancing catalytic performance.[414]

The surface energies of the ZnO surface slabs were calculated to assess stability, with notable differences between MT and OT terminated surfaces. The hexagonal crystal system exhibited the highest stability based on surface energy calculations, agreeing well with reported literature values,[364, 370, 371] confirming its thermodynamic stability. Conversely, the cubic and zinc-blende systems exhibited higher surface energies, which was consistent with the literature,[291, 362] indicating greater instability under certain conditions.

The Wulff constructions[3] based on the surface energies provided predictions of ZnO crystal morphology, which aligned well with existing literature.[297, 362] This study highlights the potential for optimising the photocatalytic performance of ZnO through further investigation of its hexagonal crystal system. Our findings aligned with experimental reports and support ongoing research in photocatalysis to exploit the unique structural stability and electronic properties of ZnO for enhanced photocatalytic applications.

In summary, Chapter 3 successfully achieved its goal of developing and validating a model for optimising and calculating the electronic and structural properties of ZnO. The study provides a refined understanding of ZnO crystal systems, supported by thorough computational modelling and comparison with experimental data.[379] The findings emphasise the importance of optimised computational parameters for accurate simulations of complex oxide materials, paving the way for future studies to enhance their electronic and structural properties for technological advancements.

In Chapter 4, the doping of Sn into the most stable ZnO crystal system, namely the hexagonal crystal system identified in Chapter 3, was explored. The Supercell program developed by Okhotnikov *et al.*[83] was used to identify unique structural configurations for 6.25%, 12.50% and 18.75% Sn-doped ZnO. These unique configurations were then optimised. The lattice parameters and cell angles for Sn-doped ZnO bulk structures closely aligned with literature values,[55, 333, 375, 376] showing deviations of only 3.648% for lattice parameters and 1.571% for cell angles observed at 6.25% and 12.50% doping concentrations, respectively. These minor differences confirmed the reliability of the approach in this study and the consistency of the modeled structures with previous studies.[55, 333, 375, 376] As Sn doping concentrations increased, there was a corresponding rise in the volume and density of the ZnO bulk structures due to the larger atomic radius of Sn compared to Zn. The 18.75% doping concentration could not be validated due to limited research available at the time of this study.

The most stable configurations of Sn-doped ZnO (within each percentage doping) based on final energies were examined to determine how varying Sn concentrations impact their structural and electronic properties.

XRD analysis confirmed the successful incorporation of Sn into the ZnO lattice, as indicated by shifts in peak intensities.[355] The (002) peak showed increased intensity with higher levels of Sn doping, suggesting that Sn atoms are substituting Zn in the lattice rather than forming separate SnO or SnO_2 phases. The increased intensity of the (002) peak in the XRD results indicated improved crystallinity along this specific plane in Sn-doped ZnO. This enhancement likely occurred because Sn atoms prefer certain substitution sites in the ZnO lattice. By replacing Zn atoms at these favoured sites, Sn contributes to a more organised and stable structure along the (002) plane, which reduces defects and structural irregularities in that direction. This improvement in atomic arrangement and crystallinity affects the electronic properties of ZnO, as the alignment of atoms influences electron movement within the lattice, thus, making doped ZnO more suitable for applications such as photocatalysis.

The higher atomic number of Sn increases the number of electrons in the system, modifying the electronic structure and affecting the DOS and band structure. The additional electrons influence defect formation and charge carrier dynamics.[415] Specifically, Sn doping shifted DOS peaks (d-band centres) to lower energies relative to pure ZnO and increased the intensity in the VB and the CB due to contributions from Sn 4d and 5s states. This adjustment introduced a shallow donor

level close to the conduction band minimum (CBM), effectively raising the electron density near the CB and enhancing n-type conductivity in ZnO.

The band gap initially decreased with increasing Sn content, then fluctuated, which was consistent with other studies.[55, 402] The study found that increasing Sn concentration at 6.25% and 12.50% resulted in an 8.84% and 15.93% difference, respectively when compared to the theoretical band gap of Sn-doped ZnO reported in the literature.[55] At the time of this study, the 18.75% Sn concentration could not be validated against theoretical literature values due to the unavailability of relevant sources. However, the calculated band gap values for Sn-doped ZnO showed significant differences compared to experimental values[321, 408-410] due to DFT/GGA method limitations. Applying the Hubbard corrections of U_d-Zn = 10 eV and U_p-O = 7 eV improved the accuracy of band gap calculations.

Sn-doping in ZnO shifted the band gap from direct to indirect as the Sn concentration increased, reducing electron transition efficiency and photocatalytic effectiveness. Some direct band gap properties were observed at lower doping levels such as 6.25%, maintaining moderate photocatalytic activity. However, higher Sn concentrations led to greater misalignment of the bands and a more pronounced indirect band gap, limiting the efficiency of Sn-doped ZnO.

Additionally, Sn doping led to notable reductions in the work function across most surfaces, particularly for the $(101)_{MT}$ and $(002)_{MT}$ surfaces. For instance, the work function of the (100) surface decreased from 4.961 eV in undoped ZnO to 3.872 eV at 6.25% Sn doping, indicating improved electronic properties beneficial for photocatalytic applications. However, the impact of Sn doping was not uniform across all surfaces. Some surfaces, such as $(101)_{MT}$ and $(102)_{MT}$, showed irregular fluctuations in work function, reflecting complex interactions between doping concentration, surface orientation (i.e. the specific Miller plane such as (101) or (102)), and electronic structure. These fluctuations were further explored using the Wulff construction method[3] and surface property analysis. It was demonstrated that doping, surface energy, and work function significantly affect the stability[416] and surface morphology of ZnO crystals.

For example, doping can lower the surface energy on certain Miller planes, such as the polar (002) plane, making these planes more stable and influencing the overall crystal morphology. This selective surface stabilisation may promote the growth of specific crystal faces, leading to morphological changes that can improve the photocatalytic efficiency of ZnO by increasing active sites or altering the surface band structure.

Using the Wulff construction method,[3] equilibrium shapes of ZnO crystals were predicted based on surface energies, highlighting the relative stability of different Miller planes. Miller planes with lower surface energies are more stable and likely to dominate the crystal's final equilibrium shape. In Sn-doped ZnO, the Wulff analysis revealed that specific crystal faces were more likely to appear due to the effect of Sn on surface energy, further influencing the morphology. The study systematically identified the most stable Sn-doped ZnO morphologies using DFT, demonstrating how Sn incorporation influences ZnO stability.

In undoped ZnO (0%), only the (100) and (103) surfaces were present, producing a hexagonal bipyramidal structure. With 6.25% Sn doping, the structure became slimmer due to decreased growth on the (100) and (103) surfaces. When the doping increased to 12.50%, the shape evolved into a truncated hexagonal prism, led by the development of the (002) surface. At 18.75% Sn, the crystal further elongated, taking on a slim hexagonal prism shape as the (103) surface disappeared and the growth of the (100) and (002) surfaces reduced. Although SEM images for each exact doping level were limited, images[69, 412, 413] at close Sn levels were used to validate the computational model, strengthening the conclusion that Sn doping significantly affects the surface morphology of ZnO as predicted. These findings could contribute to developing of advanced photocatalytic materials with notable environmental benefits.

In conclusion, this study highlights the promising role of Sn doping in ZnO for enhancing its photocatalytic properties through strategic band gap adjustment and surface morphology optimisation. These advancements hold significant promise for environmental sustainability and semiconductor technologies.

5.2 Future work

Key findings of this study include lattice expansion with increasing Sn doping, significant changes in the DOS, and a reduction in band gaps, offering valuable theoretical insights into Sn-doped ZnO. However, experimental validation is essential to corroborate computational predictions and refine doping strategies. Advanced characterisation methods such as XRD, High-Resolution Transmission Electron Microscopy (HRTEM), Scanning Electron Microscopy (SEM), and in-situ techniques can provide insights into the structural, morphological, and phase transformation changes induced by Sn doping. Specifically, exploring synthesis methodologies like chemical vapour deposition, sol-gel processes, and hydrothermal synthesis will enable precise control over

Sn doping levels, while in-situ XRD and HRTEM will allow the real-time monitoring of crystal growth and phase transitions.

Further investigation into the effects of growth conditions, including temperature, pressure, and environmental variables, is recommended, as these factors influence the kinetics of phase transformations and crystal stability. Experimental studies should systematically assess the stability of ZnO's crystal systems under various conditions and employ techniques like photoluminescence spectroscopy, time-resolved photoluminescence, and electrochemical impedance spectroscopy to unravel the mechanisms behind enhanced photocatalytic activity and charge separation in Sn-doped ZnO.

Additionally, the role of surfaces and interfaces, particularly the interactions of dopants with different Miller planes and the impact of surface energy on stability, demands detailed investigation using advanced techniques like Scanning Tunneling Microscopy (STM) and Atomic Force Microscopy (AFM). Assessing the stability of the three ZnO crystal systems requires a comprehensive analysis that considers not only surface energy but also thermodynamic and kinetic factors. A complete approach, integrating experimental observations, theoretical calculations, and a deeper understanding of the relationships between crystal structure and properties, is crucial for determining the stability of these systems. Notably, this study identified a lack of research specifically examining or validating the properties of bulk ZnO with 18.75% Sn doping, highlighting a significant gap in this area.

To complement experimental efforts, theoretical models integrating thermodynamic and kinetic factors, including DFT and molecular dynamics simulations, should be developed to predict phase transformations, energy barriers, and crystal growth pathways. By integrating experimental observations, advanced characterisation techniques, and theoretical modelling, a deeper understanding of the structural, electronic, and photocatalytic properties of Sn-doped ZnO can be achieved. This understanding enables the optimisation of its performance for applications in photocatalysis and optoelectronics.

Extending the study to include higher Sn doping concentrations beyond 18.75% and investigating larger bulk structures is recommended to explore doping limits and optimise its impact on ZnO's electronic and structural properties. This investigation would involve synthesising bulk samples with varying Sn concentrations and characterising their properties through experimental and theoretical methods. Employing multi-scale modelling techniques to bridge the gap between

atomic-scale simulations and macroscopic properties can provide a more comprehensive understanding of how atomic-level interactions influence the overall stability and properties of Sn-doped ZnO.

In addition to exploring higher Sn doping concentrations, Sn-doped ZnO can be effectively used to model degradation reactions on its surface, which is crucial for improving reaction kinetics in photocatalytic processes. By incorporating Sn into the ZnO lattice, the electronic structure of ZnO is altered, potentially creating new active sites or enhancing existing ones on the surface. These changes can improve the adsorption and activation of reactant molecules, thereby accelerating degradation reactions. Modelling these surface reactions gives understanding into the specific role that Sn plays in facilitating or hindering various reaction pathways. The reaction mechanisms can be explained through a combination of DFT calculations and kinetic modelling, allowing for the optimisation of Sn doping levels to achieve the most efficient catalytic activity. This approach not only aids in understanding the fundamental interactions at the atomic level but also in designing ZnO-based photocatalysts with superior performance in environmental remediation and other applications.

Overall, Sn doping reduces the band gap of ZnO, enhancing its efficiency as a photocatalytic material. These findings contribute to developing of advanced photocatalytic materials with substantial environmental benefits. Further exploration of Sn doping percentages and larger bulk structures is recommended to optimise these properties. By addressing the identified research gaps and employing a comprehensive approach, future research can significantly advance the understanding and application of Sn-doped ZnO in various technological and environmental fields. Future research should experimentally validate these findings and explore synthesis methods to achieve precise Sn doping levels in ZnO. Additionally, investigating the mechanisms underlying enhanced photocatalytic activity and charge separation will further improve understanding and the application potential of Sn-doped ZnO.

5.3 References

(3) Wulff, G. XXV. On the question of the rate of growth and dissolution of the crystal surfaces. *Kristallografiya* **1901**, *34*, 449-530. DOI: 10.1524/ZKRI.1901.34.1.449.

(12) Mao, T.; Liu, M.; Lin, L.; Cheng, Y.; Fang, C. A study on doping and compound of zinc oxide photocatalysts. *Polymers* **2022**, *14*. DOI: 10.3390/polym14214484.

(13) Mohamad, A. A.; Hassan, M. S.; Yaakob, M. K.; Taib, M. F. M.; Badrudin, F. W.; Hassan, O. H.; Yahya, M. Z. A. First-principles calculation on electronic properties of zinc oxide by zinc–air system. *Journal of King Saud University - Engineering Sciences* **2017**, *29* (3), 278-283. DOI: 10.1016/j.jksues.2015.08.002.

(25) Douloumis, A.; Vrithias, N. R. E.; Katsarakis, N.; Remediakis, I. N.; Kopidakis, G. Tuning the workfunction of ZnO through surface doping with Mn from first-principles simulations. *Surface Science* **2022**, *726*. DOI: 10.1016/j.susc.2022.122175.

(26) Ibrahim, A. A.; Kumar, R.; Umar, A.; Kim, S. H.; Bumajdad, A.; Ansari, Z. A.; Baskoutas, S. Cauliflower-shaped ZnO nanomaterials for electrochemical sensing and photocatalytic applications. *Electrochimica Acta* **2016**, *222*, 463-472. DOI: 10.1016/J.ELECTACTA.2016.10.199.

(49) Li, W.; Wang, G.; Feng, Y.; Li, Z. Efficient photocatalytic performance enhancement in Co-doped ZnO nanowires coupled with CuS nanoparticles. *Applied Surface Science* **2018**, *428*, 154-164. DOI: 10.1016/J.APSUSC.2017.09.049.

(50) Xiaohua, Z.; Shuai, S.; Guangli, W.; Caizhu, L.; Zhe, Q.; Xiangdong, L.; Jianguo, Z. Facile synthesis of the flower-like ternary heterostructure of Ag/ZnO encapsulating carbon spheres with enhanced photocatalytic performance. *Applied Surface Science* **2017**, *406*, 1-11.

(55) Yang, W.; Zhang, B.; Zhang, Q.; Wang, L.; Song, B.; Ding, Y.; Wong, C. Adjusting the band structure and defects of ZnO quantum dots via tin doping. *RSC Advances* **2017**, *7* (19), 11345-11354.

(60) Dawson, M. Synthesis and characterization of $CH_3NH_3SnI_3$, Mn doped $CH_3NH_3SnI_3$ and oxygen-deficient TiO_2 as visible-light active semiconductors. Universidade Federal de São Carlos, São Carlos, 2020.

(65) Henrich, V. E.; Cox, P. A. *The surface science of metal oxides*; Cambridge university press, **1994**.

(69) Agarwal, M. B.; Sharma, A.; Malaidurai, M.; Thangavel, R. Effect of Sn doping on structural, mechanical, optical and electrical properties of ZnO nanoarrays prepared by sol-gel and hydrothermal process. *Superlattices and Microstructures* **2018**, *117*, 342-350.

(80) Oyewo, O. A.; Ramaila, S.; Mavuru, L.; Onwudiwe, D. C. Enhanced photocatalytic degradation of methyl orange using Sn-ZnO/GO nanocomposite. *Journal of Photochemistry and Photobiology* **2022**, *11*. DOI: 10.1016/j.jpap.2022.100131.

(81) Dassault; Systemes. *Biovia Material Studio Castep*. **2020**. https://www.3ds.com/fileadmin/PRODUCTS-SERVICES/BIOVIA/PDF/biovia-material-studio-castep.pdf (accessed 2023 April 08, 2023).

(83) Okhotnikov, K.; Charpentier, T.; Cadars, S. Supercell program: a combinatorial structure-generation approach for the local-level modeling of atomic substitutions and partial occupancies in crystals. *Journal of Cheminformatics* **2016**, *8*, 1-15.

(234) Charifi, Z.; Baaziz, H.; Hussain Reshak, A. Ab-initio investigation of structural, electronic and optical properties for three phases of ZnO compound. *Physica Status Solidi (b)* **2007**, *244* (9), 3154-3167. DOI: 10.1002/pssb.200642471.

(238) Kim, S.-K.; Jeong, S.-Y.; Cho, C.-R. Structural reconstruction of hexagonal to cubic ZnO films on Pt/Ti/SiO_2/Si substrate by annealing. *Applied Physics Letters* **2003**, *82* (4), 562-564.

(284) Ma, X.; Wu, Y.; Lv, Y.; Zhu, Y. Correlation effects on lattice relaxation and electronic structure of ZnO within the GGA+ U formalism. *The Journal of Physical Chemistry C* **2013**, *117* (49), 26029-26039.

(291) Tang, C.; Spencer, M. J. S.; Barnard, A. S. Activity of ZnO polar surfaces: an insight from surface energies. *Physical Chemistry Chemical Physics* **2014**, *16*, 22139-22144. DOI: 10.1039/C4CP03221G.

(297) Catto, A. C.; Ferrer, M. M.; Lopes, O. F.; Mastelaro, V. R.; Andrés, J.; da Silva, L. F.; Longo, E.; Avansi, W. The role of counter-ions in crystal morphology, surface structure and photocatalytic activity of ZnO crystals grown onto a substrate. *Applied Surface Science* **2020**, *529*, 147057. DOI: 10.1016/j.apsusc.2020.147057.

(321) Supatutkul, C.; Pramchu, S.; Jaroenjittichai, A. P.; Laosiritaworn, Y. Density functional theory investigation of surface defects in Sn-doped ZnO. *Surface and Coatings Technology* **2016**, *298*, 53-57. DOI: 10.1016/j.surfcoat.2016.04.013.

(332) Clark, S. J.; Segall, M. D.; Pickard, C. J.; Hasnip, P. J.; Probert, M. I. J.; Refson, K.; Payne, M. C. First principles methods using CASTEP. *Zeitschrift für Kristallographie - Crystalline Materials* **2005**, *220* (5-6), 567-570. DOI: 10.1524/zkri.220.5.567.65075.

(333) Jain, A.; Ong, S. P.; Hautier, G.; Chen, W.; Richards, W. D.; Dacek, S.; Cholia, S.; Gunter, D.; Skinner, D.; Ceder, G.; et al. The materials project: A materials genome approach to accelerating materials innovation. *APL Materials* **2013**, *1* (1), 011002. DOI: 10.1063/1.4812323.

(351) Schleife, A.; Fuchs, F.; Furthmüller, J.; Bechstedt, F. First-principles study of ground- and excited-state properties of MgO, ZnO, and CdO polymorphs. *Physical Review B* **2006**, *73*, 245212. DOI: 10.1103/PHYSREVB.73.245212/FIGURES/9/MEDIUM.

(355) Hubbard, C.; O'Connor, B. International centre for diffraction data (ICDD). **2002**.

(359) Segura, A.; Sans, J.; Manjón, F.; Munoz, A.; Herrera-Cabrera, M. Optical properties and electronic structure of rock-salt ZnO under pressure. *Applied Physics Letters* **2003**, *83* (2), 278-280.

(360) Martínez-Pérez, L.; Muñoz-Aguirre, N.; Muñoz-Aguirre, S.; Zelaya-Angel, O. Nanometric structures of highly oriented zinc blende ZnO thin films. *Materials Letters* **2015**, *139*, 63-65. DOI: 10.1016/j.matlet.2014.10.054.

(362) Koster, R. S.; Fang, C. M.; Dijkstra, M.; Van Blaaderen, A.; Van Huis, M. A. Stabilization of rock salt ZnO nanocrystals by low-energy surfaces and Mg additions: A first-principles study. *The Journal of Physical Chemistry C* **2015**, *119* (10), 5648-5656. DOI: 10.1021/jp511503b.

(364) Sun, B.; Yang, X.; Zhao, D.; Zhang, L. First-principles study of adsorption mechanism of NH_3 on different ZnO surfaces on organics photocatalytic degradation purpose. *Computational Materials Science* **2018**, *141*, 133-140. DOI: 10.1016/J.COMMATSCI.2017.09.013.

(370) Na, S.-H.; Park, C.-H. First-principles study of the surface of wurtzite ZnO and ZnS - implications for nanostructure formation. *Journal of the Korean Physical Society* **2009**, *54* (9(2)), 867-872. DOI: 10.3938/jkps.54.867.

(371) Jiang, W.; Xia, Y.; Pan, A.; Luo, Y.; Su, Y.; Zhao, S.; Wang, T.; Zhao, L. Facet-dependent gas adsorption selectivity on ZnO: A DFT study. *Chemosensors* **2022**, *10* (10), 436. DOI: 10.3390/chemosensors10100436.

(375) Muiva, C.; Sathiaraj, S. T.; Maabong, K. Chemical spray pyrolysis path to synthesis of ZnO microsausages from aggregation of elongated double tipped nanoparticles. *Materials Science Forum* **2012**, *706-709*, 2577-2582. DOI: 10.4028/MSF.706-709.2577.

(376) Wróbel, J.; Kurzydłowski, K. J.; Hummer, K.; Kresse, G.; Piechota, J. Calculations of ZnO properties using the Heyd-Scuseria-Ernzerhof screened hybrid density functional. *Physical Review B* **2009**, *80* (15). DOI: 10.1103/PhysRevB.80.155124.

(379) Sokolov, P. S.; Baranov, A. N.; Dobrokhotov, Z. V.; Solozhenko, V. L. Synthesis and thermal stability of cubic ZnO in the salt nanocomposites. *Russian Chemical Bulletin* **2010**, *59* (2), 325-328. DOI: 10.1007/s11172-010-0082-7.

(402) Onwudiwe, D. C. Photocatalytic reduction of hexavalent chromium using Zn_2SnO_4–ZnO modified g-C_3N_4 composite. North-West University: 2023.

(408) Shanshool, H. M.; Yahaya, M.; Yunus, W. M. M.; Abdullah, I. Y. Investigation of energy band gap in polymer/ZnO nanocomposites. *Journal of Materials Science: Materials in Electronics* **2016**, *27*, 9804-9811.

(409) Yung, K. C.; Liem, H.; Choy, H. Enhanced redshift of the optical band gap in Sn-doped ZnO free standing films using the sol–gel method. *Journal of Physics D: Applied Physics* **2009**, *42* (18), 185002.

(410) Cheng, J.; Zhang, Y.; Guo, R. ZnO microtube ultraviolet detectors. *Journal of Crystal Growth* **2008**, *310* (1), 57-61.

(412) Thomas, D.; Vattappalam, S. C.; Mathew, S.; Augustine, S. Appraisal on textured grain growth and photoconductivity of ZnO thin film SILAR. *Advances in Chemistry* **2014**, *549019*.

(413) Shi, X.; Zhao, X.; Duan, L.; Sun, H.; Liu, J.; Bai, X.; Guan, M.; Cao, M.; Liu, J. Notable shift of ultraviolet intensity on Sn-doped ZnO nanostructure fabricated by sol–gel method. *Journal of Sol-gel Science and Technology* **2013**, *66*, 301-305.

(414) Chen, L.; Ren, J. T.; Yuan, Z. Y. Enabling internal electric fields to enhance energy and environmental catalysis. *Advanced Energy Materials* **2023**, *13* (11), 2203720.

(415) Su, J.; Shi, Y.; Liu, L.; An, X.; Wang, Y.; Wang, K.; Niu, Q. Tin doping modulates electron-hole recombination in Dion-Jacobson phase 2D hybrid perovskite. *Physica B: Condensed Matter* **2024**, *690*, 416276.

(416) Ameen, S.; Akhtar, M. S.; Seo, H.-K.; Kim, Y. S.; Shin, H. S. Influence of Sn doping on ZnO nanostructures from nanoparticles to spindle shape and their photoelectrochemical properties for dye sensitized solar cells. *Chemical Engineering Journal* **2012**, *187*, 351-356.

Bibliography

(1) *Manual for Masters and Doctoral Studies, 2016*. North-West University, https://services.nwu.ac.za/sites/services.nwu.ac.za/files/files/research-support/documents/2016-04-06%20ICRI%20Manual%20for%20M%20and%20D%20students.pdf (accessed July 02, 2024).

(2) Rahm, J.; Erhart, P. WulffPack: A Python package for Wulff constructions. *Journal of Open Source Software* **2020**, *5*, 1944. DOI: 10.21105/joss.01944.

(3) Wulff, G. XXV. On the question of the rate of growth and dissolution of the crystal surfaces. *Kristallografiya* **1901**, *34*, 449-530. DOI: 10.1524/ZKRI.1901.34.1.449.

(4) Rajamanickam, D.; Shanthi, M. Photocatalytic degradation of an organic pollutant by zinc oxide – solar process. *Arabian Journal of Chemistry* **2016**, *9*, S1858-S1868. DOI: 10.1016/j.arabjc.2012.05.006.

(5) Ksibi, M.; Zemzemi, A.; Boukchina, R. Photocatalytic degradability of substituted phenols over UV irradiated TiO_2. *Journal of Photochemistry and Photobiology A: Chemistry* **2003**, *159* (1), 61-70.

(6) Abou Zeid, S.; Perez, A.; Bastide, S.; Le Pivert, M.; Rossano, S.; Remita, H.; Hautière, N.; Leprince-Wang, Y. Antibacterial and photocatalytic properties of ZnO nanostructure decorated coatings. *Coatings* **2023**, *14* (1), 41.

(7) Czech, B.; Zygmunt, P.; Kadirova, Z. C.; Yubuta, K.; Hojamberdiev, M. Effective photocatalytic removal of selected pharmaceuticals and personal care products by elsmoreite/tungsten oxide@ ZnS photocatalyst. *Journal of Environmental Management* **2020**, *270*, 110870.

(8) Villani, M.; Calestani, D.; Lazzarini, L.; Zanotti, L.; Mosca, R.; Zappettini, A. Extended functionality of ZnO nanotetrapods by solution-based coupling with CdS nanoparticles. *Journal of Materials Chemistry* **2012**, *22*, 5694-5699. DOI: 10.1039/c2jm16164h.

(9) Akintelu, S. A.; Folorunso, A. S.; Folorunso, F. A.; Oyebamiji, A. K. Green synthesis of copper oxide nanoparticles for biomedical application and environmental remediation. *Heliyon* **2020**, *6* (7).

(10) Masudy-Panah, S.; Katal, R.; Khiavi, N. D.; Shekarian, E.; Hu, J.; Gong, X. A high-performance cupric oxide photocatalyst with palladium light trapping nanostructures and a hole transporting layer for photoelectrochemical hydrogen evolution. *Journal of Materials Chemistry A* **2019**, *7* (39), 22332-22345.

(11) Sabzehei, K.; Hadavi, S.; Bajestani, M. G.; Sheibani, S. Comparative evaluation of copper oxide nano-photocatalyst characteristics by formation of composite with TiO_2 and ZnO. *Solid State Sciences* **2020**, *107*, 106362.

(12) Mao, T.; Liu, M.; Lin, L.; Cheng, Y.; Fang, C. A study on doping and compound of zinc oxide photocatalysts. *Polymers* **2022**, *14*. DOI: 10.3390/polym14214484.

(13) Mohamad, A. A.; Hassan, M. S.; Yaakob, M. K.; Taib, M. F. M.; Badrudin, F. W.; Hassan, O. H.; Yahya, M. Z. A. First-principles calculation on electronic properties of zinc oxide by zinc–air system. *Journal of King Saud University - Engineering Sciences* **2017**, *29* (3), 278-283. DOI: 10.1016/j.jksues.2015.08.002.

(14) Kumar, S. G.; Rao, K. K. Comparison of modification strategies towards enhanced charge carrier separation and photocatalytic degradation activity of metal oxide semiconductors (TiO_2, WO_3 and ZnO). *Applied Surface Science* **2017**, *391*, 124-148.

(15) Hoffmann, M. R.; Martin, S. T.; Choi, W.; Bahnemann, D. W. Environmental applications of semiconductor photocatalysis. *Chemical Reviews* **1995**, *95* (1), 69-96. DOI: 10.1021/cr00033a004.

(16) Roselin, L. S.; Rajarajeswari, G.; Selvin, R.; Sadasivam, V.; Sivasankar, B.; Rengaraj, K. Sunlight/ZnO-mediated photocatalytic degradation of reactive red 22 using thin film flat bed flow photoreactor. *Solar Energy* **2002**, *73* (4), 281-285.

(17) Pelaez, M.; Nolan, N. T.; Pillai, S. C.; Seery, M. K.; Falaras, P.; Kontos, A. G.; Dunlop, P. S. M.; Hamilton, J. W. J.; Byrne, J. A.; O'Shea, K.; et al. A review on the visible light active titanium dioxide photocatalysts for environmental applications. *Applied Catalysis B: Environmental* **2012**, *125*, 331-349. DOI: 10.1016/j.apcatb.2012.05.036.

(18) Xie, L.; Du, T.; Wang, J.; Ma, Y.; Ni, Y.; Liu, Z.; Zhang, L.; Yang, C.; Wang, J. Recent advances on heterojunction-based photocatalysts for the degradation of persistent organic pollutants. *Chemical Engineering Journal* **2021**, *426*, 130617.

(19) Thompson, T. L.; Yates, J. T. Surface science studies of the photoactivation of TiO_2 new photochemical processes. *Chemical Reviews* **2006**, *106* (10), 4428-4453. DOI: 10.1021/cr050172k.

(20) Linsebigler, A. L.; Lu, G.; Yates, J. T., Jr. Photocatalysis on TiO_2 surfaces: principles, mechanisms, and selected results. *Chemical Reviews* **1995**, *95* (3), 735-758. DOI: 10.1021/cr00035a013.

(21) Goi, A.; Trapido, M.; Tuhkanen, T. A study of toxicity, biodegradability, and some by-products of ozonised nitrophenols. *Advances in Environmental Research* **2004**, *8* (3), 303-311. DOI: 10.1016/S1093-0191(02)00102-8.

(22) Derikvandi, H.; Nezamzadeh-Ejhieh, A. Increased photocatalytic activity of NiO and ZnO in photodegradation of a model drug aqueous solution: Effect of coupling, supporting, particles size and calcination temperature. *Journal of Hazardous Materials* **2017**, *321*, 629-638. DOI: 10.1016/j.jhazmat.2016.09.056.

(23) Nezamzadeh-Ejhieh, A.; Khorsandi, S. Photocatalytic degradation of 4-nitrophenol with ZnO supported nano-clinoptilolite zeolite. *Journal of Industrial and Engineering Chemistry* **2014**, *20* (3), 937-946. DOI: 10.1016/j.jiec.2013.06.026.

(24) Di Paola, A.; Augugliaro, V.; Palmisano, L.; Pantaleo, G.; Savinov, E. Heterogeneous photocatalytic degradation of nitrophenols. *Journal of Photochemistry and Photobiology A: Chemistry* **2003**, *155* (1), 207-214. DOI: 10.1016/S1010-6030(02)00390-8.

(25) Douloumis, A.; Vrithias, N. R. E.; Katsarakis, N.; Remediakis, I. N.; Kopidakis, G. Tuning the workfunction of ZnO through surface doping with Mn from first-principles simulations. *Surface Science* **2022**, *726*. DOI: 10.1016/j.susc.2022.122175.

(26) Ibrahim, A. A.; Kumar, R.; Umar, A.; Kim, S. H.; Bumajdad, A.; Ansari, Z. A.; Baskoutas, S. Cauliflower-shaped ZnO nanomaterials for electrochemical sensing and photocatalytic applications. *Electrochimica Acta* **2016**, *222*, 463-472. DOI: 10.1016/J.ELECTACTA.2016.10.199.

(27) Mohd Adnan, M. A.; Julkapli, N. M.; Abd Hamid, S. B. Review on ZnO hybrid photocatalyst: Impact on photocatalytic activities of water pollutant degradation. *Reviews in Inorganic Chemistry* **2016**, *36*, 77-104. DOI: 10.1515/revic-2015-0015.

(28) Morkoç, H.; Özgür, U. m. Zinc oxide: Fundamentals, materials and device technology. *British Library Cataloguing-in-Publication Data* **2009**, 477.

(29) Farmer, N.; O'Neill, H. S. C. The miscibility gap between the rock salt and wurtzite phases in the MgO–ZnO binary system to 3.5 GPa. *European Journal of Mineralogy* **2023**, *35* (6), 1051-1071.

(30) Shabbir, S.; Shaari, A.; Haq, B. U.; Ahmed, R.; Ahmed, M. Investigations of novel polymorphs of ZnO for optoelectronic applications. *Optik* **2020**, *206*, 164285.

(31) Qi, K.; Xing, X.; Zada, A.; Li, M.; Wang, Q.; Liu, S.-y.; Lin, H.; Wang, G. Transition metal doped ZnO nanoparticles with enhanced photocatalytic and antibacterial performances: Experimental and DFT studies. *Ceramics International* **2020**, *46* (2), 1494-1502. DOI: 10.1016/j.ceramint.2019.09.116.

(32) Dedova, T. *Chemical spray pyrolysis deposition of zinc sulfide thin films and zinc oxide nanostructured layers*; Tallinn University of Technology Tallinn, Estonia, **2007**.

(33) Yates, B.; Cooper, R.; Kreitman, M. Low-temperature thermal expansion of zinc oxide. Vibrations in zinc oxide and sphalerite zinc sulfide. *Physical Review B* **1971**, *4* (4), 1314.

(34) Sahani, R.; Dixit, A. A comprehensive review on zinc oxide bulk and nano-structured materials for ionizing radiation detection and measurement applications. *Materials Science in Semiconductor Processing* **2022**, *151*, 107040.

(35) Coleman, V. A.; Jagadish, C. Basic properties and applications of ZnO. In *Zinc oxide bulk, thin films and nanostructures*, Elsevier, **2006**; pp 1-20.

(36) Klingshirn, C. F.; Meyer, B. K.; Waag, A.; Hoffmann, A.; Geurts, J.; Geurts, J. Crystal structure, chemical binding, and lattice properties. In *In Zinc Oxide: from fundamental properties towards novel applications*, Springer, 2010; pp 7-37.

(37) Fan, Z.; Lu, J. G. Zinc oxide nanostructures: synthesis and properties. *Journal of Nanoscience and Nanotechnology* **2005**, *5* (10), 1561-1573.

(38) Kishwar, S.; Hasan, K.; Tzamalis, G.; Nur, O.; Willander, M.; Kwack, H.; Dang, D. L. S. Electro-optical and cathodoluminescence properties of low temperature grown ZnO nanorods/p-GaN white light emitting diodes. *Physica Status Solidi (a)* **2010**, *207* (1), 67-72.

(39) Ivanov, I.; Pollman, J. First surface electronic structure of a wurtzite-type semiconductor the polar and nonpolar surfaces of ZnO. *Solid State Communications* **1980**, *36* (4), 361-364.

(40) Ul Hasan, K.; Alvi, N.; Lu, J.; Nur, O.; Willander, M. Single nanowire-based UV photodetectors for fast switching. *Nanoscale Research Letters* **2011**, *6*, 1-6.

(41) Özgür, Ü.; Hofstetter, D.; Morkoc, H. ZnO devices and applications: a review of current status and future prospects. *Proceedings of the IEEE* **2010**, *98* (7), 1255-1268.

(42) Liu, K.; Sakurai, M.; Aono, M. ZnO-based ultraviolet photodetectors. *Sensors* **2010**, *10* (9), 8604-8634.

(43) Panda, N.; Sahu, D.; Acharya, B.; Nayak, P. High UV absorption efficiency of nanocrystalline ZnO synthesized by ultrasound assisted wet chemical method. *Current Applied Physics* **2015**, *15* (3), 389-396.

(44) Rahman, F. Zinc oxide light-emitting diodes: a review. *Optical Engineering* **2019**, *58* (1), 010901-010901.

(45) Sharma, D. K.; Shukla, S.; Sharma, K. K.; Kumar, V. A review on ZnO: Fundamental properties and applications. *Materials Today: Proceedings* **2022**, *49*, 3028-3035.

(46) Ahmaruzzaman, M. Metal oxides (ZnO, CuO and NiO)-based nanostructured materials for photocatalytic remediation of organic contaminants. *Nanotechnology for Environmental Engineering* **2023**, *8* (1), 219-235.

(47) Güell, F.; Galdámez-Martínez, A.; Martínez-Alanis, P. R.; Catto, A. C.; da Silva, L. F.; Mastelaro, V. R.; Santana, G.; na Dutt, A. ZnO-based nanomaterials approach for photocatalytic and sensing applications: recent progress and trends. *Materials Advances* **2023**, *4*, 3685-3707.

(48) Ong, C. B.; Ng, L. Y.; Mohammad, A. W. A review of ZnO nanoparticles as solar photocatalysts: Synthesis, mechanisms and applications. *Renewable and Sustainable Energy Reviews* **2018**, *81*, 536-551.

(49) Li, W.; Wang, G.; Feng, Y.; Li, Z. Efficient photocatalytic performance enhancement in Co-doped ZnO nanowires coupled with CuS nanoparticles. *Applied Surface Science* **2018**, *428*, 154-164. DOI: 10.1016/J.APSUSC.2017.09.049.

(50) Xiaohua, Z.; Shuai, S.; Guangli, W.; Caizhu, L.; Zhe, Q.; Xiangdong, L.; Jianguo, Z. Facile synthesis of the flower-like ternary heterostructure of Ag/ZnO encapsulating carbon spheres with enhanced photocatalytic performance. *Applied Surface Science* **2017**, *406*, 1-11.

(51) Khaki, M. R. D.; Shafeeyan, M. S.; Raman, A. A. A.; Daud, W. M. A. W. Application of doped photocatalysts for organic pollutant degradation-A review. *Journal of Environmental Management* **2017**, *198*, 78-94.

(52) Khan, H.; Shah, M. U. H. Modification strategies of TiO_2 based photocatalysts for enhanced visible light activity and energy storage ability: A review. *Journal of Environmental Chemical Engineering* **2023**, 111532.

(53) Height, M. J.; Pratsinis, S. E.; Mekasuwandumrong, O.; Praserthdam, P. Ag-ZnO catalysts for UV-photodegradation of methylene blue. *Applied Catalysis B: Environmental* **2006**, *63* (3-4), 305-312.

(54) Zhou, S. Y.; Gweon, G. H.; Fedorov, A. V.; First, P.; De Heer, W. A.; Lee, D. H.; Guinea, F.; Castro Neto, A. H.; Lanzara, A. Substrate-induced bandgap opening in epitaxial graphene. *Nature Materials* **2007**, *6* (10), 770-775.

(55) Yang, W.; Zhang, B.; Zhang, Q.; Wang, L.; Song, B.; Ding, Y.; Wong, C. Adjusting the band structure and defects of ZnO quantum dots via tin doping. *RSC Advances* **2017**, *7* (19), 11345-11354.

(56) Zhang, S.; Wang, J.; Wang, J.; Wang, K.-Y.; Zhao, M.; Zhang, L.; Wang, C. A gradient Sn^{4+}@ Sn^{2+} core@ shell structure induced by a strong metal oxide–support interaction for enhanced CO_2 electroreduction. *Dalton Transactions* **2022**, *51* (42), 16135-16144.

(57) Zatsepin, D.; Boukhvalov, D.; Kurmaev, E.; Zhidkov, I.; Kim, S.; Cui, L.; Gavrilov, N.; Cholakh, S. XPS and DFT study of Sn incorporation into ZnO and TiO_2 host matrices by pulsed ion implantation. *Physica Status Solidi (b)* **2015**, *252* (8), 1890-1896.

(58) Batzill, M.; Diebold, U. The surface and materials science of tin oxide. *Progress in Surface Science* **2005**, *79* (2-4), 47-154.

(59) Das, A.; Gautam, S. K.; Shukla, D.; Singh, F. Correlations of charge neutrality level with electronic structure and pd hybridization. *Scientific Reports* **2017**, *7* (1), 40843.

(60) Dawson, M. Synthesis and characterization of $CH_3NH_3SnI_3$, Mn doped $CH_3NH_3SnI_3$ and oxygen-deficient TiO_2 as visible-light active semiconductors. Universidade Federal de São Carlos, São Carlos, 2020.

(61) Prakash, T.; Jayaprakash, R.; Espro, C.; Neri, G.; Ranjith Kumar, E. Effect of Sn doping on microstructural and optical properties of ZnO nanoparticles synthesized by microwave irradiation method. *Journal of Materials Science* **2014**, *49*, 1776-1784.

(62) Su, Y.; Zhu, B.; Guan, K.; Gao, S.; Lv, L.; Du, C.; Peng, L.; Hou, L.; Wang, X. Particle size and structural control of $ZnWO_4$ nanocrystals via Sn^{2+} doping for tunable optical and visible photocatalytic properties. *The Journal of Physical Chemistry C* **2012**, *116* (34), 18508-18517.

(63) Bagus, P. S.; Illas, F.; Pacchioni, G.; Parmigiani, F. Mechanisms responsible for chemical shifts of core-level binding energies and their relationship to chemical bonding. *Journal of Electron Spectroscopy and Related Phenomena* **1999**, *100* (1-3), 215-236.

(64) Zhang, Y.; Zhou, J.; Chen, X.; Feng, Q.; Cai, W. MOF-derived C-doped ZnO composites for enhanced photocatalytic performance under visible light. *Journal of Alloys and Compounds* **2019**, *777*, 109-118.

(65) Henrich, V. E.; Cox, P. A. *The surface science of metal oxides*; Cambridge university press, **1994**.

(66) Zhou, W.; Fu, H. Defect-mediated electron–hole separation in semiconductor photocatalysis. *Inorganic Chemistry Frontiers* **2018**, *5* (6), 1240-1254.

(67) Rahman, F. Solid-state lighting with wide band gap semiconductors. *MRS Energy & Sustainability* **2014**, *1*, E6.

(68) Bozyigit, D.; Lin, W. M.; Yazdani, N.; Yarema, O.; Wood, V. A quantitative model for charge carrier transport, trapping and recombination in nanocrystal-based solar cells. *Nature communications* **2015**, *6* (1), 6180.

(69) Agarwal, M. B.; Sharma, A.; Malaidurai, M.; Thangavel, R. Effect of Sn doping on structural, mechanical, optical and electrical properties of ZnO nanoarrays prepared by sol-gel and hydrothermal process. *Superlattices and Microstructures* **2018**, *117*, 342-350.

(70) Aydin, H.; El-Nasser, H.; Aydin, C.; Al-Ghamdi, A. A.; Yakuphanoglu, F. Synthesis and characterization of nanostructured undoped and Sn-doped ZnO thin films via sol–gel approach. *Applied Surface Science* **2015**, *350*, 109-114.

(71) Beura, R.; Pachaiappan, R.; Thangadurai, P. A detailed study on Sn^{4+} doped ZnO for enhanced photocatalytic degradation. *Applied Surface Science* **2018**, *433*, 887-898. DOI: 10.1016/j.apsusc.2017.10.127.

(72) Beura, R.; Thangadurai, P. Effect of Sn doping in ZnO on the photocatalytic activity of ZnO-Graphene nanocomposite with improved activity. *Journal of Environmental Chemical Engineering* **2018**, *6* (4), 5087-5100.

(73) Caglar, Y.; Aksoy, S.; Ilican, S.; Caglar, M. Crystalline structure and morphological properties of undoped and Sn doped ZnO thin films. *Superlattices and Microstructures* **2009**, *46* (3), 469-475. DOI: 10.1016/j.spmi.2009.05.005.

(74) Dhamodharan, P.; Manoharan, C.; Dhanapandian, S.; Bououdina, M.; Ramalingam, S. Preparation and characterization of spray deposited Sn-doped ZnO thin films onto ITO subtracts as photoanode in dye sensitized solar cell. *Journal of Materials Science: Materials in Electronics* **2015**, *26*, 4830-4839.

(75) Fu, J.; Yu, J.; Jiang, C.; Cheng, B. g-C_3N_4-based heterostructured photocatalysts. *Advanced Energy Materials* **2018**, *8* (3). DOI: 10.1002/aenm.201701503.

(76) Ramalingam, G.; Perumal, N.; Priya, A.; Rajendran, S. A review of graphene-based semiconductors for photocatalytic degradation of pollutants in wastewater. *Chemosphere* **2022**, *300*, 134391.

(77) Weldegebrieal, G. K. Synthesis method, antibacterial and photocatalytic activity of ZnO nanoparticles for azo dyes in wastewater treatment: A review. *Inorganic Chemistry Communications* **2020**, *120*, 108140.

(78) Baibara, O.; Radchenko, M.; Karpyna, V.; Ievtushenko, A. A review of the some aspects for the development of ZnO based photocatalysts for a variety of applications. *Physics and Chemistry of Solid State* **2021**, *22* (3), 585-594.

(79) Verma, R.; Pathak, S.; Srivastava, A. K.; Prawer, S.; Tomljenovic-Hanic, S. ZnO nanomaterials: Green synthesis, toxicity evaluation and new insights in biomedical applications. *Journal of Alloys and Compounds* **2021**, *876*, 160175.

(80) Oyewo, O. A.; Ramaila, S.; Mavuru, L.; Onwudiwe, D. C. Enhanced photocatalytic degradation of methyl orange using Sn-ZnO/GO nanocomposite. *Journal of Photochemistry and Photobiology* **2022**, *11*. DOI: 10.1016/j.jpap.2022.100131.

(81) Dassault; Systemes. *Biovia Material Studio Castep*. **2020**. https://www.3ds.com/fileadmin/PRODUCTS-SERVICES/BIOVIA/PDF/biovia-material-studio-castep.pdf (accessed 2023 April 08, 2023).

(82) *National Intergrated Cyberinfrastructure System (NICIS) - Centre for High Performance Computing (CHPC)*. **2017**. https://www.chpc.ac.za/index.php/resources). (accessed 2023 April 08, 2023).

(83) Okhotnikov, K.; Charpentier, T.; Cadars, S. Supercell program: a combinatorial structure-generation approach for the local-level modeling of atomic substitutions and partial occupancies in crystals. *Journal of Cheminformatics* **2016**, *8*, 1-15.

(84) Huang, B.; Lei, C.; Wei, C.; Zeng, G. Chlorinated volatile organic compounds (Cl-VOCs) in environment—sources, potential human health impacts, and current remediation technologies. *Environment International* **2014**, *71*, 118-138.

(85) Field, J.; Sierra-Alvarez, R. Biodegradability of chlorinated aromatic compounds. *Science dossier. Euro Chlor* **2007**, 15-33.

(86) Hanafi, M. F.; Sapawe, N. A review on the water problem associate with organic pollutants derived from phenol, methyl orange, and remazol brilliant blue dyes. *Materials Today: Proceedings* **2020**, *31*, A141-A150.

(87) Alsukaibi, A. K. Various approaches for the detoxification of toxic dyes in wastewater. *Processes* **2022**, *10* (10), 1968.

(88) Cheng, M.; Zeng, G.; Huang, D.; Yang, C.; Lai, C.; Zhang, C.; Liu, Y. Tween 80 surfactant-enhanced bioremediation: toward a solution to the soil contamination by hydrophobic organic compounds. *Critical Reviews in Biotechnology* **2018**, *38* (1), 17-30.

(89) Jackson, M.; Eadsforth, C.; Schowanek, D.; Delfosse, T.; Riddle, A.; Budgen, N. Comprehensive review of several surfactants in marine environments: fate and ecotoxicity. *Environmental Toxicology and Chemistry* **2016**, *35* (5), 1077-1086.

(90) Cameotra, S. S.; Dhanjal, S. Environmental nanotechnology: nanoparticles for bioremediation of toxic pollutants. In *Bioremediation technology: recent advances*, Springer, **2010**; pp 348-374.

(91) Long, J. L.; Stensel, H. D.; Ferguson, J. F.; Strand, S. E.; Ongerth, J. E. Anaerobic and aerobic treatment of chlorinated aliphatic compounds. *Journal of Environmental Engineering* **1993**, *119* (2), 300-320.

(92) Tibui, A. Biodegradation of aliphatic chlorinated hydrocarbon (PCE, TCE and DCE) in contaminated soil. Universitetsbibliotek: **2006**.

(93) Syal, S. *Reductive dechlorination in a continuous flow electrolysis cell*; Michigan State University, **1992**.

(94) Doherty, R. E. A history of the production and use of carbon tetrachloride, tetrachloroethylene, trichloroethylene and 1, 1, 1-trichloroethane in the United States: part 1—historical background; carbon tetrachloride and tetrachloroethylene. *Environmental Forensics* **2000**, *1* (2), 69-81.

(95) Zachara, J.; Wobber, F. RG Riley. **1992**.

(96) Lash, L. H.; Parker, J. C. Hepatic and renal toxicities associated with perchloroethylene. *Pharmacological Reviews* **2001**, *53* (2), 177-208.

(97) Wuebbles, D.; Patten, K.; Wang, D.; Youn, D.; Martínez-Avilés, M.; Francisco, J. Three-dimensional model evaluation of the Ozone Depletion Potentials for n-propyl bromide, trichloroethylene and perchloroethylene. *Atmospheric Chemistry & Physics Discussions* **2010**, *10* (7).

(98) Liu, Z. *Reductive dehalogenation of chlorinated aliphatic compounds in electrolytic systems*; The University of Arizona, **1999**.

(99) Rouf, Z.; Dar, I. Y.; Javaid, M.; Dar, M. Y.; Jehangir, A. Volatile organic compounds emission from building sector and its adverse effects on human health. *Ecological and Health Effects of Building Materials* **2022**, 67-86.

(100) Alimba, C. G. Dna and systemic damage induced by landfill leachates, and health impacts of human exposure to landfills in Lagos and Ibadan, Nigeria. University of Ibadan, **2013**.

(101) Chaturvedi, S.; Khurana, S. P. Importance of actinobacteria for bioremediation. In *In Plant biotechnology: progress in genomic era*, Springer, 2019; pp 277-307.

(102) Mukherjee, A. K.; Bordoloi, N. K. Biodegradation of benzene, toluene, and xylene (BTX) in liquid culture and in soil by Bacillus subtilis and Pseudomonas aeruginosa strains and a formulated bacterial consortium. *Environmental Science and Pollution Research* **2012**, *19*, 3380-3388.

(103) Cagliari, J.; Fedrizzi, F.; Rodrigues Finotti, A.; Echevenguá Teixeira, C.; do Nascimento Filho, I. Volatilization of monoaromatic compounds (benzene, toluene, and xylenes; BTX) from gasoline: Effect of the ethanol. *Environmental Toxicology and Chemistry: An International Journal* **2010**, *29* (4), 808-812.

(104) Liu, K.; Ramirez, A.; Zhang, X.; Çağlayan, M.; Gong, X.; Gascon, J.; Chowdhury, A. D. Interplay between particle size and hierarchy of zeolite ZSM-5 during the CO_2-to-aromatics process. *ChemSusChem* **2023**, *16* (19), e202300608.

(105) Bellussi, G. Zeolite catalysts for the production of chemical commodities: BTX derivatives. In *Studies in Surface Science and Catalysis*, Vol. 154; Elsevier, **2004**; pp 53-65.

(106) Ramirez Brenes, R. G.; Alhadeff, E. M.; Bojorge, N.; Trales, L. E.; Pazos, G. A. BTX production by breaking down lignin: Current status and future prospects. *Biofuels, Bioproducts and Biorefining* **2023**, *17* (3), 664-681.

(107) Morakinyo, O. M.; Mokgobu, M. I.; Mukhola, M. S.; Engelbrecht, J. C. Health risk assessment of exposure to ambient concentrations of benzene, toluene and xylene in

Pretoria West, South Africa. *African Journal of Science, Technology, Innovation and Development* **2017**, *9* (4), 489-496.

(108) McHale, C. M.; Zhang, L.; Smith, M. T. Current understanding of the mechanism of benzene-induced leukemia in humans: implications for risk assessment. *Carcinogenesis* **2012**, *33* (2), 240-252.

(109) Snyder, R. Leukemia and benzene. *International Journal of Environmental Research and Public Health* **2012**, *9* (8), 2875-2893.

(110) Lu, X.; Qin, M.; Xie, P.; Shen, L.; Duan, J.; Liang, S.; Fang, W.; Liu, J.; Liu, W. Ambient BTX observation nearby main roads in Hefei during summer time. *Aerosol and Air Quality Research* **2017**, *17* (4), 933-943.

(111) Vaezihir, A.; Zare, M.; Raeisi, E.; Molson, J.; Barker, J. Field-scale modeling of benzene, toluene, ethylbenzene, and xylenes (BTEX) released from multiple source zones. *Bioremediation Journal* **2012**, *16* (3), 156-176.

(112) Yu, B.; Yuan, Z.; Yu, Z.; Xue-song, F. BTEX in the environment: An update on sources, fate, distribution, pretreatment, analysis, and removal techniques. *Chemical Engineering Journal* **2022**, *435*, 134825.

(113) Ma, L.; Hurtado, A.; Eguilior, S.; Borrajo, J. F. L. Acute and chronic risk assessment of BTEX in the return water of hydraulic fracturing operations in Marcellus Shale. *Science of The Total Environment* **2024**, *906*, 167638.

(114) Affat, S. S. Classifications, advantages, disadvantages, toxicity effects of natural and synthetic dyes: a review. *University of Thi-Qar Journal of Science* **2021**, *8* (1), 130-135.

(115) Hunger, K. *Industrial dyes: chemistry, properties, applications*; John Wiley & Sons, **2007**.

(116) Slama, H. B.; Chenari Bouket, A.; Pourhassan, Z.; Alenezi, F. N.; Silini, A.; Cherif-Silini, H.; Oszako, T.; Luptakova, L.; Golińska, P.; Belbahri, L. Diversity of synthetic dyes from textile industries, discharge impacts and treatment methods. *Applied Sciences* **2021**, *11* (14), 6255.

(117) Ismail, M.; Akhtar, K.; Khan, M.; Kamal, T.; Khan, M. A.; M Asiri, A.; Seo, J.; Khan, S. B. Pollution, toxicity and carcinogenicity of organic dyes and their catalytic bio-remediation. *Current Pharmaceutical Design* **2019**, *25* (34), 3645-3663.

(118) Chung, K.-T. The significance of azo-reduction in the mutagenesis and carcinogenesis of azo dyes. *Mutation Research/Reviews in Genetic Toxicology* **1983**, *114* (3), 269-281.

(119) Mathur, N.; Bhatnagar, P.; Sharma, P. Review of the mutagenicity of textile dye products. *Universal Journal of Environmental Research & Technology* **2012**, *2* (2).

(120) Ali, H. Biodegradation of synthetic dyes—a review. *Water, Air, & Soil Pollution* **2010**, *213*, 251-273.

(121) Maheshwari, K.; Agrawal, M.; Gupta, A. Dye pollution in water and wastewater. In *In Novel materials for dye-containing wastewater treatment*, Springer, 2021; pp 1-25.

(122) Sharma, J.; Sharma, S.; Soni, V. Classification and impact of synthetic textile dyes on Aquatic Flora: A review. *Regional Studies in Marine Science* **2021**, *45*, 101802.

(123) Dutta, S.; Adhikary, S.; Bhattacharya, S.; Roy, D.; Chatterjee, S.; Chakraborty, A.; Banerjee, D.; Ganguly, A.; Nanda, S.; Rajak, P. Contamination of textile dyes in aquatic environment: Adverse impacts on aquatic ecosystem and human health, and its management using bioremediation. *Journal of Environmental Management* **2024**, *353*, 120103.

(124) Tkaczyk, A.; Mitrowska, K.; Posyniak, A. Synthetic organic dyes as contaminants of the aquatic environment and their implications for ecosystems: A review. *Science of The Total Environment* **2020**, *717*, 137222.

(125) Yangxin, Y.; Jin, Z.; Bayly, A. E. Development of surfactants and builders in detergent formulations. *Chinese Journal of Chemical Engineering* **2008**, *16* (4), 517-527.

(126) Knepper, T. P.; Berna, J. L. Surfactants: properties, production, and environmental aspects. *Comprehensive Analytical Chemistry* **2003**, *40*, 1-49.

(127) Karsa, D. R.; Houston, J. What are surfactants. In *In Chemistry and technology of surfactants*, Vol. 1; Wiley, 2006.

(128) Johnson, P.; Trybala, A.; Starov, V.; Pinfield, V. J. Effect of synthetic surfactants on the environment and the potential for substitution by biosurfactants. *Advances in Colloid and Interface science* **2021**, *288*, 102340.

(129) Jardak, K.; Drogui, P.; Daghrir, R. Surfactants in aquatic and terrestrial environment: occurrence, behavior, and treatment processes. *Environmental Science and Pollution Research* **2016**, *23*, 3195-3216.

(130) Rebello, S.; Asok, A. K.; Mundayoor, S.; Jisha, M. Surfactants: chemistry, toxicity and remediation. *Pollutant Diseases, Remediation and Recycling* **2013**, 277-320.

(131) Rasheed, T.; Shafi, S.; Bilal, M.; Hussain, T.; Sher, F.; Rizwan, K. Surfactants-based remediation as an effective approach for removal of environmental pollutants—A review. *Journal of Molecular Liquids* **2020**, *318*, 113960.

(132) Badmus, S. O.; Amusa, H. K.; Oyehan, T. A.; Saleh, T. A. Environmental risks and toxicity of surfactants: overview of analysis, assessment, and remediation techniques. *Environmental Science and Pollution Research* **2021**, 1-20.

(133) Wong, M. H.; Wu, S. C.; Deng, W. J.; Yu, X.; Luo, Q.; Leung, A.; Wong, C.; Luksemburg, W.; Wong, A. Export of toxic chemicals–a review of the case of uncontrolled electronic-waste recycling. *Environmental Pollution* **2007**, *149* (2), 131-140.

(134) Vanden Bilcke, C. The Stockholm convention on persistent organic pollutants. *Rev. Eur. Comp. & Int'l Envtl. L.* **2002**, *11*, 328.

(135) Rummel-Bulska, I. United Nations Environment Programme. *Pol. Q. Int'l Aff.* **1995**, *4*, 129.

(136) Allegri Sr, T. H. The Resource Conservation and Recovery Act (RCRA). In *Handling and Management of Hazardous Materials and Waste*, Springer, **1986**; pp 361-382.

(137) Wagner, T. P. *The complete guide to the hazardous waste regulations: RCRA, TSCA, HMTA, OSHA, and Superfund*; John Wiley & Sons, **1999**.

(138) Marnell, M. F. EPA's Resonsibilities under RCRA: Administrative Law Issues. *Ecology LQ* **1980**, *9*, 555.

(139) Cooter, W. S. Clean Water Act assessment processes in relation to changing US Environmental Protection Agency management strategies. *Environmental Science & Technology* **2004**, *38* (20), 5265-5273.

(140) Rules, P. Clean Water Act methods update rule for the analysis of effluent. *Federal Register* **2015**, *80* (33).

(141) Williams, E. S.; Panko, J.; Paustenbach, D. J. The European Union's REACH regulation: a review of its history and requirements. *Critical Reviews in Toxicology* **2009**, *39* (7), 553-575.

(142) Talampas, S. I. Study on the different strategies and approaches followed by companies in Portugal and Spain to comply with Reach regulations. Universidade do Algarve (Portugal), **2017**.

(143) Voulvoulis, N.; Arpon, K. D.; Giakoumis, T. The EU Water Framework Directive: From great expectations to problems with implementation. *Science of The Total Environment* **2017**, *575*, 358-366.

(144) Brack, W.; Dulio, V.; Ågerstrand, M.; Allan, I.; Altenburger, R.; Brinkmann, M.; Bunke, D.; Burgess, R. M.; Cousins, I.; Escher, B. I. Towards the review of the European Union Water Framework Directive: recommendations for more efficient assessment and management of chemical contamination in European surface water resources. *Science of The Total Environment* **2017**, *576*, 720-737.

(145) Davies, J. CEPA—The Canadian. Environmental Protection Act. *JAPCA* **1988**, *38* (9), 1111-1113.

(146) Havas, M. Re: Canadian Environmental Protection Act (CEPA) Review. **2016**.

(147) Udom, G. J.; Frazzoli, C.; Ekhator, O. C.; Onyena, A. P.; Bocca, B.; Orisakwe, O. E. Pervasiveness, bioaccumulation and subduing environmental health challenges posed by polycyclic aromatic hydrocarbons (PAHs): A systematic review to settle a one health strategy in Niger Delta, Nigeria. *Environmental Research* **2023**, 115620.

(148) Van der Linde, M. *National Environmental Management Act 107 of 1998 (NEMA)*; Juta Law, **2009**.

(149) Terblanche, F. J. A legal framework for the transboundary movement of hazardous waste in South Africa and Lesotho. North-West University, **2007**.

(150) Behrens, A. A legal analysis of multilateral environmental agreements dealing with hazardous products and hazardous waste. University of Capetown, 2003.

(151) Nhamo, G. Environmental Law and policy reform surrounding packaging waste management in South Africa. *South African Journal of Environmental Law and Policy* **2007**, *14* (2), 136-157.

(152) Nkosi, B. R.; Odeku, K. O. Analysis of water pollution control laws in South Africa. *Mediterranean Journal of Social Sciences* **2014**, *5*, 2572-2582.

(153) Pegram, G.; Mazibuko, G.; Hollingworth, B.; Anderson, E. Strategic review of current and emerging governance systems related to water in the environment in South Africa. *Gezina, WRC Report* **2006**, (1514/1), 06.

(154) Fouad, K.; Bassyouni, M.; Alalm, M. G.; Saleh, M. Y. Recent developments in recalcitrant organic pollutants degradation using immobilized photocatalysts. *Applied Physics A* **2021**, *127* (8), 612.

(155) Hay, S. O.; Obee, T.; Luo, Z.; Jiang, T.; Meng, Y.; He, J.; Murphy, S. C.; Suib, S. The viability of photocatalysis for air purification. *Molecules* **2015**, *20* (1), 1319-1356.

(156) Li, F.; Liu, G.; Liu, F.; Yang, S. A review of self-cleaning photocatalytic surface: Effect of surface characteristics on photocatalytic activity for NO. *Environmental Pollution* **2023**, 121580.

(157) Lin, C.-P.; Chen, H.; Nakaruk, A.; Koshy, P.; Sorrell, C. Effect of annealing temperature on the photocatalytic activity of TiO_2 thin films. *Energy Procedia* **2013**, *34*, 627-636.

(158) Talinungsang; Upadhaya, D.; Kumar, P.; Purkayastha, D. D. Superhydrophilicity of photocatalytic ZnO/SnO_2 heterostructure for self-cleaning applications. *Journal of Sol-gel Science and Technology* **2019**, *92*, 575-584.

(159) Ma, Y.; Wang, H.; Sun, L.; Liu, E.; Fei, G.; Fan, J.; Kang, Y.-M. Unidirectional electron transport from graphitic-C_3N_4 for novel remote and long-term photocatalytic anti-corrosion on Q235 carbon steel. *Chemical Engineering Journal* **2022**, *429*, 132520.

(160) Panzarasa, G.; Soliveri, G. Photocatalytic lithography. *Applied Sciences* **2019**, *9* (7), 1266.

(161) Kayani, A. B. A.; Kuriakose, S.; Monshipouri, M.; Khalid, F. A.; Walia, S.; Sriram, S.; Bhaskaran, M. UV photochromism in transition metal oxides and hybrid materials. *Small* **2021**, *17* (32), 2100621.

(162) Rashmi Pradhan, S.; Colmenares-Quintero, R. F.; Colmenares Quintero, J. C. Designing microflowreactors for photocatalysis using sonochemistry: A systematic review article. *Molecules* **2019**, *24* (18), 3315.

(163) Qi, M.-Y.; Conte, M.; Anpo, M.; Tang, Z.-R.; Xu, Y.-J. Cooperative coupling of oxidative organic synthesis and hydrogen production over semiconductor-based photocatalysts. *Chemical Reviews* **2021**, *121* (21), 13051-13085.

(164) Fujishima, A.; Honda, K. Electrochemical photolysis of water at a semiconductor electrode. *Nature* **1972**, *238* (5358), 37-38.

(165) Frank, S. N.; Bard, A. J. Heterogeneous photocatalytic oxidation of cyanide and sulfite in aqueous solutions at semiconductor powders. *The Journal of Physical Chemistry* **1977**, *81* (15), 1484-1488.

(166) Konstantinou, I. K.; Albanis, T. A. TiO_2-assisted photocatalytic degradation of azo dyes in aqueous solution: kinetic and mechanistic investigations: A review. *Applied Catalysis B: Environmental* **2004**, *49* (1), 1-14. DOI: 10.1016/j.apcatb.2003.11.010.

(167) Das, A.; Adak, M. K.; Mahata, N.; Biswas, B. Wastewater treatment with the advent of TiO_2 endowed photocatalysts and their reaction kinetics with scavenger effect. *Journal of Molecular Liquids* **2021**, *338*, 116479.

(168) Chen, N.; Li, Y.; Deng, D.; Liu, X.; Xing, X.; Xiao, X.; Wang, Y. Acetone sensing performances based on nanoporous TiO_2 synthesized by a facile hydrothermal method. *Sensors and Actuators B: Chemical* **2017**, *238*, 491-500. DOI: 10.1016/j.snb.2016.07.094.

(169) Yu, Z.; Qu, X.; Yang, W.; Peng, J.; Xu, Z. A facile hydrothermal synthesis and memristive switching performance of rutile TiO_2 nanowire arrays. *Journal of Alloys and Compounds* **2016**, *688*, 37-43. DOI: 10.1016/j.jallcom.2016.07.167.

(170) Duo, S.; Li, Y.; Liu, Z.; Zhong, R.; Liu, T.; Xu, H. Preparation of ZnO from 2 D nanosheets to diverse 1 D nanorods and their structure, surface area, photocurrent, optical and photocatalytic properties by simple hydrothermal synthesis. *Journal of Alloys and Compounds* **2017**, *695*, 2563-2579. DOI: 10.1016/j.jallcom.2016.11.162.

(171) Zhou, Y.; Xu, L.; Wu, Z.; Li, P.; He, J. Optical and photocatalytic properties of nanocrystalline ZnO powders synthesized by a low-temperature hydrothermal method. *Optik* **2017**, *130*, 673-680. DOI: 10.1016/j.ijleo.2016.10.119.

(172) Jin, W. X.; Ma, S. Y.; Tie, Z. Z.; Jiang, X. H.; Li, W. Q.; Luo, J.; Xu, X. L.; Wang, T. T. Hydrothermal synthesis of monodisperse porous cube, cake and spheroid-like α-Fe_2O_3 particles and their high gas-sensing properties. *Sensors and Actuators B: Chemical* **2015**, *220*, 243-254. DOI: 10.1016/j.snb.2015.05.098.

(173) Li, Z.; Lin, Z.; Wang, N.; Huang, Y.; Wang, J.; Liu, W.; Fu, Y.; Wang, Z. Facile synthesis of α-Fe_2O_3 micro-ellipsoids by surfactant-free hydrothermal method for sub-ppm level H_2S detection. *Materials & Design* **2016**, *110*, 532-539. DOI: 10.1016/j.matdes.2016.08.035.

(174) Fang, J.; Xu, J.; Chen, J.; Huang, X.; Wang, X. Enhanced photocatalytic activity of molecular imprinted nano α-Fe_2O_3 by hydrothermal synthesis using methylene blue as structure-directing agent. *Colloids and Surfaces A: Physicochemical and Engineering Aspects* **2016**, *508*, 124-134. DOI: 10.1016/j.colsurfa.2016.08.048.

(175) Areeb, A.; Yousaf, T.; Murtaza, M.; Zahra, M.; Zafar, M. I.; Waseem, A. Green photocatalyst Cu/NiO doped zirconia for the removal of environmental pollutants. *Materials Today Communications* **2021**, *28*, 102678.

(176) Sayama, K.; Arakawa, H. Photocatalytic decomposition of water and photocatalytic reduction of carbon dioxide over zirconia catalyst. *The Journal of Physical Chemistry* **1993**, *97* (3), 531-533.

(177) Wei, S.; Han, L.; Wang, M.; Zhang, H.; Du, W.; Zhou, M. Hollow cauliflower-like WO_3 nanostructures: Hydrothermal synthesis and their CO sensing properties. *Materials Letters* **2017**, *186*, 259-262. DOI: 10.1016/j.matlet.2016.10.016.

(178) Yu, Y.; Zeng, W.; Yu, L.; Wu, S. A novel $WO_3 \cdot H_2O$ nanostructure assembled with nanorods: Hydrothermal synthesis, growth and their gas sensing properties. *Materials Letters* **2016**, *180*, 51-54. DOI: 10.1016/j.matlet.2016.05.113.

(179) Li, J.; Dai, W.; Wu, G.; Guan, N.; Li, L. Fabrication of Ta_2O_5 films on tantalum substrate for efficient photocatalysis. *Catalysis Communications* **2015**, *65*, 24-29. DOI: 10.1016/j.catcom.2015.02.006.

(180) Kusmierek, E. Semiconductor electrode materials applied in photoelectrocatalytic wastewater treatment—an overview. *Catalysts* **2020**, *10* (4), 439.

(181) Opoku, F.; Govender, K. K.; van Sittert, C. G. C. E.; Govender, P. P. Recent progress in the development of semiconductor-based photocatalyst materials for applications in photocatalytic water splitting and degradation of pollutants. *Advanced Sustainable Systems* **2017**, *1* (7), 1700006.

(182) Corrigan, N.; Shanmugam, S.; Xu, J.; Boyer, C. Photocatalysis in organic and polymer synthesis. *Chemical Society Reviews* **2016**, *45* (22), 6165-6212.

(183) Fresno, F.; Portela, R.; Suárez, S.; Coronado, J. M. Photocatalytic materials: recent achievements and near future trends. *Journal of Materials Chemistry A* **2014**, *2* (9), 2863-2884.

(184) Xu, C.; Anusuyadevi, P. R.; Aymonier, C.; Luque, R.; Marre, S. Nanostructured materials for photocatalysis. *Chemical Society Reviews* **2019**, *48* (14), 3868-3902.

(185) Mancuso, A.; Iervolino, G. Synthesis and application of innovative and environmentally friendly photocatalysts: a review. *Catalysts* **2022**, *12* (10), 1074.

(186) Kumar, S.; Kumar, A.; Kumar, A.; Krishnan, V. Nanoscale zinc oxide based heterojunctions as visible light active photocatalysts for hydrogen energy and environmental remediation. *Catalysis Reviews* **2020**, *62* (3), 346-405. DOI: 10.1080/01614940.2019.1684649.

(187) Lee, M.-H.; Peng, Y.-C.; Wu, H.-C. Effects of intrinsic defects on electronic structure and optical properties of Ga-doped ZnO. *Journal of Alloys and Compounds* **2014**, *616*, 122-127.

(188) Benzaouak, A.; Ellouzi, I.; Ouanji, F.; Touach, N.; Kacimi, M.; Ziyad, M.; El Mahi, M.; Lotfi, E. M. Photocatalytic degradation of Methylene Blue (MB) dye in aqueous solution by ferroelectric $Li_{1-x}Ta_{1-x}W_xO_3$ materials. *Colloids and Surfaces A: Physicochemical and Engineering Aspects* **2018**, *553*, 586-592.

(189) Cao, S.; Fan, B.; Feng, Y.; Chen, H.; Jiang, F.; Wang, X. Sulfur-doped g-C_3N_4 nanosheets with carbon vacancies: General synthesis and improved activity for simulated solar-light photocatalytic nitrogen fixation. *Chemical Engineering Journal* **2018**, *353*, 147-156.

(190) Wang, S.; Wang, Y.; Li, L.; Li, L.; Fu, G.; Shi, R.; Zou, X.; Zhang, Z.; Luo, F. Green synthesis of Ag/TiO_2 composite coated porous vanadophosphates with enhanced visible-light photo-degradation and catalytic reduction performance for removing organic dyes. *Dalton Transactions* **2020**, *49* (23), 7920-7931.

(191) Mohapatra, T.; Manekar, S.; Kumar Sahu, V.; Soni, A. K.; Banerjee, S.; Ghosh, P. Green synthesized Ag-TiO_2 for degradation of organic dye through visible light driven photo-reactor and its kinetics. *International Journal of Chemical Reactor Engineering* **2021**, *19* (9), 893-900.

(192) Kamat, P. V. Photochemistry on nonreactive and reactive (semiconductor) surfaces. *Chemical Reviews* **1993**, *93* (1), 267-300.

(193) John, M. J.; Anandjiwala, R. D. Recent developments in chemical modification and characterization of natural fiber-reinforced composites. *Polymer Composites* **2008**, *29* (2), 187-207.

(194) Wu, G.; Li, P.; Feng, H.; Zhang, X.; Chu, P. K. Engineering and functionalization of biomaterials via surface modification. *Journal of Materials Chemistry B* **2015**, *3* (10), 2024-2042.

(195) Qiu, P.; Zhou, N.; Chen, H.; Zhang, C.; Gao, G.; Cui, D. Recent advances in lanthanide-doped upconversion nanomaterials: synthesis, nanostructures and surface modification. *Nanoscale* **2013**, *5* (23), 11512-11525.

(196) Kusiak-Nejman, E.; Morawski, A. W. TiO_2/graphene-based nanocomposites for water treatment: A brief overview of charge carrier transfer, antimicrobial and photocatalytic performance. *Applied Catalysis B: Environmental* **2019**, *253*, 179-186.

(197) Fang, J.; Fan, H.; Ma, Y.; Wang, Z.; Chang, Q. Surface defects control for ZnO nanorods synthesized by quenching and their anti-recombination in photocatalysis. *Applied Surface Science* **2015**, *332*, 47-54.

(198) Chen, D.; Jiang, Z.; Geng, J.; Wang, Q.; Yang, D. Carbon and nitrogen co-doped TiO_2 with enhanced visible-light photocatalytic activity. *Industrial & Engineering Chemistry Research* **2007**, *46* (9), 2741-2746.

(199) Basavarajappa, P. S.; Patil, S. B.; Ganganagappa, N.; Reddy, K. R.; Raghu, A. V.; Reddy, C. V. Recent progress in metal-doped TiO_2, non-metal doped/codoped TiO_2 and TiO_2 nanostructured hybrids for enhanced photocatalysis. *International Journal of Hydrogen Energy* **2020**, *45* (13), 7764-7778.

(200) Zhu, W.; Chen, Z.; Pan, Y.; Dai, R.; Wu, Y.; Zhuang, Z.; Wang, D.; Peng, Q.; Chen, C.; Li, Y. Functionalization of hollow nanomaterials for catalytic applications: nanoreactor construction. *Advanced Materials* **2019**, *31* (38), 1800426.

(201) Amani, H.; Arzaghi, H.; Bayandori, M.; Dezfuli, A. S.; Pazoki-Toroudi, H.; Shafiee, A.; Moradi, L. Controlling cell behavior through the design of biomaterial surfaces: a focus on surface modification techniques. *Advanced Materials Interfaces* **2019**, *6* (13), 1900572.

(202) Dou, S.; Tao, L.; Wang, R.; El Hankari, S.; Chen, R.; Wang, S. Plasma-assisted synthesis and surface modification of electrode materials for renewable energy. *Advanced Materials* **2018**, *30* (21), 1705850.

(203) Dutt, M. A.; Hanif, M. A.; Nadeem, F.; Bhatti, H. N. A review of advances in engineered composite materials popular for wastewater treatment. *Journal of Environmental Chemical Engineering* **2020**, *8* (5), 104073.

(204) Kurian, M. Advanced oxidation processes and nanomaterials-a review. *Cleaner Engineering and Technology* **2021**, *2*, 100090.

(205) Pandis, P. K.; Kalogirou, C.; Kanellou, E.; Vaitsis, C.; Savvidou, M. G.; Sourkouni, G.; Zorpas, A. A.; Argirusis, C. Key points of advanced oxidation processes (AOPs) for wastewater, organic pollutants and pharmaceutical waste treatment: A mini review. *ChemEngineering* **2022**, *6* (1), 8.

(206) Papić, S.; Koprivanac, N.; Božić, A. L.; Vujević, D.; Dragičević, S. K.; Kušić, H.; Peternel, I. Advanced oxidation processes in azo dye wastewater treatment. *Water Environment Research* **2006**, *78* (6), 572-579.

(207) Rekhate, C. V.; Srivastava, J. Recent advances in ozone-based advanced oxidation processes for treatment of wastewater-A review. *Chemical Engineering Journal Advances* **2020**, *3*, 100031.

(208) Titchou, F. E.; Zazou, H.; Afanga, H.; El Gaayda, J.; Akbour, R. A.; Nidheesh, P. V.; Hamdani, M. Removal of organic pollutants from wastewater by advanced oxidation processes and its combination with membrane processes. *Chemical Engineering and Processing-Process Intensification* **2021**, *169*, 108631.

(209) Dhamorikar, R. S.; Lade, V. G.; Kewalramani, P. V.; Bindwal, A. B. Review on integrated advanced oxidation processes for water and wastewater treatment. *Journal of Industrial and Engineering Chemistry* **2024**.

(210) Arif, A.; Belahssen, O.; Gareh, S.; Benramache, S. The calculation of band gap energy in zinc oxide films. *Journal of Semiconductors* **2015**, *36* (1), 013001.

(211) Acar, C.; Dincer, I. *2.17 Photoactive Materials*; Elsevier, 2018.

(212) Li, H.; Zhou, Y.; Tu, W.; Ye, J.; Zou, Z. State-of-the-art progress in diverse heterostructured photocatalysts toward promoting photocatalytic performance. *Advanced Functional Materials* **2015**, *25* (7), 998-1013.

(213) Yanagi, R.; Zhao, T.; Solanki, D.; Pan, Z.; Hu, S. Charge separation in photocatalysts: mechanisms, physical parameters, and design principles. *ACS Energy Letters* **2021**, *7* (1), 432-452.

(214) Koe, W. S.; Lee, J. W.; Chong, W. C.; Pang, Y. L.; Sim, L. C. An overview of photocatalytic degradation: photocatalysts, mechanisms, and development of photocatalytic membrane. *Environmental Science and Pollution Research* **2020**, *27* (3), 2522-2565.

(215) Li, T.; Zhao, L.; He, Y.; Cai, J.; Luo, M.; Lin, J. Synthesis of g-C_3N_4/$SmVO_4$ composite photocatalyst with improved visible light photocatalytic activities in RhB degradation. *Applied Catalysis B: Environmental* **2013**, *129*, 255-263.

(216) Sun, M.-H.; Huang, S.-Z.; Chen, L.-H.; Li, Y.; Yang, X.-Y.; Yuan, Z.-Y.; Su, B.-L. Applications of hierarchically structured porous materials from energy storage and conversion, catalysis, photocatalysis, adsorption, separation, and sensing to biomedicine. *Chemical Society Reviews* **2016**, *45* (12), 3479-3563.

(217) Zhang, P.; Wang, T.; Gong, J. Current mechanistic understanding of surface reactions over water-splitting photocatalysts. *Chem* **2018**, *4* (2), 223-245.

(218) Corma, A.; Garcia, H. Photocatalytic reduction of CO_2 for fuel production: Possibilities and challenges. *Journal of Catalysis* **2013**, *308*, 168-175.

(219) Ling, G. Z. S.; Ng, S. F.; Ong, W. J. Tailor-engineered 2D cocatalysts: harnessing electron–hole redox center of 2D g-C_3N_4 photocatalysts toward solar-to-chemical conversion and environmental purification. *Advanced Functional Materials* **2022**, *32* (29), 2111875.

(220) Borysiewicz, M. A. ZnO as a functional material, a review. *Crystals* **2019**, *9* (10), 505.

(221) Bharti, D. B.; Bharati; V, A. Synthesis of ZnO nanoparticles using a hydrothermal method and a study its optical activity. *Luminescence* **2017**, *32* (3), 317-320. DOI: 10.1002/bio.3180.

(222) Rong, P.; Ren, S.; Yu, Q. Fabrications and applications of ZnO nanomaterials in flexible functional devices-a review. *Critical Reviews in Analytical Chemistry* **2019**, *49* (4), 336-349.

(223) Lian, P.; Qin, A.; Liao, L.; Zhang, K. Progress on the nanoscale spherical TiO2 photocatalysts: Mechanisms, synthesis and degradation applications. *Nano Select* **2021**, *2* (3), 447-467.

(224) Theerthagiri, J.; Salla, S.; Senthil, R.; Nithyadharseni, P.; Madankumar, A.; Arunachalam, P.; Maiyalagan, T.; Kim, H.-S. A review on ZnO nanostructured materials: energy, environmental and biological applications. *Nanotechnology* **2019**, *30* (39), 392001.

(225) Maiti, S.; Pal, S.; Chattopadhyay, K. K. Recent advances in low temperature, solution processed morphology tailored ZnO nanoarchitectures for electron emission and photocatalysis applications. *CrystEngComm* **2015**, *17* (48), 9264-9295.

(226) Consonni, V.; Briscoe, J.; Kärber, E.; Li, X.; Cossuet, T. ZnO nanowires for solar cells: A comprehensive review. *Nanotechnology* **2019**, *30* (36), 362001.

(227) Abou Zeid, S.; Leprince-Wang, Y. Advancements in ZnO-based photocatalysts for water treatment: A comprehensive review. *Crystals* **2024**, *14* (7), 611.

(228) Raha, S.; Ahmaruzzaman, M. ZnO nanostructured materials and their potential applications: progress, challenges and perspectives. *Nanoscale Advances* **2022**, *4* (8), 1868-1925.

(229) Gnaneswari, M. D.; Marimuthu, K.; Chandrasekar, B.; Leonora, J. M. Chemically prepared P-Type Sn doped ZnO nanoparticles: Synthesis, characterization and its antibacterial properties. *Journal of Crystal Growth* **2024**, *627*, 127548.

(230) Illy, B. N.; Ingham, B.; Toney, M. F.; Nandhakumar, I.; Ryan, M. P. Understanding the selective etching of electrodeposited ZnO nanorods. *Langmuir* **2014**, *30* (46), 14079-14085. DOI: 10.1021/la503765a.

(231) Ahmad, R.; Majhi, S. M.; Zhang, X.; Swager, T. M.; Salama, K. N. Recent progress and perspectives of gas sensors based on vertically oriented ZnO nanomaterials. *Advances in Colloid and Interface Science* **2019**, *270*, 1-27.

(232) Raizada, P.; Sudhaik, A.; Singh, P. Photocatalytic water decontamination using graphene and ZnO coupled photocatalysts: A review. *Materials Science for Energy Technologies* **2019**, *2* (3), 509-525.

(233) Maynez-Navarro, O.; Sánchez-Salas, J. Focus on zinc oxide as a photocatalytic material for water treatment. *International Journal of Bioremediation & Biodegradation* **2018**, *106*. DOI: 10.29011/IJBB-106/100006.

(234) Charifi, Z.; Baaziz, H.; Hussain Reshak, A. Ab-initio investigation of structural, electronic and optical properties for three phases of ZnO compound. *Physica Status Solidi (b)* **2007**, *244* (9), 3154-3167. DOI: 10.1002/pssb.200642471.

(235) Leitner, J.; Bartůněk, V.; Sedmidubský, D.; Jankovský, O. Thermodynamic properties of nanostructured ZnO. *Applied Materials Today* **2018**, *10*, 1-11.

(236) Kogure, T.; Bando, Y. Formation of ZnO nanocrystals in the cubic phase was reported by electron-beam induced oxidation of ZnS surfaces during TEM observations. *Journal of Electron Microscopy* **1993**, *47*, 7903-7909.

(237) Ashrafi, A. A.; Ueta, A.; Avramescu, A.; Kumano, H.; Suemune, I.; Ok, Y.-W.; Seong, T.-Y. Growth and characterization of hypothetical zinc-blende ZnO films on GaAs (001) substrates with ZnS buffer layers. *Applied Physics Letters* **2000**, *76* (5), 550-552.

(238) Kim, S.-K.; Jeong, S.-Y.; Cho, C.-R. Structural reconstruction of hexagonal to cubic ZnO films on Pt/Ti/SiO_2/Si substrate by annealing. *Applied Physics Letters* **2003**, *82* (4), 562-564.

(239) Bates, C. H.; White, W. B. New high-pressure polymorph of zinc oxide. *Science* **1962**, *137* (3534), 993.

(240) Lao, J. Y.; Huang, J. Y.; Wang, D. Z.; Ren, Z. F. ZnO nanobridges and nanonails. *Nano Letters* **2003**, *3* (2), 235-238. DOI: 10.1021/nl025884u.

(241) Maheshwary, P. B.; Handa, C. C.; Nemade, K. R. Effect of shape on thermophysical and heat transfer properties of ZnO/R-134a manorefrigerant. *Materials Today: Proceedings* **2018**, *5* (1, Part 1), 1635-1639. DOI: 10.1016/j.matpr.2017.11.257.

(242) Kimitsuka, Y.; Hosono, E.; Ueno, S.; Zhou, H.; Fujihara, S. Fabrication of porous cubic architecture of ZnO using Zn-terephthalate MOFs with characteristic microstructures. *Inorganic Chemistry* **2013**, *52* (24), 14028-14033.

(243) Savory, C. N.; Ganose, A. M.; Travis, W.; Atri, R. S.; Palgrave, R. G.; Scanlon, D. O. An assessment of silver copper sulfides for photovoltaic applications: theoretical and experimental insights. *Journal of Materials Chemistry A* **2016**, *4* (32), 12648-12657.

(244) Sathasivam, S.; Arnepalli, R. R.; Bhachu, D. S.; Lu, Y.; Buckeridge, J.; Scanlon, D. O.; Kumar, B.; Singh, K. K.; Visser, R. J.; Blackman, C. S. Single step solution processed GaAs thin films from $GaMe_3$ and T $BuAsH_2$ under ambient pressure. *The Journal of Physical Chemistry C* **2016**, *120* (13), 7013-7019.

(245) Bhachu, D. S.; Moniz, S. J.; Sathasivam, S.; Scanlon, D. O.; Walsh, A.; Bawaked, S. M.; Mokhtar, M.; Obaid, A. Y.; Parkin, I. P.; Tang, J. Bismuth oxyhalides: synthesis, structure and photoelectrochemical activity. *Chemical Science* **2016**, *7* (8), 4832-4841.

(246) Sathasivam, S.; Williamson, B. A.; Kafizas, A.; Althabaiti, S. A.; Obaid, A. Y.; Basahel, S. N.; Scanlon, D. O.; Carmalt, C. J.; Parkin, I. P. Computational and experimental study of Ta_2O_5 thin films. *The Journal of Physical Chemistry C* **2017**, *121* (1), 202-210.

(247) Körber, C.; Krishnakumar, V.; Klein, A.; Panaccione, G.; Torelli, P.; Walsh, A.; Da Silva, J.; Wei, S.-H.; Egdell, R.; Payne, D. Electronic structure of In_2O_3 and Sn-doped In_2O_3 by hard x-ray photoemission spectroscopy. *Physical Review B* **2010**, *81* (16), 165207.

(248) Williamson, B. A.; Buckeridge, J.; Brown, J.; Ansbro, S.; Palgrave, R. G.; Scanlon, D. O. Engineering valence band dispersion for high mobility p-type semiconductors. *Chemistry of Materials* **2017**, *29* (6), 2402-2413.

(249) Walsh, L. Applications of hard X-ray photoelectron spectroscopy in semiconductor materials characterisation. Dublin City University, 2014.

(250) Yeh, J.; Lindau, I. Atomic subshell photoionization cross sections and asymmetry parameters: $1 \leqslant Z \leqslant 103$. *Atomic Data and Nuclear Data Tables* **1985**, *32* (1), 1-155.

(251) Scofield, J. Lawrence Livermore Laboratory Report No. *UCRL-51326* **1973**.

(252) Li, H.; Schirra, L. K.; Shim, J.; Cheun, H.; Kippelen, B.; Monti, O. L.; Bredas, J.-L. Zinc oxide as a model transparent conducting oxide: a theoretical and experimental study of the impact of hydroxylation, vacancies, interstitials, and extrinsic doping on the electronic properties of the polar ZnO (0002) surface. *Chemistry of Materials* **2012**, *24* (15), 3044-3055.

(253) Krithiga, R.; Sankar, S.; Subhashree, G. Na to tailor the band gap and morphology of ZnO nanograins. *Journal of Materials Science: Materials in Electronics* **2014**, *25*, 103-110.

(254) Yang, C.; Li, X.; Gu, Y.; Yu, W.; Gao, X.; Zhang, Y. ZnO based oxide system with continuous bandgap modulation from 3.7 to 4.9 eV. *Applied Physics Letters* **2008**, *93* (11).

(255) Zagorac, D.; Schön, J.; Zagorac, J.; Jansen, M. Prediction of structure candidates for zinc oxide as a function of pressure and investigation of their electronic properties. *Physical Review B* **2014**, *89* (7), 075201.

(256) Abdul Hamid, S. B.; Teh, S. J.; Lai, C. W. Photocatalytic water oxidation on ZnO: a review. *Catalysts* **2017**, *7* (3), 93.

(257) Zhao, W.; Ding, J.; Zou, Y.; Di, C.-a.; Zhu, D. Chemical doping of organic semiconductors for thermoelectric applications. *Chemical Society Reviews* **2020**, *49* (20), 7210-7228.

(258) Slassi, A.; Naji, S.; Benyoussef, A.; Hamedoun, M.; El Kenz, A. On the transparent conducting oxide Al doped ZnO: First Principles and Boltzmann equations study. *Journal of Alloys and Compounds* **2014**, *605*, 118-123. DOI: 10.1016/j.jallcom.2014.03.177.

(259) Kaneva, N. V.; Dimitrov, D. T.; Dushkin, C. D. Effect of nickel doping on the photocatalytic activity of ZnO thin films under UV and visible light. *Applied Surface Science* **2011**, *257* (18), 8113-8120. DOI: 10.1016/j.apsusc.2011.04.119.

(260) Jain, V. K. Semiconductors. In *Solid State Physics*, Springer, 2022; pp 295-330.

(261) Ouyang, W.; Teng, F.; He, J. H.; Fang, X. Enhancing the photoelectric performance of photodetectors based on metal oxide semiconductors by charge-carrier engineering. *Advanced Functional Materials* **2019**, *29* (9), 1807672.

(262) Morasae, S. M., Zirak; Amene, N.; Elham, K.; Alireza, Z. M. Recent progress on doped ZnO nanostructures for visible-light photocatalysis. *Thin Solid Films* **2016**, *605*.

(263) Lee, Y.-S.; Peng, Y.-C.; Lu, J.-H.; Zhu, Y.-R.; Wu, H.-C. Electronic and optical properties of Ga-doped ZnO. *Thin Solid Films* **2014**, *570*, 464-470. DOI: 10.1016/j.tsf.2014.04.037.

(264) Huang, C.; Wang, M.; Deng, Z.; Cao, Y.; Liu, Q.; Huang, Z.; Liu, Y.; Guo, W.; Huang, Q. Effects of hydrogen annealing on the structural, optical and electrical properties of indium-doped zinc oxide films. *Journal of Materials Science: Materials in Electronics* **2010**, *21*, 1221-1227.

(265) Papadimitriou, D. N. Engineering of optical and electrical properties of electrodeposited highly doped Al: ZnO and In: ZnO for cost-effective photovoltaic device technology. *Micromachines* **2022**, *13* (11), 1966.

(266) Rezkallah, T.; Djabri, I.; Koç, M. M.; Erkovan, M.; Chumakov, Y.; Chemam, F. Investigation of the electronic and magnetic properties of Mn doped ZnO using the FP-LAPW method. *Chinese Journal of Physics* **2017**, *55* (4), 1432-1440. DOI: 10.1016/j.cjph.2017.02.021.

(267) Akcan, D.; Ozharar, S.; Ozugurlu, E.; Arda, L. The effects of Co/Cu Co-doped ZnO thin films: An optical study. *Journal of Alloys and Compounds* **2019**, *797*, 253-261. DOI: 10.1016/j.jallcom.2019.05.126.

(268) Ma, Z.; Ren, F.; Ming, X.; Long, Y.; Volinsky, A. A. Cu-doped ZnO electronic structure and optical properties studied by first-principles calculations and experiments. *Materials (Basel)* **2019**, *12* (1). DOI: 10.3390/ma12010196 From NLM PubMed-not-MEDLINE.

(269) Opoku, F.; Govender, K. K.; van Sittert, C. G. C. E.; Govender, P. P. Understanding the mechanism of enhanced charge separation and visible light photocatalytic activity of modified wurtzite ZnO with nanoclusters of ZnS and graphene oxide: from a hybrid density functional study. *New Journal of Chemistry* **2017**, *41* (16), 8140-8155.

(270) Ganesh, V.; Yahia, I.; AlFaify, S.; Shkir, M. Sn-doped ZnO nanocrystalline thin films with enhanced linear and nonlinear optical properties for optoelectronic applications. *Journal Of Physics And Chemistry Of Solids* **2017**, *100*, 115-125.

(271) Kang, Y.; Yu, F.; Zhang, L.; Wang, W.; Chen, L.; Li, Y. Review of ZnO-based nanomaterials in gas sensors. *Solid State Ionics* **2021**, *360*, 115544. DOI: 10.1016/j.ssi.2020.115544.

(272) Spencer, M. J. S. Gas sensing applications of 1D-nanostructured zinc oxide: Insights from density functional theory calculations. *Progress in Materials Science* **2012**, *57* (3), 437-486. DOI: 10.1016/j.pmatsci.2011.06.001.

(273) Ellmer, K.; Bikowski, A. Intrinsic and extrinsic doping of ZnO and ZnO alloys. *Journal of Physics D: Applied Physics* **2016**, *49* (41), 413002.

(274) Xiu, F.; Xu, J.; Joshi, P. C.; Bridges, C. A.; Parans Paranthaman, M. ZnO doping and defect engineering—A review. *Semiconductor materials for solar photovoltaic cells* **2016**, 105-140.

(275) Cheng, X.; Li, F.; Zhao, Y. A DFT investigation on ZnO clusters and nanostructures. *Journal of Molecular Structure: THEOCHEM* **2009**, *894* (1-3), 121-127. DOI: 10.1016/j.theochem.2008.10.023.

(276) Haffad, S.; Cicero, G.; Samah, M. Structural and electronic properties of ZnO nanowires: a theoretical study. *Energy Procedia* **2011**, *10*, 128-137.

(277) Yaakob, M.; Hussin, N.; Taib, M.; Kudin, T.; Hassan, O.; Ali, A.; Yahya, M. First principles LDA+ U calculations for ZnO materials. *Integrated Ferroelectrics* **2014**, *155* (1), 15-22.

(278) Wu, J.; Hu, J.; Shao, L.; Xu, J.; Song, K.; Zheng, P. First-principle investigation of K–N dual-acceptor codoping for p-ZnO. *Materials Science in Semiconductor Processing* **2015**, *29*, 245-249.

(279) Xia, C.; Wang, F.; Hu, C. Theoretical and experimental studies on electronic structure and optical properties of Cu-doped ZnO. *Journal of Alloys and Compounds* **2014**, *589*, 604-608. DOI: 10.1016/j.jallcom.2013.11.066.

(280) Cao, H.; Lu, P.; Cai, N.; Zhang, X.; Yu, Z.; Gao, T.; Wang, S. First-principles study on electronic and magnetic properties of (Mn, Fe)-codoped ZnO. *Journal of Magnetism and Magnetic Materials* **2014**, *352*, 66-71.

(281) Hamzah, N.; Samat, M.; Johari, N.; Faizal, A.; Hassan, O.; Ali, A.; Zakaria, R.; Hussin, N.; Yahya, M.; Taib, M. First-principle LDA+ U and GGA+ U calculations on structural and electronic properties of wurtzite ZnO. *Solid State Science and Technology 30* (1), 20-36.

(282) Harun, K.; Salleh, N. A.; Deghfel, B.; Yaakob, M. K.; Mohamad, A. A. DFT+ U calculations for electronic, structural, and optical properties of ZnO wurtzite structure: A review. *Results in Physics* **2020**, *16*, 102829.

(283) Liu, Y.; Xu, H.; Liu, C.; Liu, W. Recent progress in ZnO-based heterojunction ultraviolet light-emitting devices. *Chinese Science Bulletin* **2014**, *59* (12), 1219-1227. DOI: 10.1007/s11434-014-0206-9.

(284) Ma, X.; Wu, Y.; Lv, Y.; Zhu, Y. Correlation effects on lattice relaxation and electronic structure of ZnO within the GGA+ U formalism. *The Journal of Physical Chemistry C* **2013**, *117* (49), 26029-26039.

(285) Luo, J.-H.; Liu, Q.; Yang, L.-N.; Sun, Z.-Z.; Li, Z.-S. First-principles study of electronic structure and optical properties of (Zr–Al)-codoped ZnO. *Computational Materials Science* **2014**, *82*, 70-75.

(286) Benrezgua, E.; Zoukel, A.; Deghfel, B.; Boukhari, A.; Amari, R.; Kheawhom, S.; Mohamad, A. A. A review on DFT+ U scheme for structural, electronic, optical and magnetic properties of copper doped ZnO wurtzite structure. *Materials Today Communications* **2022**, *31*, 103306.

(287) Harun, K.; Yaakob, M. K.; Taib, M. F. M.; Sahraoui, B.; Ahmad, Z. A.; Mohamad, A. A. Efficient diagnostics of the electronic and optical properties of defective ZnO nanoparticles synthesized using the sol–gel method: experimental and theoretical studies. *Materials Research Express* **2017**, *4* (8), 085908.

(288) Harun, K.; Mansor, N.; Yaakob, M. K.; Taib, M. F. M.; Ahmad, Z. A.; Mohamad, A. A. On the verification of sol–gel-derived ZnO nanoparticle properties using first-principles calculation. *Journal of Sol-gel Science and Technology* **2016**, *80*, 56-67.

(289) Honglin, L.; Yingbo, L.; Jinzhu, L.; Ke, Y. Experimental and first-principles studies of structural and optical properties of rare earth (RE= La, Er, Nd) doped ZnO. *Journal of Alloys and Compounds* **2014**, *617*, 102-107.

(290) Harun, K.; Mansor, N.; Ahmad, Z. A.; Mohamad, A. A. Electronic properties of ZnO nanoparticles synthesized by Sol-gel method: a LDA+ U calculation and experimental study. *Procedia Chemistry* **2016**, *19*, 125-132.

(291) Tang, C.; Spencer, M. J. S.; Barnard, A. S. Activity of ZnO polar surfaces: an insight from surface energies. *Physical Chemistry Chemical Physics* **2014**, *16*, 22139-22144. DOI: 10.1039/C4CP03221G.

(292) Pauporté, T.; Magne, C. Impedance spectroscopy study of N719-sensitized ZnO-based solar cells. *Thin Solid Films* **2014**, *560*, 20-26. DOI: 10.1016/j.tsf.2013.11.121.

(293) Narjis, A.; El Aakib, H.; Boukendil, M.; El Hasnaoui, M.; Nkhaili, L.; Aberkouks, A.; Outzourhit, A. Controlling the structural properties of pure and aluminum doped zinc oxide nanoparticles by annealing. *Journal of King Saud University - Science* **2020**, *32* (1), 1074-1080. DOI: 10.1016/j.jksus.2019.10.004.

(294) Bougrine, A.; El Hichou, A.; Addou, M.; Ebothé, J.; Kachouane, A.; Troyon, M. Structural, optical and cathodoluminescence characteristics of undoped and tin-doped ZnO thin films prepared by spray pyrolysis. *Materials Chemistry and Physics* **2003**, *80* (2), 438-445, Article. DOI: 10.1016/S0254-0584(02)00505-9 Scopus.

(295) Liu, J.; Fan, X. F.; Sun, C. Q.; Zhu, W. Transparent conductivity modulation of ZnO by group-IVA doping. *Chemical Physics Letters* **2016**, *649*, 78-83. DOI: 10.1016/j.cplett.2016.02.033.

(296) Marana, N.; Longo, V.; Longo, E.; Martins, J.; Sambrano, J. Electronic and structural properties of the (1010) and (1120) ZnO surfaces. *The Journal of Physical Chemistry A* **2008**, *112* (38), 8958-8963.

(297) Catto, A. C.; Ferrer, M. M.; Lopes, O. F.; Mastelaro, V. R.; Andrés, J.; da Silva, L. F.; Longo, E.; Avansi, W. The role of counter-ions in crystal morphology, surface structure and photocatalytic activity of ZnO crystals grown onto a substrate. *Applied Surface Science* **2020**, *529*, 147057. DOI: 10.1016/j.apsusc.2020.147057.

(298) Ashrafi, A. B. M. A.; Jagadish, C. Review of zincblende ZnO: Stability of metastable ZnO phases. *Journal of Applied Physics* **2007**, *102*, 071101.

(299) Sun, Y.; Chen, L.; Bao, Y.; Zhang, Y.; Wang, J.; Fu, M.; Wu, J.; Ye, D. The applications of morphology controlled ZnO in catalysis. *Catalysts* **2016**, *6* (12), 188. DOI: 10.3390/catal6120188.

(300) Katea, S. N.; Broqvist, P.; Kullgren, J.; Hemmer, E.; Westin, G. Fast, low-cost synthesis of ZnO:Eu nanosponges and the nature of Ln doping in ZnO. *Inorganic Chemistry* **2020**, *59* (11), 7584-7602. DOI: 10.1021/acs.inorgchem.0c00472.

(301) Kamarulzaman, N.; Kasim, M. F.; Rusdi, R. Band gap narrowing and widening of ZnO nanostructures and doped materials. *Nanoscale Research Letters* **2015**, *10*. DOI: 10.1186/s11671-015-1034-9.

(302) Liccardo, L.; Lushaj, E.; Dal Compare, L.; Moretti, E.; Vomiero, A. Nanoscale ZnO/α-Fe_2O_3 heterostructures: Toward efficient and low-cost photoanodes for water splitting. *Small Science* **2022**, *2* (3), 2100104. DOI: 10.1002/smsc.202100104.

(303) Ul Haq, B.; Ahmed, R.; Goumri-Said, S.; Shaari, A.; Afaq, A. Electronic structure engineering of ZnO with the modified Becke–Johnson exchange versus the classical correlation potential approaches. *Phase Transitions* **2013**, *86* (12), 1167-1177. DOI: 10.1080/01411594.2012.755183.

(304) Novikov, S. V.; Kent, A.; Foxon, C. Molecular beam epitaxy as a growth technique for achieving free-standing zinc-blende GaN and wurtzite $Al_xGa_{1-x}N$. *Progress in Crystal Growth and Characterization of Materials* **2017**, *63* (2), 25-39.

(305) Xin, C. S.; Wenxia, F.; Quan, H. H.; Zhenbao, F.; Xu, W. Y. Structural and electronic properties of ZnO under high pressure. *Journal of Alloys and Compounds* **2009**, *476* (1-2), 306-310.

(306) Xu, H.; Zhang, R.; Zhang, X.; Rosa, A.; Frauenheim, T. Structural and electronic properties of ZnO nanotubes from density functional calculations. *Nanotechnology* **2007**, *18* (48), 485713.

(307) Amrani, B.; Chiboub, I.; Hiadsi, S.; Benmessabih, T.; Hamdadou, N. Structural and electronic properties of ZnO under high pressures. *Solid State Communications* **2006**, *137* (7), 395-399.

(308) Zhang, Y.; Fang, D.-Q.; Zhang, S.-L.; Huang, R.; Wen, Y.-H. Structural and electronic properties of ZnO/GaN heterostructured nanowires from first-principles study. *Physical Chemistry Chemical Physics* **2016**, *18* (4), 3097-3102.

(309) Wakhare, S. Y.; Deshpande, M. D. Structural, electronic and optical properties of metalloid element (B, Si, Ge, As, Sb, and Te) doped g-ZnO monolayer: A DFT study. *Journal of Molecular Graphics and Modelling* **2020**, *101*, 107753. DOI: 10.1016/j.jmgm.2020.107753 From NLM Medline.

(310) Gerosa, M.; Bottani, C. E.; Di Valentin, C.; Onida, G.; Pacchioni, G. Accuracy of dielectric-dependent hybrid functionals in the prediction of optoelectronic properties of metal oxide semiconductors: a comprehensive comparison with many-body GW and experiments. *Journal of Physics: Condensed Matter* **2018**, *30* (4), 044003. DOI: 10.1088/1361-648X/aa9725.

(311) Wöll, C. The chemistry and physics of zinc oxide surfaces. *Progress in Surface Science* **2007**, *82* (2), 55-120. DOI: 10.1016/j.progsurf.2006.12.002.

(312) Rohrer, J.; Albe, K. Thermodynamic stability and electronic structure of pristine wurtzite ZnO 0001 inversion domain boundaries. *Physical Review Materials* **2021**, *5* (2), 023601.

(313) Raymand, D.; Jacobsson, T. J.; Hermansson, K.; Edvinsson, T. Investigation of vibrational modes and phonon density of states in ZnO quantum dots. *The Journal of Physical Chemistry C* **2012**, *116* (12), 6893-6901.

(314) Meyer, B.; Marx, D. Density-functional study of the structure and stability of ZnO surfaces. *Physical Review B* **2003**, *67* (3). DOI: 10.1103/physrevb.67.035403.

(315) Blaha, P.; Schwarz, K.; Madsen, G. K.; Kvasnicka, D.; Luitz, J. wien2k. *An augmented plane wave plus local orbitals program for calculating crystal properties* **2001**, *60* (1).

(316) Yu, H.-G. An optimal density functional theory method for GaN and ZnO. *Chemical Physics Letters* **2011**, *512* (4-6), 231-236.

(317) Erhart, P.; Albe, K.; Klein, A. First-principles study of intrinsic point defects in ZnO: Role of band structure, volume relaxation, and finite-size effects. *Physical Review B* **2006**, *73* (20). DOI: 10.1103/PhysRevB.73.205203.

(318) Sowjanya, M.; Shariq, M.; Alajlani, Y.; Pamu, D.; Chowdhury, R.; Jayaganthan, R.; Taqiullah, S. M. Structural and optical properties of pure wurtzite ZnO under uniaxial strain based on first-principles study. *Acta Physica Polonica A* **2020**, *137* (3), 361-367. DOI: 10.12693/APhysPolA.137.361.

(319) Pandey, A.; Scherich, H.; Drabold, D. A. Density functional theory model of amorphous zinc oxide (a-ZnO) and a-X0.375Z0.625O (X= Al, Ga and In). *Journal of Non-Crystalline Solids* **2017**, *455*, 98-101. DOI: 10.1016/j.jnoncrysol.2016.10.035.

(320) Ozugurlu, E. Cd-doped ZnO nanoparticles: An experimental and first-principles DFT studies. *Journal of Alloys and Compounds* **2021**, *861*. DOI: 10.1016/j.jallcom.2021.158620.

(321) Supatutkul, C.; Pramchu, S.; Jaroenjittichai, A. P.; Laosiritaworn, Y. Density functional theory investigation of surface defects in Sn-doped ZnO. *Surface and Coatings Technology* **2016**, *298*, 53-57. DOI: 10.1016/j.surfcoat.2016.04.013.

(322) Spencer, M. J. S.; Wong, K. W. J.; Yarovsky, I. Density functional theory modelling of and surfaces: Structure, properties and adsorption of N_2O. *Materials Chemistry and Physics* **2010**, *119* (3), 505-514. DOI: 10.1016/j.matchemphys.2009.10.005.

(323) Qi, M.; Hou, Q.; Li, Y.; Gu, Y.; Yang, A. Effects and mechanism of (Be/Mg/Ca) doping and point defects (VZn, Hi) on the p-type conductivity of ZnO: A first-principles study. *Solid State Communications* **2022**, *343*. DOI: 10.1016/j.ssc.2022.114653.

(324) Sriram, S.; Lalithambika, K. C.; Thayumanavan, A. Experimental and theoretical investigations of photocatalytic activity of Cu doped ZnO nanoparticles. *Optik* **2017**, *139*, 299-308. DOI: 10.1016/j.ijleo.2017.04.013.

(325) Wen, J.-Q.; Zhang, J.-M.; Chen, G.-X.; Wu, H.; Yang, X. The structural, electronic and optical properties of Nd doped ZnO using first-principles calculations. *Physica E: Low-dimensional Systems and Nanostructures* **2018**, *98*, 168-173. DOI: 10.1016/j.physe.2018.01.002.

(326) Perdew, J. P.; Burke, K.; Ernzerhof, M. Generalized gradient approximation made simple. *Physical Review Letters* **1996**, *77* (18), 3865.

(327) Perdew, J. P.; Burke, K.; Ernzerhof, M. Generalized Gradient Approximation Made Simple. *Physical Review Letters* **1997**, *77* (18), 3865-3868. DOI: 10.1103/PhysRevLett.77.3865.

(328) Perdew, J. P. Unified theory of exchange and correlation beyond the local density approximation. *Electronic Structure of Solids' 91* **1991**, *11*.

(329) Perdew, J. P.; Wang, Y. Accurate and simple analytic representation of the electron-gas correlation energy. *Physical Review B* **1992**, *45* (23), 13244.

(330) Blöchl, P. E. Projector augmented-wave method. *Physical Review B* **1994**, *50* (24), 17953.

(331) Vanderbilt, D. Soft self-consistent pseudopotentials in a generalized eigenvalue formalism. *Physical Review B* **1990**, *41* (11), 7892-7895. DOI: 10.1103/physrevb.41.7892 From NLM PubMed-not-MEDLINE.

(332) Clark, S. J.; Segall, M. D.; Pickard, C. J.; Hasnip, P. J.; Probert, M. I. J.; Refson, K.; Payne, M. C. First principles methods using CASTEP. *Zeitschrift für Kristallographie - Crystalline Materials* **2005**, *220* (5-6), 567-570. DOI: 10.1524/zkri.220.5.567.65075.

(333) Jain, A.; Ong, S. P.; Hautier, G.; Chen, W.; Richards, W. D.; Dacek, S.; Cholia, S.; Gunter, D.; Skinner, D.; Ceder, G.; et al. The materials project: A materials genome approach to accelerating materials innovation. *APL Materials* **2013**, *1* (1), 011002. DOI: 10.1063/1.4812323.

(334) McLeod, J.; Wilks, R.; Skorikov, N.; Finkelstein, L.; Abu-Samak, M.; Kurmaev, E.; Moewes, A. Band gaps and electronic structure of alkaline-earth and post-transition-metal oxides. *Physical Review B* **2010**, *81* (24), 245123.

(335) Ferreira, L. G.; Marques, M.; Teles, L. K. Approximation to density functional theory for the calculation of band gaps of semiconductors. *Physical Review B* **2008**, *78* (12), 125116.

(336) Cococcioni, M.; De Gironcoli, S. Linear response approach to the calculation of the effective interaction parameters in the LDA+ U method. *Physical Review B* **2005**, *71* (3), 035105.

(337) Tsuneda, T.; Hirao, K. Self-interaction corrections in density functional theory. *The Journal of Chemical Physics* **2014**, *140* (18).

(338) Capdevila-Cortada, M.; Łodziana, Z.; López, N. Performance of DFT+ U approaches in the study of catalytic materials. *ACS Catalysis* **2016**, *6* (12), 8370-8379.

(339) Kohn, W.; Sham, L. J. Self-consistent equations including exchange and correlation effects. *Physical Review* **1965**, *140* (4A), A1133.

(340) Deng, X. Y.; Liu, G. H.; Jing, X. P.; Tian, G. S. On-site correlation of p-electron in d10 semiconductor zinc oxide. *International Journal of Quantum Chemistry* **2014**, *114* (7), 468-472.

(341) Farooq, R.; Mahmood, T.; Anwar, A. W.; Abbasi, G. N. First-principles calculation of electronic and optical properties of graphene like ZnO (G-ZnO). *Superlattices and Microstructures* **2016**, *90*, 165-169.

(342) Wen, J.-Q.; Han, Y.-S.; Yang, X.; Zhang, J.-M. Computational research of electronic, optical and magnetic properties of Ce and Nd co-doped ZnO. *Journal Of Physics And Chemistry Of Solids* **2019**, *125*, 90-95.

(343) Zhang, H.; Lu, S.; Xu, W.; Yuan, F. First-principles study of Si atoms adsorbed on ZnO (0001) surface and the effect on electronic and optical properties. *Surface Science* **2014**, *625*, 30-36.

(344) Getman, R. B.; Xu, Y.; Schneider, W. F. Thermodynamics of environment-dependent oxygen chemisorption on Pt(111). *The Journal of Physical Chemistry C* **2008**, *112* (26), 9559-9572. DOI: 10.1021/JP800905A.

(345) Saha, S.; Pal, S.; Sarkar, P.; Rosa, A.; Frauenheim, T. A complete set of self-consistent charge density-functional tight-binding parametrization of zinc chalcogenides (ZnX; X= O, S, Se, and Te). *Journal of Computational Chemistry* **2012**, *33* (12), 1165-1178.

(346) Paleico, M. L.; Behler, J. Global optimization of copper clusters at the ZnO ($10\bar{1}0$) surface using a DFT-based neural network potential and genetic algorithms. *The Journal of Chemical Physics* **2020**, *153* (5).

(347) Kresse, G.; Dulub, O.; Diebold, U. Competing stabilization mechanism for the polar ZnO (0001)-Zn surface. *Physical Review B* **2003**, *68* (24), 245409.

(348) Yao, G. Y.; Fan, G. H.; Zhao, F.; Ma, J. H.; Chen, J.; Zheng, S. W.; Zeng, S. M.; He, L. F.; Zhang, T. In assisted realization of p-type C-doped ZnO: A first-principles study. *Physica B: Condensed Matter* **2012**, *407* (17), 3539-3542. DOI: 10.1016/j.physb.2012.05.019.

(349) Harun, K.; Salleh, N. A.; Deghfel, B.; Yaakob, M. K.; Mohamad, A. A. DFT + U calculations for electronic, structural, and optical properties of ZnO wurtzite structure: A review. *Results in Physics* **2020**, *16*. DOI: 10.1016/j.rinp.2019.102829.

(350) Slassi, A.; Lakouari, N.; Ziat, Y.; Zarhri, Z.; Fakhim Lamrani, A.; Hlil, E. K.; Benyoussef, A. Ab initio study on the electronic, optical and electrical properties of Ti-, Sn- and Zr-doped ZnO. *Solid State Communications* **2015**, *218*, 45-48. DOI: 10.1016/j.ssc.2015.06.010.

(351) Schleife, A.; Fuchs, F.; Furthmüller, J.; Bechstedt, F. First-principles study of ground- and excited-state properties of MgO, ZnO, and CdO polymorphs. *Physical Review B* **2006**, *73*, 245212. DOI: 10.1103/PHYSREVB.73.245212/FIGURES/9/MEDIUM.

(352) Wang, Z.; Wang, F.; Wang, L.; Jia, Y.; Sun, Q. First-principles study of negative thermal expansion in zinc oxide. *Journal of Applied Physics* **2013**, *114* (6), 063508. DOI: 10.1063/1.4817902.

(353) Monkhorst, H. J.; Pack, J. D. Special points for Brillouin-zone integrations. *Physical Review B* **1976**, *13* (12), 5188-5192. DOI: 10.1103/PhysRevB.13.5188.

(354) Sikam, P.; Moontragoon, P.; Jumpatam, J.; Pinitsoontorn, S.; Thongbai, P.; Kamwanna, T. Structural, optical, electronic and magnetic properties of Fe-doped ZnO nanoparticles synthesized by combustion method and first-principle calculation. *Journal of Superconductivity and Novel Magnetism* **2016**, *29* (12), 3155-3166. DOI: 10.1007/s10948-016-3690-0.

(355) Hubbard, C.; O'Connor, B. International centre for diffraction data (ICDD). **2002**.

(356) Morkoc, b. H.; Strite, S.; Gao, G.; Lin, M.; Sverdlov, B.; Burns, M. Large-band-gap SiC, III-V nitride, and II-VI ZnSe-based semiconductor device technologies. *Journal of Applied Physics* **1994**, *76* (3), 1363-1398.

(357) Deinert, J.-C. Zinc oxide surfaces and interfaces: Electronic structure and dynamics of excited states. Technische Universität Berlin, 2016.

(358) Dixit, H.; Saniz, R.; Lamoen, D.; Partoens, B. The quasiparticle band structure of zincblende and rocksalt ZnO. *Journal of Physics: Condensed Matter* **2010**, *22* (12), 125505. DOI: 10.1088/0953-8984/22/12/125505.

(359) Segura, A.; Sans, J.; Manjón, F.; Munoz, A.; Herrera-Cabrera, M. Optical properties and electronic structure of rock-salt ZnO under pressure. *Applied Physics Letters* **2003**, *83* (2), 278-280.

(360) Martínez-Pérez, L.; Muñoz-Aguirre, N.; Muñoz-Aguirre, S.; Zelaya-Angel, O. Nanometric structures of highly oriented zinc blende ZnO thin films. *Materials Letters* **2015**, *139*, 63-65. DOI: 10.1016/j.matlet.2014.10.054.

(361) Polo, V.; Kraka, E.; Cremer, D. Electron correlation and the self-interaction error of density functional theory. *Molecular Physics* **2002**, *100* (11), 1771-1790.

(362) Koster, R. S.; Fang, C. M.; Dijkstra, M.; Van Blaaderen, A.; Van Huis, M. A. Stabilization of rock salt ZnO nanocrystals by low-energy surfaces and Mg additions: A first-principles study. *The Journal of Physical Chemistry C* **2015**, *119* (10), 5648-5656. DOI: 10.1021/jp511503b.

(363) Tran, R.; Xu, Z.; Radhakrishnan, B.; Winston, D.; Sun, W.; Persson, K. A.; Ong, S. P. Surface energies of elemental crystals. *Scientific Data* **2016**, *3* (1), 1-13.

(364) Sun, B.; Yang, X.; Zhao, D.; Zhang, L. First-principles study of adsorption mechanism of NH_3 on different ZnO surfaces on organics photocatalytic degradation purpose. *Computational Materials Science* **2018**, *141*, 133-140. DOI: 10.1016/J.COMMATSCI.2017.09.013.

(365) Kuo, F.-L.; Li, Y.; Solomon, M.; Du, J.; Shepherd, N. D. Workfunction tuning of zinc oxide films by argon sputtering and oxygen plasma: an experimental and computational study. *Journal of Physics D: Applied Physics* **2012**, *45* (6), 065301.

(366) Hofmann, O. T.; Deinert, J.-C.; Xu, Y.; Rinke, P.; Stähler, J.; Wolf, M.; Scheffler, M. Large work function reduction by adsorption of a molecule with a negative electron affinity: Pyridine on ZnO (1010) (101). *The Journal of Chemical Physics* **2013**, *139* (17).

(367) Wei, M.; Li, C.-F.; Deng, X.-R.; Deng, H. Surface work function of transparent conductive ZnO films. *Energy Procedia* **2012**, *16*, 76-80.

(368) Kim, T.; Yoshitake, M.; Yagyu, S.; Nemsak, S.; Nagata, T.; Chikyow, T. XPS study on band alignment at Pt-O-terminated ZnO interface. *Surface and Interface Analysis* **2010**, *42* (10-11), 1528-1531.

(369) Sun, W.; Jha, J. K.; Shepherd, N. D.; Du, J. Interface structures of ZnO/MoO_3 and their effect on workfunction of ZnO surfaces from first principles calculations. *Computational Materials Science* **2018**, *141*, 162-169.

(370) Na, S.-H.; Park, C.-H. First-principles study of the surface of wurtzite ZnO and ZnS - implications for nanostructure formation. *Journal of the Korean Physical Society* **2009**, *54* (9(2)), 867-872. DOI: 10.3938/jkps.54.867.

(371) Jiang, W.; Xia, Y.; Pan, A.; Luo, Y.; Su, Y.; Zhao, S.; Wang, T.; Zhao, L. Facet-dependent gas adsorption selectivity on ZnO: A DFT study. *Chemosensors* **2022**, *10* (10), 436. DOI: 10.3390/chemosensors10100436.

(372) Beltrán, A.; Andrés, J.; Calatayud, M.; Martins, J. B. L. Theoretical study of ZnO (1010) and Cu/ZnO (1010) surfaces. *Chemical Physics Letters* **2001**, *338* (4), 224-230. DOI: 10.1016/S0009-2614(01)00238-X.

(373) Hofmann, O. T.; Deinert, J.-C.; Xu, Y.; Rinke, P.; Stähler, J.; Wolf, M.; Scheffler, M. Large work function reduction by adsorption of a molecule with a negative electron affinity: Pyridine on ZnO. *The Journal of Chemical Physics* **2013**, *139* (17).

(374) Venkatesh, P. S.; Jeganathan, K. Investigations on the morphological evolution of zinc oxide nanostructures and their optical properties. *CrystEngComm* **2014**, *16* (32), 7426-7433.

(375) Muiva, C.; Sathiaraj, S. T.; Maabong, K. Chemical spray pyrolysis path to synthesis of ZnO microsausages from aggregation of elongated double tipped nanoparticles. *Materials Science Forum* **2012**, *706-709*, 2577-2582. DOI: 10.4028/MSF.706-709.2577.

(376) Wróbel, J.; Kurzydłowski, K. J.; Hummer, K.; Kresse, G.; Piechota, J. Calculations of ZnO properties using the Heyd-Scuseria-Ernzerhof screened hybrid density functional. *Physical Review B* **2009**, *80* (15). DOI: 10.1103/PhysRevB.80.155124.

(377) Oshikiri, M.; Aryasetiawan, F. Band gaps and quasiparticle energy calculations on ZnO, ZnS, and ZnSe in the zinc-blende structure by the GW approximation. *Physical Review B* **1999**, *60* (15), 10754-10757. DOI: 10.1103/PhysRevB.60.10754.

(378) Bejar, L.; Medina, A.; Vargas, R.; Herrera, G.; Alfonso, I. Microanalysis of the elemental distribution in particles of $Zn(OH)_2$ obtained by chemical precipitation. *Microscopy and Microanalysis* **2012**, *18* (S2), 1044-1045. DOI: 10.1017/s1431927612007076.

(379) Sokolov, P. S.; Baranov, A. N.; Dobrokhotov, Z. V.; Solozhenko, V. L. Synthesis and thermal stability of cubic ZnO in the salt nanocomposites. *Russian Chemical Bulletin* **2010**, *59* (2), 325-328. DOI: 10.1007/s11172-010-0082-7.

(380) Marcelino, R. B.; Amorim, C. C. Towards visible-light photocatalysis for environmental applications: band-gap engineering versus photons absorption—a review. *Environmental Science and Pollution Research* **2019**, *26*, 4155-4170.

(381) Carr, J. A.; Chaudhary, S. The identification, characterization and mitigation of defect states in organic photovoltaic devices: a review and outlook. *Energy & Environmental Science* **2013**, *6* (12), 3414-3438.

(382) Du, C.; Yan, B.; Lin, Z.; Yang, G. Enhanced carrier separation and increased electron density in 2D heavily N-doped $ZnIn_2S_4$ for photocatalytic hydrogen production. *Journal of Materials Chemistry A* **2020**, *8* (1), 207-217.

(383) Pradhan, N.; Sarma, D. Advances in light-emitting doped semiconductor nanocrystals. *The Journal of Physical Chemistry Letters* **2011**, *2* (21), 2818-2826.

(384) Leschkies, K. S.; Divakar, R.; Basu, J.; Enache-Pommer, E.; Boercker, J. E.; Carter, C. B.; Kortshagen, U. R.; Norris, D. J.; Aydil, E. S. Photosensitization of ZnO nanowires with CdSe quantum dots for photovoltaic devices. *Nano Letters* **2007**, *7* (6), 1793-1798.

(385) Cao, L.; Jiang, J.; Zhu, L. Realization of band-gap engineering of ZnO thin films via Ca alloying. *Materials Letters* **2013**, *100*, 201-203.

(386) Liqiang, J.; Baiqi, W.; Baifu, X.; Shudan, L.; Keying, S.; Weimin, C.; Honggang, F. Investigations on the surface modification of ZnO nanoparticle photocatalyst by depositing Pd. *Journal of Solid State Chemistry* **2004**, *177* (11), 4221-4227.

(387) Patil, S. S.; Mali, M. G.; Tamboli, M. S.; Patil, D. R.; Kulkarni, M. V.; Yoon, H.; Kim, H.; Al-Deyab, S. S.; Yoon, S. S.; Kolekar, S. S. Green approach for hierarchical nanostructured Ag-ZnO and their photocatalytic performance under sunlight. *Catalysis Today* **2016**, *260*, 126-134.

(388) Sharma, V.; Prasad, M.; Jadkar, S.; Pal, S. Influence of carbon and phosphorus doping on electronic properties of ZnO. *Journal of Materials Science: Materials in Electronics* **2016**, *27*, 12318-12322.

(389) He, H.; Zhuge, F.; Ye, Z.; Zhu, L.; Wang, F.; Zhao, B.; Huang, J. Strain and its effect on optical properties of Al-N codoped ZnO films. *Journal of Applied Physics* **2006**, *99* (2).

(390) Duan, X.-Y.; Zhao, Y.-J.; Yao, R.-H. Pushing p-type conductivity in ZnO by (Zr, N) codoping: A first-principles study. *Solid State Communications* **2008**, *147* (5), 194-197. DOI: 10.1016/j.ssc.2008.05.027.

(391) Gowrishankar, S.; Balakrishnan, L.; Gopalakrishnan, N. Band gap engineering in $Zn_{(1-x)}Cd_xO$ and $Zn_{(1-x)}Mg_xO$ thin films by RF sputtering. *Ceramics International* **2014**, *40* (1), 2135-2142.

(392) Sekar, A.; Kim, S.; Umar, A.; Hahn, Y. Catalyst-free synthesis of ZnO nanowires on Si by oxidation of Zn powders. *Journal of Crystal Growth* **2005**, *277* (1-4), 471-478.

(393) Nazim, V. S.; El-Sayed, G. M.; Amer, S. M.; Nadim, A. H. Optimization of metal dopant effect on ZnO nanoparticles for enhanced visible LED photocatalytic degradation of citalopram: comparative study and application to pharmaceutical cleaning validation. *Sustainable Environment Research* **2023**, *33* (1), 39.

(394) Park, Y. R.; Kim, K. J. Optical and electrical properties of Ti-doped ZnO films: observation of semiconductor–metal transition. *Solid State Communications* **2002**, *123* (3), 147-150. DOI: 10.1016/S0038-1098(02)00217-X.

(395) Paul, G. K.; Bandyopadhyay, S.; Sen, S. K.; Sen, S. Structural, optical and electrical studies on sol–gel deposited Zr doped ZnO films. *Materials Chemistry and Physics* **2003**, *79* (1), 71-75. DOI: 10.1016/S0254-0584(02)00454-6.

(396) Qu, X.; Bai, L.; Meng, Q.; Jia, D. Electronic structure and optical properties of Sn-doped ZnO. *Physica B: Condensed Matter* **2012**, *407* (2), 268-270.

(397) Bergum, K.; Hansen, P.-A.; Fjellvåg, H.; Nilsen, O. Structural, electrical and optical characterization of Ti-doped ZnO films grown by atomic layer deposition. *Journal of Alloys and Compounds* **2014**, *616*, 618-624.

(398) Noh, Y. W.; Lee, J. H.; Jin, I. S.; Park, S. H.; Jung, J. W. Tailored electronic properties of Zr-doped SnO_2 nanoparticles for efficient planar perovskite solar cells with marginal hysteresis. *Nano Energy* **2019**, *65*, 104014.

(399) Dalapati, G. K.; Sharma, H.; Guchhait, A.; Chakrabarty, N.; Bamola, P.; Liu, Q.; Saianand, G.; Krishna, A. M. S.; Mukhopadhyay, S.; Dey, A. Tin oxide for optoelectronic, photovoltaic and energy storage devices: a review. *Journal of Materials Chemistry A* **2021**, *9* (31), 16621-16684.

(400) Kondrotas, R.; Pakštas, V.; Franckevičius, M.; Suchodolskis, A.; Tumėnas, S.; Jašinskas, V.; Juškėnas, R.; Krotkus, A.; Muska, K.; Kauk-Kuusik, M. Band gap engineering by cationic substitution in $Sn(Zr_{1-x}Ti_x)Se_3$ alloy for bottom sub-cell application in solar cells. *Journal of Materials Chemistry A* **2023**, *11* (48), 26488-26498.

(401) Adelowo, E.; Fasasi, A.; Adeoye, M.; Alayande, S. Structural and optical properties of tin doped zinc oxide fibres prepared by electrospinning technique. *Chemistry and Materials Research* **2013**, *3* (13), 96-106.

(402) Onwudiwe, D. C. Photocatalytic reduction of hexavalent chromium using Zn_2SnO_4–ZnO modified g-C_3N_4 composite. North-West University: 2023.

(403) Singh, M.; Goyal, M.; Devlal, K. Size and shape effects on the band gap of semiconductor compound nanomaterials. *Journal of Taibah University for Science* **2018**, *12* (4), 470-475.

(404) Anisimov, V. I.; Zaanen, J.; Andersen, O. K. Band theory and Mott insulators: Hubbard U instead of Stoner I. *Physical Review B* **1991**, *44* (3), 943.

(405) Jiang, H.; Gomez-Abal, R. I.; Rinke, P.; Scheffler, M. First-principles modeling of localized d states with the GW LDA+ U approach. *Physical Review B* **2010**, *82* (4), 045108.

(406) File, P. D. Joint Committee on Powder Diffraction Standards (JCPDS). *ASTM, Philadelphia, PA* **1997**.

(407) Paraguay D, F.; Morales, J.; Estrada L, W.; Andrade, E.; Miki-Yoshida, M. Influence of Al, In, Cu, Fe and Sn dopants in the microstructure of zinc oxide thin films obtained by spray pyrolysis. *Thin Solid Films* **2000**, *366* (1-2), 16-27, Article. DOI: 10.1016/S0040-6090(00)00752-5 Scopus.

(408) Shanshool, H. M.; Yahaya, M.; Yunus, W. M. M.; Abdullah, I. Y. Investigation of energy band gap in polymer/ZnO nanocomposites. *Journal of Materials Science: Materials in Electronics* **2016**, *27*, 9804-9811.

(409) Yung, K. C.; Liem, H.; Choy, H. Enhanced redshift of the optical band gap in Sn-doped ZnO free standing films using the sol–gel method. *Journal of Physics D: Applied Physics* **2009**, *42* (18), 185002.

(410) Cheng, J.; Zhang, Y.; Guo, R. ZnO microtube ultraviolet detectors. *Journal of Crystal Growth* **2008**, *310* (1), 57-61.

(411) Hautier, G.; Miglio, A.; Waroquiers, D.; Rignanese, G.-M.; Gonze, X. How does chemistry influence electron effective mass in oxides? A high-throughput computational analysis. *Chemistry of Materials* **2014**, *26* (19), 5447-5458.

(412) Thomas, D.; Vattappalam, S. C.; Mathew, S.; Augustine, S. Appraisal on textured grain growth and photoconductivity of ZnO thin film SILAR. *Advances in Chemistry* **2014**, *549019*.

(413) Shi, X.; Zhao, X.; Duan, L.; Sun, H.; Liu, J.; Bai, X.; Guan, M.; Cao, M.; Liu, J. Notable shift of ultraviolet intensity on Sn-doped ZnO nanostructure fabricated by sol–gel method. *Journal of Sol-gel Science and Technology* **2013**, *66*, 301-305.

(414) Chen, L.; Ren, J. T.; Yuan, Z. Y. Enabling internal electric fields to enhance energy and environmental catalysis. *Advanced Energy Materials* **2023**, *13* (11), 2203720.

(415) Su, J.; Shi, Y.; Liu, L.; An, X.; Wang, Y.; Wang, K.; Niu, Q. Tin doping modulates electron-hole recombination in Dion-Jacobson phase 2D hybrid perovskite. *Physica B: Condensed Matter* **2024**, *690*, 416276.

(416) Ameen, S.; Akhtar, M. S.; Seo, H.-K.; Kim, Y. S.; Shin, H. S. Influence of Sn doping on ZnO nanostructures from nanoparticles to spindle shape and their photoelectrochemical properties for dye sensitized solar cells. *Chemical Engineering Journal* **2012**, *187*, 351-356.

Appendix: A3

The "accumulated density of states" refers to the total area under the pDOS plot for the d-orbitals, helping to pinpoint the band centre. Similarly, the "half-accumulated density of states" represents half the total area under the pDOS plot, which is used to locate the energy level where half of the d-band states are filled.

Table A3-1: pDOS for the Hexagonal, Cubic and Zinc-Blende crystal systems.

Density of states (electrons/eV)		Hexagonal	Cubic	Zinc-Blende
d-band (eV)	Accumulated pDOS	633.521	1250.126	1272.138
	Half Accumulated pDOS	316.760	625.063	636.069
	Band centre	7.204	6.287	6.464

Table A3-2: Calculated surface energies and surface illustrations for the hexagonal, cubic and Zinc-Blende crystal systems.

ZnO Crystal system	Surface[a]	Surface energies[b] (J/m^2)	Literature values (J/m^2)	Top view of surface
Hexagonal	(100)	**0.596**	0.68 [364]	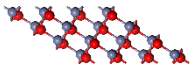 1
	$(002)_{MT}$	**0.807**	-	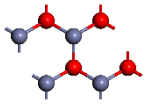 2
	$(002)_{OT}$	4.331	5.4 [230]	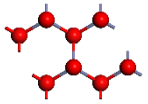 3
	$(101)_{MT}$	1.113	1.12 [370]	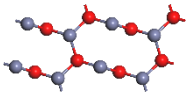 4
	$(101)_{OT}$	1.939	2.00 [371] 1.85 [372]	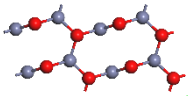 5
	$(102)_{MT}$	1.338	-	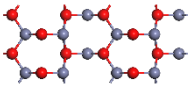 6
	$(102)_{OT}$	1.204	1.04 [322]	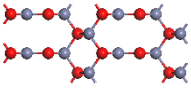 7
	(210)	0.795	0.85 [314]	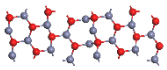 8
	$(103)_{MT}$	0.685	-	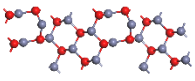 9
	$(103)_{OT}$	1.109	-	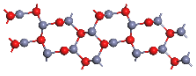 10
	(200)	2.101	-	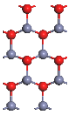 11

	$(112)_{MT}$	1.483	-	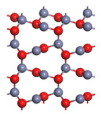 12
	$(112)_{OT}$	0.986		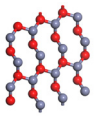 13
	$(201)_{MT}$	1.610	-	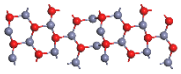 14
	$(201)_{OT}$	**0.821**	-	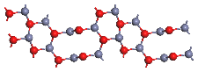 15
	$(111)_{MT}$	0.905	-	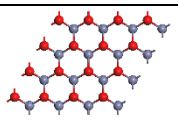 16
	$(111)_{OT}$	0.966	1.53 [362]	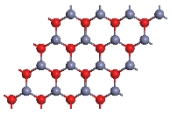 17
	(200)	0.548	-	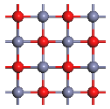 18
	(220)	0.900	-	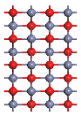 19
Cubic	$(311)_{MT}$	0.610	-	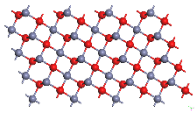 20
	$(311)_{OT}$	0.541	-	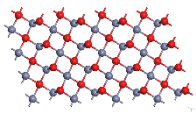 21
	$(222)_{MT}$	0.905	-	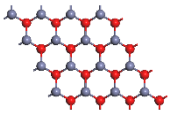 22
	$(222)_{OT}$	0.966	-	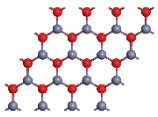 23

	(400)	**0.548**	-	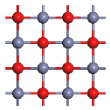 24
	$(111)_{MT}$	1.061	1.02 [291]	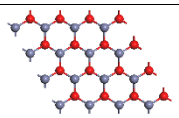 25
	$(111)_{OT}$	4.304	-	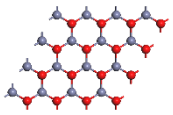 26
	$(200)_{MT}$	2.757	-	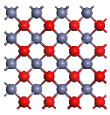 27
	$(200)_{OT}$	2.766	-	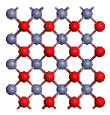 28
	(220)	**0.747**	-	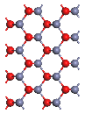 29
Zinc-Blende	$(311)_{MT}$	1.420	-	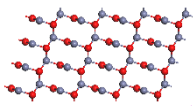 30
	$(311)_{OT}$	1.548	-	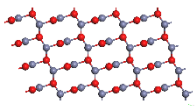 31
	$(222)_{MT}$	0.416	-	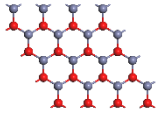 32
	$(222)_{OT}$	4.225	-	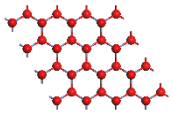 33
	$(400)_{MT}$	2.203	-	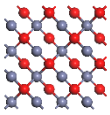 34
	$(400)_{OT}$	2.203	-	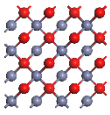 35

Appendix: A4

Table A4-1: Supercell simulation data for 6.25% Sn-doped ZnO

```
[cayo-olaojo@login2 lustre]$ ./supercell -i ZnSnOhex00625.cif -s 2x2x2 -m -o test20/ciffile10
-------------------------------------------------
-          Supercell program (v2.1)             -
-       https://orex.github.io/supercell/       -
-------------------------------------------------
-     Authors:   * Kirill Okhotnikov             -
-                (kirill.okhotnikov@gmail.com)   -
-                * Sylvian Cadars                -
-                (sylvian.cadars@cnrs-imn.fr)    -
-                * Thibault Charpentier          -
-                (Thibault.Charpentier@cea.fr)   -
-------------------------------------------------
- please cite:                                   -
-   K. Okhotnikov, T. Charpentier and S. Cadars  -
-   J. Cheminform. 8 (2016) 17 – 33.             -
-------------------------------------------------

Command line: ./supercell -i ZnSnOhex00625.cif -s 2x2x2 -m -o test20/ciffile10
Random SEED: 3430414855
CIF file info:
  INFO: Using symmetries from space group.

Initial system:
  Chemical Formula: O2 Sn0.125 Zn1.875

Supercell system (2x2x2):
  Size a=6.4747, b=6.4747, c=10.4441

Current charge balance option is "try"
Total charge oxidation state (cif):  0
Total charge cell:   0
Charge balancing:   yes
-------------------------------------------------------------
| Atom Label    |       charge          | mult  | occup x mult
|               | Ox. state     | Used  | (cif) |
-------------------------------------------------------------
|  O1           |  -2           |  -2   |  2    |  2
|  Sn0          |  2            |  2    |  2    |  0.125
|  Zn0          |  2            |  2    |  2    |  1.875
-------------------------------------------------------------

Chemical formula of the supercell: O16 Sn1 Zn15
Total charge of supercell: 0

-------------------------------------------------
```

```
 Identification of groups of crystallographic sites
 ---------------------------------------------------

 Group 1 (16 atomic positions in supercell):
  * Site #1: O1 (occ. 1) -> FIXED with occupancy 1.000.

 Group 2 (16 atomic positions in supercell):
  * Site #1: Zn0 (occ. 0.9375) -> distributed over 15 positions out of 16 (actual occ.: 0.938).
  * Site #2: Sn0 (occ. 0.0625) -> distributed over 1 positions out of 16 (actual occ.: 0.062).
  Number of combinations for the group is 16

Minimal distance between atoms of two distinct groups: 1.97279 A.

-------------------------------------------------
The total number of combinations is 16
-------------------------------------------------
96 symmetry operation found for supercell.
Total enumeration time: 0:00:0.00485069
Combinations after merge: 1
[cayo-olaojo@login2 lustre]$
```

Table A4-2: Supercell simulation data for 12.50% Sn-doped ZnO

```
[cayo-olaojo@login2 lustre]$ ./supercell -i ZnSnOhex0125.cif -s 2x2x2 -m -o
test20/ciffile15
-------------------------------------------------
-          Supercell program (v2.1)             -
-       https://orex.github.io/supercell/       -
-------------------------------------------------
-     Authors:   * Kirill Okhotnikov             -
-                (kirill.okhotnikov@gmail.com)   -
-                * Sylvian Cadars                -
-                (sylvian.cadars@cnrs-imn.fr)    -
-                * Thibault Charpentier          -
-                (Thibault.Charpentier@cea.fr)   -
-------------------------------------------------
- please cite:                                   -
-   K. Okhotnikov, T. Charpentier and S. Cadars  -
-   J. Cheminform. 8 (2016) 17 – 33.             -
-------------------------------------------------

Command line: ./supercell -i ZnSnOhex0125.cif -s 2x2x2 -m -o test20/ciffile15
Random SEED: 4019886641
CIF file info:
  INFO: Using symmetries from space group.

Initial system:
  Chemical Formula: O2 Sn0.25 Zn1.75

Supercell system (2x2x2):
  Size a=6.4747, b=6.4747, c=10.4441

Current charge balance option is "try"
Total charge oxidation state (cif):  0
Total charge cell:   0
Charge balancing:   yes
-----------------------------------------------------------------
| Atom Label   |      charge         | mult  | occup x mult
|              | Ox. state    | Used  | (cif) |
-----------------------------------------------------------------
|  O1          |  -2          |  -2   |  2    |  2
|  Sn0         |  2           |  2    |  2    |  0.25
|  Zn0         |  2           |  2    |  2    |  1.75
-----------------------------------------------------------------

Chemical formula of the supercell: O16 Sn2 Zn14
Total charge of supercell: 0

-------------------------------------------------
 Identification of groups of crystallographic sites
-------------------------------------------------
```

```
 Group 1 (16 atomic positions in supercell):
  * Site #1: O1 (occ. 1) -> FIXED with occupancy 1.000.

 Group 2 (16 atomic positions in supercell):
  * Site #1: Zn0 (occ. 0.875) -> distributed over 14 positions out of 16 (actual occ.: 0.875).
  * Site #2: Sn0 (occ. 0.125) -> distributed over 2 positions out of 16 (actual occ.: 0.125).
  Number of combinations for the group is 120

Minimal distance between atoms of two distinct groups: 1.97279 A.

------------------------------------------------
The total number of combinations is 120
------------------------------------------------
96 symmetry operation found for supercell.
Total enumeration time: 0:00:0.0079298
Combinations after merge: 5
[cayo-olaojo@login2 lustre]$
```

Table A4-3: Supercell simulation data for 18.75% Sn-doped ZnO

```
[cayo-olaojo@login2 ~]$ cd lustre
[cayo-olaojo@login2 lustre]$ ./supercell -i ZnSnOhex01875.cif -s 2x2x2 -m -o test20/ciffile20
-------------------------------------------------
-          Supercell program (v2.1)             -
-       https://orex.github.io/supercell/       -
-------------------------------------------------
-     Authors:   * Kirill Okhotnikov             -
-                (kirill.okhotnikov@gmail.com)   -
-                * Sylvian Cadars                -
-                (sylvian.cadars@cnrs-imn.fr)    -
-                * Thibault Charpentier          -
-                (Thibault.Charpentier@cea.fr)   -
-------------------------------------------------
- please cite:                                   -
-   K. Okhotnikov, T. Charpentier and S. Cadars  -
-   J. Cheminform. 8 (2016) 17 – 33.             -
-------------------------------------------------

Command line: ./supercell -i ZnSnOhex01875.cif -s 2x2x2 -m -o test20/ciffile20
Random SEED: 1252009633
CIF file info:
  INFO: Using symmetries from space group.

Initial system:
  Chemical Formula: O2 Sn0.375 Zn1.625

Supercell system (2x2x2):
  Size a=6.4747, b=6.4747, c=10.4441

Current charge balance option is "try"
Total charge oxidation state (cif):  0
Total charge cell:   0
Charge balancing:   yes
-----------------------------------------------------------------
| Atom Label    |      charge          | mult  | occup x mult
|               | Ox. state     | Used  | (cif) |
-----------------------------------------------------------------
|  O1           |  -2           |  -2   |  2    |  2
|  Sn0          |  2            |  2    |  2    |  0.375
|  Zn0          |  2            |  2    |  2    |  1.625
-----------------------------------------------------------------

Chemical formula of the supercell: O16 Sn3 Zn13
Total charge of supercell: 0

-------------------------------------------------
 Identification of groups of crystallographic sites
-------------------------------------------------
```

```
 Group 1 (16 atomic positions in supercell):
  * Site #1: O1 (occ. 1) -> FIXED with occupancy 1.000.

 Group 2 (16 atomic positions in supercell):
  * Site #1: Zn0 (occ. 0.8125) -> distributed over 13 positions out of 16 (actual occ.: 0.812).
  * Site #2: Sn0 (occ. 0.1875) -> distributed over 3 positions out of 16 (actual occ.: 0.188).
   Number of combinations for the group is 560

Minimal distance between atoms of two distinct groups: 1.97279 A.

------------------------------------------------
The total number of combinations is 560
------------------------------------------------
96 symmetry operation found for supercell.
Total enumeration time: 0:00:0.101792
Combinations after merge: 12
[cayo-olaojo@login2 lustre]$
```

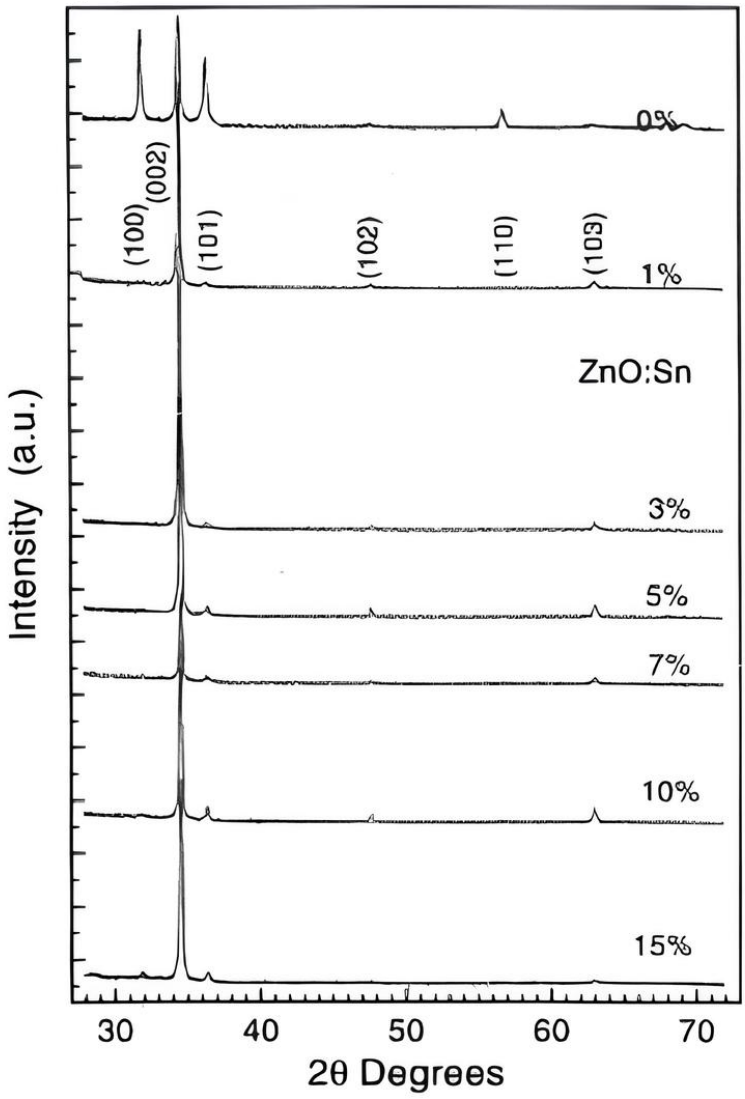

Figure A4-1: ***XRD graph culled from literature[294] for optimised Sn-doped ZnO bulk structures at various doping percentages: (a) 0%, (b) 1%, (c) 3%, (d) 5%, (e) 7%, (f) 10%, (g) 15%***

Table A4-4: Surface illustrations for the 6.25% Sn-doped ZnO crystal systems.

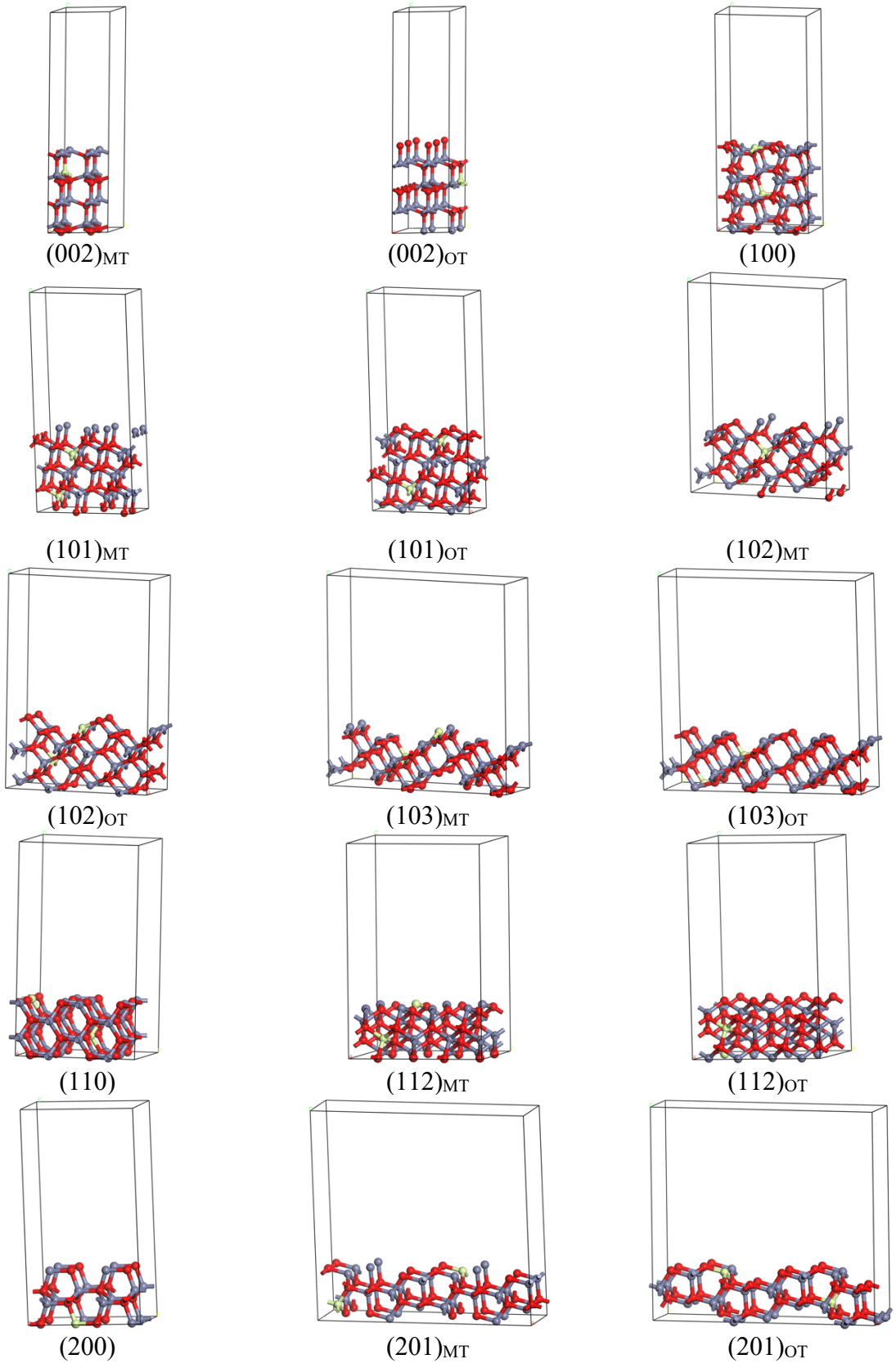

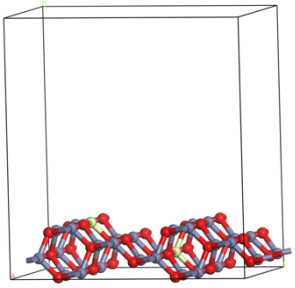

(210)

Table A4-5: Surface illustrations for the 12.50% Sn-doped ZnO crystal systems.

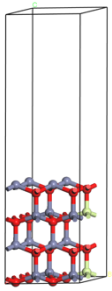

$(002)_{MT}$

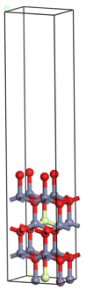

$(002)_{OT}$

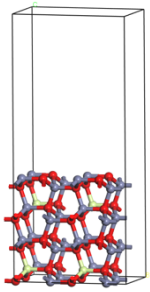

(100)

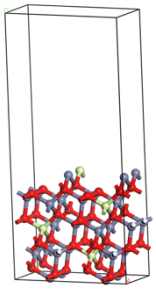

$(101)_{MT}$

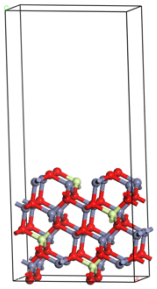

$(101)_{OT}$

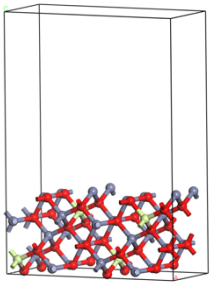

$(102)_{MT}$

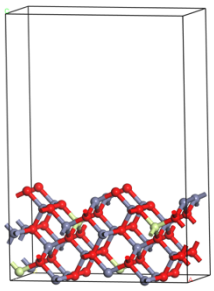

$(102)_{OT}$

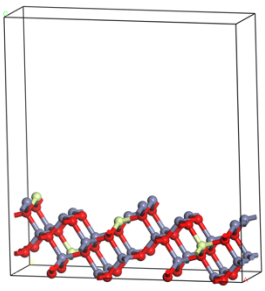

$(103)_{MT}$

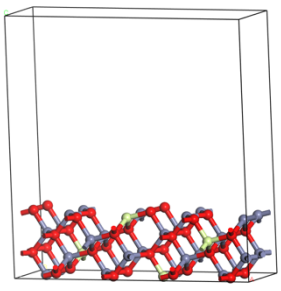

$(103)_{OT}$

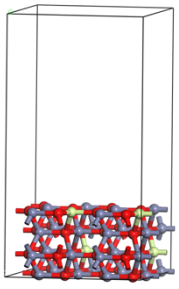

(110)

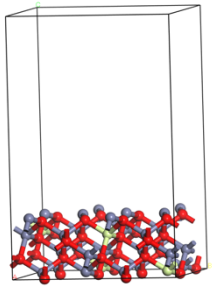

$(112)_{MT}$

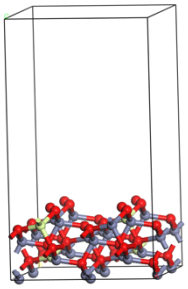

$(112)_{OT}$

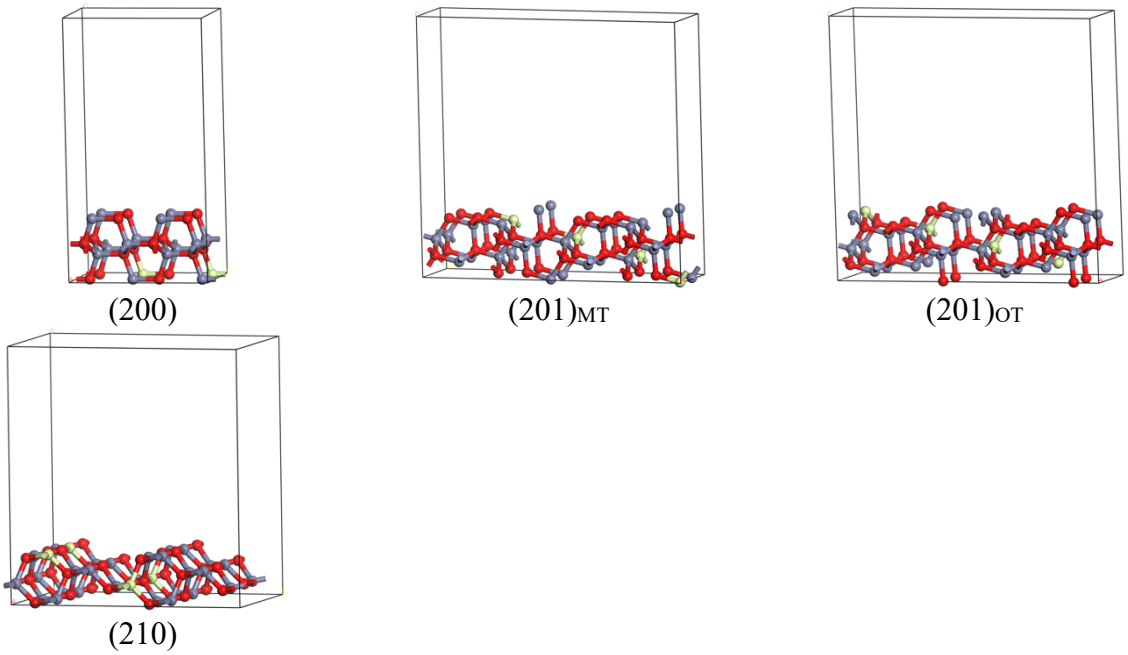

Table A4-6: Surface illustrations for the 18.75% Sn-doped ZnO crystal systems.

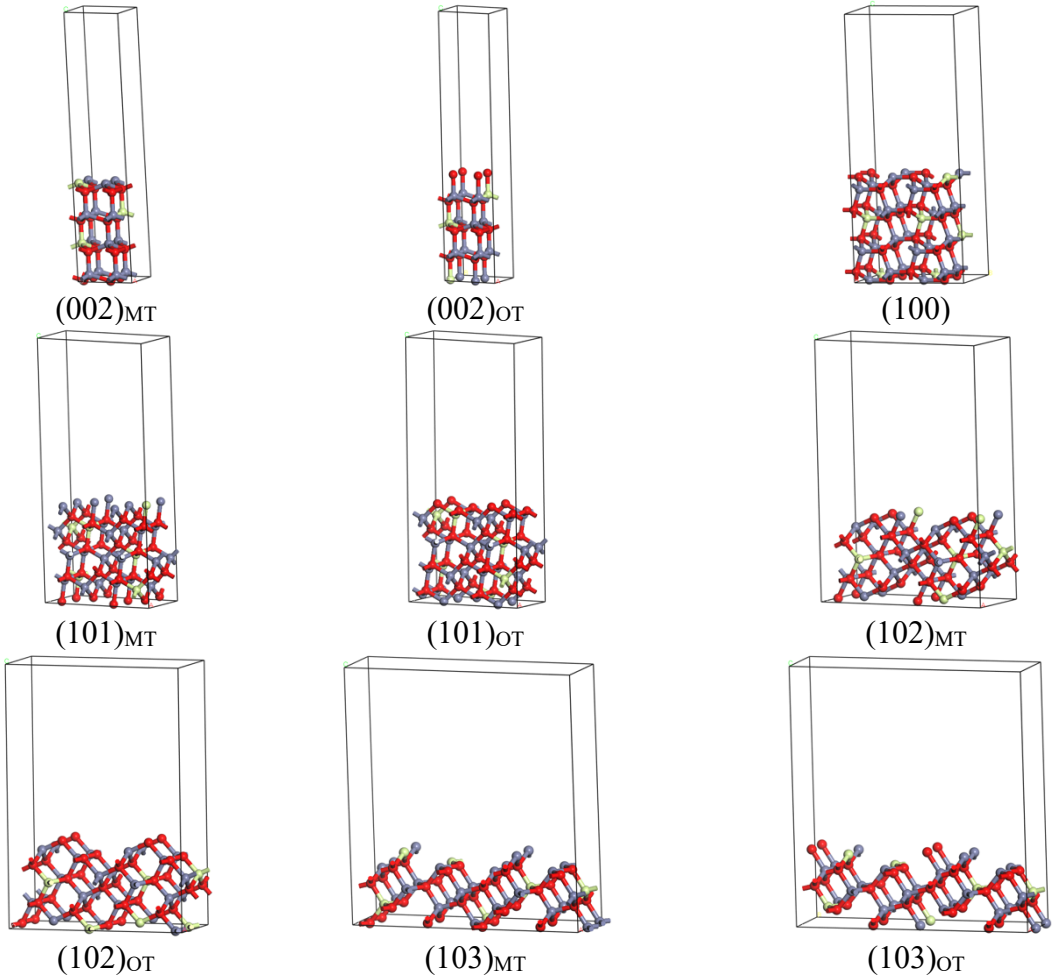

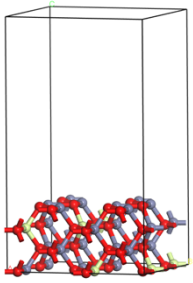

(110)

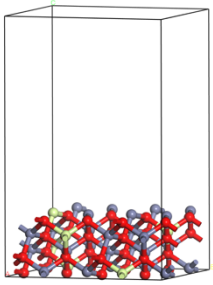

$(112)_{MT}$

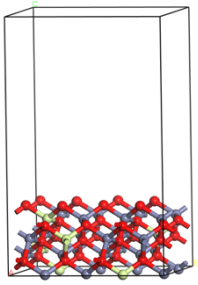

$(112)_{OT}$

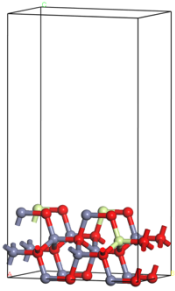

(200)

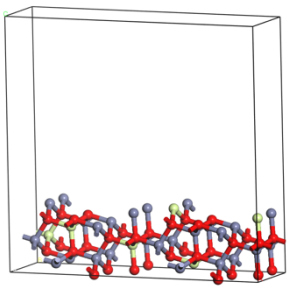

$(201)_{MT}$

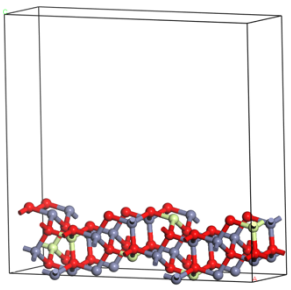

$(201)_{OT}$

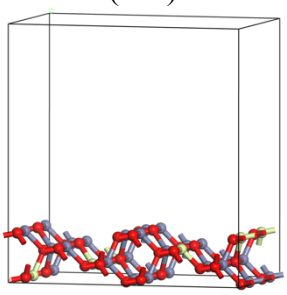

(210)

The fractional coordinates for the Sn-doped ZnO surface slabs, consisting of 2 to 8 layers and derived from a 2×2×2 Sn-doped ZnO bulk structure at doping levels of 6.25%, 12.50%, and 18.75%, are presented in Tables A4-7 to A4-54.

Table A4-7: ***Fractional coordinates of $(002)_{MT}$ 6.25% Sn-doped ZnO using 400 eV cut-off energy, 7×7×1 k-points and a Hubbard U value of $U_{d\text{-}Zn}$ = 10 eV and $U_{p\text{-}O}$ = 7 eV.***

Element	Atom Number	Fractional coordinates of atoms u	v	w
O	1	0.861568	0.683810	0.006386
O	2	0.525725	0.514178	0.109593
O	3	0.852148	0.660580	0.225263
O	4	0.534863	0.507284	0.343996
O	5	0.865616	0.177004	0.022645
O	6	0.527570	0.011494	0.116824
O	7	0.846176	0.207814	0.223809
O	8	0.519609	0.011587	0.336303
O	9	0.363148	0.681584	0.003787
O	10	0.033111	0.524581	0.110468
O	11	0.362651	0.668471	0.223714
O	12	0.029813	0.517011	0.343304
O	13	0.362270	0.179276	0.006901
O	14	0.025827	0.014152	0.143598
O	15	0.377369	0.189066	0.225064
O	16	0.018326	0.020330	0.323817
Zn	1	0.879290	0.706545	0.368162
Zn	2	0.528054	0.513539	0.015567
Zn	3	0.851450	0.666733	0.130693
Zn	4	0.529947	0.509299	0.253936
Zn	5	0.850308	0.178568	0.361989
Zn	6	0.519999	0.005983	0.022827
Zn	7	0.870299	0.184396	0.112388
Zn	8	0.522392	-0.000617	0.244529
Zn	9	0.368767	0.681509	0.361111
Zn	10	0.033432	0.521367	0.015476
Zn	11	0.359045	0.677928	0.130024
Zn	12	0.040614	0.522542	0.252839
Zn	13	0.336113	0.162723	0.367480
Zn	14	0.032320	0.014021	0.004870
Zn	15	0.374213	0.189106	0.130896
Sn	1	0.016444	0.021839	0.233444

Table A4-8: Fractional coordinates of $(002)_{OT}$ 6.25% Sn-doped ZnO using 400 eV cut-off energy, 7×7×1 k-points and a Hubbard U value of $U_{d\text{-}Zn}$ = 10 eV and $U_{p\text{-}O}$ = 7 eV.

Element	Atom Number	Fractional coordinates of atoms u	v	w
O	1	0.239030	0.751109	0.393101
O	2	0.647887	0.492598	0.076158
O	3	-0.018226	0.654836	0.178331
O	4	0.753255	0.370226	0.263046
O	5	0.069720	-0.001929	0.394990
O	6	0.654340	0.982816	0.075987
O	7	-0.021443	0.157674	0.187826
O	8	0.666224	0.960900	0.309095
O	9	0.644845	0.482476	0.363384
O	10	0.153432	0.483918	0.076420
O	11	0.474248	0.672500	0.190821
O	12	0.178353	0.457104	0.303227
O	13	0.288589	-0.002141	0.396989
O	14	0.146640	0.985510	0.075686
O	15	0.483082	0.157098	0.176734
O	16	0.173558	0.956087	0.289485
Zn	1	-0.030771	0.613612	0.338297
Zn	2	0.668549	0.487368	-0.009555
Zn	3	-0.019411	0.650302	0.098884
Zn	4	0.631450	0.501815	0.213124
Zn	5	0.009224	0.128666	0.327271
Zn	6	0.668573	0.986697	-0.009336
Zn	7	-0.017405	0.154731	0.102272
Zn	8	0.650811	1.017781	0.228179
Zn	9	0.482183	0.645821	0.341306
Zn	10	0.157122	0.464810	-0.009430
Zn	11	0.480346	0.656500	0.105456
Zn	12	0.120936	0.489602	0.227326
Zn	13	0.532633	0.177088	0.329611
Zn	14	0.156078	0.964250	-0.009957
Zn	15	0.485825	0.155427	0.093130
Sn	1	0.156882	0.985758	0.209735

Table A4-9: ***Fractional coordinates of (100) 6.25% Sn-doped ZnO using 400 eV cut-off energy, 7×7×1 k-points and a Hubbard U value of $U_{d\text{-}Zn}$ = 10 eV and $U_{p\text{-}O}$ = 7 eV.***

Element	Atom Number	Fractional coordinates of atoms u	v	w
O	1	0.110703	0.843291	0.114027
O	2	0.612417	0.840787	0.351960
O	3	0.107661	0.089207	0.032713
O	4	0.612829	0.089796	0.270465
O	5	0.143001	0.337847	0.114288
O	6	0.637906	0.342623	0.350701
O	7	0.112910	0.587121	0.033164
O	8	0.609405	0.590095	0.269775
O	9	0.611490	0.841310	0.114357
O	10	0.110338	0.839713	0.351985
O	11	0.614190	0.085481	0.030959
O	12	0.109387	0.089585	0.270680
O	13	0.695985	0.314106	0.100144
O	14	0.134165	0.344641	0.351118
O	15	0.608831	0.587402	0.033015
O	16	0.112233	0.590367	0.269692
O	17	0.360513	0.839714	-0.002671
O	18	0.860863	0.838038	0.231821
O	19	0.864990	0.086303	0.154169
O	20	0.362012	0.091913	0.386574
O	21	0.361869	0.335029	-0.002435
O	22	0.863795	0.341230	0.229365
O	23	0.862428	0.588694	0.151865
O	24	0.363017	0.592598	0.387144
O	25	0.861780	0.833114	-0.002314
O	26	0.361090	0.842750	0.231837
O	27	0.362898	0.088810	0.152594
O	28	0.862896	0.094698	0.386900
O	29	0.867007	0.347109	-0.010539
O	30	0.359225	0.333903	0.234502
O	31	0.357302	0.604054	0.153094
O	32	0.862244	0.583781	0.385170
Zn	1	0.108504	0.656405	0.113959
Zn	2	0.612569	0.649731	0.350767
Zn	3	0.109401	0.897689	0.032426
Zn	4	0.611562	0.900627	0.269412
Zn	5	0.109595	0.144508	0.114096
Zn	6	0.610358	0.151226	0.350789
Zn	7	0.109995	0.395903	0.031844
Zn	8	0.613262	0.401000	0.269566
Zn	9	0.612659	0.655668	0.114278
Zn	10	0.110830	0.647057	0.350744

Zn	11	0.612039	0.895863	0.032293
Zn	12	0.109473	0.900450	0.269463
Zn	13	0.612712	0.138260	0.113767
Zn	14	0.112211	0.153406	0.350708
Zn	15	0.613324	0.396742	0.030296
Zn	16	0.109425	0.401628	0.270136
Zn	17	0.360287	0.661750	-0.001086
Zn	18	0.860438	0.647728	0.231313
Zn	19	0.860666	0.897619	0.152950
Zn	20	0.360323	0.913691	0.384611
Zn	21	0.361012	0.156792	-0.001131
Zn	22	0.860567	0.151621	0.231494
Zn	23	0.890867	0.398648	0.151170
Zn	24	0.389535	0.415568	0.384269
Zn	25	0.860958	0.655682	-0.001211
Zn	26	0.360344	0.655126	0.232164
Zn	27	0.360348	0.898030	0.152571
Zn	28	0.861080	0.916448	0.384607
Zn	29	0.859639	0.170578	-0.001042
Zn	30	0.360227	0.142601	0.231719
Sn	1	0.424303	0.398484	0.150496

Table A4-10: ***Fractional coordinates of $(101)_{MT}$ 6.25% Sn-doped ZnO using 400 eV cut-off energy, 7×7×1 k-points and Hubbard U value of $U_{d\text{-}Zn}$ = 10 eV and $U_{p\text{-}O}$ = 7 eV.***

Element	Atom Number	Fractional coordinates of atoms u	v	w
O	1	0.788027	0.024496	0.115063
O	2	0.005142	0.638666	0.328941
O	3	0.518900	0.923504	0.098402
O	4	0.734623	0.504648	0.309654
O	5	0.103628	0.177821	0.023814
O	6	0.396932	0.820620	0.216824
O	7	0.880293	0.178096	-0.001622
O	8	0.126314	0.696258	0.209325
O	9	0.788424	0.522340	0.112354
O	10	0.005326	0.139588	0.328720
O	11	0.508255	0.390151	0.097826
O	12	0.735173	0.001638	0.309577
O	13	0.081904	0.681307	0.023102
O	14	0.394868	0.350445	0.217009
O	15	0.829293	0.335165	-0.001670
O	16	0.124122	0.194193	0.209094
O	17	0.705160	0.254569	0.014872
O	18	0.893822	0.830279	0.224427
O	19	0.324849	-0.010212	0.015052
O	20	0.632059	0.705055	0.203770
O	21	0.278532	0.027915	0.123102
O	22	0.505186	0.638762	0.325994
O	23	-0.002123	0.886195	0.108396
O	24	0.237111	0.506150	0.308979
O	25	0.618273	0.707250	0.023371
O	26	0.891232	0.330110	0.224115
O	27	0.335949	0.606996	0.006994
O	28	0.619354	0.203909	0.207287
O	29	0.261407	0.518570	0.116993
O	30	0.503678	0.139160	0.324471
O	31	0.010074	0.390498	0.107507
O	32	0.241731	0.009136	0.307941
Zn	1	0.954003	0.113362	0.072157
Zn	2	0.147381	0.707100	0.287006
Zn	3	0.673151	0.979984	0.056200
Zn	4	0.881740	0.576166	0.267512
Zn	5	0.557769	0.920964	0.173389
Zn	6	0.788659	0.518573	0.386088
Zn	7	0.259611	0.764114	0.158461
Zn	8	0.452466	0.363088	0.369753
Zn	9	0.948588	0.608951	0.073374
Zn	10	0.147807	0.210213	0.286527
Zn	11	0.663844	0.483036	0.056704
Zn	12	0.882362	0.075105	0.267375
Zn	13	0.552000	0.423602	0.173189

Zn	14	0.789021	0.017243	0.386299
Zn	15	0.258059	0.270849	0.158434
Zn	16	0.455526	0.859616	0.369853
Zn	17	0.042526	0.898898	0.182264
Zn	18	0.288381	0.518263	0.386866
Zn	19	0.788770	0.771599	0.158030
Zn	20	0.950891	0.360209	0.368775
Zn	21	0.422371	0.106988	0.072992
Zn	22	0.650183	0.708506	0.283049
Zn	23	0.176792	0.962779	0.047319
Zn	24	0.382555	0.579246	0.267647
Zn	25	0.042084	0.399288	0.182594
Zn	26	0.289662	0.017938	0.394465
Zn	27	0.787710	0.272972	0.158037
Zn	28	0.954648	0.862216	0.368768
Zn	29	0.462787	0.640312	0.055282
Zn	30	0.656729	0.211462	0.283892
Sn	1	0.180302	0.485601	0.040043
Sn	2	0.386105	0.079943	0.260140

Table A4-11: ***Fractional coordinates of (101)$_{OT}$ 6.25% Sn-doped ZnO using 400 eV cut-off energy, 7×7×1 k-points and Hubbard U value of $U_{d\text{-}Zn}$ = 10 eV and $U_{p\text{-}O}$ = 7 eV.***

Element	Atom Number	Fractional coordinates of atoms u	v	w
O	1	0.000519	0.647825	0.160939
O	2	0.225196	0.403702	0.368185
O	3	0.732080	0.506210	0.142350
O	4	0.943743	0.093684	0.344992
O	5	0.392777	0.674512	0.006693
O	6	0.609842	0.485791	0.274360
O	7	0.131936	0.698706	0.030769
O	8	0.339485	0.324614	0.245869
O	9	-0.000177	0.137281	0.159730
O	10	0.219404	0.634558	0.367944
O	11	0.734297	0.004620	0.136126
O	12	0.940048	0.566877	0.343965
O	13	0.398420	0.305853	0.057773
O	14	0.614517	0.956943	0.263516
O	15	0.131746	0.201147	0.031093
O	16	0.336688	0.815194	0.245175
O	17	0.897621	0.829799	0.049875
O	18	0.108859	0.431547	0.261336
O	19	0.631419	0.689716	0.032191
O	20	0.834359	0.308960	0.244299
O	21	0.497072	0.643842	0.158649
O	22	0.694526	0.113004	0.367405
O	23	0.234122	0.510266	0.135347
O	24	0.433576	0.136869	0.343839
O	25	0.895763	0.334819	0.049750
O	26	0.113447	0.944559	0.276563
O	27	0.618605	0.173829	0.031960
O	28	0.840064	0.814663	0.250100
O	29	0.507175	0.157019	0.166695
O	30	0.727529	0.645696	0.376646
O	31	0.229363	0.009697	0.143986
O	32	0.460519	0.663685	0.352135
Zn	1	0.143344	0.710139	0.123103
Zn	2	0.370504	0.370673	0.335829
Zn	3	0.879182	0.577190	0.105929
Zn	4	0.094614	0.208510	0.325746
Zn	5	0.533587	0.885310	0.015269
Zn	6	0.753286	0.523197	0.233366
Zn	7	0.283214	0.827508	-0.009971
Zn	8	0.492328	0.397426	0.217696
Zn	9	0.145081	0.214149	0.123144
Zn	10	0.359863	0.843468	0.336227
Zn	11	0.883178	0.077580	0.100949
Zn	12	0.089034	0.650765	0.318489
Zn	13	0.544054	0.400928	0.016423

Zn	14	0.758856	0.018869	0.224558
Zn	15	0.281727	0.202465	-0.007673
Zn	16	0.487355	0.886415	0.216213
Zn	17	0.045688	0.904530	0.016117
Zn	18	0.253395	0.523865	0.224719
Zn	19	0.777485	0.766366	-0.009258
Zn	20	0.982610	0.386768	0.211373
Zn	21	0.645151	0.709524	0.123297
Zn	22	0.844181	0.280987	0.336701
Zn	23	0.381443	0.567934	0.098084
Zn	24	0.594061	0.246469	0.328144
Zn	25	0.045660	0.404897	0.016591
Zn	26	0.253319	0.027901	0.234229
Zn	27	0.772637	0.265435	-0.009300
Zn	28	0.990789	0.891781	0.218327
Zn	29	0.649586	0.212786	0.123555
Zn	30	0.870537	0.798583	0.344245
Sn	1	0.385426	0.019901	0.105669
Sn	2	0.626236	0.793635	0.338762

Table A4-12: Fractional coordinates of (102)$_{MT}$ 6.25% Sn-doped ZnO using 400 eV cut-off energy, 7×7×1 k-points and Hubbard U value of $U_{d\text{-}Zn}$ = 10 eV and $U_{p\text{-}O}$ = 7 eV.

Element	Atom Number	Fractional coordinates of atoms u	v	w
O	1	0.230642	0.141342	0.317193
O	2	0.958949	0.637335	0.133835
O	3	0.584519	0.260561	-0.010188
O	4	0.759612	0.645598	0.170382
O	5	0.455967	0.123933	0.132517
O	6	0.730070	0.639634	0.317560
O	7	0.263557	0.141362	0.170943
O	8	1.039605	0.742232	-0.009948
O	9	0.230564	0.635597	0.317223
O	10	0.961224	0.136900	0.131873
O	11	0.584782	0.502130	-0.010250
O	12	0.759840	0.132269	0.170325
O	13	0.456480	0.649556	0.132785
O	14	0.730073	0.137756	0.317632
O	15	0.264477	0.634362	0.171546
O	16	1.065380	-0.035649	-0.010900
O	17	0.092232	0.389460	0.226762
O	18	0.832438	0.889131	0.048170
O	19	0.606513	0.886851	0.064874
O	20	0.894306	0.388946	0.253158
O	21	0.331919	0.388421	0.047835
O	22	0.586773	0.889518	0.232934
O	23	0.117515	0.360113	0.080721
O	24	0.395337	0.889265	0.258859
O	25	0.091018	0.889653	0.229238
O	26	0.801366	0.388267	0.056360
O	27	0.596976	0.388119	0.112779
O	28	0.894431	0.889413	0.254394
O	29	0.319724	0.890343	0.048561
O	30	0.595595	0.389175	0.237295
O	31	0.134749	0.856032	0.091560
O	32	0.401354	0.388671	0.250014
Zn	1	0.046773	0.634519	0.072513
Zn	2	0.314686	0.139516	0.257853
Zn	3	0.120634	0.140511	0.284564
Zn	4	0.840611	0.638970	0.100163
Zn	5	0.545136	0.143235	0.066357
Zn	6	0.813933	0.639690	0.258391
Zn	7	0.334624	0.136471	0.096779
Zn	8	0.613265	0.641225	0.301387
Zn	9	0.051600	0.083358	0.072525
Zn	10	0.314708	0.640308	0.257943
Zn	11	0.120600	0.639544	0.284555
Zn	12	0.841376	0.140417	0.100379
Zn	13	0.545175	0.632810	0.066152

Zn	14	0.813886	0.140119	0.258475
Zn	15	0.335706	0.642200	0.097786
Zn	16	0.613282	0.138950	0.301440
Zn	17	0.186427	0.389114	0.166707
Zn	18	0.481612	0.890088	0.325020
Zn	19	0.717496	0.889945	0.039557
Zn	20	0.976805	0.388713	0.184854
Zn	21	0.688179	0.889417	0.184558
Zn	22	0.984894	0.390099	0.316628
Zn	23	0.214193	0.391156	0.031758
Zn	24	0.474705	0.888910	0.191351
Zn	25	0.188043	0.889195	0.170867
Zn	26	0.481278	0.390084	0.326010
Zn	27	0.693650	0.389978	0.023699
Zn	28	0.975846	0.889534	0.185908
Zn	29	0.692170	0.389342	0.174650
Zn	30	0.984929	0.890070	0.317294
Sn	1	0.199166	0.816156	0.003901
Sn	2	0.491496	0.385525	0.180223

Table A4-13: Fractional coordinates of (102)$_{OT}$ 6.25% Sn-doped ZnO using 400 eV cut-off energy, 7×7×1 k-points and Hubbard U value of $U_{d\text{-}Zn}$ = 10 eV and $U_{p\text{-}O}$ = 7 eV.

Element	Atom Number	Fractional coordinates of atoms u	v	w
O	1	0.696771	0.139402	0.058186
O	2	0.961909	0.640147	0.238194
O	3	0.490886	0.140258	0.089528
O	4	0.752790	0.638418	0.259291
O	5	0.200076	0.610166	0.064768
O	6	0.465384	0.110655	0.241669
O	7	0.252197	0.136310	0.260108
O	8	0.998657	0.639518	0.086593
O	9	0.695855	0.638246	0.058187
O	10	0.962490	0.134792	0.237984
O	11	0.491159	0.635345	0.088459
O	12	0.753297	0.136025	0.259458
O	13	0.200383	0.115219	0.064948
O	14	0.465689	0.612361	0.241276
O	15	0.251814	0.639697	0.259714
O	16	0.998566	0.137902	0.086739
O	17	0.094313	0.361438	0.332584
O	18	0.836296	0.889778	0.143197
O	19	0.358340	0.361464	-0.001770
O	20	0.618670	0.887323	0.174437
O	21	0.335334	0.387472	0.149840
O	22	0.600085	0.861916	0.335414
O	23	0.121311	0.388642	0.182311
O	24	0.856035	0.862090	-0.002620
O	25	0.097433	0.860292	0.334852
O	26	0.837745	0.389683	0.144037
O	27	0.348331	0.861614	0.000316
O	28	0.624228	0.387952	0.175714
O	29	0.342792	0.887419	0.148506
O	30	0.597679	0.358704	0.326005
O	31	0.120836	0.887549	0.180862
O	32	0.857225	0.362947	-0.002533
Zn	1	0.049002	0.635850	0.171624
Zn	2	0.796573	0.111169	0.005082
Zn	3	0.580599	0.139831	0.030961
Zn	4	0.842651	0.640743	0.200650
Zn	5	0.293036	0.604966	-0.001211
Zn	6	0.551874	0.141157	0.175288
Zn	7	0.081419	0.638399	0.020084
Zn	8	0.348368	0.141264	0.208195
Zn	9	0.049974	0.142031	0.171482
Zn	10	0.795802	0.610712	0.005178
Zn	11	0.580229	0.640472	0.028888
Zn	12	0.842946	0.139318	0.200660
Zn	13	0.293078	0.117204	-0.001182

Zn	14	0.551028	0.636477	0.173673
Zn	15	0.081836	0.141116	0.020762
Zn	16	0.348724	0.637287	0.208702
Zn	17	0.185988	0.389580	0.277101
Zn	18	0.920645	0.889276	0.074916
Zn	19	0.712661	0.889607	0.118071
Zn	20	0.999853	0.390974	0.283135
Zn	21	0.414425	0.388938	0.080015
Zn	22	0.694926	0.889522	0.283787
Zn	23	0.214451	0.361597	0.125379
Zn	24	0.508578	0.859675	0.283719
Zn	25	0.193894	0.889979	0.285486
Zn	26	0.920119	0.389352	0.074979
Zn	27	0.716220	0.389725	0.116982
Zn	28	1.005976	0.891134	0.283651
Zn	29	0.422647	0.888954	0.073696
Zn	30	0.685422	0.389399	0.269031
Sn	1	0.217365	0.862752	0.120277
Sn	2	0.466965	0.359627	0.315085

Table A4-14: ***Fractional coordinates of (103)$_{MT}$ 6.25% Sn-doped ZnO using 400 eV cut-off energy, 7×7×1 k-points and Hubbard U value of $U_{d\text{-}Zn}$ = 10 eV and $U_{p\text{-}O}$ = 7 eV.***

Element	Atom Number	Fractional coordinates of atoms u	v	w
O	1	0.698350	0.984224	0.038031
O	2	0.949739	0.586979	0.156223
O	3	0.552390	0.906983	0.095256
O	4	0.801133	0.538828	0.214026
O	5	0.339538	0.292141	0.061933
O	6	0.554833	0.922338	0.259392
O	7	0.168567	0.208230	0.175867
O	8	0.952553	0.605447	-0.009859
O	9	0.698358	0.484141	0.038039
O	10	0.949331	0.086915	0.155464
O	11	0.552548	0.417282	0.094969
O	12	0.801803	0.039866	0.213608
O	13	0.340663	0.805446	0.067988
O	14	0.555025	0.407923	0.259399
O	15	0.165938	0.707696	0.175238
O	16	0.951028	0.103025	-0.009801
O	17	0.054220	0.391805	0.260415
O	18	0.837357	0.793489	0.075427
O	19	0.458775	0.105936	-0.016656
O	20	0.664778	0.708612	0.176486
O	21	0.198828	0.485585	0.036925
O	22	0.450549	0.113235	0.149785
O	23	0.053406	0.403183	0.096488
O	24	0.300044	0.040386	0.204754
O	25	0.054356	0.896118	0.260612
O	26	0.837694	0.295399	0.075155
O	27	0.453275	0.607267	-0.013249
O	28	0.662157	0.207657	0.176965
O	29	0.198008	0.983014	0.036659
O	30	0.448337	0.611303	0.158260
O	31	0.053319	0.904285	0.096957
O	32	0.290376	0.538868	0.251751
Zn	1	0.014541	0.637002	0.063469
Zn	2	0.255703	0.270562	0.223290
Zn	3	0.099391	0.166524	0.242384
Zn	4	0.855813	0.548391	0.135493
Zn	5	0.411061	0.329616	-0.001933
Zn	6	0.646578	0.952987	0.118669
Zn	7	0.244348	0.256895	0.035737
Zn	8	0.494850	0.889820	0.184102
Zn	9	0.013858	0.136182	0.063372
Zn	10	0.255572	0.764519	0.215836
Zn	11	0.095928	0.664698	0.242445
Zn	12	0.855243	0.048764	0.133560
Zn	13	0.408684	0.837550	-0.000966

Zn	14	0.646591	0.451568	0.118715
Zn	15	0.245258	0.759279	0.043787
Zn	16	0.495292	0.382659	0.184125
Zn	17	0.147711	0.451343	0.118776
Zn	18	0.906884	0.830903	0.008074
Zn	19	0.745432	0.758487	0.044612
Zn	20	0.993164	0.357457	0.186341
Zn	21	0.514101	0.142402	0.062205
Zn	22	0.755687	0.767724	0.213491
Zn	23	0.355690	0.073414	0.128869
Zn	24	0.595533	0.685586	0.242501
Zn	25	0.147779	0.952641	0.118820
Zn	26	0.908281	0.333257	0.008073
Zn	27	0.745541	0.258658	0.044533
Zn	28	0.992990	0.858736	0.186413
Zn	29	0.515987	0.643631	0.055902
Zn	30	0.754996	0.266270	0.213447
Sn	1	0.344969	0.546129	0.138790
Sn	2	0.622207	0.198036	0.278264

Table A4-15: Fractional coordinates of (103)$_{OT}$ 6.25% Sn-doped ZnO using 400 eV cut-off energy, 7×7×1 k-points and Hubbard U value of $U_{d\text{-}Zn}$ = 10 eV and $U_{p\text{-}O}$ = 7 eV.

Element	Atom Number	Fractional coordinates of atoms u	v	w
O	1	0.717371	0.981489	0.016123
O	2	0.951702	0.602250	0.174291
O	3	0.561372	0.921251	0.078941
O	4	0.799558	0.540335	0.233992
O	5	0.334219	0.284996	0.090867
O	6	0.577411	0.925628	0.252067
O	7	0.187300	0.232018	0.159498
O	8	0.942633	0.607147	0.008953
O	9	0.716574	0.480863	0.016436
O	10	0.951459	0.100860	0.174254
O	11	0.561275	0.419716	0.079341
O	12	0.801459	0.040708	0.240548
O	13	0.334144	0.802518	0.090493
O	14	0.577298	0.426883	0.251907
O	15	0.187001	0.732059	0.159271
O	16	0.943706	0.105504	0.008707
O	17	0.078449	0.424923	0.245250
O	18	0.832550	0.794969	0.096307
O	19	0.443485	0.106286	0.006319
O	20	0.683649	0.732469	0.156308
O	21	0.216768	0.480029	0.018364
O	22	0.451131	0.103471	0.172607
O	23	0.064858	0.420376	0.080497
O	24	0.303640	0.017251	0.240471
O	25	0.077072	0.924419	0.252285
O	26	0.833084	0.292252	0.096129
O	27	0.438842	0.603809	0.007231
O	28	0.683747	0.231489	0.156332
O	29	0.210356	0.977128	0.018930
O	30	0.455115	0.605341	0.171489
O	31	0.065900	0.920302	0.085287
O	32	0.301376	0.516732	0.241935
Zn	1	0.005010	0.640806	0.088528
Zn	2	0.251336	0.234527	0.231574
Zn	3	0.626044	0.952685	0.010246
Zn	4	0.854094	0.549193	0.151931
Zn	5	0.395415	0.327977	0.008885
Zn	6	0.627078	0.955010	0.171713
Zn	7	0.232116	0.234371	0.069409
Zn	8	0.492895	0.861885	0.221398
Zn	9	0.005257	0.141856	0.088335
Zn	10	0.250861	0.744998	0.231702
Zn	11	0.625174	0.452288	0.010044
Zn	12	0.853926	0.049041	0.153826
Zn	13	0.395491	0.836333	0.008841

Zn	14	0.627214	0.455130	0.171628
Zn	15	0.232711	0.736717	0.069519
Zn	16	0.493061	0.355175	0.221404
Zn	17	0.125754	0.453761	0.163134
Zn	18	0.895343	0.833180	0.019148
Zn	19	0.736458	0.737219	0.070331
Zn	20	0.990722	0.359194	0.221077
Zn	21	0.504157	0.141865	0.086305
Zn	22	0.753047	0.768694	0.230748
Zn	23	0.122527	0.453079	-0.000378
Zn	24	0.354139	0.049624	0.153839
Zn	25	0.126374	0.954169	0.171679
Zn	26	0.896249	0.332006	0.019049
Zn	27	0.736808	0.237409	0.070335
Zn	28	0.991300	0.859465	0.221243
Zn	29	0.506097	0.642966	0.079617
Zn	30	0.753459	0.265293	0.230746
Sn	1	0.110174	0.919079	-0.015529
Sn	2	0.353412	0.552467	0.150825

Table A4-16: Fractional coordinates of (110) 6.25% Sn-doped ZnO using 400 eV cut-off energy, 7×7×1 k-points and Hubbard U value of $U_{d\text{-}Zn}$ = 10 eV and $U_{p\text{-}O}$ = 7 eV.

Element	Atom Number	Fractional coordinates of atoms u	v	w
O	1	0.846133	0.588604	-0.002931
O	2	0.836736	0.089154	0.163152
O	3	0.088507	0.012013	0.081036
O	4	0.078937	0.510640	0.250615
O	5	0.325468	0.607099	-0.031556
O	6	0.337701	0.088681	0.162731
O	7	0.589099	0.011239	0.079126
O	8	0.589671	0.510888	0.246399
O	9	0.844960	0.339236	0.082750
O	10	0.828867	0.837994	0.250801
O	11	0.088976	0.263577	-0.003157
O	12	0.087688	0.761479	0.163171
O	13	0.340153	0.332173	0.078190
O	14	0.341354	0.843899	0.242184
O	15	0.591338	0.261019	-0.002531
O	16	0.589776	0.759112	0.161919
O	17	0.839793	0.838960	0.082395
O	18	0.833516	0.335665	0.251134
O	19	0.089457	0.767049	-0.002672
O	20	0.088147	0.262173	0.163697
O	21	0.339249	0.838799	0.077696
O	22	0.335918	0.340121	0.243718
O	23	0.585411	0.760834	-0.002187
O	24	0.589114	0.261111	0.162347
O	25	0.843146	0.087684	-0.003048
O	26	0.842463	0.589531	0.163005
O	27	0.094379	0.512644	0.080774
O	28	0.081361	0.008213	0.244768
O	29	0.333960	0.080141	-0.004107
O	30	0.336484	0.591386	0.169636
O	31	0.601523	0.509544	0.080120
O	32	0.577921	0.008903	0.242589
Zn	1	0.670932	0.613770	0.007949
Zn	2	0.646389	0.092910	0.165739
Zn	3	0.898632	0.005691	0.079123
Zn	4	0.900934	0.491465	0.240297
Zn	5	0.157898	0.610511	0.007182
Zn	6	0.146209	0.094546	0.167240
Zn	7	0.398099	0.005426	0.078754
Zn	8	0.412307	0.493817	0.240902
Zn	9	0.656037	0.341339	0.078802
Zn	10	0.650804	0.855631	0.239305
Zn	11	0.912173	0.242037	0.008435
Zn	12	0.896720	0.758567	0.169378
Zn	13	0.144857	0.342780	0.078968

Zn	14	0.161063	0.856066	0.238739
Zn	15	0.416166	0.228011	0.007087
Zn	16	0.399015	0.758740	0.160850
Zn	17	0.649299	0.844236	0.078442
Zn	18	0.656453	0.354803	0.239682
Zn	19	0.914411	0.743921	0.008603
Zn	20	0.897242	0.255991	0.169479
Zn	21	0.148782	0.845578	0.078917
Zn	22	0.157327	0.359577	0.240064
Zn	23	0.403080	0.752950	-0.002026
Zn	24	0.398278	0.255782	0.165506
Zn	25	0.666943	0.107797	0.007611
Zn	26	0.654400	0.595099	0.168365
Zn	27	0.901846	0.506574	0.078973
Zn	28	0.902167	-0.008617	0.239795
Zn	29	0.158256	0.108838	0.008046
Zn	30	0.143128	0.593739	0.169806
Sn	1	0.395299	0.517567	0.066048
Sn	2	0.382549	0.025865	0.268153

Table A4-17: Fractional coordinates of $(112)_{MT}$ 6.25% Sn-doped ZnO using 400 eV cut-off energy, 7×7×1 k-points and Hubbard U value of $U_{d\text{-}Zn}$ = 10 eV and $U_{p\text{-}O}$ = 7 eV.

Element	Atom Number	Fractional coordinates of atoms u	v	w
O	1	0.406643	0.705309	-0.003408
O	2	0.920929	0.833250	0.146793
O	3	0.355592	0.445723	-0.003674
O	4	0.843127	0.541296	0.166250
O	5	0.927973	0.163914	-0.011470
O	6	0.412218	0.341893	0.147319
O	7	0.341468	0.086329	0.146800
O	8	0.850457	0.902706	0.007496
O	9	0.160212	0.773940	0.070084
O	10	0.666182	0.919594	0.219676
O	11	0.092765	0.519088	0.062908
O	12	0.593677	0.669021	0.220446
O	13	0.656288	0.267252	0.070545
O	14	0.167271	0.418422	0.210498
O	15	0.594740	0.021470	0.071049
O	16	0.094949	0.166695	0.219123
O	17	0.662577	0.774032	0.071487
O	18	0.166319	0.916331	0.220981
O	19	0.592487	0.531198	0.070792
O	20	0.098944	0.666111	0.219813
O	21	0.168211	0.273928	0.067104
O	22	0.655323	0.414760	0.219780
O	23	0.096717	0.021164	0.071832
O	24	0.595264	0.166096	0.220589
O	25	0.905662	0.645697	0.009410
O	26	0.421791	0.836217	0.147585
O	27	0.832121	0.394356	0.010399
O	28	0.336605	0.589265	0.145889
O	29	0.413046	0.210320	-0.003709
O	30	0.921260	0.311132	0.150148
O	31	0.838893	0.098252	0.134780
O	32	0.347998	0.947914	-0.002248
Zn	1	0.442194	0.117720	0.219901
Zn	2	0.927733	0.980580	0.080480
Zn	3	0.840659	0.762050	0.061204
Zn	4	0.319585	0.869187	0.219569
Zn	5	0.422938	0.478714	0.080995
Zn	6	0.947194	0.617799	0.219340
Zn	7	0.338673	0.228402	0.081446
Zn	8	0.815568	0.384595	0.208692
Zn	9	0.676586	0.055013	0.166644
Zn	10	0.195660	0.914382	0.020047
Zn	11	0.070723	0.667165	0.019655
Zn	12	0.592759	0.804290	0.166557
Zn	13	0.666007	0.416584	0.020102

Zn	14	0.163066	0.553886	0.156130
Zn	15	0.552843	0.150205	0.019605
Zn	16	0.096645	0.299677	0.161089
Zn	17	0.172159	0.053192	0.166908
Zn	18	0.687476	0.917737	0.019962
Zn	19	0.559277	0.677950	0.020086
Zn	20	0.088752	0.804199	0.166694
Zn	21	0.202749	0.415159	0.019134
Zn	22	0.664312	0.554290	0.166517
Zn	23	0.086494	0.160284	0.019385
Zn	24	0.581204	0.301632	0.166834
Zn	25	0.938547	0.116503	0.219351
Zn	26	0.423480	0.974313	0.081482
Zn	27	0.332594	0.727181	0.081118
Zn	28	0.827132	0.886339	0.220373
Zn	29	0.911166	0.508442	0.061812
Zn	30	0.440215	0.617492	0.220350
Sn	1	0.840829	0.242510	0.063310
Sn	2	0.340935	0.398379	0.244001

Table A4-18: Fractional coordinates of (112)$_{OT}$ 6.25% Sn-doped ZnO using 400 eV cut-off energy, 7×7×1 k-points and Hubbard U value of $U_{d\text{-}Zn}$ = 10 eV and $U_{p\text{-}O}$ = 7 eV.

Element	Atom Number	Fractional coordinates of atoms u	v	w
O	1	0.474719	0.713758	0.017402
O	2	0.948248	0.834987	0.150519
O	3	0.290643	0.468578	0.008348
O	4	0.795302	0.598415	0.171531
O	5	0.935382	0.241119	0.082091
O	6	0.460991	0.348133	0.180685
O	7	0.309680	0.108247	0.181215
O	8	0.825879	0.963732	0.028535
O	9	0.221692	0.773551	0.087859
O	10	0.707535	0.848926	0.240946
O	11	0.038629	0.529086	0.088784
O	12	0.558069	0.596824	0.240230
O	13	0.691402	0.275017	0.097467
O	14	0.228676	0.381350	0.250687
O	15	0.555018	0.019224	0.098784
O	16	0.057058	0.160316	0.211232
O	17	0.723193	0.779238	0.080088
O	18	0.174862	0.893259	0.239950
O	19	0.542259	0.527118	0.079737
O	20	0.063290	0.627823	0.231631
O	21	0.225552	0.285672	0.089138
O	22	0.712455	0.343564	0.231484
O	23	0.064007	0.032245	0.088744
O	24	0.556085	0.099581	0.240972
O	25	0.971172	0.698282	0.008159
O	26	0.453821	0.839470	0.182175
O	27	0.794783	0.445581	0.007818
O	28	0.308103	0.585693	0.162428
O	29	0.448969	0.209290	0.017924
O	30	0.954647	0.379149	0.202210
O	31	0.815262	0.090867	0.190642
O	32	0.319392	0.966749	0.037343
Zn	1	0.390206	0.837868	0.020275
Zn	2	0.934549	0.997475	0.151174
Zn	3	0.394138	0.582585	0.019667
Zn	4	0.802784	0.758411	0.180452
Zn	5	0.842568	0.294606	-0.000074
Zn	6	0.454064	0.505467	0.181322
Zn	7	0.858897	0.104840	-0.001223
Zn	8	0.313632	0.268887	0.182047
Zn	9	0.686053	0.002830	0.231642
Zn	10	0.172902	0.920117	0.089764
Zn	11	0.094942	0.675162	0.078653
Zn	12	0.570806	0.753297	0.231652
Zn	13	0.660439	0.420978	0.069100

Zn	14	0.195834	0.529609	0.231258
Zn	15	0.577975	0.165301	0.078846
Zn	16	0.087493	0.303599	0.241937
Zn	17	0.171005	0.040784	0.221976
Zn	18	0.673021	0.928559	0.069096
Zn	19	0.617814	0.665246	0.078442
Zn	20	0.073498	0.780464	0.221327
Zn	21	0.159158	0.427721	0.078682
Zn	22	0.692885	0.501387	0.222059
Zn	23	0.092295	0.184633	0.110963
Zn	24	0.571158	0.250339	0.222020
Zn	25	0.889461	0.820873	0.039892
Zn	26	0.444957	1.006517	0.181290
Zn	27	0.894473	0.564215	0.010494
Zn	28	0.332444	0.740503	0.161848
Zn	29	0.373632	0.341976	0.019768
Zn	30	0.952335	0.534394	0.180828
Sn	1	0.287816	0.120523	0.000641
Sn	2	0.837968	0.258041	0.170192

Table A4-19: ***Fractional coordinates of (200) 6.25% Sn-doped ZnO using 400 eV cut-off energy, 7×7×1 k-points and Hubbard U value of $U_{d\text{-}Zn}$ = 10 eV and $U_{p\text{-}O}$ = 7 eV.***

Element	Atom Number	Fractional coordinates of atoms u	v	w
O	1	0.109346	0.844446	0.244158
O	2	0.111198	0.081357	0.145370
O	3	0.042442	0.335309	0.242233
O	4	0.109117	0.581386	0.149000
O	5	0.609341	0.843766	0.244175
O	6	0.611519	0.081528	0.145935
O	7	0.542642	0.336741	0.242434
O	8	0.607756	0.581479	0.148763
O	9	0.359583	0.829351	0.090384
O	10	0.359572	0.093235	-0.007067
O	11	0.356967	0.329435	0.093585
O	12	0.327155	0.584141	-0.004351
O	13	0.859540	0.829078	0.090361
O	14	0.859125	0.095723	-0.005149
O	15	0.855656	0.336838	0.090974
O	16	0.828922	0.581797	-0.001133
Zn	1	0.109051	0.676743	0.229914
Zn	2	0.109019	0.892397	0.151010
Zn	3	0.110196	0.171875	0.229327
Zn	4	0.109134	0.391710	0.152010
Zn	5	0.608897	0.676103	0.229898
Zn	6	0.609469	0.892404	0.151094
Zn	7	0.610082	0.173234	0.229495
Zn	8	0.610664	0.391852	0.152295
Zn	9	0.359700	0.638715	0.087564
Zn	10	0.359178	0.926475	0.009940
Zn	11	0.359538	0.141016	0.087139
Zn	12	0.356716	0.416659	0.009684
Zn	13	0.860246	0.636804	0.088668
Zn	14	0.859245	0.927848	0.010330
Zn	15	0.859530	0.145729	0.088322
Sn	1	0.817949	0.392275	-0.015978

Table A4-20: ***Fractional coordinates of $(201)_{MT}$ 6.25% Sn-doped ZnO using 400 eV cut-off energy, 7×7×1 k-points and Hubbard U value of $U_{d\text{-}Zn}$ = 10 eV and $U_{p\text{-}O}$ = 7 eV.***

Element	Atom Number	Fractional coordinates of atoms u	v	w
O	1	0.565767	0.385890	0.068069
O	2	0.074976	0.137875	0.212847
O	3	0.348090	0.148242	0.019274
O	4	0.944101	0.073881	0.136096
O	5	0.724201	0.467813	-0.012178
O	6	0.324075	0.265387	0.161182
O	7	0.184838	0.191882	0.095387
O	8	0.703594	0.948133	0.221768
O	9	0.565252	0.883774	0.068031
O	10	0.076391	0.636032	0.222024
O	11	0.348324	0.914573	0.019282
O	12	0.944984	0.580017	0.134847
O	13	0.723976	0.960775	-0.012069
O	14	0.324060	0.763454	0.160594
O	15	0.177026	0.696560	0.096754
O	16	0.704296	0.450301	0.221665
O	17	0.066558	0.381913	0.068470
O	18	0.574705	0.136085	0.221386
O	19	0.848613	0.296068	0.029752
O	20	0.445334	0.077611	0.127510
O	21	0.232874	0.472407	-0.002109
O	22	0.835784	0.264615	0.189926
O	23	0.686921	0.197727	0.095414
O	24	0.204187	0.949107	0.224033
O	25	0.062426	0.886568	0.068384
O	26	0.573721	0.636147	0.212984
O	27	0.860452	0.796833	0.009842
O	28	0.440174	0.574871	0.120441
O	29	0.214261	0.961404	-0.013393
O	30	0.812241	0.755461	0.139838
O	31	0.686938	0.698044	0.093350
O	32	0.208541	0.451705	0.222253
Zn	1	0.651832	0.424207	0.048613
Zn	2	0.165181	0.176911	0.190236
Zn	3	0.032678	0.118578	0.106726
Zn	4	0.539365	0.864860	0.250771
Zn	5	0.393407	0.297578	0.098277
Zn	6	0.946925	0.078918	0.230986
Zn	7	0.261950	0.218482	0.018318
Zn	8	0.782770	0.994310	0.181864
Zn	9	0.651412	0.927789	0.048574
Zn	10	0.164063	0.676592	0.190952
Zn	11	0.031939	0.614174	0.098377
Zn	12	0.539885	0.370875	0.250826
Zn	13	0.393559	0.804035	0.098055

Zn	14	0.951412	0.578462	0.230018
Zn	15	0.260792	0.753128	0.018175
Zn	16	0.783582	0.483528	0.181772
Zn	17	0.154128	0.426987	0.048959
Zn	18	0.663837	0.177414	0.190686
Zn	19	0.532787	0.117407	0.098424
Zn	20	0.040548	0.870867	0.251195
Zn	21	0.892763	0.298519	0.108605
Zn	22	0.448238	0.079524	0.222168
Zn	23	0.763632	0.232345	0.018204
Zn	24	0.280843	0.991187	0.180961
Zn	25	0.148269	0.926729	0.048659
Zn	26	0.664177	0.677109	0.190664
Zn	27	0.531025	0.616110	0.098761
Zn	28	0.039831	0.365512	0.251472
Zn	29	0.896733	0.800014	0.097373
Zn	30	0.441100	0.577820	0.228715
Sn	1	0.769364	0.736458	0.029448
Sn	2	0.303660	0.504083	0.223965

Table A4-21: Fractional coordinates of (201)$_{OT}$ 6.25% Sn-doped ZnO using 400 eV cut-off energy, 7×7×1 k-points and Hubbard U value of $U_{d\text{-}Zn}$ = 10 eV and $U_{p\text{-}O}$ = 7 eV.

Element	Atom Number	Fractional coordinates of atoms u	v	w
O	1	0.538830	0.363398	0.086744
O	2	0.076991	0.142675	0.231396
O	3	0.401167	0.296036	0.026664
O	4	0.934869	0.068761	0.170423
O	5	0.777888	0.476265	0.016249
O	6	0.310905	0.263541	0.165122
O	7	0.167022	0.193649	0.107097
O	8	0.707050	0.950800	0.241968
O	9	0.538977	0.861340	0.086222
O	10	0.077162	0.640979	0.231160
O	11	0.400956	0.798115	0.026465
O	12	0.935072	0.569135	0.170430
O	13	0.778536	1.008232	0.017184
O	14	0.311248	0.756857	0.162955
O	15	0.166626	0.695047	0.095206
O	16	0.707565	0.450620	0.241866
O	17	0.038297	0.362290	0.088573
O	18	0.577531	0.142258	0.230589
O	19	0.903309	0.297245	0.027999
O	20	0.436538	0.070284	0.169342
O	21	0.270348	0.489376	0.026958
O	22	0.810578	0.253438	0.160368
O	23	0.668942	0.196966	0.088496
O	24	0.206151	0.949828	0.242320
O	25	0.037200	0.862915	0.088509
O	26	0.577392	0.642509	0.230805
O	27	0.898889	0.794462	0.028728
O	28	0.436482	0.570127	0.169285
O	29	0.268924	0.991377	0.025757
O	30	0.808209	0.752771	0.157875
O	31	0.668732	0.696746	0.078160
O	32	0.208361	0.452075	0.240626
Zn	1	0.623805	0.421229	0.069515
Zn	2	0.161602	0.177228	0.221171
Zn	3	0.487697	0.358403	0.009277
Zn	4	0.023161	0.109349	0.160729
Zn	5	0.865247	0.522654	-0.002170
Zn	6	0.400823	0.301141	0.140098
Zn	7	0.254479	0.234390	0.079462
Zn	8	0.786025	0.990917	0.210588
Zn	9	0.623792	0.930182	0.069519
Zn	10	0.161503	0.675577	0.224449
Zn	11	0.487460	0.858440	0.009237
Zn	12	0.023324	0.609532	0.160567
Zn	13	0.865549	0.031427	-0.002166

Zn	14	0.401035	0.802446	0.139993
Zn	15	0.254739	0.733176	0.078929
Zn	16	0.786910	0.486047	0.210792
Zn	17	0.126480	0.423582	0.079405
Zn	18	0.660898	0.176168	0.222273
Zn	19	0.990998	0.359516	0.009059
Zn	20	0.522985	0.109452	0.160933
Zn	21	0.353495	0.520726	0.008425
Zn	22	0.902098	0.302388	0.140181
Zn	23	0.756072	0.233482	0.078446
Zn	24	0.285522	0.992902	0.209871
Zn	25	0.125677	0.926953	0.079320
Zn	26	0.660634	0.675467	0.232140
Zn	27	0.988797	0.858776	0.008918
Zn	28	0.523214	0.609397	0.160813
Zn	29	0.352088	0.020330	0.008504
Zn	30	0.903094	0.802851	0.140169
Sn	1	0.760957	0.732787	0.065653
Sn	2	0.304725	0.505770	0.242594

Table A4-22: ***Fractional coordinates of (210) 6.25% Sn-doped ZnO using 400 eV cut-off energy, 7×7×1 k-points and Hubbard U value of $U_{d\text{-}Zn}$ = 10 eV and $U_{p\text{-}O}$ = 7 eV.***

Element	Atom Number	Fractional coordinates of atoms u	v	w
O	1	0.847805	0.676847	-0.011168
O	2	0.833753	0.315349	0.125739
O	3	0.076028	0.290789	0.018620
O	4	0.075277	0.931624	0.135715
O	5	0.331801	0.683353	-0.014043
O	6	0.333751	0.315232	0.119445
O	7	0.589772	0.290997	0.020243
O	8	0.586697	0.929687	0.136156
O	9	0.848413	0.495473	0.060750
O	10	0.830897	0.130033	0.174275
O	11	0.084792	0.106082	0.070818
O	12	0.090632	0.757283	0.198733
O	13	0.328548	0.492261	0.050110
O	14	0.341666	0.139180	0.171230
O	15	0.586444	0.107705	0.071669
O	16	0.579476	0.750123	0.190155
O	17	0.838406	0.175724	-0.001909
O	18	0.834065	0.814275	0.114782
O	19	0.089881	0.794485	0.017222
O	20	0.090868	0.429541	0.137401
O	21	0.331200	0.178466	-0.002179
O	22	0.334162	0.821190	0.115236
O	23	0.582546	0.788909	0.015908
O	24	0.581282	0.429546	0.135270
O	25	0.832066	0.995032	0.050535
O	26	0.846782	0.638504	0.172407
O	27	0.092645	0.613097	0.072074
O	28	0.088542	0.245610	0.189806
O	29	0.334262	0.998999	0.052065
O	30	0.331024	0.638110	0.177042
O	31	0.614569	0.608398	0.070567
O	32	0.571945	0.243224	0.189610
Zn	1	0.671844	0.694620	-0.000718
Zn	2	0.640837	0.322641	0.123785
Zn	3	0.899913	0.272877	0.031064
Zn	4	0.900410	0.920252	0.114131
Zn	5	0.153413	0.691681	-0.000656
Zn	6	0.141891	0.323883	0.114700
Zn	7	0.415157	0.269273	0.030218
Zn	8	0.412471	0.925624	0.114014
Zn	9	0.671556	0.498401	0.074034
Zn	10	0.655118	0.150034	0.166156
Zn	11	0.893635	0.098574	0.072543
Zn	12	0.915003	0.740293	0.187278
Zn	13	0.152169	0.505540	0.073195

Zn	14	0.164184	0.150420	0.157479
Zn	15	0.395590	0.104286	0.072005
Zn	16	0.400437	0.741986	0.187591
Zn	17	0.661545	0.189916	0.008870
Zn	18	0.640975	0.823850	0.114629
Zn	19	0.914240	0.773479	0.021568
Zn	20	0.913562	0.418386	0.124343
Zn	21	0.154280	0.191846	0.008167
Zn	22	0.142063	0.827976	0.116660
Zn	23	0.402118	0.780473	0.020555
Zn	24	0.405823	0.418685	0.113951
Zn	25	0.657981	1.003909	0.072723
Zn	26	0.672021	0.660401	0.166568
Zn	27	0.896676	0.604661	0.071753
Zn	28	0.912113	0.227862	0.187600
Zn	29	0.158758	1.000800	0.072918
Zn	30	0.154489	0.660081	0.166304
Sn	1	0.405072	0.605192	0.068827
Sn	2	0.379561	0.249454	0.222631

12.50%

Table A4-23: Fractional coordinates of $(002)_{MT}$ 12.50% Sn-doped ZnO using 400 eV cut-off energy, 7×7×1 k-points and Hubbard U value of $U_{d\text{-}Zn}$ = 10 eV and $U_{p\text{-}O}$ = 7 eV.

Element	Atom Number	Fractional coordinates of atoms u	v	w
O	1	0.249115	0.538732	-0.003382
O	2	0.916687	0.389440	0.106721
O	3	0.248455	0.543835	0.217769
O	4	0.921649	0.379234	0.341720
O	5	0.244066	0.055633	-0.003238
O	6	0.919099	0.881708	0.107065
O	7	0.248946	0.049325	0.218431
O	8	0.919516	0.888764	0.341669
O	9	0.754352	0.544957	-0.002672
O	10	0.422058	0.385864	0.107212
O	11	0.749864	0.548836	0.223647
O	12	0.412513	0.380553	0.341801
O	13	0.761064	0.049980	-0.003529
O	14	0.419669	0.883861	0.105287
O	15	0.760364	0.054462	0.216644
O	16	0.415293	0.884127	0.395972
Zn	1	0.260658	0.567825	0.362417
Zn	2	0.917720	0.381219	0.016737
Zn	3	0.245772	0.544488	0.131366
Zn	4	0.918542	0.381587	0.251788
Zn	5	0.255941	0.043553	0.362502
Zn	6	0.912889	0.868926	0.016917
Zn	7	0.250888	0.054363	0.132186
Zn	8	0.917265	0.882091	0.251680
Zn	9	0.751594	0.549873	0.360488
Zn	10	0.430505	0.387337	0.016989
Zn	11	0.750461	0.554018	0.137277
Zn	12	0.416098	0.378972	0.251842
Zn	13	0.731720	0.039925	0.362437
Zn	14	0.760401	0.059007	0.129540
Sn	1	0.416666	0.883406	0.015673
Sn	2	0.425376	0.882977	0.260745

Table A4-24: ***Fractional coordinates of (002)$_{OT}$ 12.50% Sn-doped ZnO using 400 eV cut-off energy, 7×7×1 k-points and Hubbard U value of $U_{d\text{-}Zn}$ = 10 eV and $U_{p\text{-}O}$ = 7 eV.***

Element	Atom Number	Fractional coordinates of atoms u	v	w
O	1	0.381001	0.744676	0.395131
O	2	0.903994	0.409127	0.076567
O	3	0.235347	0.566798	0.182505
O	4	0.956954	0.250182	0.268347
O	5	0.388060	-0.031816	0.395027
O	6	0.909486	0.894510	0.076256
O	7	0.240139	0.080785	0.186845
O	8	0.955497	0.825290	0.297118
O	9	0.894914	0.423125	0.364326
O	10	0.412185	0.403110	0.076806
O	11	0.727941	0.580873	0.192366
O	12	0.410673	0.378329	0.306990
O	13	0.636632	-0.195775	0.386777
O	14	0.402355	0.897523	0.071225
O	15	0.730709	0.064238	0.175510
O	16	0.429332	0.861516	0.290589
Zn	1	0.180825	0.508677	0.323291
Zn	2	0.920540	0.394845	-0.009501
Zn	3	0.235073	0.563183	0.099955
Zn	4	0.889035	0.410698	0.213635
Zn	5	0.257087	0.038143	0.326988
Zn	6	0.879996	0.872098	-0.009070
Zn	7	0.240584	0.070313	0.101720
Zn	8	0.904311	0.940644	0.229662
Zn	9	0.723014	0.585234	0.346503
Zn	10	0.440293	0.431726	-0.008786
Zn	11	0.736438	0.571324	0.109462
Zn	12	0.398297	0.413098	0.228034
Zn	13	0.735864	0.098118	0.345414
Zn	14	0.743966	0.070982	0.093707
Sn	1	0.414801	0.893157	-0.017982
Sn	2	0.409864	0.904148	0.212183

Table A4-25: Fractional coordinates of (100) 12.50% Sn-doped ZnO using 400 eV cut-off energy, 7×7×1 k-points and Hubbard U value of $U_{d\text{-}Zn}$ = 10 eV and $U_{p\text{-}O}$ = 7 eV.

Element	Atom Number	Fractional coordinates of atoms u	v	w
O	1	0.424829	0.002433	-0.010809
O	2	0.921818	0.011579	0.228039
O	3	0.922461	0.257658	0.153541
O	4	0.429892	0.234821	0.384906
O	5	0.424829	0.502431	-0.010809
O	6	0.921818	0.511579	0.228039
O	7	0.922461	0.757658	0.153541
O	8	0.429892	0.734821	0.384906
O	9	0.964665	-0.039914	-0.017665
O	10	0.424175	0.010427	0.226192
O	11	0.419803	0.257428	0.153475
O	12	0.912618	0.234208	0.384866
O	13	0.964661	0.460086	-0.017664
O	14	0.424175	0.510428	0.226192
O	15	0.419803	0.757427	0.153475
O	16	0.912618	0.734209	0.384866
O	17	0.171227	0.000770	0.109842
O	18	0.671252	-0.005545	0.346195
O	19	0.180051	0.237445	0.034027
O	20	0.671288	0.255188	0.268474
O	21	0.171227	0.500770	0.109842
O	22	0.671252	0.494455	0.346195
O	23	0.180051	0.737445	0.034027
O	24	0.671288	0.755188	0.268474
O	25	0.674131	0.014695	0.107205
O	26	0.171160	-0.031573	0.395333
O	27	0.649682	0.279083	0.039482
O	28	0.171583	0.269774	0.270269
O	29	0.674130	0.514695	0.107205
O	30	0.171160	0.468427	0.395333
O	31	0.649682	0.779090	0.039482
O	32	0.171583	0.769774	0.270269
Zn	1	0.408325	0.823627	-0.001663
Zn	2	0.919948	0.818436	0.231178
Zn	3	0.922479	0.066991	0.150666
Zn	4	0.421847	0.056940	0.385576
Zn	5	0.408328	0.323625	-0.001663
Zn	6	0.919948	0.318436	0.231178
Zn	7	0.922479	0.566991	0.150666
Zn	8	0.421847	0.556939	0.385575
Zn	9	0.919666	0.787386	-0.002151
Zn	10	0.423171	0.818201	0.230922
Zn	11	0.421393	0.067881	0.149662
Zn	12	0.921062	0.056466	0.385517
Zn	13	0.919666	0.287386	-0.002151

Zn	14	0.423171	0.318201	0.230922
Zn	15	0.421393	0.567880	0.149662
Zn	16	0.921062	0.556467	0.385517
Zn	17	0.171669	0.810092	0.111269
Zn	18	0.671475	0.803771	0.350970
Zn	19	0.173308	0.047192	0.030438
Zn	20	0.670895	0.066498	0.269610
Zn	21	0.171669	0.310092	0.111269
Zn	22	0.671475	0.303771	0.350970
Zn	23	0.173308	0.547191	0.030438
Zn	24	0.670896	0.566498	0.269610
Zn	25	0.671472	0.822318	0.116100
Zn	26	0.171176	0.802218	0.361192
Zn	27	0.671472	0.322317	0.116100
Zn	28	0.171176	0.302218	0.361192
Sn	1	0.709623	0.066159	0.016509
Sn	2	0.178136	0.064383	0.282700
Sn	3	0.709622	0.566160	0.016509
Sn	4	0.178135	0.564383	0.282700

Table A4-26: Fractional coordinates of $(101)_{MT}$ 12.50% Sn-doped ZnO using 400 eV cut-off energy, 7×7×1 k-points and Hubbard U value of $U_{d\text{-}Zn}$ = 10 eV and $U_{p\text{-}O}$ = 7 eV.

Element	Atom Number	Fractional coordinates of atoms u	v	w
O	1	0.613512	0.216840	0.029675
O	2	0.821116	0.825723	0.240970
O	3	0.346493	0.100528	0.012048
O	4	0.561745	0.713024	0.223136
O	5	0.236745	0.042440	0.134023
O	6	0.444694	0.654924	0.343457
O	7	0.949637	0.897854	0.120602
O	8	0.171965	0.509575	0.326506
O	9	0.615921	0.755073	0.028807
O	10	0.817372	0.336670	0.241092
O	11	0.346368	0.597288	0.012567
O	12	0.560058	0.203218	0.223245
O	13	0.234658	0.546785	0.138413
O	14	0.444930	0.130228	0.343115
O	15	0.950897	0.395846	0.122271
O	16	0.171161	-0.005947	0.326581
O	17	0.726304	0.033971	0.134017
O	18	0.941240	0.632894	0.333978
O	19	0.453692	0.900312	0.119926
O	20	0.661161	0.497602	0.326685
O	21	0.115990	0.238157	0.040266
O	22	0.329249	0.833822	0.241518
O	23	0.852540	0.106049	0.010586
O	24	0.060540	0.711342	0.217867
O	25	0.722719	0.532356	0.133288
O	26	0.941143	0.136382	0.367679
O	27	0.460643	0.407739	0.117082
O	28	0.680849	0.008159	0.326086
O	29	0.115402	0.735937	0.039732
O	30	0.334480	0.334717	0.241779
O	31	0.817948	0.585602	0.015862
O	32	-0.003687	0.176397	0.250672
Zn	1	0.765838	0.296002	-0.002067
Zn	2	0.973629	0.922316	0.199259
Zn	3	0.706203	0.772791	0.182598
Zn	4	0.952320	0.447436	0.401221
Zn	5	0.375848	0.111560	0.089383
Zn	6	0.592590	0.713517	0.302672
Zn	7	0.099460	0.979405	0.080643
Zn	8	0.315667	0.579974	0.291508
Zn	9	0.769862	0.827233	-0.002048
Zn	10	0.970237	0.420925	0.201110
Zn	11	0.703439	0.266839	0.182475
Zn	12	0.952732	0.841099	0.394886
Zn	13	0.371092	0.613402	0.090033

Zn	14	0.593354	0.209758	0.302827
Zn	15	0.100830	0.481011	0.081578
Zn	16	0.315464	0.076046	0.291617
Zn	17	0.875344	0.112090	0.090034
Zn	18	0.093672	0.710939	0.299584
Zn	19	0.598355	0.975719	0.081473
Zn	20	0.804302	0.576286	0.292178
Zn	21	0.260304	0.305007	0.006404
Zn	22	0.471787	0.917775	0.199070
Zn	23	0.212422	0.790532	0.183528
Zn	24	0.446592	0.392746	0.393212
Zn	25	0.881149	0.612897	0.089951
Zn	26	0.098636	0.215390	0.318218
Zn	27	0.262652	0.806518	0.006411
Zn	28	0.480281	0.422012	0.205807
Sn	1	0.604918	0.482584	0.070014
Sn	2	0.840224	0.092005	0.293908
Sn	3	0.192357	0.265785	0.187152
Sn	4	0.429231	0.887586	0.404546

Table A4-27: Fractional coordinates of (101)$_{OT}$ 12.50% Sn-doped ZnO using 400 eV cut-off energy, 7×7×1 k-points and Hubbard U value of $U_{d\text{-}Zn}$ = 10 eV and $U_{p\text{-}O}$ = 7 eV.

Element	Atom Number	Fractional coordinates of atoms u	v	w
O	1	0.616813	0.222673	-0.011732
O	2	0.822382	0.825507	0.198804
O	3	0.560481	0.698593	0.176092
O	4	0.763665	0.322625	0.384400
O	5	0.228778	0.019098	0.095888
O	6	0.437338	0.647110	0.301003
O	7	0.961313	0.924993	0.088798
O	8	0.174641	0.515905	0.291198
O	9	0.602344	0.736107	-0.011015
O	10	0.820688	0.333988	0.199761
O	11	0.560824	0.198707	0.176321
O	12	0.766314	0.798447	0.384492
O	13	0.233605	0.570554	0.092220
O	14	0.437036	0.131481	0.302788
O	15	0.961181	0.387028	0.088887
O	16	0.175772	-0.000344	0.292028
O	17	0.722629	0.030905	0.092032
O	18	0.941790	0.654626	0.307979
O	19	0.459535	0.911998	0.075931
O	20	0.667830	0.504445	0.276481
O	21	0.164102	0.258484	0.007312
O	22	0.332175	0.833729	0.200170
O	23	0.061873	0.707618	0.188304
O	24	0.307172	0.326395	0.385554
O	25	0.739352	0.542294	0.089970
O	26	1.006538	0.193799	0.352969
O	27	0.465229	0.407020	0.074143
O	28	0.657928	-0.000418	0.283855
O	29	0.034669	0.694465	0.007495
O	30	0.323760	0.330279	0.199140
O	31	0.007873	0.179098	0.215185
O	32	0.290778	0.807566	0.385867
Zn	1	0.978845	0.922492	0.166338
Zn	2	0.224278	0.518518	0.367804
Zn	3	0.708289	0.770326	0.140825
Zn	4	0.908382	0.388596	0.352007
Zn	5	0.373518	0.115606	0.064567
Zn	6	0.582798	0.708514	0.263925
Zn	7	0.103064	0.979014	0.030406
Zn	8	0.315164	0.578263	0.249284
Zn	9	0.976259	0.416968	0.166655
Zn	10	0.239137	0.045393	0.367765
Zn	11	0.708220	0.269622	0.140841
Zn	12	0.910614	0.897228	0.351939
Zn	13	0.380467	0.617321	0.064398

Zn	14	0.581623	0.213110	0.264532
Zn	15	0.104231	0.479422	0.030127
Zn	16	0.316203	0.076261	0.249365
Zn	17	0.874561	0.113141	0.065253
Zn	18	0.087086	0.712129	0.267866
Zn	19	0.604785	0.978866	0.031833
Zn	20	0.818951	0.582227	0.250113
Zn	21	0.474823	0.904346	0.157500
Zn	22	0.664227	0.513314	0.368573
Zn	23	0.207119	0.772938	0.148250
Zn	24	0.461876	0.408701	0.352819
Zn	25	0.909837	0.630117	0.063402
Zn	26	0.090423	0.212514	0.284079
Zn	27	0.474391	0.403674	0.165081
Zn	28	0.705022	0.029701	0.368687
Sn	1	0.617624	0.483024	0.027350
Sn	2	0.835909	0.083821	0.256210
Sn	3	0.180621	0.273968	0.138576
Sn	4	0.463501	0.892774	0.365015

Table A4-28: ***Fractional coordinates of $(102)_{MT}$ 12.50% Sn-doped ZnO using 400 eV cut-off energy, 7×7×1 k-points and Hubbard U value of $U_{d\text{-}Zn}$ = 10 eV and $U_{p\text{-}O}$ = 7 eV.***

Element	Atom Number	Fractional coordinates of atoms u	v	w
O	1	0.520291	0.411989	-0.003953
O	2	0.784078	0.923138	0.175654
O	3	0.302436	0.427888	0.025775
O	4	0.573180	0.924746	0.202907
O	5	0.014474	0.911377	-0.004246
O	6	0.282617	0.422906	0.174983
O	7	0.072800	0.422113	0.202935
O	8	0.801123	0.923331	0.025707
O	9	0.521098	0.945079	-0.010552
O	10	0.783679	0.424721	0.175197
O	11	0.302758	0.919513	0.025590
O	12	0.573054	0.420940	0.202888
O	13	0.014526	0.440691	-0.003940
O	14	0.282279	0.925178	0.174718
O	15	0.072806	0.923426	0.202953
O	16	0.801093	0.424345	0.025737
O	17	0.649827	0.172351	0.088582
O	18	0.918073	0.672562	0.269168
O	19	0.440995	0.172098	0.114034
O	20	0.701050	0.672994	0.288356
O	21	0.145974	0.672956	0.088398
O	22	0.414704	0.172589	0.268675
O	23	0.200017	0.173013	0.288579
O	24	0.938133	0.673123	0.116604
O	25	0.641724	0.674449	0.083803
O	26	0.917796	0.172679	0.269573
O	27	0.441964	0.674494	0.112458
O	28	0.696359	0.173207	0.297404
O	29	0.145138	0.172973	0.083523
O	30	0.418838	0.672716	0.269083
O	31	0.199196	0.673189	0.297547
O	32	0.941393	0.173017	0.113475
Zn	1	0.128377	0.418252	0.290568
Zn	2	0.867628	0.919734	0.100744
Zn	3	0.661646	0.922360	0.139232
Zn	4	0.973639	0.425428	0.316708
Zn	5	0.369901	0.419828	0.100698
Zn	6	0.626890	0.916554	0.290586
Zn	7	0.161351	0.422558	0.139103
Zn	8	0.472470	0.925887	0.316633
Zn	9	0.128335	0.927503	0.290567
Zn	10	0.867856	0.425590	0.100723
Zn	11	0.660749	0.422740	0.138968
Zn	12	0.973377	0.919352	0.316699
Zn	13	0.368902	0.925631	0.100886

Zn	14	0.626796	0.429395	0.290603
Zn	15	0.161264	0.922475	0.139071
Zn	16	0.472435	0.418926	0.316644
Zn	17	-0.000077	0.672515	0.195043
Zn	18	0.742910	0.173801	0.026034
Zn	19	0.533287	0.172014	0.044923
Zn	20	0.800263	0.673567	0.234994
Zn	21	0.238521	0.673624	0.026182
Zn	22	0.497634	0.172450	0.195183
Zn	23	0.028069	0.676252	0.045614
Zn	24	0.297101	0.174031	0.234402
Zn	25	0.000743	0.172508	0.195002
Zn	26	0.742158	0.673691	0.025700
Zn	27	0.246577	0.173644	0.025718
Zn	28	0.504405	0.672664	0.194398
Sn	1	0.523372	0.683379	0.033411
Sn	2	0.793593	0.175449	0.235350
Sn	3	0.024981	0.175674	0.036408
Sn	4	0.294954	0.675288	0.234548

Table A4-29: ***Fractional coordinates of (102)$_{OT}$ 12.50% Sn-doped ZnO using 400 eV cut-off energy, 7×7×1 k-points and Hubbard U value of $U_{d\text{-}Zn}$ = 10 eV and $U_{p\text{-}O}$ = 7 eV.***

Element	Atom Number	Fractional coordinates of atoms u	v	w
O	1	0.044290	0.422733	0.335843
O	2	0.783572	0.920139	0.146059
O	3	0.306482	0.426814	-0.001498
O	4	0.574465	0.922076	0.182725
O	5	0.281351	0.420742	0.145804
O	6	0.544080	0.922784	0.335679
O	7	0.076252	0.425383	0.183122
O	8	0.807728	0.922662	-0.001056
O	9	0.044230	0.923471	0.335871
O	10	0.783660	0.427520	0.145929
O	11	0.306725	0.919101	-0.001424
O	12	0.574585	0.423780	0.182813
O	13	0.281120	0.927274	0.145380
O	14	0.544000	0.423406	0.335673
O	15	0.076131	0.920499	0.183353
O	16	0.806882	0.423496	-0.000865
O	17	0.650010	0.174367	0.064098
O	18	0.910874	0.672742	0.238470
O	19	0.443931	0.174604	0.090361
O	20	0.707061	0.672901	0.267990
O	21	0.145983	0.674313	0.063291
O	22	0.412881	0.172701	0.237810
O	23	0.208095	0.172902	0.267225
O	24	0.945330	0.674409	0.090713
O	25	0.642758	0.673929	0.060664
O	26	0.914682	0.172831	0.236690
O	27	0.442818	0.673826	0.088855
O	28	0.707574	0.173013	0.269912
O	29	0.145907	0.173998	0.060054
O	30	0.412703	0.672875	0.236466
O	31	0.207657	0.673047	0.270396
O	32	0.946194	0.173954	0.089280
Zn	1	0.139292	0.417573	0.284713
Zn	2	0.874414	0.921258	0.074305
Zn	3	0.655416	0.921711	0.116280
Zn	4	0.953697	0.425936	0.284670
Zn	5	0.373097	0.420723	0.073854
Zn	6	0.638967	0.918052	0.284717
Zn	7	0.155201	0.421880	0.115702
Zn	8	0.453568	0.925371	0.284398
Zn	9	0.139271	0.927720	0.284735
Zn	10	0.873990	0.424924	0.074618
Zn	11	0.655372	0.423710	0.116211
Zn	12	0.953691	0.918842	0.284694
Zn	13	0.372910	0.925703	0.074314

Zn	14	0.638903	0.427179	0.284692
Zn	15	0.154123	0.923509	0.115515
Zn	16	0.453488	0.419355	0.284421
Zn	17	0.002702	0.672541	0.172529
Zn	18	0.745459	0.172519	0.006401
Zn	19	0.533536	0.166349	0.021224
Zn	20	0.790439	0.673345	0.207146
Zn	21	0.241106	0.672853	0.006378
Zn	22	0.505442	0.172701	0.171884
Zn	23	0.029706	0.666374	0.020163
Zn	24	0.293501	0.173178	0.206963
Zn	25	0.010237	0.172687	0.170179
Zn	26	0.744965	0.673259	0.006768
Zn	27	0.248537	0.172641	0.006404
Zn	28	0.506302	0.672524	0.168571
Sn	1	0.522169	0.695483	0.004265
Sn	2	0.791331	0.174272	0.201988
Sn	3	0.025334	0.195125	0.004461
Sn	4	0.289506	0.674969	0.201557

Table A4-30: ***Fractional coordinates of $(103)_{MT}$ 12.50% Sn-doped ZnO using 400 eV cut-off energy, 7×7×1 k-points and Hubbard U value of $U_{d\text{-}Zn}$ = 10 eV and $U_{p\text{-}O}$ = 7 eV.***

Element	Atom Number	Fractional coordinates of atoms u	v	w
O	1	0.037757	0.454323	0.233577
O	2	0.809177	0.800575	0.079300
O	3	0.405786	0.140484	-0.004655
O	4	0.623206	0.737872	0.184720
O	5	0.168660	0.488530	0.007680
O	6	0.410452	0.144941	0.158693
O	7	0.011025	0.433670	0.091608
O	8	0.260678	0.055334	0.214213
O	9	0.036491	0.948922	0.231913
O	10	0.799233	0.348395	0.077909
O	11	0.406532	0.630150	-0.002336
O	12	0.649857	0.276921	0.137166
O	13	0.169096	0.007969	0.007980
O	14	0.416579	0.630030	0.164393
O	15	0.011631	0.947041	0.090691
O	16	0.265815	0.529469	0.214685
O	17	0.697508	-0.010098	0.064702
O	18	0.915358	0.641171	0.158079
O	19	0.517822	0.944766	0.098654
O	20	0.764496	0.531191	0.223049
O	21	0.294255	0.324858	0.081285
O	22	0.514548	0.950221	0.264041
O	23	0.146458	0.235986	0.141510
O	24	0.911557	0.630940	-0.011372
O	25	0.700438	0.496593	-0.018078
O	26	0.899586	0.139590	0.158553
O	27	0.527019	0.449442	0.072689
O	28	0.751993	0.042568	0.212236
O	29	0.296798	0.821531	0.076705
O	30	0.526880	0.415444	0.240009
O	31	0.150808	0.735292	0.142324
O	32	0.902532	0.137698	-0.010409
Zn	1	0.092913	0.455583	0.139410
Zn	2	0.865650	0.856312	-0.000328
Zn	3	0.705053	0.736960	0.026176
Zn	4	0.953177	0.406877	0.184640
Zn	5	0.475370	0.176291	0.063874
Zn	6	0.714198	0.746796	0.214975
Zn	7	0.315237	0.080025	0.134222
Zn	8	0.551959	0.709392	0.251936
Zn	9	0.094587	0.958690	0.139409
Zn	10	0.856863	0.368902	-0.000178
Zn	11	0.693003	0.297603	0.047569
Zn	12	0.953311	0.922073	0.177656
Zn	13	0.475947	0.671757	0.064936

Zn	14	0.697866	0.272435	0.232556
Zn	15	0.322662	0.577904	0.136677
Zn	16	0.584259	0.198644	0.270639
Zn	17	0.204593	0.268558	0.224014
Zn	18	0.973040	0.670685	0.061793
Zn	19	0.090574	0.228960	0.269909
Zn	20	0.819779	0.576165	0.147465
Zn	21	0.356635	0.360717	0.008811
Zn	22	0.614077	0.979047	0.127715
Zn	23	0.196239	0.262518	0.054726
Zn	24	0.458278	0.919775	0.186194
Zn	25	0.233395	0.774643	0.214518
Zn	26	0.973787	0.173991	0.053183
Zn	27	0.365848	0.864990	0.000078
Zn	28	0.580628	0.453556	0.148191
Sn	1	0.070013	0.721711	0.291937
Sn	2	0.797593	0.072112	0.125110
Sn	3	0.195518	0.761003	0.048414
Sn	4	0.416066	0.375133	0.235964

Table A4-31: Fractional coordinates of (103)$_{OT}$ 12.50% Sn-doped ZnO using 400 eV cut-off energy, 7×7×1 k-points and Hubbard U value of $U_{d\text{-}Zn}$ = 10 eV and $U_{p\text{-}O}$ = 7 eV.

Element	Atom Number	Fractional coordinates of atoms u	v	w
O	1	0.038902	0.457525	0.253801
O	2	0.797460	0.814678	0.089929
O	3	0.407387	0.143911	0.008132
O	4	0.647585	0.739343	0.160604
O	5	0.173098	0.500226	0.016781
O	6	0.417509	0.135762	0.171496
O	7	0.029185	0.452345	0.086518
O	8	0.264103	0.045207	0.232169
O	9	0.038812	0.956049	0.253423
O	10	0.795464	0.333463	0.090029
O	11	0.406908	0.628761	0.007912
O	12	0.647408	0.234210	0.160600
O	13	0.170178	0.013749	0.016135
O	14	0.413779	0.639336	0.171300
O	15	0.027413	0.945184	0.085541
O	16	0.261794	0.545012	0.232774
O	17	0.679441	0.010311	0.018241
O	18	0.913712	0.633326	0.172974
O	19	0.529405	0.947897	0.082733
O	20	0.766609	0.546079	0.240238
O	21	0.293485	0.321330	0.094355
O	22	0.536860	0.954489	0.259543
O	23	0.146150	0.235716	0.158955
O	24	0.908199	0.631238	0.007291
O	25	0.674084	0.508162	0.018885
O	26	0.917124	0.135383	0.171469
O	27	0.530417	0.452454	0.079711
O	28	0.764656	0.045373	0.241173
O	29	0.297375	0.825617	0.089290
O	30	0.533856	0.455326	0.243543
O	31	0.146985	0.737285	0.157175
O	32	0.903915	0.138639	0.008307
Zn	1	0.086735	0.452040	0.174249
Zn	2	0.864506	0.860461	0.008901
Zn	3	0.693784	0.765764	0.069910
Zn	4	0.954368	0.393088	0.221418
Zn	5	0.473912	0.173856	0.088513
Zn	6	0.713951	0.763895	0.231396
Zn	7	0.074435	0.451803	-0.003473
Zn	8	0.322056	0.081117	0.151420
Zn	9	0.086141	0.957302	0.173008
Zn	10	0.856854	0.364708	0.008936
Zn	11	0.693180	0.265849	0.069646
Zn	12	0.954431	0.886921	0.221490
Zn	13	0.470735	0.671961	0.088652

Zn	14	0.713782	0.275165	0.231488
Zn	15	0.071390	0.954659	-0.004979
Zn	16	0.317480	0.577221	0.151485
Zn	17	0.214551	0.269051	0.230747
Zn	18	0.969393	0.670174	0.088028
Zn	19	0.584731	0.953674	-0.000334
Zn	20	0.816428	0.580185	0.152993
Zn	21	0.356793	0.360974	0.018632
Zn	22	0.586537	0.954853	0.179268
Zn	23	0.195696	0.265399	0.071188
Zn	24	0.454258	0.892069	0.221014
Zn	25	0.215925	0.772799	0.231901
Zn	26	0.974548	0.174260	0.079407
Zn	27	0.368400	0.867403	0.009015
Zn	28	0.587049	0.454738	0.168912
Sn	1	0.575714	0.481485	-0.020180
Sn	2	0.815766	0.082557	0.149236
Sn	3	0.196608	0.771377	0.066243
Sn	4	0.434028	0.389070	0.253421

Table A4-32: Fractional coordinates of (110) 12.50% Sn-doped ZnO using 400 eV cut-off energy, 7×7×1 k-points and Hubbard U value of $U_{d\text{-}Zn}$ = 10 eV and $U_{p\text{-}O}$ = 7 eV.

Element	Atom Number	Fractional coordinates of atoms u	v	w
O	1	0.863825	0.806256	-0.030658
O	2	0.876034	0.286789	0.165959
O	3	0.125043	0.213157	0.081563
O	4	0.129679	0.710520	0.251863
O	5	0.363825	0.806262	-0.030659
O	6	0.376028	0.286787	0.165951
O	7	0.625048	0.213157	0.081567
O	8	0.629678	0.710519	0.251863
O	9	0.870913	0.517149	0.079554
O	10	0.874722	0.043775	0.242701
O	11	0.125605	0.459964	-0.002477
O	12	0.127461	0.958053	0.163118
O	13	0.370913	0.517155	0.079554
O	14	0.374724	0.043778	0.242701
O	15	0.625604	0.459968	-0.002478
O	16	0.627461	0.958054	0.163118
O	17	0.870931	0.036665	0.078800
O	18	0.877931	0.536770	0.251528
O	19	0.114538	0.973035	-0.002749
O	20	0.125716	0.462323	0.165135
O	21	0.370931	0.036660	0.078798
O	22	0.377938	0.536767	0.251527
O	23	0.614558	0.973033	-0.002750
O	24	0.625717	0.462318	0.165134
O	25	0.875133	0.273288	-0.004812
O	26	0.883917	0.791811	0.171220
O	27	0.210358	0.717066	0.078338
O	28	0.115956	0.205895	0.244248
O	29	0.375145	0.273288	-0.004810
O	30	0.383915	0.791809	0.171219
O	31	0.710360	0.717063	0.078339
O	32	0.615971	0.205900	0.244251
Zn	1	0.689330	0.821067	-0.003208
Zn	2	0.684455	0.293174	0.168049
Zn	3	0.934605	0.202587	0.080105
Zn	4	0.951895	0.690819	0.241428
Zn	5	0.189332	0.821081	-0.003208
Zn	6	0.184433	0.293174	0.168048
Zn	7	0.434607	0.202582	0.080106
Zn	8	0.451894	0.690819	0.241428
Zn	9	0.678501	0.542865	0.079268
Zn	10	0.693872	0.054013	0.239390
Zn	11	0.951929	0.424094	0.008094
Zn	12	0.936927	0.959611	0.161678
Zn	13	0.178500	0.542866	0.079268

Zn	14	0.193871	0.054011	0.239389
Zn	15	0.451930	0.424099	0.008094
Zn	16	0.436925	0.959610	0.161678
Zn	17	0.680657	0.044864	0.079494
Zn	18	0.700040	0.556453	0.240641
Zn	19	0.936002	0.953792	-0.001594
Zn	20	0.934193	0.454948	0.169185
Zn	21	0.180654	0.044864	0.079494
Zn	22	0.200048	0.556456	0.240641
Zn	23	0.436021	0.953790	-0.001594
Zn	24	0.434191	0.454940	0.169184
Zn	25	0.701452	0.306887	0.008469
Zn	26	0.691609	0.793798	0.172005
Zn	27	0.201464	0.306886	0.008469
Zn	28	0.191606	0.793798	0.172003
Sn	1	0.921788	0.708605	0.066073
Sn	2	0.919794	0.223710	0.270588
Sn	3	0.421786	0.708607	0.066071
Sn	4	0.419802	0.223714	0.270585

Table A4-33: Fractional coordinates of $(112)_{MT}$ 12.50% Sn-doped ZnO using 400 eV cut-off energy, 7×7×1 k-points and Hubbard U value of $U_{d\text{-}Zn}$ = 10 eV and $U_{p\text{-}O}$ = 7 eV.

Element	Atom Number	Fractional coordinates of atoms u	v	w
O	1	0.271814	0.006793	0.072838
O	2	0.759747	0.143547	0.221177
O	3	0.197656	0.757752	0.068578
O	4	0.701614	0.891850	0.220504
O	5	0.771803	0.506798	0.072844
O	6	0.259715	0.643569	0.221178
O	7	0.697656	0.257752	0.068585
O	8	0.201619	0.391868	0.220503
O	9	0.028222	0.055161	0.152697
O	10	0.514563	0.891693	0.018436
O	11	0.452019	0.631560	0.009629
O	12	0.948617	0.836349	0.137104
O	13	0.014549	0.391691	0.018435
O	14	0.528222	0.555113	0.152783
O	15	0.952006	0.131571	0.009625
O	16	0.448606	0.336350	0.137100
O	17	0.507678	0.026366	0.170869
O	18	0.021775	0.888924	-0.002058
O	19	0.956956	0.632474	0.009613
O	20	0.441800	0.776945	0.162158
O	21	0.521783	0.388922	-0.002057
O	22	0.007681	0.526381	0.170860
O	23	0.456964	0.132471	0.009614
O	24	0.941810	0.276958	0.162174
O	25	0.759651	0.006269	0.071150
O	26	0.285443	0.157356	0.218157
O	27	0.696924	0.756415	0.063024
O	28	0.195389	0.893692	0.220990
O	29	0.259657	0.506270	0.071149
O	30	0.785472	0.657355	0.218160
O	31	0.196924	0.256417	0.063021
O	32	0.695398	0.393670	0.220992
Zn	1	0.294100	0.152144	0.019759
Zn	2	0.761763	0.275715	0.165806
Zn	3	0.693009	0.028007	0.167291
Zn	4	0.180495	0.902380	0.019881
Zn	5	0.794092	0.652142	0.019759
Zn	6	0.261756	0.775727	0.165804
Zn	7	0.680504	0.402377	0.019882
Zn	8	0.193015	0.528017	0.167288
Zn	9	0.010605	0.250035	0.063263
Zn	10	0.540280	0.322009	0.229921
Zn	11	0.460537	0.146851	0.230875
Zn	12	0.946711	0.988298	0.062601
Zn	13	0.510606	0.750036	0.063261

Zn	14	0.040287	0.822011	0.229922
Zn	15	0.446724	0.488293	0.062606
Zn	16	0.960561	0.646858	0.230875
Zn	17	0.512947	0.256344	0.059836
Zn	18	0.038984	0.375135	0.209888
Zn	19	0.922092	0.128865	0.209396
Zn	20	0.461492	1.008403	0.073626
Zn	21	0.012944	0.756346	0.059833
Zn	22	0.538987	0.875093	0.209885
Zn	23	0.961483	0.508406	0.073622
Zn	24	0.422054	0.628859	0.209401
Zn	25	0.789266	0.151153	0.020710
Zn	26	0.286968	0.299698	0.158077
Zn	27	0.289274	0.651150	0.020709
Zn	28	0.786978	0.799693	0.158077
Sn	1	0.202314	0.036283	0.170696
Sn	2	0.693893	0.898133	-0.009624
Sn	3	0.193882	0.398135	-0.009625
Sn	4	0.702335	0.536276	0.170713

Table A4-34: Fractional coordinates of (112)$_{OT}$ 12.50% Sn-doped ZnO using 400 eV cut-off energy, 7×7×1 k-points and Hubbard U value of $U_{d\text{-}Zn}$ = 10 eV and $U_{p\text{-}O}$ = 7 eV.

Element	Atom Number	Fractional coordinates of atoms u	v	w
O	1	0.307785	0.019828	0.130601
O	2	0.819428	0.101706	0.241369
O	3	0.164292	0.773247	0.089220
O	4	0.655026	0.863966	0.231605
O	5	0.807813	0.519841	0.130595
O	6	0.319487	0.601696	0.241372
O	7	0.664294	0.273253	0.089220
O	8	0.155057	0.363945	0.231607
O	9	0.075259	0.087153	0.182878
O	10	0.563484	0.949383	0.052126
O	11	0.425114	0.702258	0.007759
O	12	0.932412	0.845900	0.172753
O	13	0.063507	0.449328	0.052096
O	14	0.575282	0.587151	0.182836
O	15	0.925111	0.202239	0.007758
O	16	0.432409	0.345906	0.172751
O	17	0.551659	0.084746	0.182292
O	18	0.088197	0.947978	0.016897
O	19	0.926439	0.687427	0.018102
O	20	0.414832	0.804284	0.159651
O	21	0.588201	0.447993	0.016899
O	22	0.051739	0.584726	0.182289
O	23	0.426432	0.187443	0.018104
O	24	0.914843	0.304292	0.159652
O	25	0.844196	0.035021	0.090099
O	26	0.305914	0.148828	0.271728
O	27	0.697190	0.769664	0.100200
O	28	0.211862	0.873726	0.261232
O	29	0.344199	0.535023	0.090097
O	30	0.805877	0.648858	0.271728
O	31	0.197184	0.269641	0.100200
O	32	0.711876	0.373753	0.261232
Zn	1	0.309659	0.161993	0.088249
Zn	2	0.808244	0.255587	0.231892
Zn	3	0.679343	0.017019	0.231887
Zn	4	0.231717	0.919038	0.069075
Zn	5	0.809648	0.662004	0.088233
Zn	6	0.308247	0.755572	0.231893
Zn	7	0.731725	0.419045	0.069074
Zn	8	0.179424	0.516984	0.231886
Zn	9	0.454825	0.041044	-0.001647
Zn	10	0.076156	0.249750	0.171786
Zn	11	0.438576	0.851144	-0.001304
Zn	12	0.923051	1.008557	0.181128
Zn	13	-0.045169	0.541025	-0.001646

Zn	14	0.576152	0.749757	0.171785
Zn	15	0.938591	0.351124	-0.001304
Zn	16	0.423074	0.508555	0.181124
Zn	17	-0.011427	0.065791	0.019642
Zn	18	0.546420	0.233459	0.161806
Zn	19	1.026306	0.807194	0.019819
Zn	20	0.478100	0.954394	0.150140
Zn	21	0.488579	0.565811	0.019643
Zn	22	0.046413	0.733443	0.161808
Zn	23	0.526291	0.307219	0.019820
Zn	24	0.978120	0.454399	0.150142
Zn	25	0.807691	0.189996	0.080777
Zn	26	0.303481	0.285172	0.223328
Zn	27	0.307693	0.689996	0.080778
Zn	28	0.803454	0.785205	0.223323
Sn	1	0.224282	0.025981	0.227503
Sn	2	0.744110	0.904290	0.038845
Sn	3	0.244145	0.404257	0.038848
Sn	4	0.724288	0.525999	0.227489

Table A4-35: Fractional coordinates of (200) 12.50% Sn-doped ZnO using 400 eV cut-off energy, 7×7×1 k-points and Hubbard U value of $U_{d\text{-}Zn}$ = 10 eV and $U_{p\text{-}O}$ = 7 eV.

Element	Atom Number	Fractional coordinates of atoms u	v	w
O	1	0.388344	0.851309	0.244619
O	2	0.389711	0.091106	0.148070
O	3	0.388344	0.351308	0.244619
O	4	0.389711	0.591106	0.148070
O	5	0.888112	0.851130	0.245188
O	6	0.888901	0.090996	0.148042
O	7	0.888112	0.351131	0.245189
O	8	0.888901	0.590996	0.148042
O	9	0.638421	0.838036	0.092730
O	10	0.640141	0.095268	-0.005089
O	11	0.638421	0.338035	0.092731
O	12	0.640141	0.595265	-0.005089
O	13	0.137990	0.848477	0.090671
O	14	0.141366	0.099728	-0.000846
O	15	0.137990	0.348477	0.090671
O	16	0.141366	0.599728	-0.000846
Zn	1	0.390063	0.683799	0.230108
Zn	2	0.388723	0.901546	0.151673
Zn	3	0.390063	0.183798	0.230108
Zn	4	0.388723	0.401546	0.151673
Zn	5	0.889750	0.683765	0.230127
Zn	6	0.890680	0.901381	0.152166
Zn	7	0.889749	0.183766	0.230127
Zn	8	0.890680	0.401381	0.152166
Zn	9	0.639826	0.649396	0.087932
Zn	10	0.636376	0.927417	0.009930
Zn	11	0.639826	0.149396	0.087932
Zn	12	0.636376	0.427414	0.009930
Zn	13	0.140339	0.654603	0.089856
Zn	14	0.140339	0.154604	0.089856
Sn	1	0.094921	0.912525	-0.014988
Sn	2	0.094921	0.412525	-0.014988

Table A4-36: Fractional coordinates of $(201)_{MT}$ 12.50% Sn-doped ZnO using 400 eV cut-off energy, 7×7×1 k-points and Hubbard U value of $U_{d\text{-}Zn}$ = 10 eV and $U_{p\text{-}O}$ = 7 eV.

Element	Atom Number	Fractional coordinates of atoms u	v	w
O	1	0.540621	0.646696	0.059255
O	2	0.062614	0.392487	0.205972
O	3	0.387419	0.580470	0.036403
O	4	0.917491	0.324694	0.181601
O	5	0.730995	0.729890	0.016837
O	6	0.306381	0.515789	0.151842
O	7	0.142183	0.419938	0.099322
O	8	0.698990	0.231175	0.241669
O	9	0.541255	0.133949	0.059581
O	10	0.052373	0.886472	0.205978
O	11	0.386601	0.074371	0.026653
O	12	0.896069	0.803612	0.196307
O	13	0.728654	0.246177	0.008891
O	14	0.307364	0.014707	0.149830
O	15	0.138910	0.940045	0.098999
O	16	0.706762	0.721568	0.231502
O	17	0.048648	0.605979	0.048464
O	18	0.564154	0.392393	0.210944
O	19	0.902334	0.664412	0.030531
O	20	0.444029	0.323093	0.159307
O	21	0.247689	0.735304	0.019105
O	22	0.803702	0.509518	0.143131
O	23	0.655126	0.453133	0.104948
O	24	0.194805	0.217762	0.231487
O	25	-0.008900	0.077774	0.079675
O	26	0.573568	0.893819	0.216954
O	27	0.860559	0.081646	0.039318
O	28	0.440654	0.830213	0.160368
O	29	0.255679	0.242072	0.018714
O	30	0.797262	0.027569	0.151085
O	31	0.664854	0.961330	0.101475
O	32	0.197063	0.732190	0.221805
Zn	1	0.642862	0.698874	0.057879
Zn	2	0.152482	0.453995	0.209728
Zn	3	0.464526	0.607075	-0.001655
Zn	4	0.050700	0.354360	0.109085
Zn	5	0.395970	0.544354	0.130932
Zn	6	0.984709	0.330526	0.240311
Zn	7	0.297493	0.516809	0.038032
Zn	8	0.774473	0.267674	0.200611
Zn	9	0.641594	0.199663	0.057363
Zn	10	0.144042	0.953802	0.209746
Zn	11	0.467617	0.110844	-0.002000
Zn	12	0.048397	0.860884	0.108751
Zn	13	0.396350	0.055546	0.120481

Zn	14	0.973498	0.828416	0.240137
Zn	15	0.294864	1.004377	0.037427
Zn	16	0.789410	0.760330	0.201251
Zn	17	0.167535	0.695380	0.058965
Zn	18	0.653185	0.456135	0.213237
Zn	19	0.974502	0.573836	0.008282
Zn	20	0.532101	0.390135	0.121178
Zn	21	0.893061	0.552119	0.129177
Zn	22	0.492308	0.256202	0.250528
Zn	23	0.748149	0.488355	0.068242
Zn	24	0.271644	0.241691	0.189674
Zn	25	0.178873	0.199926	0.059383
Zn	26	0.662592	0.955096	0.211283
Zn	27	0.895852	0.053039	0.134255
Zn	28	0.422549	0.936520	0.261127
Sn	1	0.935465	-0.015355	-0.008599
Sn	2	0.533254	0.883167	0.130157
Sn	3	0.764518	1.012479	0.053624
Sn	4	0.293029	0.762777	0.219820

Table A4-37: Fractional coordinates of (201)$_{OT}$ 12.50% Sn-doped ZnO using 400 eV cut-off energy, 7×7×1 k-points and Hubbard U value of $U_{d\text{-}Zn}$ = 10 eV and $U_{p\text{-}O}$ = 7 eV.

Element	Atom Number	Fractional coordinates of atoms u	v	w
O	1	0.540621	0.646696	0.059255
O	2	0.062614	0.392487	0.205972
O	3	0.387419	0.580470	0.036403
O	4	0.917491	0.324694	0.181601
O	5	0.730995	0.729890	0.016837
O	6	0.306381	0.515789	0.151842
O	7	0.142183	0.419938	0.099322
O	8	0.698990	0.231175	0.241669
O	9	0.541255	0.133949	0.059581
O	10	0.052373	0.886472	0.205978
O	11	0.386601	0.074371	0.026653
O	12	0.896069	0.803612	0.196307
O	13	0.728654	0.246177	0.008891
O	14	0.307364	0.014707	0.149830
O	15	0.138910	0.940045	0.098999
O	16	0.706762	0.721568	0.231502
O	17	0.048648	0.605979	0.048464
O	18	0.564154	0.392393	0.210944
O	19	0.902334	0.664412	0.030531
O	20	0.444029	0.323093	0.159307
O	21	0.247689	0.735304	0.019105
O	22	0.803702	0.509518	0.143131
O	23	0.655126	0.453133	0.104948
O	24	0.194805	0.217762	0.231487
O	25	-0.008900	0.077774	0.079675
O	26	0.573568	0.893819	0.216954
O	27	0.860559	0.081646	0.039318
O	28	0.440654	0.830213	0.160368
O	29	0.255679	0.242072	0.018714
O	30	0.797262	0.027569	0.151085
O	31	0.664854	0.961330	0.101475
O	32	0.197063	0.732190	0.221805
Zn	1	0.642862	0.698874	0.057879
Zn	2	0.152482	0.453995	0.209728
Zn	3	0.464526	0.607075	-0.001655
Zn	4	0.050700	0.354360	0.109085
Zn	5	0.395970	0.544354	0.130932
Zn	6	0.984709	0.330526	0.240311
Zn	7	0.297493	0.516809	0.038032
Zn	8	0.774473	0.267674	0.200611
Zn	9	0.641594	0.199663	0.057363
Zn	10	0.144042	0.953802	0.209746
Zn	11	0.467617	0.110844	-0.002000
Zn	12	0.048397	0.860884	0.108751
Zn	13	0.396350	0.055546	0.120481

Zn	14	0.973498	0.828416	0.240137
Zn	15	0.294864	1.004377	0.037427
Zn	16	0.789410	0.760330	0.201251
Zn	17	0.167535	0.695380	0.058965
Zn	18	0.653185	0.456135	0.213237
Zn	19	0.974502	0.573836	0.008282
Zn	20	0.532101	0.390135	0.121178
Zn	21	0.893061	0.552119	0.129177
Zn	22	0.492308	0.256202	0.250528
Zn	23	0.748149	0.488355	0.068242
Zn	24	0.271644	0.241691	0.189674
Zn	25	0.178873	0.199926	0.059383
Zn	26	0.662592	0.955096	0.211283
Zn	27	0.895852	0.053039	0.134255
Zn	28	0.422549	0.936520	0.261127
Sn	1	0.935465	-0.015355	-0.008599
Sn	2	0.533254	0.883167	0.130157
Sn	3	0.764518	1.012479	0.053624
Sn	4	0.293029	0.762777	0.219820

Table A4-38: Fractional coordinates of (210) 12.50% Sn-doped ZnO using 400 eV cut-off energy, 7×7×1 k-points and Hubbard U value of $U_{d\text{-}Zn}$ = 10 eV and $U_{p\text{-}O}$ = 7 eV.

Element	Atom Number	Fractional coordinates of atoms u	v	w
O	1	0.825479	0.584156	-0.023221
O	2	0.829148	0.208600	0.121446
O	3	0.078780	0.184227	0.018154
O	4	0.076925	0.827287	0.138912
O	5	0.325499	0.584154	-0.023222
O	6	0.329148	0.208601	0.121446
O	7	0.578780	0.184227	0.018154
O	8	0.576926	0.827287	0.138913
O	9	0.829658	0.384971	0.050280
O	10	0.831673	0.034983	0.168758
O	11	0.082148	0.000108	0.068203
O	12	0.070396	0.650367	0.190261
O	13	0.329659	0.384969	0.050280
O	14	0.331674	0.034983	0.168758
O	15	0.582148	0.000108	0.068203
O	16	0.570394	0.650362	0.190259
O	17	0.831144	0.069059	-0.003333
O	18	0.826498	0.712545	0.115963
O	19	0.074879	0.693380	0.016520
O	20	0.077602	0.321478	0.135925
O	21	0.331144	0.069059	-0.003333
O	22	0.326499	0.712544	0.115963
O	23	0.574878	0.693385	0.016518
O	24	0.577606	0.321478	0.135925
O	25	0.830440	0.890258	0.059208
O	26	0.818219	0.532343	0.188222
O	27	0.122429	0.505192	0.066933
O	28	0.073593	0.139125	0.188607
O	29	0.330441	0.890258	0.059209
O	30	0.318180	0.532347	0.188220
O	31	0.622429	0.505194	0.066939
O	32	0.573592	0.139126	0.188607
Zn	1	0.649948	0.594923	-0.001609
Zn	2	0.637038	0.216382	0.115712
Zn	3	0.904631	0.161645	0.030815
Zn	4	0.900896	0.816447	0.123601
Zn	5	0.149973	0.594925	-0.001609
Zn	6	0.137037	0.216383	0.115712
Zn	7	0.404630	0.161645	0.030815
Zn	8	0.400897	0.816446	0.123601
Zn	9	0.652181	0.393746	0.073208
Zn	10	0.653284	0.046960	0.157034
Zn	11	0.892068	-0.004631	0.072374
Zn	12	0.893519	0.633030	0.188261
Zn	13	0.152181	0.393745	0.073208

Zn	14	0.153285	0.046959	0.157034
Zn	15	0.392068	-0.004631	0.072374
Zn	16	0.393515	0.633023	0.188261
Zn	17	0.655353	0.084460	0.007783
Zn	18	0.635373	0.723136	0.115371
Zn	19	0.898109	0.674111	0.020654
Zn	20	0.902975	0.311450	0.114133
Zn	21	0.155352	0.084460	0.007783
Zn	22	0.135375	0.723136	0.115371
Zn	23	0.398109	0.674113	0.020655
Zn	24	0.402979	0.311449	0.114133
Zn	25	0.653702	0.895824	0.072891
Zn	26	0.646708	0.555229	0.166586
Zn	27	0.153702	0.895824	0.072891
Zn	28	0.146662	0.555220	0.166585
Sn	1	0.888423	0.504486	0.068794
Sn	2	0.880814	0.140825	0.223138
Sn	3	0.388419	0.504485	0.068797
Sn	4	0.380813	0.140826	0.223138

18.75%

Table A4-39: Fractional coordinates of $(002)_{MT}$ 18.75% Sn-doped ZnO using 400 eV cut-off energy, 7×7×1 k-points and Hubbard U value of $U_{d\text{-}Zn}$ = 10 eV and $U_{p\text{-}O}$ = 7 eV.

Element	Atom Number	Fractional coordinates of atoms u	v	w
O	1	0.540836	0.691271	0.004555
O	2	0.210420	0.547868	0.107695
O	3	0.530781	0.705652	0.215800
O	4	0.203035	0.520139	0.331613
O	5	0.536763	0.195890	0.004458
O	6	0.214571	0.016177	0.108157
O	7	0.543749	0.198644	0.218679
O	8	0.198803	0.034368	0.327719
O	9	0.037961	0.695708	0.004428
O	10	0.700522	0.528412	0.107923
O	11	0.042558	0.696721	0.217468
O	12	0.706663	0.521557	0.380685
O	13	0.034802	0.195863	0.025240
O	14	0.683505	0.019349	0.107846
O	15	0.040456	0.196845	0.209544
O	16	0.719546	0.034342	0.331993
Zn	1	0.538670	0.701084	0.368626
Zn	2	0.213003	0.539880	0.013454
Zn	3	0.536166	0.692459	0.131656
Zn	4	0.204958	0.525225	0.248190
Zn	5	0.519266	0.169783	0.369573
Zn	6	0.207078	0.025510	0.013253
Zn	7	0.541976	0.203767	0.132636
Zn	8	0.209549	0.029786	0.246077
Zn	9	0.057799	0.713061	0.369339
Zn	10	0.707797	0.526462	0.015051
Zn	11	0.024994	0.688499	0.132365
Zn	12	0.690333	0.019154	0.013486
Zn	13	0.712558	0.031993	0.248305
Sn	1	0.703296	0.541517	0.261435
Sn	2	0.049003	0.194111	0.386307
Sn	3	0.037721	0.194181	0.118146

Table A4-40: ***Fractional coordinates of (002)$_{OT}$ 18.75% Sn-doped ZnO using 400 eV cut-off energy, 7×7×1 k-points and Hubbard U value of $U_{d\text{-}Zn}$ = 10 eV and $U_{p\text{-}O}$ = 7 eV.***

Element	Atom Number	Fractional coordinates of atoms u	v	w
O	1	0.556974	0.737434	0.075058
O	2	0.229645	0.595843	0.183598
O	3	0.487399	0.532721	0.285414
O	4	0.308110	0.688242	0.386040
O	5	0.556325	0.245872	0.075597
O	6	0.224611	0.099834	0.181959
O	7	0.414286	-0.020836	0.270178
O	8	-0.000454	-0.099585	0.376973
O	9	0.051235	0.738757	0.074979
O	10	0.733897	0.599847	0.188484
O	11	-0.057942	0.544634	0.284863
O	12	0.629297	0.248701	0.377675
O	13	0.052174	0.242232	0.070133
O	14	0.720890	0.086840	0.181902
O	15	0.004402	0.150291	0.292301
O	16	0.561516	-0.250296	0.393620
Zn	1	0.560795	0.729151	-0.009985
Zn	2	0.225627	0.577196	0.100243
Zn	3	0.562284	0.774151	0.226756
Zn	4	0.195586	0.497079	0.321989
Zn	5	0.583054	0.243021	-0.009108
Zn	6	0.220534	0.073018	0.099387
Zn	7	0.576556	0.282309	0.228048
Zn	8	0.311297	-0.006434	0.346280
Zn	9	0.048705	0.708603	-0.009325
Zn	10	0.723535	0.573420	0.108748
Zn	11	0.075955	0.787327	0.225733
Zn	12	0.716172	0.069101	0.099802
Zn	13	0.791276	0.069199	0.357243
Sn	1	0.734101	0.580299	0.346830
Sn	2	0.049592	0.237126	-0.018614
Sn	3	0.051703	0.260177	0.214795

Table A4-41: Fractional coordinates of (100) 18.75% Sn-doped ZnO using 400 eV cut-off energy, 7×7×1 k-points and Hubbard U value of $U_{d\text{-}Zn}$ = 10 eV and $U_{p\text{-}O}$ = 7 eV.

Element	Atom Number	Fractional coordinates of atoms u	v	w
O	1	0.421910	0.248188	0.114998
O	2	0.924780	0.245412	0.358757
O	3	0.421432	0.493901	0.026406
O	4	0.958080	0.484889	0.284479
O	5	0.455739	0.736649	0.099838
O	6	0.916590	0.752717	0.357799
O	7	0.414364	-0.001980	0.025551
O	8	0.948588	0.001191	0.278610
O	9	0.925209	0.251905	0.109821
O	10	0.422036	0.248980	0.354212
O	11	0.927258	0.497189	0.026759
O	12	0.418861	0.498723	0.279127
O	13	0.941341	0.748416	0.107328
O	14	0.431767	0.753500	0.356386
O	15	0.936486	-0.002386	0.024753
O	16	0.404971	0.002038	0.277341
O	17	0.669167	0.243207	-0.002504
O	18	0.174393	0.253990	0.232629
O	19	0.173717	0.500447	0.151838
O	20	0.673165	0.503719	0.393927
O	21	0.676963	0.750460	-0.012191
O	22	0.171025	0.729264	0.250243
O	23	0.170972	0.016787	0.150591
O	24	0.672861	-0.011128	0.386279
O	25	0.177681	0.247911	-0.002045
O	26	0.679904	0.328878	0.231157
O	27	0.675420	0.492587	0.141546
O	28	0.175602	0.507518	0.401019
O	29	0.174467	0.732198	-0.003588
O	30	0.675536	0.835140	0.226936
O	31	0.674141	-0.013257	0.133430
O	32	0.175532	-0.000532	0.401007
Zn	1	0.420696	0.062437	0.106346
Zn	2	0.928253	0.052799	0.359553
Zn	3	0.424398	0.303354	0.037127
Zn	4	0.924372	0.294326	0.278500
Zn	5	0.420541	0.550316	0.106594
Zn	6	0.926781	0.562665	0.359664
Zn	7	0.424101	0.805901	0.023775
Zn	8	0.920830	0.807529	0.276624
Zn	9	0.925094	0.063758	0.105985
Zn	10	0.419063	0.056117	0.358953
Zn	11	0.921394	0.304810	0.030569
Zn	12	0.422186	0.306168	0.275589
Zn	13	0.925573	0.556763	0.106649

Zn	14	0.419950	0.562656	0.359014
Zn	15	0.924163	0.805416	0.024696
Zn	16	0.424093	0.810075	0.276220
Zn	17	0.675471	0.065387	-0.001508
Zn	18	0.174937	0.064666	0.231823
Zn	19	0.170768	0.307967	0.152648
Zn	20	0.672431	0.327330	0.385005
Zn	21	0.673053	0.574112	-0.001566
Zn	22	0.175641	0.547079	0.232784
Zn	23	0.675111	0.303012	0.151408
Zn	24	0.173219	0.334019	0.385121
Zn	25	0.680871	0.797790	0.146660
Zn	26	0.174722	0.824704	0.384948
Sn	1	0.206420	0.803962	0.157339
Sn	2	0.673142	0.803102	0.417605
Sn	3	0.178952	0.062402	-0.033479
Sn	4	0.681599	0.046678	0.226085
Sn	5	0.176640	0.544126	-0.032743
Sn	6	0.696988	0.546134	0.233311

Table A4-42: ***Fractional coordinates of $(101)_{MT}$ 18.75% Sn-doped ZnO using 400 eV cut-off energy, 7×7×1 k-points and Hubbard U value of $U_{d\text{-}Zn}$ = 10 eV and $U_{p\text{-}O}$ = 7 eV.***

Element	Atom Number	Fractional coordinates of atoms u	v	w
O	1	0.428045	0.136088	0.125822
O	2	0.702977	0.770990	0.328656
O	3	0.158604	0.010563	0.107461
O	4	0.452837	0.642693	0.307280
O	5	0.812717	0.330424	0.015917
O	6	0.077210	0.972156	0.219082
O	7	0.549151	0.075323	0.006907
O	8	0.812922	0.830307	0.212414
O	9	0.430206	0.654020	0.126103
O	10	0.707293	0.280105	0.332820
O	11	0.157948	0.518915	0.108338
O	12	0.446715	0.145321	0.308256
O	13	0.812724	0.840866	0.015945
O	14	0.071972	0.452853	0.221875
O	15	0.548206	0.838716	0.006955
O	16	0.817236	0.330005	0.212670
O	17	0.338127	0.352442	0.024041
O	18	0.595648	0.983723	0.221771
O	19	0.068578	0.206094	0.006138
O	20	0.284928	0.823049	0.218701
O	21	0.924845	0.138060	0.119575
O	22	0.287806	0.792302	0.370392
O	23	0.667536	0.015258	0.110633
O	24	0.937219	0.647997	0.310570
O	25	0.316777	0.842417	0.023290
O	26	0.603202	0.475539	0.215823
O	27	0.038322	0.697309	-0.000823
O	28	0.321111	0.342676	0.205491
O	29	0.915220	0.633378	0.123060
O	30	0.201909	0.265376	0.329522
O	31	0.655529	0.509329	0.099725
O	32	0.937373	0.143218	0.316945
Zn	1	0.670420	0.240085	0.056103
Zn	2	0.853387	0.857134	0.291079
Zn	3	0.410026	0.133578	0.039078
Zn	4	0.603068	0.731818	0.259955
Zn	5	0.277762	0.066943	0.165979
Zn	6	0.492899	0.674650	0.393278
Zn	7	1.002140	0.922725	0.149300
Zn	8	0.166374	0.516702	0.376879
Zn	9	0.669852	0.792133	0.055811
Zn	10	0.855718	0.359791	0.291499
Zn	11	0.408047	0.642325	0.039232
Zn	12	0.602386	0.230452	0.266760
Zn	13	0.281376	0.581746	0.165926

Zn	14	0.495300	0.173071	0.393332
Zn	15	1.000310	0.421208	0.150115
Zn	16	0.175520	-0.036787	0.376630
Zn	17	0.767988	0.058095	0.173519
Zn	18	0.990736	0.673264	0.391779
Zn	19	0.514984	0.940536	0.149909
Zn	20	0.662064	0.508124	0.376176
Zn	21	0.190389	0.289636	0.055999
Zn	22	0.355463	0.841568	0.292954
Zn	23	0.496036	0.426876	0.149252
Zn	24	0.651693	-0.003390	0.368845
Zn	25	0.893997	0.626575	0.031717
Zn	26	0.071446	0.206573	0.266869
Sn	1	0.913615	0.136665	0.032835
Sn	2	0.114637	0.734279	0.267293
Sn	3	0.761217	0.551431	0.168709
Sn	4	0.981139	0.142151	0.405420
Sn	5	0.161356	0.765723	0.051919
Sn	6	0.351361	0.350017	0.286664

Table A4-43: Fractional coordinates of (101)$_{OT}$ 18.75% Sn-doped ZnO using 400 eV cut-off energy, 7×7×1 k-points and Hubbard U value of $U_{d\text{-}Zn}$ = 10 eV and $U_{p\text{-}O}$ = 7 eV.

Element	Atom Number	Fractional coordinates of atoms u	v	w
O	1	0.473008	0.173515	0.159457
O	2	0.704476	0.733813	0.367855
O	3	0.215402	0.043686	0.143517
O	4	0.440469	0.635459	0.351809
O	5	0.862911	0.430604	0.030986
O	6	0.098531	0.973293	0.269131
O	7	0.586690	0.206936	0.041469
O	8	0.826199	0.845154	0.249708
O	9	0.472513	0.670291	0.159574
O	10	0.701206	0.300418	0.367707
O	11	0.216988	0.543483	0.145075
O	12	0.421015	0.139854	0.351642
O	13	0.875472	0.885322	0.054447
O	14	0.098747	0.494004	0.275130
O	15	0.586762	0.721845	0.040667
O	16	0.831581	0.334827	0.249737
O	17	0.365186	0.361500	0.049989
O	18	0.586047	0.961782	0.267604
O	19	0.098545	0.248575	0.033117
O	20	0.324609	0.846506	0.251405
O	21	1.002001	0.175822	0.167425
O	22	0.222662	0.618361	0.374624
O	23	0.703326	0.021791	0.148898
O	24	0.941872	0.644310	0.351814
O	25	0.356509	0.857930	0.049172
O	26	0.582661	0.454335	0.260206
O	27	0.087926	0.743078	-0.019522
O	28	0.318319	0.345318	0.258317
O	29	0.972511	0.666634	0.166064
O	30	0.178240	0.098436	0.374565
O	31	0.713633	0.535770	0.143222
O	32	0.930209	0.138750	0.343321
Zn	1	0.620220	0.235815	0.122749
Zn	2	0.849148	0.847306	0.345353
Zn	3	0.360770	0.109268	0.098915
Zn	4	0.586498	0.708725	0.319410
Zn	5	0.020983	0.465020	0.013676
Zn	6	0.242841	0.054105	0.231293
Zn	7	0.727370	0.294690	-0.012146
Zn	8	0.977997	0.920933	0.216351
Zn	9	0.617933	0.738747	0.121360
Zn	10	0.846861	0.343752	0.344981
Zn	11	0.361374	0.610497	0.098590
Zn	12	0.574158	0.201144	0.326203
Zn	13	0.022804	0.951842	0.014369

Zn	14	0.240256	0.556145	0.232532
Zn	15	0.736042	0.802260	-0.010552
Zn	16	0.985853	0.421215	0.216747
Zn	17	0.516541	0.430277	0.014928
Zn	18	0.733343	0.047758	0.233756
Zn	19	0.256914	0.300701	-0.018396
Zn	20	0.468954	0.922025	0.210426
Zn	21	0.136017	0.257485	0.115590
Zn	22	0.354112	0.841602	0.343196
Zn	23	0.250188	0.798726	-0.018522
Zn	24	0.454622	0.416470	0.209058
Zn	25	0.858904	0.616512	0.098661
Zn	26	0.082225	0.233340	0.326258
Sn	1	0.865303	0.159456	0.104645
Sn	2	0.107748	0.765847	0.338771
Sn	3	0.509358	0.925659	-0.014407
Sn	4	0.740795	0.542798	0.230766
Sn	5	0.119571	0.740961	0.111412
Sn	6	0.321691	0.350740	0.352697

Table A4-44: Fractional coordinates of (102)$_{MT}$ 18.75% Sn-doped ZnO using 400 eV cut-off energy, 7×7×1 k-points and Hubbard U value of $U_{d\text{-}Zn}$ = 10 eV and $U_{p\text{-}O}$ = 7 eV.

Element	Atom Number	Fractional coordinates of atoms u	v	w
O	1	0.479946	0.425036	0.138844
O	2	0.742996	0.921980	0.326044
O	3	-0.024613	0.917533	0.004990
O	4	0.279890	0.443229	0.182667
O	5	0.247963	0.426389	0.326367
O	6	0.985816	0.933053	0.138585
O	7	0.504722	0.311028	0.007418
O	8	0.784890	0.938391	0.185319
O	9	0.479724	0.922303	0.139762
O	10	0.744586	0.424864	0.325481
O	11	-0.023867	0.430891	0.005005
O	12	0.282044	0.917499	0.172526
O	13	0.251992	0.920752	0.320349
O	14	0.985831	0.419779	0.139127
O	15	0.520903	1.086255	-0.001141
O	16	0.779899	0.417554	0.184815
O	17	0.358290	0.683367	0.040709
O	18	0.611351	0.173482	0.230564
O	19	0.146096	0.673061	0.080050
O	20	0.411641	0.175366	0.257069
O	21	0.115956	0.674200	0.228168
O	22	0.813196	0.175070	0.058130
O	23	0.640653	0.171446	0.091785
O	24	0.914550	0.674256	0.260573
O	25	0.313533	0.181601	0.075560
O	26	0.620828	0.674692	0.220638
O	27	0.136013	0.173673	0.079587
O	28	0.415568	0.674615	0.259697
O	29	0.120543	0.173492	0.223665
O	30	0.811568	0.674182	0.074814
O	31	0.635372	0.682860	0.082790
O	32	0.919580	0.174715	0.265652
Zn	1	0.570637	0.422083	0.074791
Zn	2	0.832836	0.924730	0.270164
Zn	3	0.390489	0.419370	0.073947
Zn	4	0.648018	0.924252	0.276226
Zn	5	0.065851	0.921929	0.057630
Zn	6	0.333246	0.422583	0.266957
Zn	7	0.148032	0.421855	0.282779
Zn	8	0.881314	0.924343	0.056374
Zn	9	0.560832	0.929828	0.070964
Zn	10	0.832628	0.420690	0.267981
Zn	11	0.374088	0.921404	0.092061
Zn	12	0.648734	0.421864	0.276136
Zn	13	0.066829	0.423269	0.057371

Zn	14	0.333280	0.923152	0.258810
Zn	15	0.147072	0.923747	0.283170
Zn	16	0.882874	0.422217	0.056925
Zn	17	0.708504	0.173470	0.164547
Zn	18	0.974625	0.671310	0.343387
Zn	19	0.239835	0.672333	0.022517
Zn	20	0.495162	0.173955	0.189784
Zn	21	0.210346	0.674597	0.158249
Zn	22	0.467891	0.169398	0.334930
Zn	23	0.227187	0.172834	0.006818
Zn	24	0.495701	0.671526	0.189114
Zn	25	0.719104	0.669934	0.007877
Zn	26	0.993772	0.175136	0.191757
Sn	1	0.702968	0.190377	0.002734
Sn	2	0.994819	0.677595	0.187881
Sn	3	0.727605	0.681659	0.153132
Sn	4	1.001056	0.197522	0.344630
Sn	5	0.218393	0.187477	0.153058
Sn	6	0.493554	0.698361	0.337982

Table A4-45: Fractional coordinates of (102)$_{OT}$ 18.75% Sn-doped ZnO using 400 eV cut-off energy, 7×7×1 k-points and Hubbard U value of $U_{d\text{-}Zn}$ = 10 eV and $U_{p\text{-}O}$ = 7 eV.

Element	Atom Number	Fractional coordinates of atoms u	v	w
O	1	0.481438	0.425190	0.148585
O	2	0.736219	0.922137	0.336736
O	3	0.001150	0.921347	0.001402
O	4	0.280213	0.429286	0.177175
O	5	0.250553	0.423705	0.336137
O	6	0.985873	0.950163	0.146041
O	7	0.506776	0.420162	0.003942
O	8	0.784075	0.932718	0.176153
O	9	0.482734	0.922350	0.147840
O	10	0.736272	0.427357	0.336697
O	11	0.000728	0.437899	0.000524
O	12	0.279976	0.927510	0.176550
O	13	0.250309	0.925713	0.336389
O	14	0.985070	0.424487	0.149852
O	15	0.506432	0.935901	0.003441
O	16	0.779426	0.425956	0.175738
O	17	0.346452	0.673745	0.058635
O	18	0.612687	0.173597	0.235240
O	19	0.144333	0.672643	0.093097
O	20	0.413556	0.174461	0.270730
O	21	0.116784	0.674165	0.242212
O	22	0.843002	0.177403	0.057654
O	23	0.647238	0.176508	0.089586
O	24	0.907084	0.674379	0.275700
O	25	0.346993	0.174442	0.057126
O	26	0.609497	0.674249	0.237468
O	27	0.145348	0.177217	0.088532
O	28	0.414948	0.675124	0.273955
O	29	0.108699	0.174107	0.244422
O	30	0.851221	0.675189	0.058915
O	31	0.644553	0.674509	0.087754
O	32	0.907411	0.174640	0.275156
Zn	1	0.566355	0.420730	0.082082
Zn	2	0.838687	0.927524	0.294582
Zn	3	0.365898	0.422134	0.109615
Zn	4	0.644600	0.927342	0.286428
Zn	5	0.073488	0.920334	0.073542
Zn	6	0.356252	0.423554	0.294394
Zn	7	0.151697	0.423645	0.293550
Zn	8	0.867157	0.924363	0.107718
Zn	9	0.569927	0.926993	0.080810
Zn	10	0.838453	0.419663	0.294340
Zn	11	0.366586	0.924250	0.109485
Zn	12	0.645400	0.419179	0.285706

Zn	13	0.068111	0.426835	0.074783
Zn	14	0.355738	0.924653	0.294429
Zn	15	0.151617	0.922334	0.293608
Zn	16	0.866900	0.423546	0.109643
Zn	17	0.448732	0.678348	0.006170
Zn	18	0.705133	0.176077	0.172572
Zn	19	0.228322	0.672794	0.019831
Zn	20	0.488096	0.172582	0.203396
Zn	21	0.210368	0.678496	0.172291
Zn	22	0.946579	0.179492	0.005274
Zn	23	0.229897	0.172375	0.014334
Zn	24	0.481553	0.673259	0.203155
Zn	25	0.731202	0.670272	0.013958
Zn	26	0.985671	0.176756	0.209837
Sn	1	0.720164	0.199328	0.004270
Sn	2	0.991108	0.691827	0.205399
Sn	3	0.426318	0.179732	-0.029176
Sn	4	0.703948	0.683671	0.171445
Sn	5	0.201787	0.179227	0.174098
Sn	6	0.919848	0.681838	-0.030552

Table A4-46: Fractional coordinates of $(103)_{MT}$ 18.75% Sn-doped ZnO using 400 eV cut-off energy, 7×7×1 k-points and Hubbard U value of $U_{d\text{-}Zn}$ = 10 eV and $U_{p\text{-}O}$ = 7 eV.

Element	Atom Number	Fractional coordinates of atoms u	v	w
O	1	0.302482	0.571942	0.037128
O	2	0.558473	0.203000	0.155289
O	3	0.153528	0.493906	0.090995
O	4	0.407906	0.125898	0.212826
O	5	0.166426	0.498423	0.260618
O	6	0.946931	0.897672	0.087993
O	7	0.553291	0.189495	-0.009690
O	8	0.800803	0.846126	0.135312
O	9	0.303367	0.085305	0.037028
O	10	0.558488	0.708267	0.155583
O	11	0.154343	0.014344	0.091435
O	12	0.407779	0.643547	0.212863
O	13	0.167294	0.020188	0.260988
O	14	0.947113	0.392924	0.092185
O	15	0.553055	0.710645	-0.009185
O	16	0.801785	0.304797	0.135963
O	17	0.445819	0.398835	0.075908
O	18	0.682379	0.015564	0.240388
O	19	0.034867	0.690683	0.006855
O	20	0.270195	0.307974	0.177061
O	21	0.066518	0.710077	0.167315
O	22	0.887955	0.117412	-0.002196
O	23	0.669930	0.013353	0.091452
O	24	0.907890	0.637458	0.222272
O	25	0.443932	0.897840	0.073784
O	26	0.696604	0.518485	0.211494
O	27	0.052379	0.202334	-0.018590
O	28	0.284913	0.817011	0.157688
O	29	0.051623	0.199834	0.168573
O	30	0.810240	0.579567	0.033789
O	31	0.655714	0.505844	0.079456
O	32	0.905001	0.135281	0.224318
Zn	1	0.615030	0.208381	0.062986
Zn	2	0.853256	0.863699	0.234101
Zn	3	0.463822	0.163492	0.131848
Zn	4	0.739442	0.793606	0.269900
Zn	5	0.248125	0.546315	0.118548
Zn	6	0.996244	0.947273	0.001499
Zn	7	0.105657	0.453597	0.184976
Zn	8	0.848715	0.877904	0.045285
Zn	9	0.615384	0.763379	0.062948
Zn	10	0.853325	0.357402	0.234107
Zn	11	0.463880	0.670019	0.131914
Zn	12	0.738880	0.295461	0.269910
Zn	13	0.248684	0.049625	0.118313

Zn	14	0.995641	0.394664	0.008178
Zn	15	0.107762	1.006785	0.185216
Zn	16	0.852760	0.328992	0.045303
Zn	17	0.515771	0.430523	0.007822
Zn	18	0.741842	0.047582	0.157904
Zn	19	0.353464	0.354664	0.044271
Zn	20	0.603289	0.979414	0.187163
Zn	21	0.112428	0.735001	0.063718
Zn	22	0.365139	0.363365	0.211587
Zn	23	0.345559	0.850018	0.054294
Zn	24	0.605420	0.480035	0.177756
Zn	25	0.199916	0.775017	0.278111
Zn	26	0.958363	0.142289	0.149444
Sn	1	0.235629	0.294607	0.279447
Sn	2	0.966917	0.661312	0.143873
Sn	3	0.483418	0.915393	-0.028106
Sn	4	0.751263	0.548769	0.118433
Sn	5	0.157085	0.253375	0.013739
Sn	6	0.344562	0.853273	0.242322

Table A4-47: Fractional coordinates of (103)$_{OT}$ 18.75% Sn-doped ZnO using 400 eV cut-off energy, 7×7×1 k-points and Hubbard U value of $U_{d\text{-}Zn}$ = 10 eV and $U_{p\text{-}O}$ = 7 eV.

Element	Atom Number	Fractional coordinates of atoms u	v	w
O	1	0.309915	0.582927	0.026177
O	2	0.558037	0.223639	0.152122
O	3	0.161875	0.495783	0.072278
O	4	0.411647	0.130864	0.212234
O	5	0.175021	0.472424	0.242543
O	6	0.946775	0.888720	0.091652
O	7	0.027243	0.307853	0.279631
O	8	0.794883	0.853528	0.118346
O	9	0.309234	0.077214	0.026212
O	10	0.557963	0.709005	0.150907
O	11	0.161929	0.011656	0.072694
O	12	0.411741	0.641565	0.211776
O	13	0.178997	0.003030	0.244161
O	14	0.947854	0.398727	0.095198
O	15	0.066253	1.131305	0.288916
O	16	0.796507	0.295867	0.125329
O	17	0.445926	0.414813	0.073776
O	18	0.753631	-0.011082	0.239920
O	19	0.290207	0.315262	0.147725
O	20	0.619623	1.008773	0.277656
O	21	0.056947	0.709691	0.168582
O	22	0.900313	0.133330	-0.003011
O	23	0.659323	0.013148	0.083663
O	24	0.878041	0.606765	0.215478
O	25	0.447552	0.915982	0.073831
O	26	0.700963	0.511205	0.193751
O	27	0.276775	0.804801	0.161466
O	28	0.619850	0.533790	0.290484
O	29	0.059811	0.205107	0.146590
O	30	0.818861	0.580680	0.026242
O	31	0.659407	0.514144	0.053499
O	32	0.899021	0.100502	0.216316
Zn	1	0.607592	0.233551	0.063901
Zn	2	0.829540	0.854790	0.213370
Zn	3	0.461856	0.170931	0.130809
Zn	4	0.678883	0.787198	0.270257
Zn	5	0.256119	0.546478	0.108281
Zn	6	0.997141	0.888930	0.007926
Zn	7	0.082135	0.455052	0.213486
Zn	8	0.855029	0.879810	0.036420
Zn	9	0.605310	0.740170	0.062374
Zn	10	0.841713	0.302479	0.212927
Zn	11	0.461449	0.671177	0.130502
Zn	12	0.656436	0.289058	0.279027
Zn	13	0.256622	0.047917	0.108922

Zn	14	0.994549	0.451365	0.008072
Zn	15	0.092442	1.006720	0.204572
Zn	16	0.854666	0.325202	0.044320
Zn	17	0.517601	0.421223	0.008368
Zn	18	0.728492	0.043837	0.147631
Zn	19	0.353644	0.351338	0.036634
Zn	20	0.579790	0.976342	0.194985
Zn	21	0.123322	0.734028	0.063728
Zn	22	0.363777	0.362376	0.203953
Zn	23	0.355127	0.852952	0.035047
Zn	24	0.593718	0.486176	0.196757
Zn	25	0.213241	0.754084	0.240618
Zn	26	0.961884	0.144544	0.149401
Sn	1	0.173779	0.236988	0.315008
Sn	2	0.955463	0.653397	0.152829
Sn	3	0.509791	0.944882	-0.013395
Sn	4	0.747469	0.549799	0.104528
Sn	5	0.097460	0.221874	0.051585
Sn	6	0.352258	0.855941	0.243682

Table A4-48: Fractional coordinates of (110) 18.75% Sn-doped ZnO using 400 eV cut-off energy, 7×7×1 k-points and Hubbard U value of $U_{d\text{-}Zn}$ = 10 eV and $U_{p\text{-}O}$ = 7 eV.

Element	Atom Number	Fractional coordinates of atoms u	v	w
O	1	0.207414	0.391173	-0.002498
O	2	0.216519	0.889347	0.163632
O	3	0.461442	0.814695	0.077739
O	4	0.446712	0.310030	0.263614
O	5	0.721073	0.412719	-0.011465
O	6	0.710461	0.884472	0.170322
O	7	0.960363	0.813805	0.078017
O	8	0.958966	0.293455	0.271040
O	9	0.211542	0.141899	0.086973
O	10	0.215980	0.642742	0.259108
O	11	0.447228	0.051888	-0.002656
O	12	0.457934	0.597493	0.170607
O	13	0.701795	0.172244	0.049259
O	14	0.711062	0.644584	0.252384
O	15	0.970266	0.055178	-0.002539
O	16	0.959952	0.586651	0.171022
O	17	0.209483	0.639321	0.080993
O	18	0.210147	0.135870	0.251455
O	19	0.465983	0.564431	-0.001605
O	20	0.467625	0.075195	0.163325
O	21	0.718052	0.640489	0.079985
O	22	0.698471	0.140317	0.271375
O	23	0.958530	0.563481	-0.001749
O	24	0.959588	0.060416	0.163734
O	25	0.203871	0.889226	-0.001191
O	26	0.296074	0.400574	0.163243
O	27	0.459695	0.309712	0.066002
O	28	0.458429	0.841861	0.251617
O	29	0.700220	0.907063	0.007325
O	30	0.799172	0.388768	0.169401
O	31	0.963833	0.307033	0.070570
O	32	0.972363	0.831836	0.251518
Zn	1	0.029435	0.409187	-0.000838
Zn	2	0.026498	0.894333	0.161375
Zn	3	0.269199	0.806310	0.079183
Zn	4	0.269357	0.293383	0.241266
Zn	5	0.542463	0.407049	-0.000961
Zn	6	0.512488	0.902487	0.161508
Zn	7	0.767274	0.812485	0.080829
Zn	8	0.780568	0.288251	0.251734
Zn	9	0.022014	0.141690	0.078915
Zn	10	0.043319	0.676456	0.242000
Zn	11	0.269578	0.045051	0.009817
Zn	12	0.265528	0.573528	0.170652
Zn	13	0.522702	0.143533	0.070065

Zn	14	0.540120	0.691980	0.241897
Zn	15	0.788146	0.056036	-0.001676
Zn	16	0.765412	0.563754	0.169700
Zn	17	0.016047	0.643972	0.079759
Zn	18	0.030532	0.145027	0.241901
Zn	19	0.289110	0.540178	0.008967
Zn	20	0.273989	0.058029	0.169994
Zn	21	0.526398	0.647055	0.079950
Zn	22	0.521754	0.158065	0.250592
Zn	23	0.269520	0.307720	0.078346
Zn	24	0.286853	0.795872	0.241319
Zn	25	0.775096	0.326145	0.070221
Zn	26	0.799803	0.791686	0.241731
Sn	1	0.766027	0.593491	-0.029843
Sn	2	0.748167	0.075111	0.165968
Sn	3	0.009019	0.873643	-0.027486
Sn	4	0.009956	0.391929	0.175521
Sn	5	0.509282	0.876263	-0.027468
Sn	6	0.508723	0.402936	0.170483

Table A4-49: ***Fractional coordinates of (112)$_{MT}$ 18.75% Sn-doped ZnO using 400 eV cut-off energy, 7×7×1 k-points and Hubbard U value of $U_{d\text{-}Zn}$ = 10 eV and $U_{p\text{-}O}$ = 7 eV.***

Element	Atom Number	Fractional coordinates of atoms u	v	w
O	1	0.385503	0.582366	0.069639
O	2	0.893483	0.723016	0.210864
O	3	0.325346	0.332409	0.063136
O	4	0.813146	0.478870	0.210471
O	5	0.889106	0.070841	0.063314
O	6	0.401488	0.214419	0.209501
O	7	0.820831	0.830438	0.072259
O	8	0.308680	0.971382	0.219581
O	9	0.620459	0.461926	0.011539
O	10	0.140438	0.661581	0.147012
O	11	0.556295	0.228108	0.011034
O	12	0.072360	0.411689	0.145062
O	13	0.152807	-0.038716	-0.001110
O	14	0.642604	0.106300	0.157740
O	15	0.072379	0.712994	0.010016
O	16	0.570268	0.874487	0.167594
O	17	0.130103	0.463874	0.007711
O	18	0.640660	0.652279	0.136891
O	19	0.066985	0.205239	0.018929
O	20	0.589589	0.352591	0.166723
O	21	0.654786	0.026902	-0.014896
O	22	0.146198	0.134806	0.156008
O	23	0.557097	0.787418	-0.001389
O	24	0.061854	0.914909	0.136030
O	25	0.886342	0.584056	0.062574
O	26	0.390354	0.700986	0.220590
O	27	0.822976	0.335910	0.063995
O	28	0.317657	0.456470	0.210133
O	29	0.390840	0.075239	0.063689
O	30	0.900474	0.221531	0.210933
O	31	0.323993	0.821524	0.078868
O	32	0.834879	0.980341	0.221064
Zn	1	0.423757	0.713630	0.019954
Zn	2	0.901459	0.862902	0.167256
Zn	3	0.292347	0.480758	0.019364
Zn	4	0.810947	0.621602	0.157447
Zn	5	0.897409	0.214478	0.018266
Zn	6	0.405622	0.351737	0.156195
Zn	7	0.319765	0.106176	0.157882
Zn	8	0.777827	0.956580	0.019688
Zn	9	0.140760	0.798191	0.081560
Zn	10	0.672410	0.961428	0.219496
Zn	11	0.068395	0.571606	0.071987
Zn	12	0.540599	0.631227	0.231317
Zn	13	0.636471	0.322717	0.069807

Zn	14	0.186495	0.367742	0.231492
Zn	15	0.574594	0.085065	0.061716
Zn	16	0.074665	0.206480	0.240009
Zn	17	0.644093	0.791022	0.082558
Zn	18	0.152169	0.899143	0.231432
Zn	19	0.555813	0.552827	0.081083
Zn	20	0.058862	0.725207	0.230709
Zn	21	0.141183	0.328068	0.061883
Zn	22	0.643763	0.468588	0.231268
Zn	23	0.779876	0.491855	0.019006
Zn	24	0.287956	0.593324	0.168152
Zn	25	0.823029	0.105594	0.157840
Zn	26	0.315310	0.954722	0.019487
Sn	1	0.075560	0.054814	0.072322
Sn	2	0.577980	0.210363	0.239252
Sn	3	0.894083	0.725364	-0.012142
Sn	4	0.394590	0.847269	0.175329
Sn	5	0.378848	0.213177	-0.014205
Sn	6	0.903984	0.364939	0.160933

Table A4-50: Fractional coordinates of (112)$_{OT}$ 18.75% Sn-doped ZnO using 400 eV cut-off energy, 7×7×1 k-points and Hubbard U value of $U_{d\text{-}Zn}$ = 10 eV and $U_{p\text{-}O}$ = 7 eV.

Element	Atom Number	Fractional coordinates of atoms u	v	w
O	1	0.438518	0.584520	0.017264
O	2	0.889823	0.729009	0.192755
O	3	0.280460	0.344375	0.037385
O	4	0.810295	0.464197	0.190913
O	5	0.892851	0.084406	0.039931
O	6	0.403045	0.234577	0.182220
O	7	0.788604	0.825769	0.028365
O	8	0.301572	0.961241	0.181843
O	9	0.201470	0.624763	0.068685
O	10	0.591886	0.799500	0.251269
O	11	0.053221	0.397478	0.110351
O	12	0.535040	0.497117	0.240401
O	13	0.646066	0.155175	0.119253
O	14	0.099635	0.287707	0.250937
O	15	0.043100	-0.004172	0.251596
O	16	0.539567	0.896250	0.100717
O	17	0.643494	0.645441	0.123252
O	18	0.158798	0.748101	0.195848
O	19	0.536940	0.379175	0.082053
O	20	0.058964	0.506135	0.241151
O	21	0.139289	0.144002	0.120309
O	22	0.657283	0.266061	0.263113
O	23	0.545838	0.010347	0.240917
O	24	0.046136	0.893594	0.088522
O	25	0.904285	0.593444	0.059206
O	26	0.413274	0.715003	0.181406
O	27	0.806966	0.336035	0.017510
O	28	0.304423	0.476828	0.169839
O	29	0.400000	0.102673	0.048603
O	30	0.901643	0.217302	0.191188
O	31	0.290596	0.842481	0.028007
O	32	0.807370	0.969948	0.170323
Zn	1	0.372627	0.718190	0.018970
Zn	2	0.926351	0.865696	0.151449
Zn	3	0.305229	0.495237	0.041003
Zn	4	0.807151	0.612023	0.150104
Zn	5	0.941760	0.243482	-0.000941
Zn	6	0.452762	0.400536	0.171189
Zn	7	0.300007	0.115968	0.150607
Zn	8	0.759218	0.987517	0.018050
Zn	9	0.174583	0.791556	0.098531
Zn	10	0.696459	0.910119	0.223567
Zn	11	0.059597	0.538488	0.070091
Zn	12	0.555178	0.648527	0.229146
Zn	13	0.681549	0.288706	0.069698

Zn	14	0.200891	0.398337	0.221906
Zn	15	0.564090	0.037302	0.049230
Zn	16	0.049570	0.139313	0.221789
Zn	17	0.651958	0.784704	0.079493
Zn	18	0.159060	0.899434	0.230901
Zn	19	0.586357	0.538670	0.058203
Zn	20	0.024103	0.650483	0.222054
Zn	21	0.125811	0.278308	0.059127
Zn	22	0.671967	0.410383	0.232437
Zn	23	0.776815	0.490062	0.007807
Zn	24	0.275105	0.628912	0.171414
Zn	25	0.820219	0.115782	0.139145
Zn	26	0.297772	0.992836	0.009488
Sn	1	0.075589	0.042626	0.040301
Sn	2	0.559524	0.165957	0.210629
Sn	3	0.871931	0.700222	-0.024049
Sn	4	0.456372	0.875542	0.190906
Sn	5	0.438195	0.268920	0.006635
Sn	6	0.962356	0.373467	0.198760

Table A4-51: Fractional coordinates of (200) 18.75% Sn-doped ZnO using 400 eV cut-off energy, 7×7×1 k-points and Hubbard U value of $U_{d\text{-}Zn}$ = 10 eV and $U_{p\text{-}O}$ = 7 eV.

Element	Atom Number	Fractional coordinates of atoms u	v	w
O	1	0.958844	0.221921	0.106099
O	2	1.006379	0.384453	-0.012215
O	3	0.983870	0.707723	0.047214
O	4	0.885629	1.036368	-0.001204
O	5	0.432671	0.269003	0.078943
O	6	0.425861	0.533506	0.000982
O	7	0.429995	0.712666	0.116601
O	8	0.456771	0.881872	-0.004579
O	9	0.732823	0.273213	0.229196
O	10	0.737050	0.506635	0.129211
O	11	0.551739	0.596588	0.261472
O	12	0.635886	0.989913	0.151412
O	13	0.286526	0.138015	0.231227
O	14	0.233323	0.456169	0.173032
O	15	0.145500	0.753345	0.231460
O	16	0.144015	0.949798	0.130145
Zn	1	0.888599	0.043138	0.106898
Zn	2	0.929285	0.212310	-0.000591
Zn	3	0.918794	0.523462	0.048276
Zn	4	0.919186	0.863974	0.007625
Zn	5	0.422922	-0.042887	0.080627
Zn	6	0.298287	0.368677	0.008651
Zn	7	0.425581	0.519085	0.106483
Zn	8	0.421241	0.710428	0.006417
Zn	9	0.576122	0.120262	0.220431
Zn	10	0.699661	0.306930	0.121807
Zn	11	0.670402	0.440289	0.241641
Zn	12	0.205119	0.267834	0.160666
Zn	13	0.138002	0.751749	0.131705
Sn	1	0.685108	0.725102	0Z183318
Sn	2	0.093237	-0.027987	0.240122
Sn	3	0.217848	0.565020	0.267312

Table A4-52: Fractional coordinates of (201)$_{MT}$ 18.75% Sn-doped ZnO using 400 eV cut-off energy, 7×7×1 k-points and Hubbard U value of $U_{d\text{-}Zn}$ = 10 eV and $U_{p\text{-}O}$ = 7 eV.

Element	Atom Number	Fractional coordinates of atoms u	v	w
O	1	0.277784	0.069187	-0.012161
O	2	0.876241	0.841096	0.152196
O	3	0.729431	0.792846	0.071622
O	4	0.263573	0.574644	0.221775
O	5	0.112071	0.996138	0.057535
O	6	0.626453	0.733792	0.209078
O	7	0.971995	0.758547	0.017325
O	8	0.494749	0.660032	0.139013
O	9	0.278475	0.583867	-0.003382
O	10	0.879230	0.361720	0.162221
O	11	0.729852	0.277357	0.071503
O	12	0.263649	0.063203	0.222740
O	13	0.111051	0.458808	0.057336
O	14	0.626523	0.225129	0.209328
O	15	0.971472	0.541660	0.017804
O	16	0.495498	0.175859	0.139257
O	17	0.869395	0.107236	0.030981
O	18	0.396190	0.877104	0.192973
O	19	0.197202	0.767391	0.099123
O	20	0.750570	0.538549	0.211943
O	21	0.596658	0.960248	0.060215
O	22	0.126062	0.753059	0.212817
O	23	0.409403	0.895005	0.029511
O	24	1.008696	0.672750	0.144768
O	25	0.805291	0.574126	-0.001203
O	26	0.374906	0.366589	0.160724
O	27	0.230016	0.283230	0.091401
O	28	0.757428	0.041275	0.210811
O	29	0.612432	0.468785	0.069551
O	30	0.129745	0.264437	0.221689
O	31	0.409275	0.390680	0.006865
O	32	0.992193	0.167045	0.135240
Zn	1	0.948965	0.891494	0.097624
Zn	2	0.494811	0.669174	0.248346
Zn	3	0.822423	0.839573	0.038241
Zn	4	0.348095	0.613869	0.191489
Zn	5	0.204341	0.018089	0.038186
Zn	6	0.716905	0.774112	0.178853
Zn	7	0.585814	0.703417	0.108968
Zn	8	0.080518	0.481882	0.260272
Zn	9	0.943218	0.389757	0.097047
Zn	10	0.494976	0.173957	0.248437
Zn	11	0.821505	0.322565	0.035872
Zn	12	0.348741	0.094246	0.191701
Zn	13	0.201835	0.516423	0.038391

Zn	14	0.717402	0.266942	0.179090
Zn	15	0.586076	0.206422	0.108910
Zn	16	0.087050	0.987626	0.251345
Zn	17	0.450309	0.893646	0.108077
Zn	18	0.994628	0.700920	0.240627
Zn	19	0.327551	0.854320	0.007616
Zn	20	0.832037	0.579662	0.181490
Zn	21	0.683303	0.013764	0.048416
Zn	22	0.218816	0.798562	0.191352
Zn	23	0.320178	0.347010	0.007714
Zn	24	0.839238	0.081121	0.180445
Zn	25	0.071352	0.206769	0.095132
Zn	26	0.586898	0.958525	0.249943
Sn	1	0.097566	0.720994	0.106665
Sn	2	0.612864	0.472752	0.277796
Sn	3	0.448953	0.392406	0.093674
Sn	4	0.972844	0.160104	0.243821
Sn	5	0.699378	0.520212	0.007467
Sn	6	0.219288	0.296544	0.188844

Table A4-53: Fractional coordinates of (201)$_{OT}$ 18.75% Sn-doped ZnO using 400 eV cut-off energy, 7×7×1 k-points and Hubbard U value of $U_{d\text{-}Zn}$ = 10 eV and $U_{p\text{-}O}$ = 7 eV.

Element	Atom Number	Fractional coordinates of atoms u	v	w
O	1	0.859074	0.857269	0.094330
O	2	0.399385	0.610284	0.231696
O	3	0.722339	0.758588	0.028986
O	4	0.264568	0.572489	0.171433
O	5	0.095467	0.987952	0.011594
O	6	0.630588	0.728818	0.168468
O	7	0.488532	0.655586	0.098840
O	8	0.032597	0.470265	0.242846
O	9	0.855523	0.348201	0.090423
O	10	0.398868	0.109338	0.231914
O	11	0.721160	0.275098	0.028419
O	12	0.267364	0.058442	0.171596
O	13	0.096573	0.472621	0.018494
O	14	0.630864	0.243185	0.166696
O	15	0.487951	0.177558	0.098784
O	16	0.022672	0.985449	0.241387
O	17	0.363418	0.858287	0.085543
O	18	0.919961	0.501631	0.200316
O	19	0.217370	0.791167	0.040883
O	20	0.759679	0.545610	0.171521
O	21	0.594783	0.959062	0.027082
O	22	0.157349	0.771315	0.222202
O	23	0.982419	0.666982	0.047726
O	24	0.531135	0.444860	0.242011
O	25	0.357157	0.357441	0.086195
O	26	0.892138	0.023971	0.230817
O	27	0.221790	0.290926	0.035200
O	28	0.751379	0.040949	0.170832
O	29	0.597151	0.461452	0.028763
O	30	0.134389	0.248679	0.170516
O	31	0.988410	0.175263	0.105669
O	32	0.528607	0.945260	0.243466
Zn	1	0.942338	0.897499	0.068885
Zn	2	0.483965	0.672365	0.231450
Zn	3	0.811074	0.829682	0.009317
Zn	4	0.357523	0.609409	0.151843
Zn	5	0.182417	0.017765	-0.002074
Zn	6	0.718428	0.768155	0.140140
Zn	7	0.578897	0.702718	0.080420
Zn	8	0.117095	0.494600	0.221749
Zn	9	0.940347	0.396691	0.069278
Zn	10	0.483040	0.175661	0.231470
Zn	11	0.809733	0.325008	0.008475
Zn	12	0.358040	0.109392	0.151592
Zn	13	0.183262	0.522915	-0.001829

Zn	14	0.719017	0.278196	0.139900
Zn	15	0.578614	0.203252	0.079933
Zn	16	0.107077	0.982104	0.221488
Zn	17	0.453106	0.898301	0.079306
Zn	18	0.983722	0.712365	0.223382
Zn	19	0.308964	0.827703	0.008550
Zn	20	0.846206	0.606539	0.161180
Zn	21	0.679817	-0.006646	0.009125
Zn	22	0.218592	0.796431	0.149617
Zn	23	0.311258	0.328108	-0.001093
Zn	24	0.837658	0.104157	0.160911
Zn	25	0.075144	0.212239	0.068749
Zn	26	0.608240	0.976992	0.210989
Sn	1	0.075348	0.725690	0.077048
Sn	2	0.626774	0.482363	0.246118
Sn	3	0.452673	0.399693	0.035381
Sn	4	0.968102	0.225102	0.214532
Sn	5	0.674624	0.495395	-0.033002
Sn	6	0.227370	0.293276	0.140757

Table A4-54: Fractional coordinates of (210) 18.75% Sn-doped ZnO using 400 eV cut-off energy, 7×7×1 k-points and Hubbard U value of $U_{d\text{-}Zn}$ = 10 eV and $U_{p\text{-}O}$ = 7 eV..

Element	Atom Number	Fractional coordinates of atoms u	v	w
O	1	0.203814	0.959183	-0.002253
O	2	0.199306	0.597921	0.124306
O	3	0.440608	0.574479	0.018573
O	4	0.450473	0.215444	0.133640
O	5	0.703138	0.962247	-0.002180
O	6	0.701090	0.599014	0.119675
O	7	0.956709	0.572621	0.019912
O	8	0.950389	0.213909	0.125950
O	9	0.192848	0.775406	0.051566
O	10	0.196497	0.418939	0.176465
O	11	0.445643	0.390277	0.073909
O	12	0.446023	0.026618	0.189711
O	13	0.707798	0.777025	0.061026
O	14	0.701221	0.414554	0.177164
O	15	0.945510	0.389373	0.073172
O	16	0.958371	0.027466	0.189438
O	17	0.200126	0.457428	-0.002779
O	18	0.198670	0.104470	0.115490
O	19	0.457137	0.072898	0.020277
O	20	0.450507	0.709907	0.126229
O	21	0.693760	0.463543	-0.001270
O	22	0.701743	0.104868	0.116833
O	23	0.941925	0.065027	0.019690
O	24	0.940049	0.706992	0.126438
O	25	0.190414	0.280924	0.061963
O	26	0.198236	0.921861	0.167643
O	27	0.451114	0.885988	0.070849
O	28	0.457717	0.529482	0.197368
O	29	0.687372	0.282395	0.062578
O	30	0.696287	0.926560	0.167471
O	31	0.953940	0.886407	0.072137
O	32	0.944615	0.528826	0.199078
Zn	1	0.026017	0.968481	0.009561
Zn	2	0.005930	0.602223	0.124077
Zn	3	0.265694	0.553752	0.030502
Zn	4	0.269369	0.208999	0.124768
Zn	5	0.523245	0.968849	0.010074
Zn	6	0.508341	0.602462	0.116286
Zn	7	0.780888	0.555275	0.029812
Zn	8	0.768004	0.210787	0.125508
Zn	9	0.012766	0.778704	0.061889
Zn	10	0.017805	0.433095	0.166506
Zn	11	0.251326	0.385949	0.075749
Zn	12	0.266471	0.023356	0.178388
Zn	13	0.527346	0.782315	0.061840

Zn	14	0.524688	0.430640	0.166030
Zn	15	0.750458	0.387915	0.073567
Zn	16	0.778946	0.024558	0.177466
Zn	17	0.023598	0.471125	0.009098
Zn	18	0.005747	0.105130	0.114792
Zn	19	0.281698	0.052522	0.029366
Zn	20	0.272002	0.701929	0.113403
Zn	21	0.514804	0.474466	0.009048
Zn	22	0.509855	0.106921	0.124127
Zn	23	0.255291	0.879846	0.070571
Zn	24	0.281024	0.515747	0.188514
Zn	25	0.763062	0.886630	0.071408
Zn	26	0.767093	0.516495	0.188197
Sn	1	0.748536	0.083658	-0.006778
Sn	2	0.749328	0.717352	0.161357
Sn	3	-0.001941	0.273035	0.027009
Sn	4	0.003124	0.905429	0.193269
Sn	5	0.493755	0.271712	0.030796
Sn	6	0.501062	0.905863	0.192900